Development of a Human Body Model for the Analysis of Side Impact Automotive Thoracic Trauma

by

Patrick A. Forbes

A thesis
presented to the University of Waterloo
in fulfillment of the
thesis requirement for the degree of

Master of Applied Science

in

Mechanical Engineering

Waterloo, Ontario, Canada, 2005

I hereby declare that I am the sole author of this thesis. This is a true copy of the thesis, including any required final revisions, as accepted by my examiners.

I understand that my thesis may be made electronically available to the public.

Abstract

Occupant thoracic injury incurred during side impact automotive crashes constitutes a significant portion of all fatal and non-fatal automotive injuries. The limited space between the impacting vehicle and occupant can result in significant loads and corresponding injury prior to deceleration of the impacting vehicle. Within the struck vehicle, impact occurs between the occupant and various interior components. Injury is sustained to human structural components such as the thoracic cage or shoulder, and to the internal visceral components such as the heart, lungs, or aorta. Understanding the mechanism behind these injuries is an important step in improving the side impact crash safety of vehicles. This study is focused on the development of a human body numerical model for the purpose of predicting thoracic response and trauma in side impact automotive crash.

The human body model has been created using a previously developed thoracic numerical model, originally used for predicting thoracic trauma under simple impact conditions. The original version of the thorax model incorporated three-dimensional finite element representations of the spine, ribs, heart, lungs, major blood vessels, rib cage surface muscles and upper limbs. The present study began with improvements to the original thorax model and furthered with the development of remaining body components such that the model could be assessed in side impact conditions.

The improvements to the thoracic model included improved geometry and constitutive response of the surface muscles, shoulder and costal cartilage. This detailed thoracic model was complimented with a pelvis, lower limbs, an abdomen and a head to produce the full body model. These components were implemented in a simplified fashion to provide representative response without significant computational costs. The model was

developed and evaluated in a stepwise fashion using experimental data from the literature including side abdominal and pelvic pendulum impact tests.

The accuracy of the model response was investigated using experimental testing performed on post mortem human subjects (PMHS) during side and front thoracic pendulum impacts. The model produced good agreement for the side thoracic and side shoulder pendulum impact tests and reasonable correlation during the frontal thoracic pendulum impact test. Complex loading via side sled impact tests was then investigated where the body was loaded unbelted in a NHTSA-type and WSU-type side sled test system. The thorax response was excellent when considering force, compression and injury (viscous criterion) versus time. Compression in the thorax was influenced by the arm position, which when aligned with the coronal plane produced the most aggressive form of compressive loading possible. The simplified components provided good response, falling slightly outside experimental response corridors defined as one standard deviation from the average of the experimental PMHS data. Overall, the predicted model response showed reasonable agreement with the experimental data, while at the same time highlighting areas for future developments. The results from this study suggested that the numerical finite element model developed herein could be used as a powerful tool for improving side impact automotive safety.

Acknowledgements

I wish to gratefully thank my supervisor Professor Duane S. Cronin for the support he has provided to me throughout this research. Without his academic guidance, numerical wizardry and moral support, this project may never have been completed.

I am thankful for the financial support from my industry sponsors Dr. Yih-Charng Deng of General Motors, who supplied the model used throughout this research, and Mr. Marc Boismenu of General Motors of Canada Limited. As well, I am extremely thankful of the Natural Sciences and Engineering Research Council of Canada who provided me with the financial support during the second half of this work.

I would especially like to thank my family and friends who have shown unwavering support throughout this entire endeavor, without whom none of this would have been possible. A very special thank you goes to Kyra Stuurman who has provided an unending string of encouragement and motivation during the dark hours and late nights observed throughout this project. My parents, Barrie and Susan Forbes who have provided support with knowledge of their own experiences and intuition only a parent can provide. My co-workers and friends, Chris Carr, Alex Greer and Christian Kaufmann, have provided guidance both technically and personally till the very end of this thesis. I hope that my life will always be filled with people possessing such extreme competence and open heartedness. Thank you.

Table of Contents

CHAPTER 3

CHAPTER 6

List of Figures

List of Tables

Nomenclature

Acronyms:

AIS	Abbreviated Injury Scale
AMVO	Anthropometry of Motor Vehicle Occupants
ATD	Anthropometric Test Devices
BioSID	Bio Side Impact Dummy
C	Compression Criteria
CE	Contractile Element
EuroSID	European Side Impact Dummy
FMVSS	Federal Motor Vehicle Safety Standard
GEBOD	GEnerator of BOdy Data
GM	General Motors
L1,L2,L3,L4	First, Second, Third, Fourth Lumbar Vertebrae
NHTSA	National Highway Traffic Safety Administration
HUMOS	HUman MOdel for Safety
NISS	New Injury Severity Score
PE	Parallel Element
PMHS	Post Mortem Human Subject
RAMSIS	Rechnergestiitztes Anthropologisch-Matchematisches System zur Insassen-Simulation
SID	Side Impact Dummy
T1..T12	First to Twelfth Thoracic Vertebrae
THUMS	Total Human Model for Safety
UMTRI	University of Michigan Transportation Research Institute
VC	Viscous Criteria
WSU	Wayne State University
WorldSID	World Side Impact Dummy

Mathematical Symbols:

$Accel$	Measured acceleration response
$Accel_{norm}$	Normalized acceleration response
B	Overall dummy biofidelity rating
B_i	Body region biofidelity
C	Chest compression
$C,C_1,C_2,$	Lung model material constants
C,b_1,b_2,b_3	Heart model material constants
C_o	Sound speed
D	Chest depth

$Deflection$	Measured subject deflection response
$Deflection_{norm}$	Normalized deflection response
E_{ij}	Lagrangian strain components
F_{CE}	Active muscle force
F_{PE}	Passive muscle force
F_{max}	Peak isometric muscle force
f_{pe}	Normalized passive muscle force
$Force$	Measured subject force response
$Force_{norm}$	Normalized force response
G	Shear modulus
I_1,I_2,I_3	Strain invariants
I_{xx},I_{yy},I_{zz}	Head principal moment of inertia
K	Bulk modulus
K_{sh}	Dimensionless shape parameter
k_{12}	Lobdell model skin elasticity
k_{23},c_{23}	Lobdell model Voigt element
kve_{23},cve_{23}	Lobdell model Maxwell element
L_0	Initial muscle length
L_{max}	Muscle length at which maximum force is generated
m_1,m_2,m_3	Lobdell model masses
M_{std}	Mass of 50th percentile male
$MASS$	Mass of test subject
n	Number of beams representing muscle
Δ	Typical alveolar diameter when unstressed
$PCSA$	Physiological Cross-Sectional Area of muscle
P	Chest penetration
p	Hydrostatic pressure
$RIBY$	4th or 8th rib lateral acceleration
$R_{i,j,k}$	Response rating
$T12Y$	Twelfth thoracic vertebrae lateral acceleration
TTI	Thoracic trauma index
U_i	Body region weighting factor
$V_{i,j}$	Test condition weighting factor
$W_{i,j,k}$	Response measurement weighting factor
W	Strain energy
α,β	Lung model material constants
μ	Damping coefficient for simplified rubber model
ρ	Density
σ_{max}	Peak isometric muscle stress

-- CHAPTER 1 --

Introduction

1.1 Background

Injuries sustained to the human body during automotive collisions range from minor to fatal and inflict substantial societal costs. This is particularly true during side impact collision resulting in thoracic injury, which in 2001 was shown to account for 38% of fatalities and 59% of non-fatal injuries (NHTSA, 2004). Today, the desire to improve safety to minimize or avoid any fatalities and injuries is a primary field of research for both automotive designers and legislators. However, this area of research is relatively new, initiating in the 1950's, but not really addressed significantly until the latter 1960's, when designers recognized the substantial loss of life as a result of automotive crashes, and the ability to prevent this loss through improved crash design.

Colonel John Stapp, pioneered much of the research in human tolerance and subjected himself to rocket sled tests in order to establish human acceleration tolerances (Stapp, 1951) commonly experienced during automotive impacts. Often times Stapp was left with debilitating injuries, however his research inspired a plethora of investigators to further the understanding of human tolerance and injury through the development of injury assessment techniques.

Considering that ethical circumstances do not allow for live human subject testing in the regimes of interest (i.e. trauma injury), researchers undertook post mortem human subject (PMHS) testing programs in the 1960's, where numerous subjects were tested in simulated automotive impacts in order to evaluate the injury mechanisms and tolerance to impact. The results provided significant insight, allowing for the correlation of globally measurable responses such as thoracic compression with injury. However, the significant costs and complications inherent with this type of research result in the several limitations. First, injuries incurred during the impact allow only for the use of each subject under a single impact condition this leads to small data sets and high variability. Second, the subjects lack the physiological response of a living human, where aspects such as muscle tone and circulation can play an important role in the injury response. Third, PMHS are generally of an advanced age, unrepresentative of the majority of the driving population. And lastly, the results provide only global responses, which lack the local injury response of individual organs and tissues best described through stress and strain.

In an effort to reduce some of the complications associated with PMHS testing, automotive engineers set out to develop an artificial human surrogate that would provide representative human body response that was repeatable. One of the first artificial human surrogates, known as the crash test dummy, was the Hybrid III developed in 1973. While this was not the first artificial human surrogate ever developed, it represented the first surrogate designed to provide response characteristics comparable to post mortem human subject testing. Since then, advancements in design have given dummies the ability to provide estimations of injury, in some cases differentiating between specific organs. A more recent development, the World Side Impact Dummy (WorldSID) is considered the most advanced artificial human surrogate, for evaluation of side impact trauma. At present, crash test dummies are used in full automotive impacts in order to design and assess new vehicle safety features. For example, seats, seatbelts, airbags and even automotive structural components have all been designed and evaluated by studying the resultant injury response of the crash test dummies. However, the use of these dummies and the testing itself possess several limitations. The surrogate dummies lack the ability

to provide organ specific injury response information through local stress and strain, while the testing often involves the destruction of at least a portion of an automobile, resulting in substantial costs as well as long cycle times.

1.2 Research Justification

In an effort to alleviate the costs and limitations of the automotive safety research techniques described above, engineers have pursued the development of advanced finite element models. Finite element modeling can utilize detailed numerical representations of the human body with accurate geometric and material properties. These models can be subjected to a given loading condition, producing response characteristics intended to mimic the human body in a real world scenario. The primary advantage of human body models, however, is that they provide insight into the onset of injury and resultant local response characteristics thereafter through the use of stress and strain data measured throughout the entire model. Such information is unobtainable during volunteer or post mortem human subject testing. These models remove the issue of repeatability, allowing for the implementation of parametric studies often used by vehicle designers to improve automotive safety.

Ideally, a highly detailed model of the entire human body is desired for predictive evaluation of injury under a variety of loading conditions. Although computing power has increased significantly over the past several years, some simplifications are still required to minimize the size of the calculation. This aspect is also important if these models are to be used in a practical sense by vehicle designers. By identifying the key human structures of interest in a particular impact situation, a highly detailed model of these components can be completed with simplified, but representative models of the remaining components used to ensure that the global impact response is appropriate.

As previously noted, crash statistics show that for side impact collisions, injuries sustained to the thoracic region constitute a substantial portion of non-fatal and fatal injuries. Compared to frontal impacts, occupants are at a more substantial risk to injury during side impacts due to the reduced automotive structure between the occupant and

the impacting object. In frontal collisions, the vehicle engine compartment and frame are designed to crush and absorb the energy of the impact, thereby minimizing intrusion of the vehicle interior on the occupant. Although a similar design approach is taken for side collisions, the reduced amount of space in this area inherently results in an increased level of intrusion. As such, the research presented here involves the development of a full human body model for the study of side impact thoracic injury with detailed representations of the thoracic region and simplified, but representative models of the remaining components.

1.3 Research Objective and Scope

The objective of this research has been outlined with two main goals. The first goal was to develop a full human body model based on a thoracic model through the integration of simplified body components. Several improvements to the thoracic model were also addressed. Deng et al. (1999) developed the first iteration of the detailed thoracic model and incorporated three-dimensional finite element representation of the spine, ribs, heart, lungs and major blood vessels. Chang (2001) developed the second iteration, expanding the model to include rib cage surface muscles and upper limbs, with improvements to several material models. The iteration presented here included improvements to the thoracic geometries, finite element mesh and material models. This detailed thorax has been integrated with a simplified pelvis, legs, abdomen and head. The second goal of this research was to validate the full body model using progressively more complex loading scenarios, starting with simple pendulum impacts to the thorax (front and side) and shoulder, and moving up to full body impact scenarios such as side sled tests. Validation was achieved by comparing the model response to post mortem human subject responses. By developing the model such that validation was achieved in a variety of impact scenarios, the model can further be used to evaluate thoracic injury in real world crashes. This constitutes the future goal for this model.

A detailed knowledge and understanding of the key thoracic structures and impact situation is presented in Chapter 2; beginning with automotive crash statistics justifying the need for this type of research. The anatomy, method of injury, and injury threshold

data of the thorax and its separate components are reviewed from an automotive crash perspective. Development details of the thorax model during the first two iterations are summarized throughout the anatomical descriptions. The current methods of experimental thoracic injury analysis are reviewed, detailing the research conducted throughout their development. A review of physical human surrogates used to improve automotive safety, including dummies and post mortem human subjects, is also presented. Finally, this chapter summarizes the development of previous numerical thoracic models, along with the limits of each model and the benefits each has provided for improving automotive safety.

The knowledge presented in Chapter 2 forms a basis for the additional developments and improvements performed on the existing thoracic model (Deng et al., 1999, Chang, 2001), which are detailed in Chapter 3. The additions and improvements made to the detailed thoracic model were identified as necessary based on preliminary analysis of the model during the validation impact scenarios. It was believed that these improvements would provide a more accurate response of the thorax. Chapter 4 presents the experimental resources used to validate the model under the various impact scenarios, along with the modeling techniques used to accurately simulate the experiments. Validation of the model is discussed and evaluated in Chapter 5 showing correlation to experimental data and highlighting areas requiring improvement. Chapter 6 presents conclusions derived during the development and validation of the model and recommendations for future work to improve the response of the model and for possible uses of the model.

An Appendix follows, detailing a preliminary study conducted to investigate the applicability of this human body model under even more complex loading conditions. The study involves loading the model in a blunt ballistic impact scenario. The Appendix represents a self-contained analysis of the model under the specific loading condition and follows a similar analysis technique as described in the body of the thesis.

-- CHAPTER 2 --

Literature Review – Modeling Human Body Response

2.1 Introduction

The task of investigating the thoracic injury response of the human body during automotive side impacts requires the understanding of a significant amount of information. Firstly, a detailed comprehension of the human thoracic anatomy and physiology is required. The thoracic region is comprised of several major organs, surrounded by a protective structure that is connected to adjacent body regions through complicated joints and attachments. Each organ or substructure presents its own level of complexity in terms of geometry, material properties and mechanical response. Secondly, a detailed understanding of how and when injury is incurred is also essential. In the literature, this aspect has been investigated using two different approaches, termed global and local in this thesis. On a global level, the human body can be observed during simulated automotive impacts using externally measurable responses. Researchers develop injury criteria based on these measurements, which are correlated to the resultant injury; providing information regarding what forms of loading cause specific forms of

injury. On a local level, researchers may use excised organs subjected to standard forms of loading (i.e. tensile, compressive, shear, etc.) and measure the resultant responses. Force and deflection may be measured to generate standard engineering relations such as stress and strain to assign material properties to each organ.

When applied to numerical modeling of the human thorax, bridging the gap between global and local measures is essential. Within any model, the anatomical geometry of the individual organs and structures provide the overall shape and connectivity of the human body, while the material properties govern the response of the different structures under loading. To ensure that a model provides responses comparable to real life, it is first validated to globally measurable responses as obtained from experimentation. Once achieved, the model can then be used with confidence to predict and further the understanding of injury on a local tissue level. For the research presented in this thesis, the model has been developed to produce the globally measurable response characteristics observed in existing experimental data. It is intended that model be used to analyze the local injury response in future research.

This chapter intends to present the relevant background information required to both justify and understand the substantial undertaking that is involved in human body modeling. Automotive crash statistics are presented highlighting the need for the extensive automotive crash research performed in the past and still required for the future. Necessary anatomy and physiology of the human thorax are presented, along with material properties and mechanical threshold values of individual thoracic organs and structures. The development of pertinent automotive injury criteria is reviewed and a summary of the threshold values along with government-approved injury criteria has been listed. Finally, the current methods used to predict thoracic response during automotive impacts are summarized, which includes the use of post mortem and artificial human surrogates, and numerical models.

2.2 Automotive Crash Statistics

A study by the department of the National Highway Traffic Safety Administration (NHTSA) showed that the cost of motor vehicle accidents occurring in the United States in 2000 totaled $230.6 billion dollars (Blincoe et al., 2000). This was approximately 2.3 percent of the U.S. Gross Domestic Product and accounted for productivity losses, property damage, medical costs, rehabilitation costs, travel delay, legal and court costs, emergency services (medical, police and fire), insurance administration costs and the costs to employers. The direct medical costs due to injuries were $32.6 billion dollars, representing 14 percent of the total cost.

Safety features such as the seatbelt help to reduce automotive crash injuries and fatalities, and the associated costs. In the year 2000 it was estimated that the seatbelt prevented 11,900 fatalities and 325,000 serious injuries, saving society $50 billion in resultant costs (Blincoe et al., 2000). Over the previous 26 years, the seatbelt prevented 135,000 fatalities and 3.8 million injuries, saving society an estimated $585 billion. Blincoe et al. went on to say that had full use of the seatbelt been implemented during that 26-year period, approximately 315,000 additional fatalities and 5.2 million additional serious injuries could have been prevented, saving society $913 billion in resultant costs.

In the year 2001, the Fatal Analysis Reporting System (FARS) reported 42,116 fatalities and 3.0 million injuries as a result of automotive crashes (NHTSA, 2001). A study of the same data reported by the 2001 FARS indicated that 26.8% of all fatalities were caused by side impact collisions (NHTSA, 2004). Some 19,554 people were reported involved in side impact collisions, resulting in a 58% fatality rate. The NHTSA (2004) report also highlighted that 38% of side impact fatalities and 59% of side impact non-fatal injuries were incurred in the thoracic region.

The above statistics highlight three important points. First, the cost of automotive injury has a severe economic impact. Second, the advancement of automotive safety features reduces injuries and deaths sustained during automotive crashes, thereby lessening the

economic impact. Third, injury to the thoracic region in side impact collisions poses a serious threat to automotive passengers. These aspects cement the need for improved understanding and reduction of thoracic trauma in side impact.

2.3 Automotive Thoracic Trauma

An automotive crash is commonly subdivided into three events known as the primary, secondary and tertiary impacts. The primary impact occurs between the vehicle and the outside impact surface, the secondary impact is between the vehicle occupant and various components within the vehicle, and the tertiary impact is between the internal organs of the occupant and the enveloping human body structure. Thoracic trauma sustained during the secondary and tertiary impact, is caused by deformation of biological tissues, resulting in damage to anatomical structures or alterations in normal function (Viano et al., 1989a). These injuries are termed non-penetrating and are defined as any injury sustained when the body is struck by or strikes a blunt object at a moderate velocity, such that the energy of the impact is dissipated throughout the body (Viano et al., 1989a). The present section discusses the thoracic anatomy and physiology, and the potential thoracic injuries to various organs that can result during automotive impact. Available mechanical thresholds and material properties for relevant organs as obtained from previous research are also presented. Throughout, a description of the original model used throughout the present research as developed by Deng et al. (1999) and Chang (2001) is provided. It should be made clear though, that these descriptions constitute the state of the model available to the present researcher at the beginning of the study. Improvements made to the model during the present study follow in another chapter.

2.3.1 Thoracic Cage

Thoracic Cage Anatomy and Physiology

The human thorax is designated as the section of the body between the neck and abdomen. The thorax is made up of 12 pairs of rib, 12 thoracic vertebrae and intervertebral discs, a sternum, costal cartilage and internal organs. It provides support to the shoulder system and acts as a cage (thoracic cage) to protect the heart, lungs, pleurae,

trachea and great vessels. Figure 2.1(a) shows a detailed diagram of the thoracic cage. In the original model by Deng et al. (1999) these components were present, excluding the intervertebral discs. Instead each vertebra was connected using spherical joints that were given moment and damping-rotation curves based on Panjabi (1976). Figure 2.1(b) shows the model as developed with the aforementioned components. Although not apparent within this figure, the lumbar and cervical vertebrae were also modeled. The geometry for these components as well as all components within the model was obtained from a commercial data package of human geometry (Viewpoint Data Labs, Orem, Utah).

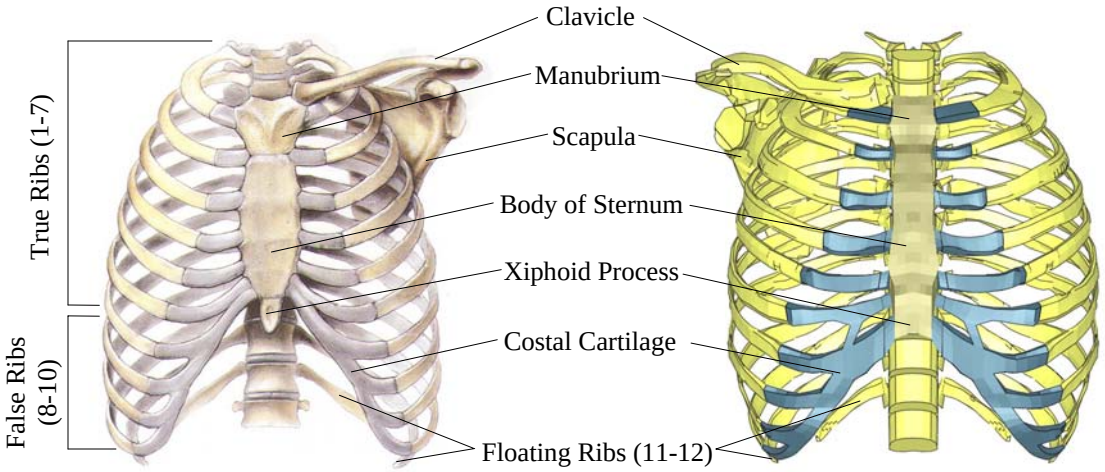

Figure 2.1 Thoracic cage skeletal structure (a) anatomy text (modified from Moore and Dalley, 1999) (b) numerical model

Each rib is different in length, shape and orientation, accounting for variable mechanical properties of the thoracic cage. The ribs are classified as true ribs (1-7), false ribs (8-10) or floating ribs (11-12). True ribs connect between the vertebrae and sternum; false ribs connect between the vertebrae and the rib immediately above it; and floating ribs connect only to the vertebrae. Similar to many human bones, the ribs are made up of a spongy interior termed trabecular and a hard exterior termed cortical. Within the model each rib presented characteristic lengths, cross-sectional areas and curvature using eight elements through thickness and approximately sixty elements along its length. Although this may

be considered a relatively coarse mesh, simulations of rib bending tests indicated the mesh was acceptable. A uniform material model was used to represent both the trabecular and cortical components of the ribs with properties that are detailed in a following section.

A typical rib has two ends, a posterior and an anterior, and an intermediate region called the body. The posterior end of the rib connects to the vertebrae and has three facets for connection. Two facets connect directly to the body of the vertebrae superior and inferior, while the remaining facet connects to the transverse process of the vertebrae. Figure 2.2 shows the posterior end of the 7th rib as connected to the 6th and 7th vertebrae. Within the model, this connection was accommodated using a single spherical joint to represent the three facets with moment and damping-rotation properties as obtained from Schultz et al. (1974a).

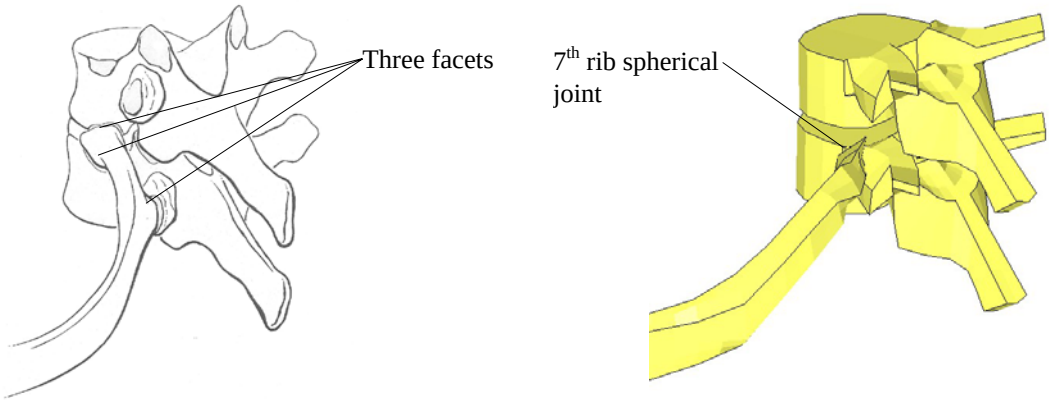

Figure 2.2 Costovertebral articulation of the 7th rib (a) anatomical (modified from Moore and Dalley, 1999) (b) thoracic numerical model

Costal cartilage, which is attached at the anterior end of every rib, connects true ribs to the sternum, connects false ribs to the rib superior and rounds off the floating ribs. Sternocostal ligaments connect the cartilage to the sternum at the sternocostal joints. These joints along with the relatively high ductility of the costal cartilage facilitate the majority of the thoracic elasticity. Within the model, the costal cartilage was given elastic material properties as reported by Viano (1986), however augmentation was performed to account for the bone-cartilage-bone complex (Deng, 1999). This is further

examined in a following chapter. The connection to the sternum was accommodated using two connective schemes. The first pair of costal cartilages was connected directly to the sternum representing a primary cartilaginous joint with zero freedom of motion, while the remaining pairs were connected using a spherical joint representing a synovial joint with three degrees of freedom. Moment and damping-rotation curves as obtained from Shultz et al. (1974) were used to represent the effects of the joint and surrounding ligamentous structures.

The sternum is a flat elongated bone that forms the middle of the front part of the thorax. It is divided into the three following parts: manubrium, body, and xiphoid process. The clavicle and first ribs are attached to the manubrium, the second to seventh ribs are attached to the body and no ribs are attached to the xiphoid process. The sternum is composed of a trabecular core that is covered by a thin cortical coating. Within the model, a uniform material was used to represent the trabecular and cortical bone with properties that are detailed in a following section.

The thoracic vertebrae increase in size moving from top to bottom (T1 to T12). Each vertebra is made up of two regions, the body and the arch, which join to make a vertebral canal. The body connects to superior and inferior vertebrae through intervertebral discs and facet joints. Similar to the costal cartilage and costovertebral joints, these joints contribute to the elasticity and mobility of the thoracic cage. As previously mentioned, within the model all of these connections were accommodated using spherical joints. Both the body and arch of the thoracic vertebrae were modeled while only the body of the lumbar and cervical vertebrae was modeled. All vertebrae were rigid parts with uniform material properties to represent both the trabecular and cortical bone as obtained from Yamada (1971). Figure 2.3 shows three thoracic vertebrae as compared to the modeled vertebrae.

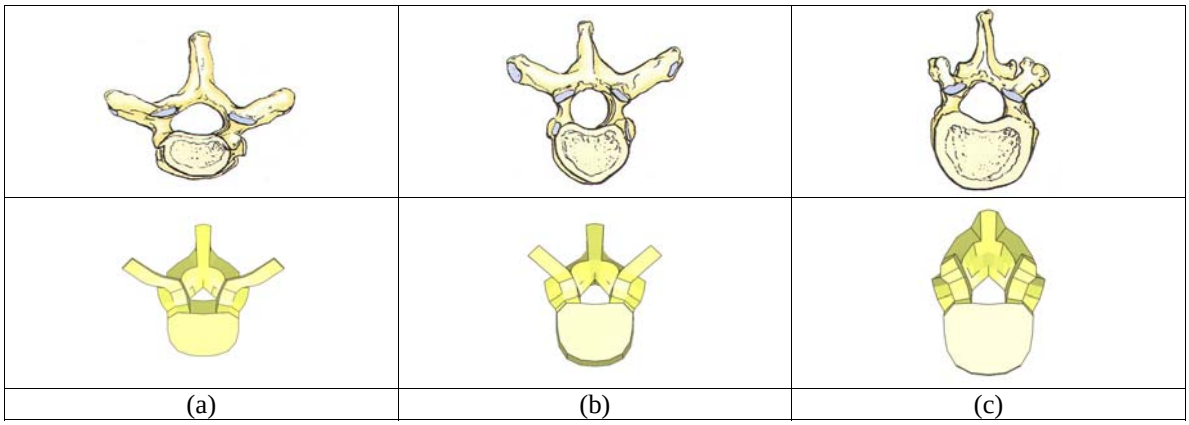

Figure 2.3 Thoracic vertebrae, anatomical vs. numerical (a) T1 (b) T6 (c) T12

Thoracic Cage Injury

Injury to the thoracic cage is most commonly experienced through rib fracture occurring when the ultimate strength of the bone is exceeded. Although rib fracture itself is not life threatening, multiple fractures may indicate significant levels of trauma. More importantly, the number of rib fractures is commonly reported in PMHS testing and used as a trauma evaluation parameter. In bone, numerous failure modes can occur, however, it is probable that during blunt impact to the ribs, as is most often the case for automotive trauma, failure occurs in bending (Nahum and Melvin, 2002). Figure 2.4(a) shows a simple beam in bending. The upper part of the beam experiences tensile loading while the lower part of the beam experiences compressive loading.

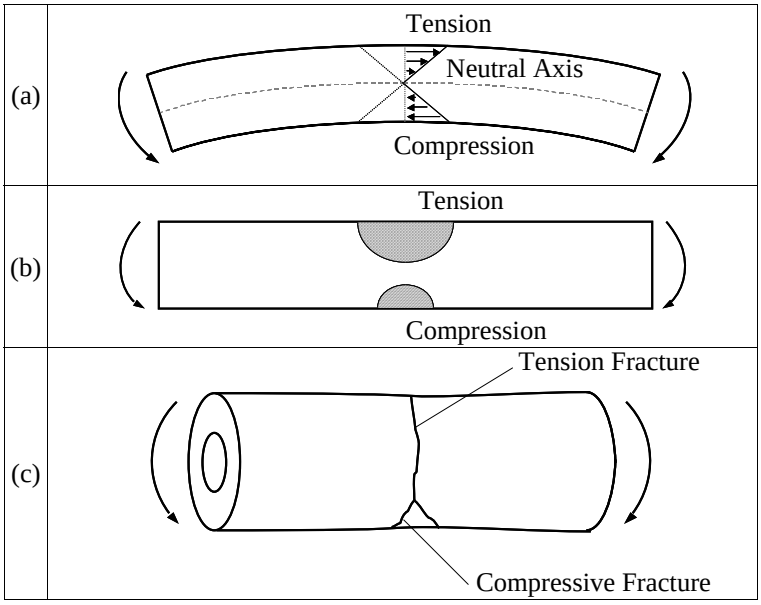

Figure 2.4 Bone in bending: (a) stress pattern (b) yielding pattern (c) fracture pattern

As bending progresses the bone will initially yield on the tensile side due to bone being weaker in tension than in compression (Nahum and Melvin, 2002). Figure 2.4(b) shows the plastic zones on both sides during the yielding stage. However, it should be noted that bone does not present a significant amount of yielding before fracture and the diagram above is exaggerated for clarity. At fracture, the tensioned side of the bone fails along a direction perpendicular to loading and the compressed side fails along a diagonal or oblique plane. Figure 2.4(c) shows this fracture mechanism and outlines the dominant influence of the tensile failure.

Ribs located in the middle of the cage are the most prone to fracture due to their lower cross-sectional area (Nahum and Melvin, 2002). Multiple rib fractures are a clear indication of violent trauma, which can consist of high forces and/or combined loading conditions. Flail chest occurs when at least three successive ribs fracture at two points and is an example of a severe case of multiple rib fracture. When this happens a significant portion of the cage is free to move and opposes the direction of breathing; impairing ventilation, thereby reducing blood oxygenation, which can cause the onset of shock (Nahum and Melvin, 2002).

Costochondral separation occurs when a single rib or multiple ribs separate from the costal cartilage (Chapon, 1984). This type of injury can be found with or without rib fracture and is not life threatening. Because the rib still remains connected to the cage through intercostal muscles, the most significant effects are impaired breathing and discomfort (Chapon, 1984).

Injury to the thoracic cage can often be an indication of visceral damage to the soft tissue encased therein (Nahum and Melvin, 2002). Fractures to the eleventh and twelfth rib suggest visceral damage of the liver, spleen and diaphragm; since these organs are located near the bottom of the thoracic cage. Fracture of the first rib is rare due to its strength and protected position, but is considered very serious due to the high forces required and commonly results in severe visceral damage (Nahum and Melvin, 2002).

Fracture of the sternum is also an indication of serious injury. However, with modern safety features such as seatbelts and airbags, this type of injury is less prevalent in automotive impacts. In the case where both of these features are not present, the sternum is most commonly fractured at the sternum angle due to impact with the steering wheel (Chapon, 1984).

Thoracic Cage Mechanical Properties and Thresholds

The mechanical properties and threshold values associated with any bone in the human body are influenced by many factors including age, sex, disease, hormone levels, direction of loading, shape and size. Extensive research has been conducted to obtain response and failure characteristics of various bones in numerous loading patterns. Early work summarized by Yamada (1970) listed quasi-static tensile, compressive, bending and torsion test results of compact, cancellous and whole bones of both human and animals. More recent data can be found in Cowin (2001), however the data from Yamada's (1970) work still remains a consistent resource for elastic modulii and failure properties. Figure 2.5 shows properties associated with the bending of the whole femur evaluated over specific age ranges and Table 2.1 shows bending properties of various whole bones for subjects 20-39 years old. Both highlight the high level of variability present with age and within individual human body. To model each bony component accurately, these variations must be taken into account.

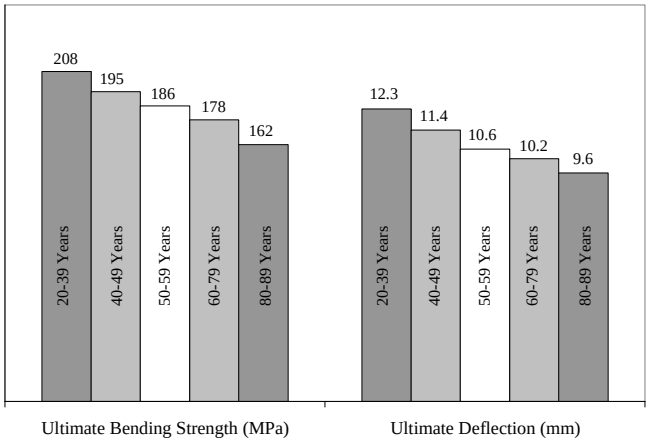

Figure 2.5 Age effects on bending properties of the whole femur

Table 2.1 Human bone properties of varying location for people 20-39 years of age (Yamada, 1970)

Bone	Bending Breaking Load (kg)	Ultimate Bending Strength (kg/mm^2)	Ultimate Deflection (mm)	Cross-sectional Area (mm^2)	Elastic Modulus (kg/mm^2)
Femur	277 ± 11	21.2 ± 0.8	12.3 ± 0.34	295	1870
Tibia	296 ± 11	21.7 ± 0.4	10.0 ± 0.42	210	1220
Fibula	45 ± 2	20.6 ± 0.9	16.2 ± 0.56	60	1260
Humerus	151 ± 12	19.5 ± 0.4	10.0 ± 0.15	180	1020
Radius	60 ± 7	21.9 ± 0.6	10.4 ± 0.24	75	1620
Ulna	72 ± 5	21.6 ± 0.5	11.1 ± 0.13	80	1570

Load and failure characteristics of ribs have been studied to a lesser degree than whole long bones. Because of their geometric irregularities it is difficult to conduct standard tensile and compressive tests (Granik and Stein, 1973). Granik and Stein (1973) investigated the modulus of elasticity and ultimate strength of the 6^{th} and 7^{th} rib by subjecting four-inch long segments to simply supported bending tests. The results suggested that the modulus of elasticity and ultimate strength of rib bone were 15-50% lower than values measured for many long bones.

Schultz et al. (1974b) investigated the load deflection characteristic of whole ribs. Right ribs 2, 4, 6, 8, 9 and 10 were loaded in a fixed-free fashion in increments of 0.25 kg to a maximum load of 0.75 kg. Each rib was secured at its vertebral end and loaded at its sternal end in 6 directions; medial and lateral, superior and inferior, and anterior and posterior. These results have been used extensively to validate the response of ribs within many numerical models, and were used by Deng et al. (1999) in the development of the original thoracic numerical model.

More recently, Yoganandan and Pintar (1998) conducted simply supported bending tests, similar to Granik and Stein (1973), on 100mm rib segments from the right and left 7^{th} and 8^{th} ribs. For each rib, a total of 120 samples were tested producing an extensive sample size to determine the elastic modulus. Table 2.2 shows the elastic modulus results of

both simply supported bending tests, which highlights a significant difference between the two sources. For the model presented here Deng et al. (1999) used an elastic modulus of 26000 MPa. This value is clearly elevated from both resources, however, was justified because of the integration scheme used in the model. The rib elements use a single point integration scheme, reducing the apparent bending stiffness of the ribs and requiring an elevated cumulus to compensate. Even still, this value is only twice the value of Granik and Stein (1973) and ten times the value of Yoganandan and Pintar (1998).

Table 2.2 Rib elastic modulus

Source	Rib Elastic Modulus (MPa)
Granik and Stein (1973)	11,100
Yoganandan and Pintar (1998)	2,102

Both the sternum and the ribs were modeled using a linear elastic rate-dependent model, which accounts for rate effects and fracture. When an element reaches the critical failure stress it is deleted and rib fracture is predicted. Deng et al. (1999) reported that due to the single point integration scheme, the ribs cannot produce a full through rib fracture due to bending. However, the model still provides accurate prediction of potential rib fractures. While it is known that ribs present a non-linear stress-strain response, implementing such properties was considered unnecessary for the current model because the linear model was shown to present characteristics comparable to actual ribs. Additionally, this would have produced a high computational cost.

2.3.2 Pleurae and Lungs

Pleurae and Lung Anatomy and Physiology

The pleurae and lungs work together to facilitate the process of respiration. The pleurae are two separate membranes, the visceral and parietal, that enclose the lung. The visceral pleura is attached directly to the lung and cannot be separated. The parietal pleura lines the internal surface of the thoracic wall, mediastinum and diaphragm, and completely encases both the visceral pleura and lungs. The space created between the two pleura surfaces is referred to as the pleural sac and is filled with pleural fluid. The pleural fluid

acts to lubricate the pleural surfaces and allows them to slide against each other during respiration.

The left and right lungs are divided into separate lobes as shown in Figure 2.6(a). The right lung has three lobes, while the left lung only has two; making the right lung bigger primarily due to the heart taking up space on the left side of the thorax. The main function of the lung is to oxygenate blood by bringing inspired air, through the bronchi, into close proximity of the venous blood, through the pulmonary capillaries. Each lung is attached to the heart, which brings blood in and out, and to a tracheal branch, which brings air in and out. The attachment to both is at the root of the lung, which is also the location where the visceral and parietal pleurae join.

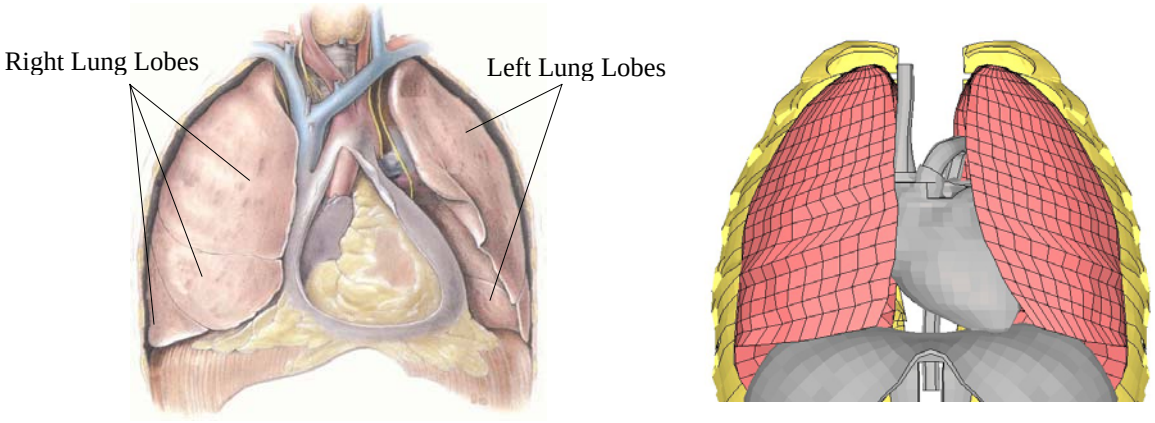

(a) (b)

Figure 2.6 Lungs (a) anatomical (modified from Moore and Dalley, 1999) (b) numerical model

Although the lung is known to be a complex hierarchical structure on both a macroscopic and microscopic scale, it was modeled here as a continuous material with element edge lengths of approximately 10 mm. This is considered acceptable for modeling the general response of the lung in auto crash and as a result, further details of the lung and its function are not required. Figure 2.6(b) shows the lungs as originally modeled by Deng et al. (1999) with geometry obtained from ViewPoint Data Labs.

Lung and Pleurae Injury

Injury to the lung experienced during automotive trauma can take on two separate modes: laceration and contusion. Laceration is usually induced when ribs are fractured and the

fractured ends intrude into the lung tissue resulting in pneumothorax or hemothorax. Pneumothorax occurs when either pleura is lacerated and air is free to enter the pleural sac. This causes the lung to recoil due to its inherent elasticity and is termed a collapsed lung (Moore and Dalley, 1999). Hemothorax occurs when either pleura is lacerated and blood is free to enter the pleural sac. This method of injury often occurs due to both the laceration of either pleura and the laceration of a major blood vessel (Moore and Dalley, 1999). Figure 2.7 shows both lungs with the right lung (left side of this figure) undergoing collapse due to either pneumothorax or hemothorax. From a modeling perspective, predicting intrusion of the fractured ribs into the lungs is sufficient to suggest the possibility of pneumothorax or hemothorax.

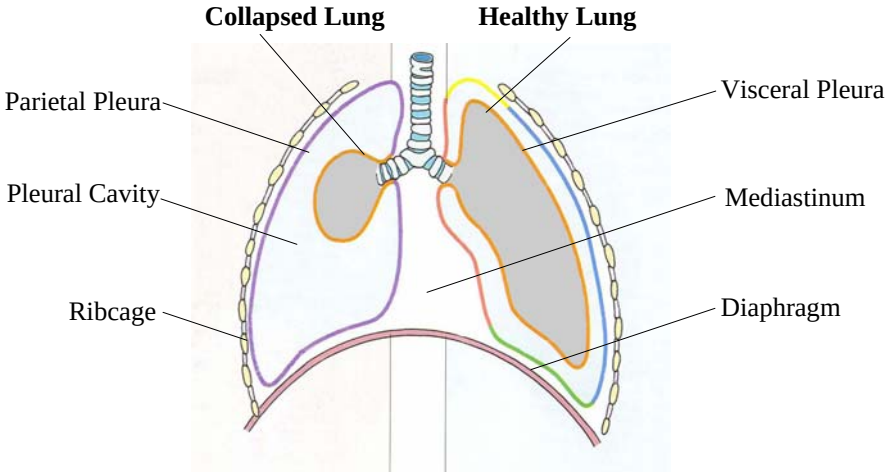

Figure 2.7 Lung injury mechanism (modified from Moore and Dalley, 1999)

Research has shown that contusion of the lung due to blunt impact occurs following the initial impact. Jonsson et al. (1979), Fung et al. (1988) and Yen et al. (1988) investigated this phenomenon and found that the injury is due to a compressive stress wave that is developed after the impact. The wave reflects, refracts and focuses throughout the ribcage and surrounding structures inducing severe stresses and strains, which cause injury within the soft lung tissues. Two types of contusion are found to occur: edema and hemorrhage. Edema results in the internal flooding of the lung with interstitium fluid and hemmorage results in the internal flooding of the lung with blood. In either case, the intruding fluid in the lung acts as a barrier to normal oxygen exchange. The mechanism of both injuries has been found to occur on a microscopic level, and extensive research

has been performed to understand the response. However, because this was not represented within the model, details of this research have not been presented here.

Lung and Pleurae Mechanical Properties and Thresholds

Unlike bone, determining specific failure measures for the lung is very difficult. The complex and microscopic nature of lung injury makes it difficult to associate specific failure stresses or strains at a macroscopic level. However, understanding the cumulative effects of this injury can be very beneficial. The first step in exploring this topic is to understand the pre-failure characteristics of the lung. Zeng et al. (1987) and Yen (1999) performed bi-axial tensile tests of lung tissue highlighting differences in the loading and unloading characteristics and a non-linear stress-strain relationship. Stress relaxation and creep tests performed by Fung (1993) suggested that lung is viscoelastic. However, when the lung was tested over a specific range of strain rates, no effect could be observed. As a result, Fung (1993) proposed that within the strain rates tested the lung could be considered a pseudo-elastic body, which describes independent stress-strain relationships for loading and unloading.

To model these properties, Deng et al. (1999) adopted the modeling approaches developed by Fung et al. (1978) and Vawter et al. (1980), which used the following strain energy equation:

$$W = \frac{C}{2\Delta}\exp(\alpha\ I_1^2 + \beta\ I_2) + \frac{12C_1}{\Delta(1+C_2)}\left[A^{(1+C_2)} - 1\right] \tag{2.1}$$

$$A^2 = \frac{4}{3}(I_1 + I_2) - 1 \tag{2.2}$$

Where C, C_1, C_2 α and β are material constants, Δ is the typical alveolar diameter when unstressed, and I_1 and I_2 are the strain invariants. This material takes into account both the air interaction and the surface energy present in the lung. The coefficients required to complete this model were obtained from results presented by Vawter et al. (1980) and extensive bi-axial testing by Yen (1999).

2.3.3 Heart

Heart Anatomy and Physiology

The heart lies between the lungs in an area termed the mediastinum, and facilitates the circulation of blood around the body. Great vessels carrying blood stem from the heart and branch throughout the body. The heart and roots of the great vessels are surrounded by the pericardium, a double walled fibroserous sac that allows the heart to expand and contract during pumping. Figure 2.8(a) shows an anatomical representation and Figure 2.8(b) shows the numerical model implementation. The pericardium is attached to the diaphragm through ligaments, which are flexible enough to sustain low amounts of displacement associated with thoracic deformation during impact (Moore and Dalley, 1999). Within the model this connection is represented by constraining four nodes on the inferior portion of the heart to four nodes on the diaphragm.

(a) (b)

Figure 2.8 Heart (b) anatomical (modified from Moore and Dalley, 1999) (b) numerical model

The heart has four chambers: the left and right atria, and the left and right ventricles. The following three layers make up the heart: the endocardium, a thin internal layer which contacts the blood, the myocardium, a middle layer of thick muscle that generates the pumping mechanism, and the epicardium, also termed the visceral pericardium. Within the model, a single part was used to model all three layers. The four chambers of the heart were modeled without valve mechanisms and filled linear elastic fluid material to represent blood. The material properties of the heart are detailed in a following section.

The pumping of the heart is coordinated by the impulse-conducting system; a group of cardiac muscles that are initiated by impulses generated by conducting fibers. The conducting fibers are specialized tissues that consist of the following main components: the sinoatrial node, the atrioventricular node and the atrioventricular bundle. The sinoatrial node is located in the right atrium and is the source of the impulse that controls the rhythm of the heart. This impulse causes the cardiac muscles in the atria to contract. The atrioventricular node then receives the impulse from the sinoatrial node and distributes it to the atrioventricular bundle. The atrioventricular bundle branches into two separate bundles, the left and right. Each bundle branches further into the subendocardial branches and terminate in the wall of the ventricles. The impulse signal, traveling through these branches, causes the ventricles to contract. The entire cycle can be observed by measuring electrical impulses on the surface of the body. Figure 2.9 shows a full cardiac cycle, which is important since it is directly related to one of the injury mechanisms discussed below. The first part of the cycle is called the P-R interval, which includes the P-wave. The P-wave represents the sequential activation (depolarization) of the right and left atria. The second part of the cycle is called the QRS complex, which represents the simultaneous activation (depolarization) of the ventricles. During this time, the atria also deactivate (depolarize). The third part is called the S-T interval, which includes the T-wave. The T-wave represents the deactivation (depolarization) of the ventricle.

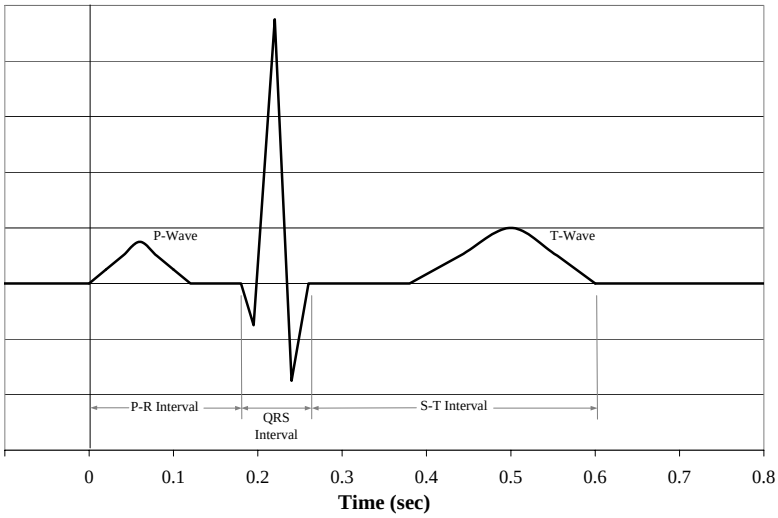

Figure 2.9 Cardiac cycle

Heart Injury

Injury to the heart due to blunt thoracic impact follows one of the four following injury mechanisms: contusion, laceration, cardiac arrest or rupture (Nahum and Melvin, 2002). Contusion is the most common heart injury and is due to both the compression and velocity of compression of the heart. Contusion is the destruction of muscular fibers and if severe can lead to heart failure, heart rupture, defective rhythm or a ventricular aneurism. The myocardium is the most susceptible to contusion since it is the biggest muscle in the heart (Nahum and Melvin, 2002). This mode of injury is not specifically tracked in the current model, but can be related to the mechanical stresses and strains in the heart and should be investigated in future revisions.

Laceration can occur due to fractured rib interaction with the heart or severe compression of the thorax and can be considered in the current thoracic model. When the pericardial sac is lacerated it can fill with fluid preventing the heart from fully expanding, thereby reducing blood flow to the body. This phenomenon is called tamponade and if left untreated will lead to shock, breathing impairment and eventual death. If tamponade does not cause significant circulatory effects, pericarditis (an inflammation of the pericardium) can result. This is often diagnosed by significant chest pain.

Fatal injuries to the heart can occur during impact without significant physical damage. High rate, direct impacts to the thorax over the heart can result in cardiac arrest. Impacts at velocities between fifteen and twenty meters per second can interrupt the cycle and cause commotio cordis (Nahum and Melvin, 2002). Commotio cordis causes death as a result of ventricular fibrillation or cardiac arrhythmia aggravated by traumatic apnea (Bir, 1999). Animal research has shown that the heart is especially susceptible to commotio cordis at the start of the T-wave (Janda et al., 1998).

Heart rupture is rare but often results in death at the scene of the accident or shortly thereafter. Rupture occurs when the heart is compressed between the sternum and the thoracic vertebrae and most often occurs in the right ventricle. Which operates at a lower

pressure, as compared to the other heart chambers, and has a reduced ability to sustain overpressure (Chapon, 1984).

Heart Material Properties and Thresholds

Yamada (1970) summarized the failure properties of heart muscle from a variety of locations in the heart. Tensile failure stress and strain properties of the human cardiac muscle, as obtained from the myocardium of the left ventricle, were measured and tabulated in age groups. The specimens were pulled in directions parallel to the muscle fibers and Table 2.3 summarizes these results. A maximum ultimate strength and strain was observed at approximately 20 years of age, after which point both measures decrease with increasing age. In a direction transverse to the muscle fibers, the ultimate strength was found to be about one-third of the strength in the parallel direction and the ultimate elongation is 1.3 times the elongation in the parallel direction. The stress strain curves obtained from these tests also showed the hyperelasticity of the muscle tissue.

Table 2.3 Tensile properties of cardiac myocardium muscle (Yamada, 1970)

Age Group	Ultimate Tensile Strength (g/mm^2)	Ultimate Percent Elongation
0-9 years	12.4 ± 0.97	62.6 ± 6.9
10-19 years	13.4 ± 1.01	79.2 ± 4.2
20-29 years	14.1 ± 0.82	69.2 ± 3.0
30-39 years	12.8 ± 1.18	65.2 ± 4.9
40-49 years	11.1 ± 0.75	63.9 ± 4.3
50-59 years	10.1 ± 0.86	63.2 ± 4.0
60-79 years	9.2 ± 0.95	60.8 ± 3.5
Adult Average	11.1	63.8

Yen et al. (1999) performed bi-axial tensile tests on human myocardium, endocardium and epicardium in an effort to understand the combined loading effects. These tests showed different loading and unloading characteristics in both the direction parallel and transverse to the fibers. All specimens exhibited a higher stiffness in the parallel direction. The endocardium and epicardium were found to be stiffer than the myocardium overall, while the endocardium was stiffer in the low strain range.

To model these properties, Deng et al. (1999) adopted the modeling approaches developed by Guccione et al. (1991), Guccione and McCulloch (1991) and McCulloch and Omens (1991) to represent the passive heart properties, which uses the following strain energy equation:

$$W = \frac{C}{2}(e^{Q} - 1) - \frac{p}{2}(I_3 - 1) \tag{2.3}$$

$$Q = b_1 E_{11}^2 + b_2(E_{22}^2 + E_{33}^2 + E_{23}^2 + E_{32}^2) + b_3(E_{12}^2 + E_{21}^2 + E_{13}^2 + E_{31}^2) \tag{2.4}$$

Where E_{ij} are Lagrangian strain components, p is the hydrostatic pressure variable, I_3 is the third principal strain invariant, and C, b_1, b_2, b_3 are constants. The coefficients required to complete this model were obtained from the results of the experimental testing by Yen et al. (1999) and Guccione et al. (1991).

A single material model has been implemented to represent all three layers of the heart using only the myocardium tissues coefficients. This was justified by the fact that myocardium makes up the majority of the heart muscle tissue (Moore and Dalley, 1999). In the future, it may be beneficial to model all three layers.

It is noted that this model represents only the hyperelasticity of heart tissue and does not represent the inherent viscoelasticity of heart tissue. While it is understood that such properties are important when modeling the impact response of the heart, improvement of the heart model was not a primary goal during this study, and such developments have not been completed here.

2.3.4 Aorta

The aorta is considered separately from the heart due to the significant differences in material properties and the relevant injury mechanisms in auto crash.

Aorta Anatomy and Physiology

The aorta originates from the left ventricle of the heart and ascends to the sternal angle where it forms the aortic arch. The aortic arch has three branching arteries called the subclavian, the left common cartoid and the brachiochephalic. These three arteries supply blood for the arms, shoulders and head. Beyond the arterial branches, the aortic arch forms the thoracic aorta. The thoracic aorta continues down the thorax in behind the heart and just left of the vertebral column. Further branching from the thoracic aorta continues to facilitate the supply of blood to the rest of the body. Figure 2.10(a) highlights the aorta when looking medially from the left of the human thorax and Figure 2.10(b) shows the numerical model implementation from the same viewpoint. The model has also been implemented with the superior vena cava, however the anatomy and injury of this great vessel have not been detailed here, as injuries sustained by this organ are quite rare (Nahum and Melvin, 2003). Both vessels were modeled using shelled elements filled with linear elastic solid elements to represent blood.

It is noted that the model may appear to present slight differences in size and shape as compared to the anatomical drawing. However, slight variations are inevitable since no two hearts are the exact same size. The geometry used to model the great vessels was obtained from ViewPoints Data Labs.

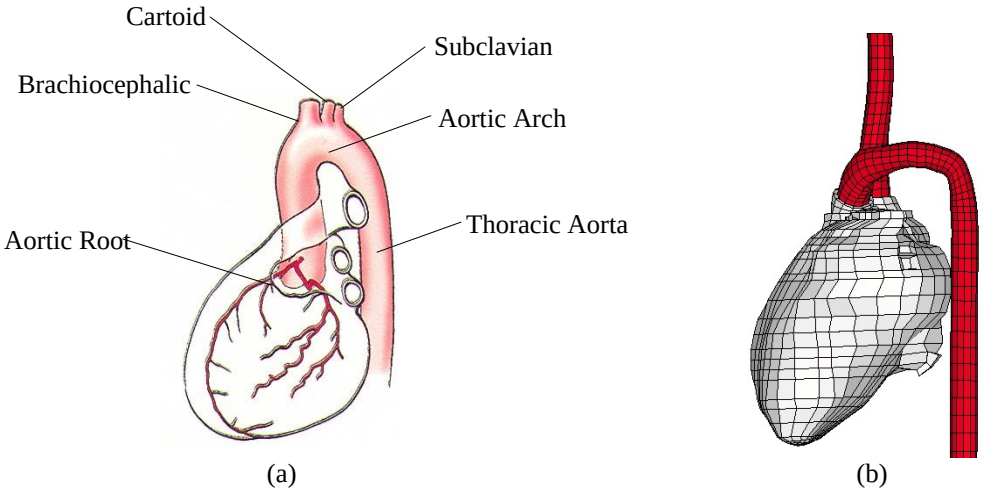

Figure 2.10 Heart and aorta – left medial view (a) anatomical (modified from Moore and Dalley, 2002) (b) numerical model

The aorta is anchored in several places. The first three branches of the aorta anchor through their interactions with other functioning parts of the body such as veins or lymph nodes. The ligamentum arteriosum also anchors the aorta to the left pulmonary artery (originates from the left atrium). The ligamentum arteriosum connects to the bottom of the aortic arch and the top of the left pulmonary artery. The region of the aortic arch between the left subclavian artery and the ligamentum arteriosum is termed the aortic isthmus. Figure 2.11 highlights the ligamentum arteriosum and its surroundings.

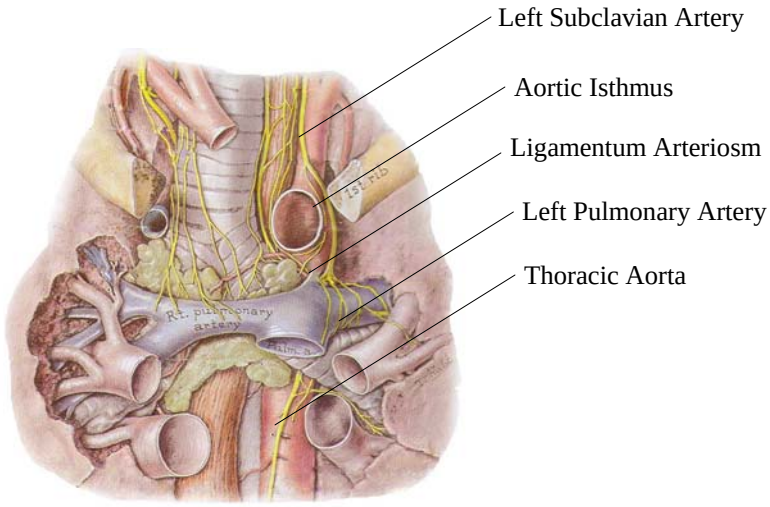

Figure 2.11 Dissection of the chest near the thoracic aorta (modified from Moore and Dalley, 2002)

Within the model, the anchoring effects of the first three branching arteries has been accommodated through the use of beam elements connecting the aortic arch to the left and right first ribs. The inferior end of the aorta has been connected to the diaphragm by constraining two nodes on the aorta to two nodes on the diaphragm. Similarly, the superior end of the superior vena cava was attached to the first ribs using constrained nodes.

Aorta Injury

Several studies have shown that rupture of the aorta within the thorax accounts for 10-25% of all fatalities in motor vehicle accidents (Greendyke, 1966, Ochsner et al., 1989). The rupture is usually due to laceration occurring perpendicular to the axis of the aorta (Chapon, 1984). An investigation of road traffic accidents by Newman and Rastogi

(1984) showed that in cases of aortic rupture the corresponding impact was not directly frontal. Therefore, all occupants must have been subjected to a transverse component of impact that imposed laceration between fixed and mobile potions of the aorta.

The mechanism behind aortic rupture due to laceration has the following three general hypotheses: traction or shear forces due to relative motion of the aorta and points of anchor, direct compression between the sternum and vertebral column, and excessive pressure within the aorta (Creasy et al., 1997). The first mechanism usually results in laceration of either the aortic isthmus, the root of the aorta, or the thoracic aorta at entry to diaphragm due to heart displacement in either the vertical, lateral or oblique direction. Such motion pulls against the anchored main branches of the aorta. The aortic isthmus is especially susceptible to laceration due to its narrowed cross-section. Prediction of these injuries with the model in its current state is possible. However, for the purposes of this study, such injuries have not been explored since the goal outlined here was to develop the model such that its global response can predict injuries, while highlighting areas for future improvements.

Aorta Mechanical and Trauma Thresholds

Due to the diverse loading conditions in the aorta, as mentioned in the above section, obtaining appropriate mechanical properties is key to understanding injury. Aortic properties are complex due to the non-linear stress-strain relationship and material anisotropy (Viano, 1983). As with most biological materials the aortic material is also strain-rate sensitive. Mohan and Melvin (1982, 1983) explored the material failure properties for aortic tissue extensively. Table 2.4 outlines the major mechanical strength properties as gathered from these studies. The data clearly indicates large variations, which was explained by subject age differences and pathological conditions (Mohan and Melvin, 1982). However, it is easily observed that this material is rate sensitive as evidenced by the significant increase in ultimate stress when the aorta is loaded dynamically. Mohan and Melvin (1982, 1983) also theorized that although the failure stress varies with the loading conditions, a maximum strain theory could be used as a failure theory as strain at rupture is consistently around 1.5.

Table 2.4 Aortic tissue failure properties (Mohan and Melvin, 1982)

Test Condition and Sample Orientation			Ultimate Stress (MPa)	Ultimate Strain (mm/mm)
Uniaxial	Quasi-Static	Longitudinal	1.47 ± 0.90	1.47 ± 0.23
		Transverse	1.72 ± 0.89	1.53 ± 0.28
	Dynamic (100/s)	Longitudinal	3.53 ± 2.04	1.64 ± 0.28
		Transverse	5.07 ± 3.29	1.60 ± 0.30
Biaxial	Quasi-Static		1.14 ± 0.32	1.44 ± 0.10
	Dynamic (100/s)		1.97 ± 0.59	1.28 ± 0.12

The material properties used in the model follow a linear elastic relationship with properties as obtained from Abe et al. (1996). This is noted to be quite unrepresentative of the hyperelastic and viscoelastic properties of the common aorta, however as this studies intention was not to focus on the injury response of the aorta, the linear elastic material was left unchanged. This may be a consideration for future studies and would require the development of a detailed hyperelastic and viscoelastic material model, which is a considerable undertaking.

2.4 Thoracic Injury Criteria

The most difficult aspect of predicting trauma to the human body is linking measurable parameters observable during PMHS experimental testing to actual levels of injury. More often than not, it is difficult or impossible to measure tissue response at an appropriate scale to allow for local injury prediction. For example, in a simple tensile test of steel, levels of strain can be measured at many points along with the dimensions of the sample to predict yielding and subsequent failure. However, due to the complexity and variety of the tissues in the human body, and the damaging invasiveness of making such measurements, injury is commonly predicted from more convenient global measurements. The most common method used is to perform experiments on PMHS under various forms of loading and measure global parameters such as thoracic compression. Input parameters such as the magnitude and rate of loading are controlled, output measurements such as deflection or velocity are recorded, and injuries such as rib

fracture or lung contusion are observed throughout the experiment or during autopsy. Statistical correlation of the measured outputs to the various levels of injury facilitates the development of injury criteria. This method allows researchers to assign specific experimental measures to predicted levels of injury.

The following describes several widely used global trauma scales to evaluate human body injury. Although it is expected that this detailed body model will one day be evaluated on a more local level, comparison to these scales is essential to make use of the large body of data available in this context.

2.4.1 Abbreviated Injury Scale

The abbreviated injury scale (AIS) was first introduced and presented by John D. States for the Association for the Advancement of Automotive Medicine in 1969. Its intention was to meet the demand for a widely accepted injury scale that could be used by medical engineering automotive accident investigation teams to classify the level of injury sustained by a body region or organ (States, 1969). Today it is used for the development of injury prediction research and triage assessments during emergency medical situations.

The AIS uses a numerical rating system to assess impact injury severity. The scale starts at 0 where no injury is sustained, and moves up to 6 where a maximum level of injury is sustained, often termed "virtually unsurvivable" (Nahum and Melvin, 2002). The greater the AIS number, the greater the threat to life. However, it should be noted that the AIS is strictly ordinal in nature and should not be taken as a continuous function (Nahum and Melvin, 2002). Table 2.5 shows the ranking codes used to assess injury (AIS, 1990).

Table 2.5 AIS ranking codes (AIS, 1990)

AIS Level	Injury Severity
1	Minor
2	Moderate
3	Serious (not life threatening)
4	Severe (life threatening but survivable)
5	Critical (survival uncertain)
6	Fatal

Since its initial implementation the AIS has undergone several revisions. Various scales have been created to reflect trauma associated with specific regions of the body and the resulting injury severity. Table 2.6 shows typical injuries to the rib cage and thoracic soft tissues as categorized by the AIS levels of injury (AIS, 1990).

Table 2.6 Rib cage and soft tissue injuries ranked by AIS level (AIS, 1990)

AIS Level	Rib Cage Injury	Thoracic Soft Tissue Injury
1	1 rib fracture	Contusions of the bronchus
2	2-3 rib fractures; sternum fracture	Partial thickness bronchus tear
3	4 or more rib fractures on one side; 2-3 rib fractures with hemothorax or pneumothorax	Lung contusion; minor heart contusion
4	Flail chest; 4 or more rib fractures on each of two sides; 4 or more rib fractures with hemothorax or pneumothorax.	Bilateral lung laceration; minor aortic laceration; major heart contusion
5	Bilateral flail chest	Major aortic laceration; lung laceration with tension pneumothorax
6		Aortic laceration with hemorrhage not confined to mediastinum

One drawback of the AIS approach is the inability to account for several injuries of differing degrees (Nahum and Melvin, 2002). As a result, the AIS has been used as the foundation to develop methods for assessing multiple injuries and for assessing the cumulative effects of multiple injuries. These include the maximum AIS (MAIS) and the New Injury Severity Score (NISS). The MAIS uses the single highest AIS from the various points of injury and applies the same injury assessment methods as used with the AIS.

The NISS is a measure of the probability of survival to assess patients with multiple injuries. The NISS sums the square of the three highest AIS ratings as observed in any of the six possible body regions (head, face, chest, abdomen, extremities including pelvis and external). The NISS score ranges from 0 to 75, where 0 indicates full survival probability and 75 indicates one hundred percent fatality probability (Baker et al., 1974).

At the moment the NISS remains the most widely accepted predictor of multiple injury scenarios. However, the abbreviated injury scale has been used extensively for establishing the injury tolerance levels for automotive injury criteria as described in the following sections.

2.4.2 Global Acceleration Criteria

The acceleration criterion was first developed by Stapp (1951, 1970) in an effort to protect military personnel exposed to rapid decelerations in airplanes. Stapp conducted rocket-sled deceleration tests on himself to establish whole-body deceleration tolerance limits with belt restraints.

Subsequently, Eiband used this data along with others to show that the body deceleration tolerance increased as duration of exposure decreased (Eiband, 1959). This tolerance is outlined in Figure 2.12. This led to the first well-received deceleration tolerance and is currently used in both European and North American safety standards. The Federal Motor Vehicle Safety Standard (FMVSS) 208 for occupant crash protection states that the "resultant acceleration… shall not exceed 60 g's, except for intervals whose cumulative duration is not more than 3 milliseconds."

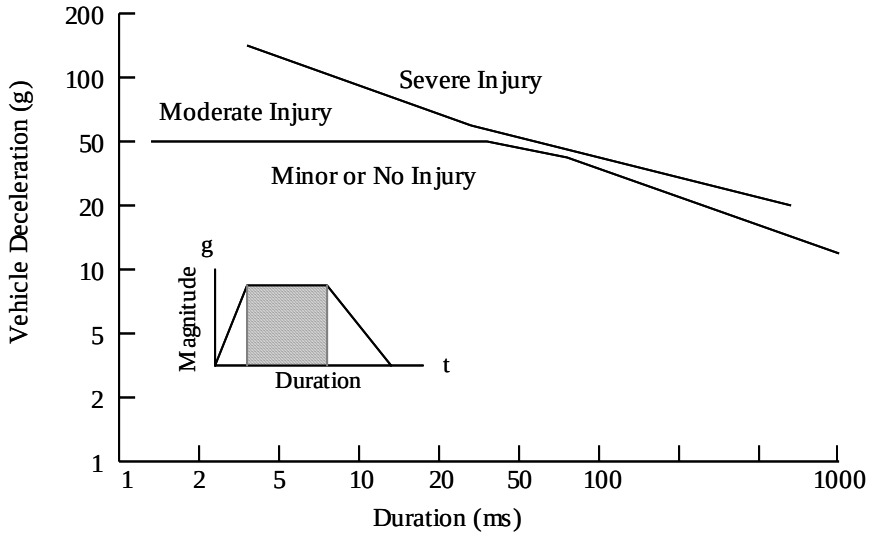

Figure 2.12 Vehicle deceleration vs. duration of exposure for human volunteers (Eiband, 1959)

Albeit this injury criterion can be used to describe acceleration limits of the entire body, it is sensitive to the changing loading conditions and can provide misleading results when evaluating acceptable levels of injury (Patrick et al., 1965).

2.4.3 Force Criteria

The development of a force criterion rose from the increasing injuries resulting in blunt thoracic impact to the steering wheel. Research engineers set out to design an energy absorbing steering column with the objective to obtain the maximum yield force that could be tolerated by the human body, to maximize energy absorbing potential. In collaboration with General Motors, Wayne State University developed a crash simulation facility to conduct experiments on human tolerance in automotive trauma. Early tests measured loads sustained by PMHS during frontal impact sled tests (Patrick et al., 1965). This data along with the results of further experimentation (Gadd and Patrick, 1968) was used in the design of the first energy-absorbing steering wheel and revealed a maximum force of 3.29 kN applied to the sternum and a maximum force of 8.0 kN applied to the chest and shoulders resulted in only minor trauma.

As with acceleration criteria, force criteria predicts injury from a macroscopic parameter (total force) and is therefore very sensitive to loading conditions with the potential to create misleading injury tolerance levels (Neathery, 1975).

2.4.4 Compression Criteria

Throughout the late 60's and early 70's numerous PMHS experiments were performed to provide improved understanding of injury tolerance and thoracic impact response (Patrick et al., 1965, 1967; Kroell et al., 1971, 1974). Researchers realized that, although acceleration and force could be used to evaluate whole body motions, the local loading was ignored. For example, during frontal thoracic pendulum impact tests the whole body acceleration was found to be quite negligible, while the injury sustained was quite severe. As a result, the local chest compression was found to be a better predictor of injury.

Patrick et al. (1965, 1967) performed many frontal sled tests as well as frontal pendulum impact tests in an effort to establish the compression criterion. Using regression techniques, Kroell et al. (1974) showed that chest compression, over spinal acceleration or thorax force, more accurately predicted injury AIS levels for frontal impact PMHS tests.

Neathery et al. (1974, 1975) was the first to formulate compression injury tolerance levels by analyzing the Kroell et al. (1971, 1974) data. The statistical analysis showed that a normalized compression of 34%, or 78.7 mm penetration, was required to produce an AIS 3 level injury, with 25% probability. Neathery went on to use non-dimensional analysis techniques to develop the following predictive AIS equation based on 24 PMHS tests:

$$AIS = -5.1508 + 17.4338P/D + 0.3128Age \tag{2.5}$$

Where P is chest penetration measured in mm, D is chest depth measured in mm and Age is subject age measured in years. The report suggested using an age of 45 when validating human surrogate responses to represent the mean driving population.

Viano and Lau (1988) then subjected the same experimental data to Logist analysis to produce more extensive injury tolerance levels. Analysis indicated a 25% probability of an AIS≥4 injury due to a chest compression of 35%, and a 50% probability of an AIS≥4 injury due to a chest compression of 37.86%. Table 2.7 summarizes the various findings.

In an effort to develop lateral compression injury criteria, Viano et al. (1989b, 1989c) subjected PMHS to pendulum impacts at an angle of 30° from the coronal plane. The PMHS were hit with a rigid 25 kg impactor at velocities between 3.6 m/s and 10.2 m/s and C_{max} values were calculated for injury levels AIS≥3 and AIS≥4 for 25% and 50% probability. These results are also summarized in Table 2.7.

Table 2.7 Normalized compression criteria for the thorax

Injury Level	25% Probability	50% Probability
Frontal C_{max}		
AIS ≥ 3 (Neathery et al., 1974)	34%	*
AIS ≥ 4 (Viano and Lau, 1988)	35%	37.9%
Lateral C_{max}		
MAIS ≥ 3 (Viano et al., 1989b)	*	33.9%
MAIS ≥ 4 (Viano et al., 1989c)	38.4%	39.8%
* Data not provided in paper.		

Mertz et al. (1997) reanalyzed the results from Neathery (1974) and found that frontal chest compression criteria could be associated with specific thoracic injuries. Based on up-to-date AIS rankings, rib fractures were shown to be the predominant injury in an AIS ≥ 3, while heart and/or aortic rupture were shown to be the predominant injury in an AIS≥4. Sternal deflection was used to generate the criteria for each injury type across a range of probabilities. The normalized chest compression has been calculated here and summarized with sternal deflection in Table 2.8.

Table 2.8 Risk of rib fractures and heart/aorta injury as a function of chest compression

Injury Level	25% Probability	50% Probability
Sternal Deflection (mm) : Normalized C_{max}		
AIS ≥ 3 (Rib Fractures)	50 mm : 27.5%	55 mm : 29.7%
AIS ≥ 4 (Heart/Aorta Injury)	67 mm : 34.9%	74 mm : 38%

2.4.5 Viscous Criteria

The development of the viscous criteria was initiated as researchers began discovering the importance of loading rate in non-penetrating impacts. Studies showed that although compression criteria adequately described the effects of deformation on both the ribs and the soft tissue within, it failed to represent the rate sensitivity of the soft tissue. Subsequent research was undertaken to determine these effects.

Kroell et al. (1981) examined the effects of velocity and chest compression on the blunt thoracic impact of swine. The results showed that in high velocity-low compression impacts, the level of injury was much greater than that observed in low velocity-high compression impacts. Lau and Viano (1981) performed abdominal impact tests on rabbits with variable impact velocities and analyzed the effects on hepatic injury. These tests showed that at constant abdominal compression, low impact velocities (8 m/s) generated no discernable injury but higher velocities (20 m/s) tended to inflict minor to multiple liver lacerations. Viano and Lau (1983) performed further rabbit impact testing that produced increasingly severe cardiac injuries as both impact velocity and chest compression were increased. The first official Viscous Criterion was formulated by Lau and Viano (1985) and is defined as "any generic biomechanical index of injury potential for soft tissue defined by rate sensitive torso compression" and also stated that the viscous tolerance is the "risk of soft tissue injury associated with a specific impact-induced viscous response". The derivation of the criterion is highlighted in Figure 2.13, which produces the following formulation for calculating the maximum viscous criterion (Lau and Viano, 1986):

$$[VC]_{\max} = V(t) \cdot C(t) \tag{2.6}$$

Where $[VC]_{\max}$ is the maximum value generated by the product of the velocity of deformation, $V(t) = \frac{d[D(t)]}{dt}$, and normalized chest compression, $C(t) = \frac{D(t)}{D_o}$.

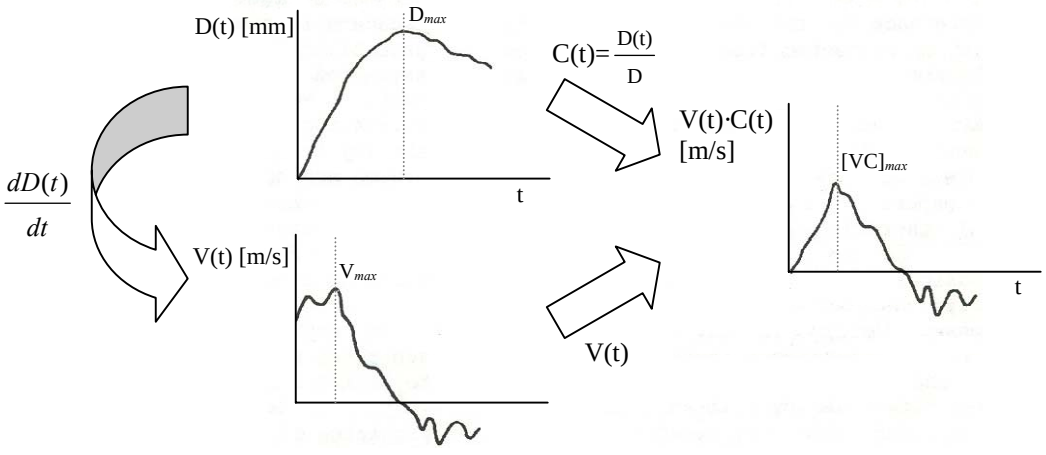

Figure 2.13 Viscous Criterion derivation (Lau and Viano, 1986)

Using this criteria Viano and Lau (1988) performed Logist analysis on the Kroell et al. (1971, 1975) PMHS experiments and developed $[VC]_{max}$ values for frontal injury levels AIS≥4 of 25% and 50% probability. Ridella and Viano (1990) performed a similar analysis with a subset of the Kroell data and produced comparable results for the same injury levels. Both results are listed in Table 2.9.

In an effort to develop lateral $[VC]_{max}$ injury criteria, Viano et al. (1989b, 1989c) subjected PMHS to pendulum impacts at an angle of 30° from the coronal plane. The PMHS were hit with a rigid 25 kg impactor at velocities between 3.6 m/s and 10.2 m/s and $[VC]_{max}$ values were calculated for injury levels AIS≥3 and AIS≥4 for 25% and 50% probability. The results are listed in Table 2.9.

Table 2.9 Viscous criteria results for the thorax

Injury Level	**25% Probability**	**50% Probability**
Frontal $[VC]_{max}$ (m/s)		
AIS ≥ 4 (Viano and Lau, 1988)	1.00	1.08
AIS ≥ 4 (Ridella and Viano, 1990)	1.087	1.09
Lateral $[VC]_{max}$ (m/s)		
AIS ≥ 3 (Viano et al., 1989c)	*	1.00
AIS ≥ 4 (Viano et al., 1989c)	1.47	1.65
* Data not provided in paper.		

Lau and Viano (1986) also examined the applicability of the compression and viscous criteria. They stated that Equation (2.6) relates the instantaneous risk of injury due to the extent of compression and the rate of deformation. As a result, the level of risk will increase at contact and reach zero once compression has reached its maximum. Therefore, this equation suggests that maximum risk of injury will occur early in the impact scenario prior to maximum compression and that zero risk of injury will occur once maximum compression is reached (Viano and Lau, 1988). However, the previous section outlined the damaging effects of high compression levels on the human torso. As a result ranges of deformation velocities were established where both compression and

viscous criterion are applicable. Extensive experimental data was analyzed and a hypothesis was generated that stated compression criteria should be used for impact velocities less than 3 m/s and viscous criteria should be used for impact velocities between 3 m/s and 30 m/s (Lau and Viano, 1986). Above 30 m/s the rate of loading becomes such a predominating factor that neither compression criteria nor viscous criteria can adequately describe the resulting injury. Such high velocities resemble injuries incurred during blast exposures, which is most evident in the trauma to the lung. Figure 2.14 outlines this hypothesis and plots the range of velocity that each injury criteria applies to.

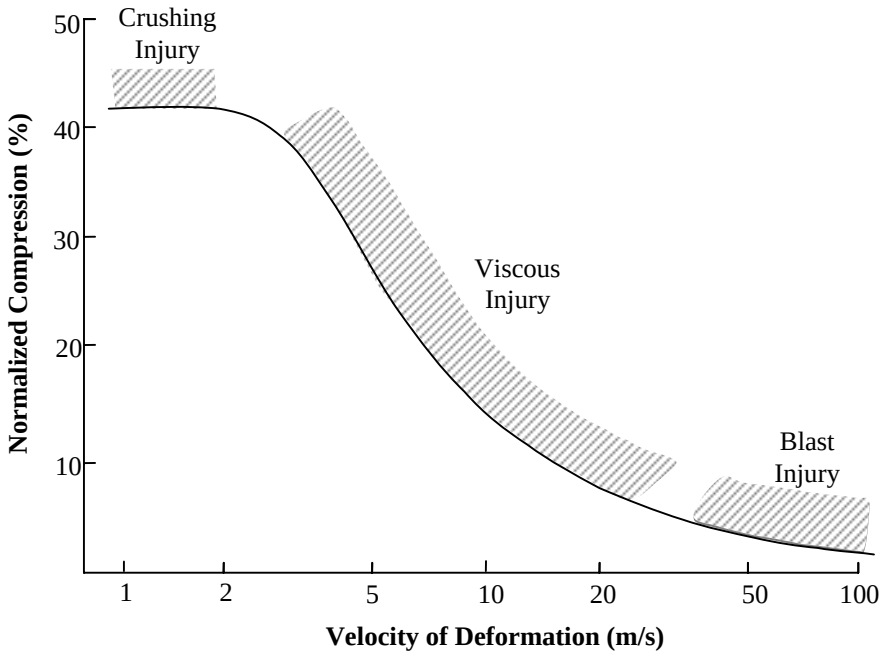

Figure 2.14 Range of validity for compression and viscous criterion

Since this was only a proposed theory, Ridella and Viano (1990) set out to establish a statistically based "transition" impact velocity that would define where compression and viscous criteria should be used. Kroell et al. (1975) data was divided into 6 data sets based on impact velocity and for each a goodness of fit for both compression and viscous criteria was established. The results suggested a transition velocity of 4.5 m/s.

2.4.6 Thoracic Trauma Index

The development of the thoracic trauma index (*TTI*) began in 1976 and was formally presented by Eppinger et al. (1984) in an effort to establish lateral impact injury indices. At the time, frontal impact research had been the primary focus while lateral impact was lacking in data. NHTSA's Thoracic Side Impact Protection Research Program was initiated to fill the lateral impact automobile crash information void. The use of *TTI* was based upon results obtained from laterally impacting PMHS seated in actual cars and in side sled test devices. The results (Klaus et al., 1983, 1984) suggested that spine and/or rib acceleration might relate to thoracic injury and *TTI* was first defined by the following equation:

$$TTI = 1.4Age + 0.5(RIBY + T12Y)\frac{MASS}{M_{std}} \tag{2.7}$$

Where *Age* is the age of the test subject in years, *RIBY* is the absolute maximum value of acceleration of either the upper (4^{th}) or lower (8^{th}) rib in the lateral direction in G's, *T12Y* is the absolute value of the twelfth thoracic vertebrae in the later direction in G's, *MASS* is the mass of the test subject in kg and M_{std} is the mass of the 50^{th} percentile male (75kg).

Validation of this injury criterion was completed by Morgan et al. (1986) who analyzed PMHS side impact experiments and concluded that *TTI* reasonably predicted specific AIS injury severity levels. Table 2.10 lists the 25% and 50% probability of AIS≥3, AIS≥4 and AIS≥5. This report also went on to show that the Side Impact Dummy (SID) exhibited good biofidelity.

Table 2.10 TTI criteria results for the thorax (Morgan et al., 1986)

Injury Level	**25% Probability**	**50% Probability**
TTI (G's)		
AIS ≥ 3	110	130
AIS ≥ 4	150	168
AIS ≥ 5	223	265

However, the following year Viano (1987a) performed similar analysis of different PMHS experiments in side impact and found the opposite. It was stated that because the *TTI* is determined within the first milliseconds of impact, long before human injuries could occur, this criterion may indicate a safe exposure to injury when in-fact the full events of the impact indicate extensive injury. This analysis also found that *TTI* was insensitive to the total kinetic energy of impact (Viano, 1987a).

2.4.7 Currently Used Criteria and Tolerance Levels

As discussed above, differing opinions exist over which criterion best predicts injury during non-penetrating impacts as experienced during automotive collisions. No one measure has been shown to produce perfect correlation with all impact conditions, and only a few are selected from the numerous methods available for both frontal and lateral impact. Further, when comparing criteria used by differing governing bodies, discrepancy also exists. For example, for lateral impact North American governing bodies use *TTI* while European governing bodies use VC_{max}. As well, even if the same injury criterion is used, varying tolerance levels can exist between the governing bodies. Table 2.11 outlines the criteria available and indicates the tolerance levels accepted by North American and European governing bodies (Workgroup Data Processing Vehicle Safety, 2004).

Table 2.11 Government enforced criteria and tolerance levels

Criteria	**North America**		**Europe**	
	FMVSS208*	FMVSS214*	ECE-R94*	ECE-R95*
	Front Impact	Side Impact	Front Impact	Side Impact
Acceleration, 3ms	≤ 60 G	------	≤ 60 G	------
Chest Compression	≤ 76.2 mm	------	≤ 50 mm	≤ 42 mm
VC	≤ 1.0 m/s	------	≤ 1.0 m/s	≤ 1.0 m/s
TTI	------	85/90 G †	------	------

* - Reference document number from respective regions
† - 85g's is for passenger cars with four side doors, while 90g's is for passenger cars with two side doors

2.5 Surrogates to Predict Human Body Response

The use of physical surrogates, also known as crash test dummies, has provided significant insights into human body response in crash and led to many new safety developments in the automotive field. Although these devices will continue to be used in this capacity for many years to come, the development and validation of advanced numerical models is now providing significant advances in the area of automotive safety. For the current numerical model, the surrogates provide a basis for many of the physical dimensions and masses of the various body components, known as anthropometric data. This is important for the development of representative numerical models. In the following section the available anthropometric data is discussed, including the history of crash test dummies for completeness and the introduction of the biofidelity index. It should however be noted that validation and verification of the numerical model in this thesis has been undertaken using available PMHS test data.

2.5.1 Anthropometric Data

The study and understanding of human body geometry is a fundamental component in understanding body vehicle interaction and predicting subsequent injury. Anthropometrics is defined as the study of human body measurements for use in anthropological classification and comparison. In numerical modeling applications, such data is pertinent to the development of representative human body models. Ideally, it would be best to model every existing body shape such that crash safety can be designed and customized for all body sizes and types. However, due to financial and computational costs researchers commonly use data averaged to represent a certain percentile of the driver or passenger population. In the case of the model described in this thesis, the 50^{th} percentile male data is used. Similarly, the 95^{th} percentile male, 5^{th} percentile female, 6-year-old child, 3-year-old child and 12-month-old infant are common groupings used to represent average classes of passengers or drivers.

Such information comes from extensive measurements obtained from volunteers and several anthropometric databases currently exist. Typical databases record length and

weight measurements of people and categorize them based on age, race, gender and geographic residence. For the use of crash analysis, an extremely high level of detail, in terms of geometric measurements, is required. Information such as joint center locations, segment masses, segment center of gravity locations and inertial properties are all required whether using surrogate dummies or numerical models to simulate crash scenarios (Moss et al., 2000).

Two databases have been identified with information at the appropriate level of detail: the Anthropometry of Motor Vehicle Occupants (AMVO) database and the RAMSIS (Rechnergestiitztes Anthropologisch-Matchematisches System zur Insassen Simulation – computer supported anthropological mathematical system for passenger simulation) database. The AMVO database was created by The University of Michigan Transportation Research Institute (UMTRI), in conjunction with the U.S. Department of Transportation National Highway Traffic Safety Administration (NHTSA). The data was gathered to determine the anthropometric specifications of a mid-sized male dummy, i.e. 50^{th} percentile dummy. All data was gathered from 25 adult males of similar stature.

RAMSIS is a software tool that predicts internal and external anthropometry based on three primary parameters; sitting height, stature and waist circumference. Inputting additional information such as age, secular growth and gender can further refine the results. As well, RAMSIS references the following sources: Germany, US and Canada (Hanes, 1979), and Japan and Korea (HQL). Table 2.12 shows simple anthropometric data for a 50^{th} percentile male from the AMVO and RAMSIS studies.

Table 2.12 Summary of anthropometric databases

Body Measurement	AMVO	RAMSIS Database		
		US & Canada	Germany	Japan & Korea
Stature (mm)	1753	1755	1771	1695
Sitting Height (mm)	911	917	931	921
Chest Width (mm)	312	296	308	300
Hip Breadth – Sitting (mm)	322	339	351	326
Body Mass (kg)	76.7	72.7	79.2	66.6

The data shows only slight variations in measurements when comparing the sources. For the model being developed here, it is believed that the AMVO data provides a reasonable source of anthropometric data representative of the 50th percentile male. Moss et al. (2000) confirmed this belief and even used the data for the development of the World Side Impact Dummy (World SID).

2.5.2 Crash Test Dummies

Development History

The need for human body surrogate development and validation arose as safety standards for auto crash increased, requiring testing at higher speeds, which prevented the use of live human volunteers. As well, volunteer or PMHS responses had high variability responses, while researchers were looking for consistency to make sound scientific judgments. Surrogate dummies allow researchers to replace human volunteers in high-speed crashes to gain insight into trauma. Since the late 1940's surrogate dummies have evolved from rigid mannequin-type figures to highly instrumented human representations known as Anthropomorphic Test Devices (ATD). Such devices report various measures for calculating injury criteria. The results are used to evaluate the crashworthiness of automobiles.

In the late 1940's the first surrogate was designed by Sierra Engineering Co. ("Sierra Sam") under contract with the U.S. Air Force to evaluate the effects on pilots during airplane seat ejection. The dummy was constructed with a skeleton made of laminated plastic, fiberglass and stainless steel joints. The outer skin was made of poly-vinyl chloride to approximate human flesh. Joint movement was regulated to represent a limp and rigid human, and springs within the neck could be adjusted to mimic muscle tone. The dummy was 200lbs, which represented a 95th percentile male. Another dummy was later created to represent the 50th percentile male.

Following a conference in 1956, hosted by military researchers wherein information was shared on the results of ejection seat testing, automotive companies began investigating the use of surrogate crash dummies to improve automobile safety. In 1966 Alderson Research laboratories released the VIP-50 dummy for use by General Motors (GM) and Ford. In 1967 Sierra Engineering released "Sierra Stan" as a competitive model to the VIP-50. Recognizing the distinct need for a better representation of the human body, GM engineers began designing a new dummy, which took the desirable aspects from both of the previous models. In 1971 GM designed the Hybrid I crash test dummy, which was used and validated internally. Primarily this surrogate was used to improve and validate the effectiveness of safety belts (General Motors Limited, 2004).

In 1972 GM released the Hybrid II as an improvement to the Hybrid I following meetings between the vehicle industry and government bodies that outlined issues regarding the repeatability of existing dummies. Again this dummy was intended for seat belt validation and became the standard dummy used for frontal impacts simulations to meet government standards.

Immediately after the Hybrid II release, GM set out to develop a dummy that would more closely represent human-impact response characteristics. In 1973 GM released the Hybrid III, a highly detailed ATD that would go on to be the only US government accepted test device for evaluating automobile crash-worthiness during frontal impacts (FMVSS No. 208). For this version GM studied the posture of drivers, investigated new materials to more closely represent the stiffness of biomechanical data and introduced internal elements such as the ribcage. Since then, the Hybrid III has been continually improved with modifications such as a new head and better joint characteristics. Data is typically gathered using accelerometers, potentiometers and load cells to measure the acceleration, deflection and forces that the dummies undergo during frontal crash. Such values have in turn been used to improve the safety of cars well beyond seat belt design. Figure 2.15 shows a Hybrid III dummy.

Figure 2.15 Hybrid III surrogate dummy

Throughout the frontal impact dummy development researchers began to investigate the significant injuries being sustained during side impact collisions. As a result, several different research bodies set out to design appropriate side impact dummies to represent the human body and measure relevant parameters during a side impact collision. In the late 1970's the National Highway Traffic Safety Administration (NHTSA) developed the Side-Impact Dummy (SID). This dummy was designed primarily to measure injury risk to the head, chest and pelvis and used the head and neck developed for the Hybrid III dummy. It is currently the only side-impact dummy used in US automobile side impact compliance tests (FMVSS No. 214). As with the Hybrid III, this model was also developed to include rib structures for the evaluation of injury due to compression, a major source of injury during side impact collisions.

During the 1980's both American and European automakers set out to design increasingly improved side impact dummies. The European Experimental Vehicles Committee developed their own side-impact dummy, called the EuroSID, to evaluate automobile compliance with side-impact requirements in Europe. General Motors released the BioSID based on a torso design in conjunction with the Society of Automotive Engineers (SAE). The BioSID represented a more biofidelic ATD than the SID and was integrated with more sensors.

In 2004 the International Standardization Organization released the WorldSID in an effort to develop an internationally accepted side impact dummy and end the dispute between nationally developed side impact dummies. The WorldSID's biofidelity has been evaluated using the International Standards Organization (ISO) method for evaluating lateral impact dummy biofidelity has been considered the best of all lateral impact dummies and is intended for use in any lateral impact compliance test. Figure 2.16 lists the ISO biofidelity results of the WorldSID as compared to several lateral impact dummies and Figure 2.17 shows the WorldSID.

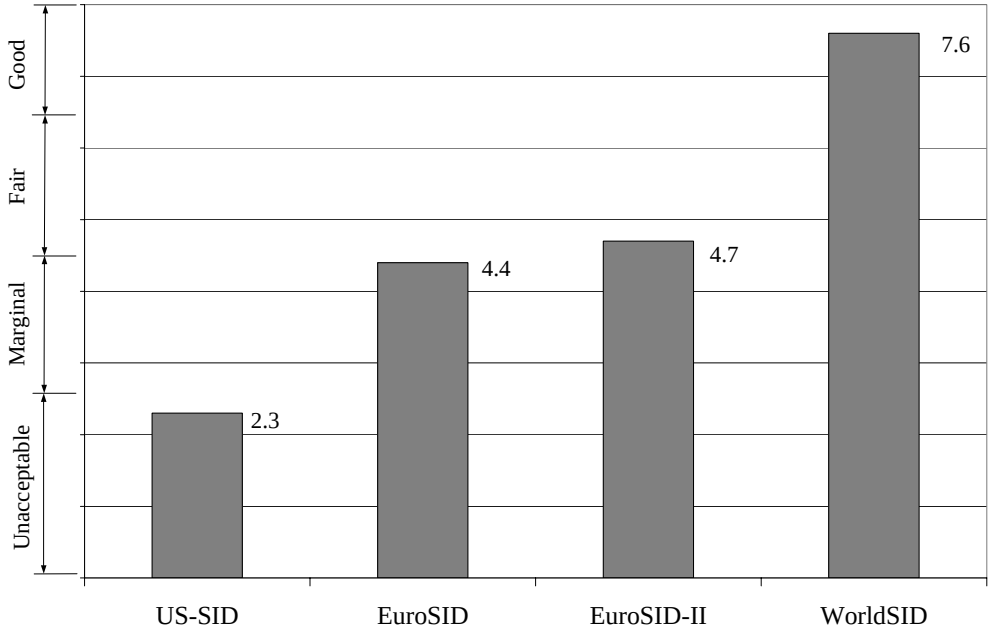

Figure 2.16 Lateral impact biofidelity ratings (WorldSID Home Page)

Figure 2.17 WorldSID surrogate dummy

Dummy Biofidelity

The "biofidelity" of surrogate impact dummies, represents a dummies ability to replicate human response in automotive impact. As noted above, the WorldSID surrogate dummy has been shown to possess the highest level of biofidelity of all surrogate side impact dummies. The procedure for evaluating the side impact dummy biofidelity has been presented in this section with the intention of highlighting the evaluation techniques, such that a similar analysis can be adopted and applied for validation of the model presented in this thesis. The adopted technique are presented here.

The WorldSID was subjected to an extensive series of tests, which simulate various forms of automotive side impact including regional pendulum impacts of the head, neck, shoulder, thoracic, abdomen and pelvis, as well as side sled tests evaluating the same impact regions. The resultant responses were plotted against the experimental corridors, as developed by industry experts, and a measure of biofidelity is developed using the following formula:

$$B = \frac{\sum_{i=1}^{6} U_i B_i}{\sum_{i=1}^{6} U_i} \tag{2.8}$$

Where:

- B — The overall rating having a value between 0 (poorest) and 10 (best).
- B_i — The biofidelity rating of each of the six body regions.
- U_i — The weighting factor for each body region developed by industry experts (ISO, 1999).
- i — Subscript denoting the specific body region (1=Head, 2=Neck, 3=Shoulder, 4=Thorax, 5=Abdomen and 6=Pelvis).

The biofidelity of the six body regions were developed using the following formula:

$$B_i = \frac{\sum_{j=1}^{m} V_{i,j} \left(\sum_{k=1}^{n} W_{i,j,k} R_{i,j,k} \Big/ \sum_{k=1}^{n} W_{i,j,k} \right)}{\sum_{j=1}^{m} V_{i,j}} \tag{2.9}$$

Where:

- $V_{i,j}$ The weighting factor for each test condition for a given body region as developed by industry experts (ISO, 1999).
- $W_{i,j,k}$ The weighting factor for each response measurement for which a requirement is given as developed by industry experts (ISO, 1999).
- $R_{i,j,k}$ The rating of how well a given response meets its requirement.
- i The subscript denoting the body region.
- j The subscript denoting the test condition for a given body region.
- k The subscript denoting the response measurement for a given test condition, j, and body region, i.

The $R_{i,j,k}$ ratings are defined using the following values:

- $R_{i,j,k} = 10$ If response falls within corridor.
- $R_{i,j,k} = 5$ If response falls outside corridor, but lies within one corridor width.
- $R_{i,j,k} = 0$ If response falls outside corridor by more than one width.

The basic function of this analysis was to provide a comprehensive and comparable measure of any dummy's ability to replicate the human side impact response.

2.5.3 Post Mortem Human Subjects

As outlined in previous sections, post mortem human subject testing has been used in many research programs to further the understanding of human injury. Material properties of individual organs have been derived from standard tensile, compression, shear and torsion testing. Bone, lung, heart, muscle, liver and a multitude of other organ properties can be used to develop appropriate numerical representations within a model. The entire human body has been subjected to various forms of loading to evaluate the global onset of injury and develop injury criteria. As well, results from these tests have been used to validate numerical models. Accelerations, forces and deflections are

compared to models to ensure appropriate representation during loading. This technique is used for the analysis of the model presented in this research.

A significant drawback to post mortem human subject testing is the variability of response each human body presents during identical forms of loading. As a result, researchers commonly use response corridors and probability functions to describe response. The corridors represent a range of values a typical human subject will exhibit for a measured response during an impact. For example, during side thoracic pendulum impacts, force versus compression response corridors represent the average thoracic stiffness response. Probability functions are used to develop injury criteria as detailed in a previous section (Viano, 1989a, 1989b, 1989c, Kroell, 1971, 1974).

2.6 Numerical Models to Predict Thoracic Response and Injury

Attempts to numerically model and understand the human body during crash scenarios has been under investigation for the past fifty years. Analytical models were first developed to represent the overall response of the human thorax using a series of springs and dampers. Static analysis was first performed and as computers were developed some limited dynamic analysis was made possible. These models were often validated against PMHS impacts and used as the basis for developing surrogate dummies. Rigid body models were also used to evaluate the kinematics and dynamics of human bodies during crash simulations. This allowed researchers to understand how the body moves during impacts and design the cars to reduce any adverse effects. Finite element models combine both analytical deformation modeling and rigid body modeling techniques to evaluate the combined effects during various crash simulations. The following section presents an overview of various models developed that have been used for improving automotive crashworthiness.

2.6.1 Analytical Models

The first thoracic analytical model was developed by Lobdell et al. (1973) using a variety of springs, masses and dampers to represent the anteroposterior impact response. Figure 2.18 shows the model, which consisted of three masses, two springs and three dampers.

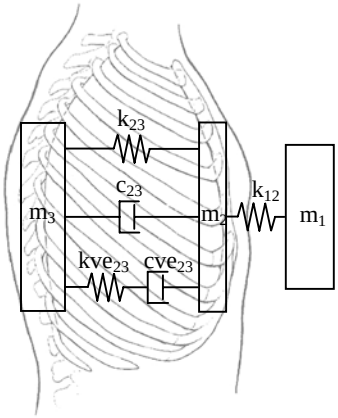

Figure 2.18 Lobdell (1973) thoracic lumped-mass model

Mass m_1 represents the impacting object and can be assigned an initial velocity. Mass m_2 represents the mass of the sternum and portion of the rib structure and thoracic contents. Mass m_3 represents the mass of the remaining part of the thorax and part of the total body mass that is coupled to the vertebral column. Spring k_{12} represents the elasticity of the skin and other material and couples the impacting mass (m_1) and the sternum mass (m_2). The components coupling the sternum mass (m_2) and thoracic mass (m_3) consist of a parallel Voigt (k_{23}, c_{23}) and Maxwell (kve_{23}, cve_{23}) material model. Within the Voigt element, the spring (k_{23}) represents the elasticity of the rib cage and directly coupled viscera, while the damper (c_{23}) represents the air in the lungs and blood in the vessels. The Maxwell element represents the viscoelastic tissue such as the thoracic muscle tissue. The element input parameters were adjusted until the modeled impact response matched the force-deflection response of PMHS under similar impacts as observed in the Kroell et al. (1965, 1967) tests.

As these parameters were developed it was observed that each parameter affected different portions of the force-deflection curve. Sample force-deflection corridors of the

thorax can be seen in Figure 2.19. The sternum mass (m_2) affects the initial portion of the curve, while the thorax mass (m_3) affects the maximum deflection and the force at that deflection. The damper (c_{23}) primarily affects the mid-range force level, maximum deflection and shape of the curve during force decay, while the Maxwell element affects the mid-range force level and the shape and location of the curve at the maximum force and deflection. Finally, the spring (k_{12}) affects the response at low deflections and the spring (k_{23}) affects the remainder of the response. This model was used as the basis for developing the thoracic components of the Hybrid III dummy.

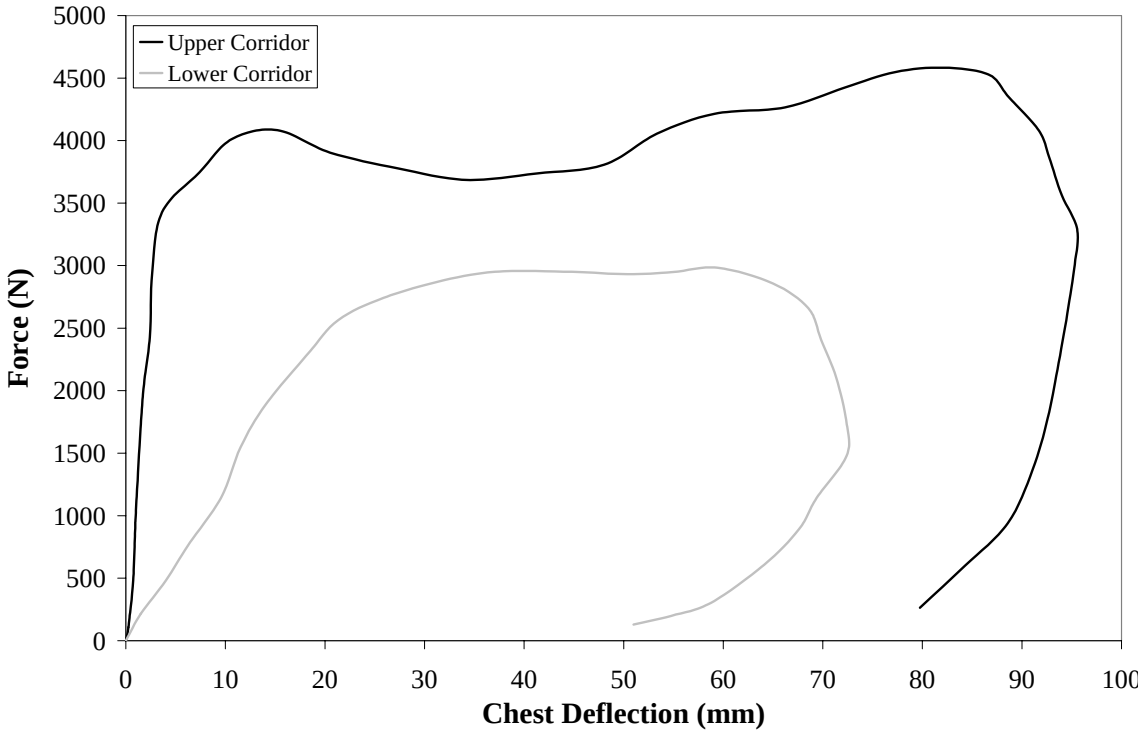

Figure 2.19 Thoracic compression corridors (Kroell, 1974)

Shortly thereafter, Viano (1978) developed a modified Lobdell model that included a secondary spring (k_{23S}) to represent the thoracic bilinear increase in stiffness due to high levels of compression. Figure 2.20(a), shows the modified Lobdell model. The modified model also included the computation of kinetic energy, power and momentum of the masses, and the energy absorbed in springs and dissipated in dampers. Furthermore this model was scaled to represent the 95th percentile male, 5th percentile female and the 6-year-old child. Viano (1987b, 1987c) went on to use this model to evaluate the benefit of

energy-absorbing materials used for side impact protection. The parameters were also developed to represent a laterally impacted thorax as can be seen in Figure 2.20(b).

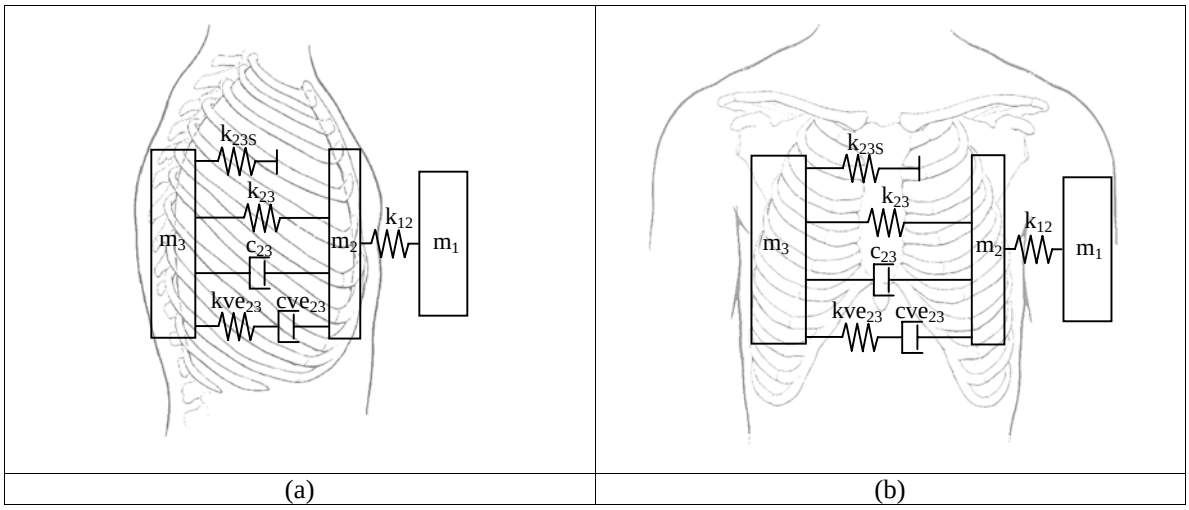

Figure 2.20 Lobdell lumped-mass models for front and lateral impact (Viano, 1988)

2.6.2 Rigid Body Models

Rigid body models are used to investigate the kinematic and dynamic motion of the human body under a variety of loading conditions. This modeling technique assumes the human body is made up of rigid body components joined at points. Each body component is assumed to have prescribed masses and moments of inertia and are connected using rotational joints with prescribed rotational stiffness curves.

Numerous models have been developed in a variety of numerical codes to analyze a multitude of impact scenarios. Detailing every single model would be an arduous task with little merit for the thesis presented here. As a result, a single rigid body model is analyzed, as it is the basis for the modeling techniques employed during this research. Further details of this are provided in a following chapter. Cheng (1994) developed the GEnerator of BOdy Data (GEBOD) program that can be used to generate a rigid body model using ellipsoid body segments with individual geometry and mass properties in LSDYNA code. Figure 2.21 shows the GEBOD model.

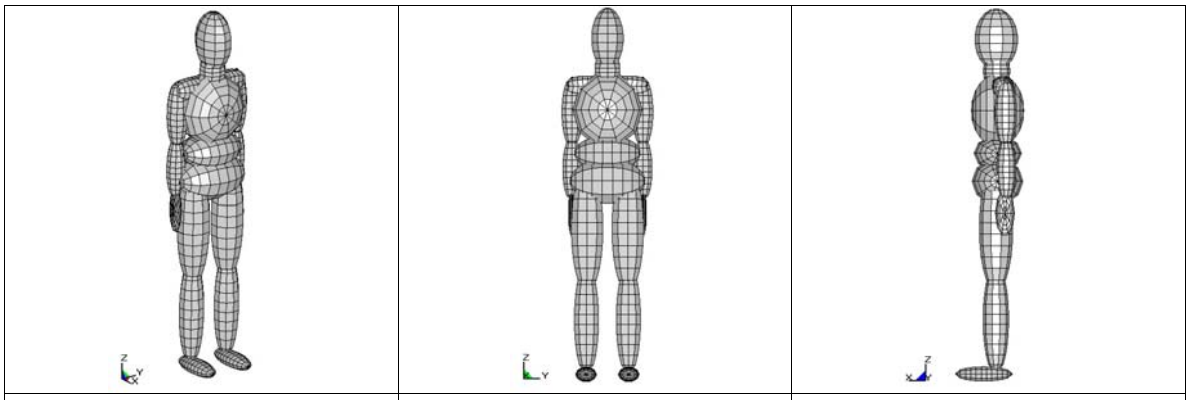

(a) (b) (c)

Figure 2.21 GEBOD model (a) isometric view (b) front view (c) left side view

Mass and geometry parameters are assigned to correlate to the 5th, 50th and 95th percentile male and female. Table 2.13 lists common anthropometric data of the 50th percentile GEBOD as compared to the AMVO database with reasonable correlation.

Table 2.13 50th percentile human and GEBOD geometric and mass properties (Cheng, 1994)

Data		GEBOD	AMVO
Lengths (mm)	Stature	1776.8	1751
	Waist Circumference	943	903
	Upper Arm Length	306	329
	Upper Leg Length	545	447
	Knee Height	499	530
Mass (kg)	Head	4.22	4.14
	Neck	1.03	0.965
	Upper Torso	14.99	37.54
	Lower Torso	24.03	
	Upper Legs	19.12	17.23
	Lower Legs and Feet	9.35	9.14
	Upper Arms	4.21	3.54
	Lower Arms and Hands	2.86	4.04
	Total Body Mass	79.81	76.59

It is noted that the GEBOD lengths and masses appear to be slightly elevated from the AMVO study. This is most likely due to the fact that the GEBOD lengths and masses

were based on measurements of military personal who tend to be taller, larger and leaner than the general population (McConville, 1980).

In the GEBOD approach, the body is separated into 19 rigid segments joined by 10 three-degree of freedom spherical joints and 4 one degree of freedom revolute joints. The knees and elbows use the one-degree of freedom revolute joints. Each joint is modeled as a torsion spring with a damping component. Prescribed stop angles define the limits of rotation and torque-rotation curves govern the motion within the stop angles. A typical torque-rotation curve is shown in Figure 2.22.

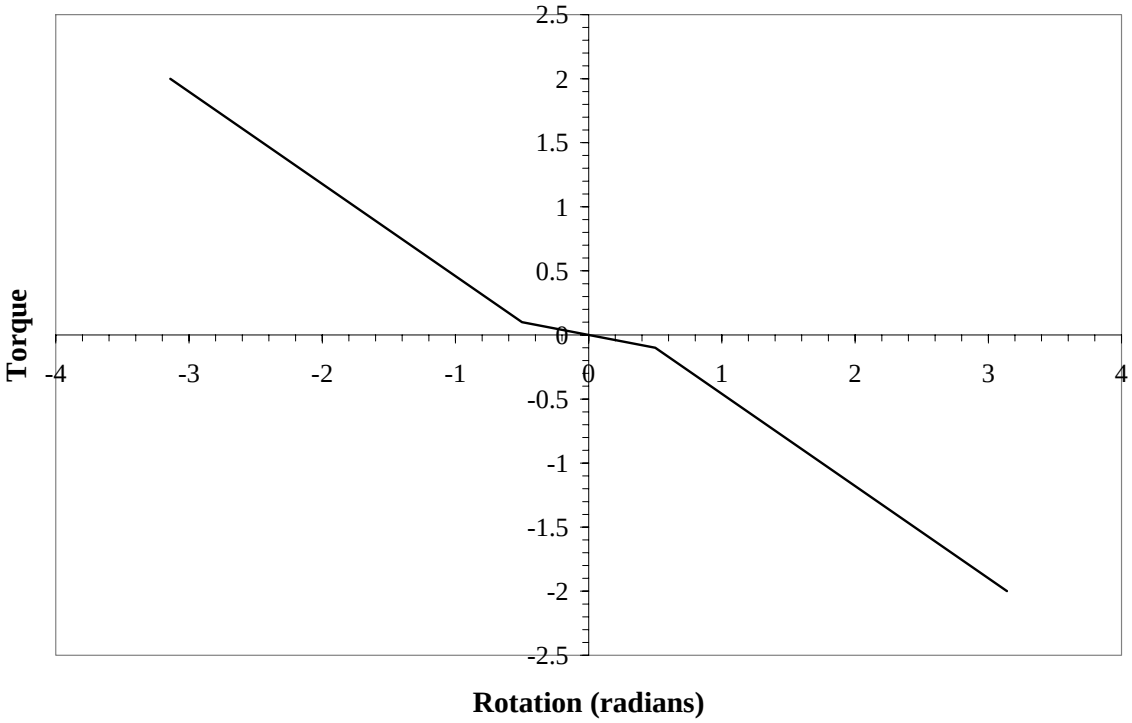

Figure 2.22 Characteristic load curve for surrogate body joints (LSTC, 2003)

Not all joints have the same stiffness characteristics, so a scale factor is applied to a standard torque curve to determine the specific torque curve for each joint. A single damping coefficient is used to define the damping-rotation curve. These coefficients are listed in Table 2.14.

Table 2.14 Joint curve scale factors (Cheng, 1994)

Joint	Torque Curve Scale Factor (Nm)	Friction Curve Scale Factor (Nms/rad)
Pelvis	7344	0.652
Waist	7344	
Shoulder	11.3	
Elbow	11.3	
Hip	1130	
Knee	11.3	
Ankle	11.3	

The stop angles are used to describe the high and low range of motion for each degree of freedom for each joint. At these angles, the joint stiffness increases so as to force the joint back into its range of motion. Each angle is measured from the nominal position found in Figure 2.21. The stop angles are defined in Table 2.15.

Table 2.15 GEBOD joint range of motion (LSTC, 2003)

Joint	R_x		R_y		R_z	
	Low	High	Low	High	Low	High
Pelvis	-20	20	-20	20	-5	5
Waist	-20	20	-20	20	-35	35
Left Shoulder	-30	175	-175	60	-65	65
Right Shoulder	-175	30	-175	60	-65	65
Elbow	N/A		-140	1	N/A	
Left Hip	-25	70	-140	40	-70	70
Right Hip	-70	25	-140	40	-70	70
Knee	N/A		-1	120	N/A	
Left Ankle	-30	20	-20	45	-30	30
Right Ankle	-20	30	-20	45	-30	30

2.6.3 Thoracic Finite Element Models for Auto Crash

Three-dimensional finite element models have been under continual development with increasing complexity as the power of computers has increased. Andriacchi et al. (1974) developed one of the first finite element models to study the interaction between the spine and the rib cage. The ribs, vertebrae and sternum were rigid bodies connected to deformable elements using spring or beam elements. Sundaram and Feng (1977) developed a more complex model using similar techniques, however, it included the rib cage, muscles, lung, heart and spine. Beams, plates, membranes and solid elements were used to model the components and stresses and displacements were reported under static loading. Only a symmetric half of the thorax was developed to reduce computation requirements. These models were very coarse in their element discretization as seen in Figure 2.23 and only described gross thoracic deformations.

Figure 2.23 Andriacchi model (a) anterior view (b) lateral view (Andriacchi et al., 1974)

Several years later, Plank and Eppinger (1989) developed a seven rib thoracic model to investigate the dynamic response under crash scenarios. Plank and Eppinger (1991) made further improvements by improving the rib geometry and adding the remaining five ribs and an abdominal mass. The ribs were modeled using four elements along its cross-section with a uniform cross-sectional area. The internal organ continuum viscoelastic properties were adjusted to generate appropriate responses. This model was validated against PMHS tests and was used to analyze the PMHS interaction with restraint systems (Plank and Eppinger, 1994).

Huang et al. (1994a) developed a finite element model of gross PMHS motion as seen in Figure 2.24. The model consisted of deformable ribs, spinal segments, shoulder components, visceral contents and pelvic components. The thoracic visceral contents did not discern between individual organs and the abdominal visceral contents were approximated using beams to create a damping matrix. The model was validated against PMHS pendulum impact tests and side impact sled tests. The model was also impacted against a variety of soft materials to evaluate their ability to reduce the injury response during side impact scenarios.

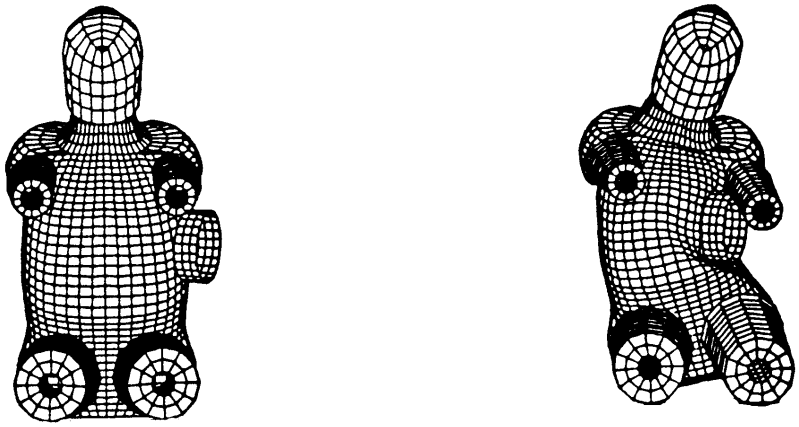

(a) (b)

Figure 2.24 Huang model during side pendulum impacts (a) before impact (b) during impact (Huang et al., 1994a)

Wang (1995) also produced a thoracic model with representations of individual internal thoracic organs. The model included the lungs, heart, aorta, vena cava and pulmonary arteries and veins. Lateral pendulum impact PMHS tests were used for validation and the model matched well. The heart model developed was further modified to study the stress and strain of the heart and specific points of injury (Shah et al., 2001). This model was further integrated with a detailed shoulder model as seen in Figure 2.25 (Iwamoto et al., 2000, Iwamoto et al., 2001), which helped provide insight into the complex injury mechanisms present during lateral shoulder impacts.

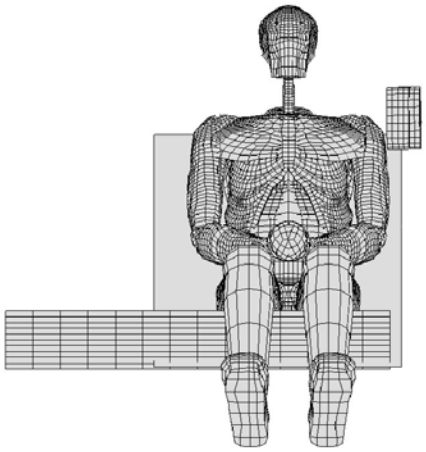

Figure 2.25 Wang thoracic model with Iwamoto shoulder model (Iwamoto et al, 2000)

As the importance of numerical modeling became clear, industrial automotive firms began developing their own models. TNO Automotive, a Dutch crash-safety research centre, has developed several human body models using the MADYMO finite element software package (Happee, 1998, TNO Automotive, 2003). Most notably, the mid-size male model includes thoracic, head and neck, abdominal, pelvic and lower limb components and has been validated against a variety of PMHS pendulum and frontal sled impact tests.

Toyota Inc. developed the THUMS (Total Human Model for Safety) as seen in Figure 2.26(a), which also included the same major body components as those observed in the MADYMO model (Furusu et al., 2001, Oshita et al., 2002). However, the internal organs were represented using single simplified continuum parts to represent the thoracic and abdominal contents. Further research is underway to implement more detailed representations of these components and to develop models representing different body types. A conglomerate of car manufacturers, suppliers, software developers, universities and public research organizations joined together to develop the HUMOS (Human Model for Safety) model as seen in Figure 2.26(b). This model contained the same anatomical components as the MADYMO and THUMS model with detailed representations of pertinent internal organs such as the heart, lungs, kidneys and liver (HUMOS, 2001, Thollon et al., 2002).

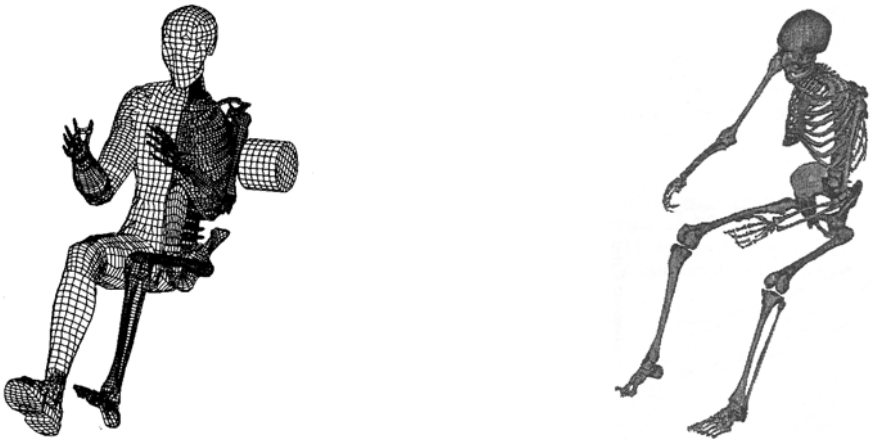

(a) (b)

Figure 2.26 Industrial finite element models (a) THUMS (Furusu et al., 2001) (b) HUMOS (Thollon et al, 2002)

Most recently, the Ford Motor Company developed a detailed full human body model for the prediction of human thoracic impact responses and injuries (Ruan et al., 2003). The thoracic model was based on the model originally developed by Wang (1995) with significant improvements to geometry, articulation and internal organs. Individual abdominal organs were modeled representing the liver, spleen, kidneys, abdominal aorta and inferior vena cava, while the remaining abdominal organs were modeled using a single compressible solid. The pelvis was modeled with accurate geometry and material properties with connection made to a detailed leg model as previously developed by Schuster et al. (2000), previously used to study the injury effects of pedestrian impacts. The model was validated against a variety of frontal and side pendulum impact responses, showing good correlation to force and deflection of PMHS data.

While these models provide accurate correlation of experimental results with an extremely high level of detail, they also possess a significant computational cost. For example, Ruan et al. (2003) suggested that while their model produces excellent correlation to the PMHS pendulum impacts, it remains too CPU intensive to accurately model simulated vehicular crashes such as frontal or side sled tests like the ones presented in this study. As well, Ruan et al. (2003) stated that the direct prediction of rib fractures could not be made also due to the computational costs. As a result, the effects of lost structural integrity from rib fractures could not be modeled. To alleviate these

problems, this study uses a detailed numerical model of the region of interest, the human thorax, while implementing simplified models of all remaining regions to approximate the human body response as outlined in the next chapter.

-- CHAPTER 3 --

Model Development

3.1 Introduction

The original thoracic model underwent two major development cycles before the author began work. The first iteration of the detailed thoracic model (Deng et al., 1999) incorporated three-dimensional representations of the spine, ribs, heart, lungs and major blood vessels. The components and developments of the first iteration were detailed in Chapter 2, along side the presentation of thoracic injuries common to automotive impact. The second iteration of the detailed thoracic model (Chang, 2001) was expanded to include rib cage surface muscles and upper limbs, with improvements to several material constitutive models within the thorax. The components and developments of the second iteration have been detailed in this chapter, which was done as a substantial portion of the developments presented in this study (i.e. the third iteration) involved improvements made to the second iteration. Both of these early iterations were compared to frontal and side impact pendulum tests on PMHS and produced impact force and deflection results that were in good agreement with the PMHS tests. However, use of the model was limited to simple pendulum tests since only the thoracic structure was modeled.

The current study is focused on three aspects: improvement of the thoracic model, based on anatomical data, improved material models and data, and simple validation tests;

completion of the thoracic model with representative body components; and validation of the model using side impact sled tests. In doing this, seven key components of the human body model were highlighted as pertinent areas requiring improvements to ensure this model could be applied to a variety of impact scenarios for evaluation of thoracic impact trauma. The components identified include the surface muscles, the shoulder, the costal cartilage, the pelvis, the lower limbs, the abdomen and the head. The surface muscles and shoulder constitute improvements made to the existing detailed thoracic model, while the pelvis, lower limbs, abdomen and head constitute the development of parts not currently implemented in the model. The costal cartilage was identified as requiring significant improvements during the advanced stages of this study and some preliminary steps were taken to account for its effects. The main goal of these improvements was to expand the applicability of this model to a variety of loading scenarios more representative of automotive impact.

Since the objective of this project was to produce a human body model that can predict thoracic trauma, particularly in side impact, representation of the newly developed components at a similar level of detail to the thorax was deemed computationally inefficient. As a result a simplified modeling approach was taken to develop the geometric and material properties of the new components with the intent of providing representative response with modest computational cost.

The following chapter presents the implementation of these improvements and newly developed components. The improvements made to the existing detailed thoracic model are presented first, followed by the development of the new body components to generate the full body model. Each section outlines the need for the development performed, along with anatomical and physiological information intended for comparison to and justification of the modeling assumptions.

3.2 Muscle Tissue Improvements

The outer tissue of the thorax plays a strong role in the initial response to impact and is an important component in overall thoracic response. During the second iteration of this

model, Chang (2001) implemented this part using a layer of solid elements to cover the thoracic area and upper arms as seen in Figure 3.1. The tissue produced an accurate response when implemented during the side and frontal pendulum impact tests (Chang, 2001).

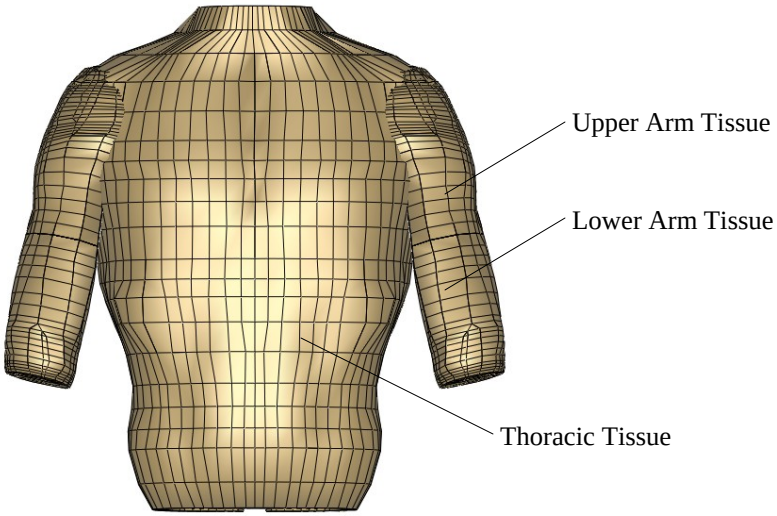

Figure 3.1 Original thoracic and arm tissue model

However, preliminary analysis during side sled impact conditions, as performed by the author, revealed the presence of exceedingly high levels of strain in both the thoracic and arm tissues. In some cases, the strain was recorded as high as 1000 percent. The analysis also indicated that the mesh of the thoracic tissue as compared to the underlying thoracic components was overly coarse, allowing for interpenetration of the underlying components into the tissue. To alleviate these problems, the thoracic and arm tissue material properties were improved, and refinement of the thoracic tissue mesh was completed to produce more realistic responses. The following section provides further details regarding the improvements, with an outline of the original implementation by Chang (2001).

3.2.1 Original Muscle Tissue Material Model

The response of typical human muscle tissue is known to depend on strain rate, fiber orientation, age, moisture level and usage, among other factors (Yamada, 1971, Fung, 1993). To accurately represent a soft tissue in a finite element constitutive model, all of

these factors should be accounted for; however, such a task is often deemed computationally unfeasible for models as large as the one presented here. More importantly, many of these factors do not play a strong role in the short-term compression response, which is primarily rate dependent.

Initially, Chang (2001) used a heart material model (Guccione et al., 1991) (Guccione and McCulloch, 1991) (McCulloch and Omens, 1991) to represent the muscle tissue. This was the same material Deng et al. (1999) used to model the actual heart and follows the same strain energy formula as listed in Equation (2.3). The material is an incompressible hyperelastic material with transversely isotropic properties, with respect to a fiber axis whose orientation varies through the thickness of the tissue wall (Guccione et al., 1991). The material constants were obtained from bi-axial tensile testing of excised human myocardium performed by Yen (1999) and from the original material model development by Guccione and McCulloch (1991). While this material provided adequate results during thoracic pendulum impact simulations, its lack of rate dependent effects became clear when the model was subjected to side impact sled tests, by the author, leading to inaccurate results.

Another important aspect was an inconsistency in the material properties regarding the density of the arm and thoracic tissue as developed by Chang (2001). While both materials used the same constitutive model, the arm tissue was assigned a density of 1000 kg/m^3, approximately correct for soft tissue, while the thoracic tissue was assigned a density of 2400 kg/m^3. Chang (2001) reported that the elevated density of the thoracic tissue was to provide appropriate mass distribution throughout the thorax due to voids spaces between the internal organs and thoracic cage. In reality, these void spaces do not exist in the human torso and were an artifact in the model. Since replacing these voids with actual tissue material was not completed within this study, the elevated density was also used in the current work. The elevated density provided an extra 8.19 kg distributed evenly over the thoracic cage, resulting in a total thorax mass of 21.6 kg, which was shown by Chang (2001) to be comparable to available anthropometric data.

3.2.2 Improved Muscle Tissue Material Model

Experimental Resources

To accurately model the thoracic tissue, experimental material data was obtained in order to apply it to a constitutive model. Numerous studies have been performed on the tensile properties of muscle tissue from both humans and animals. Yamada (1970) and Abe (1996) presented extensive data regarding the tensile stress-strain relationship of both individual muscle fibers and whole muscles. However, compression testing performed on muscle tissue is very limited. McElhaney (1965) loaded bovine muscle tissue in a pneumatic testing machine at the following strain rates: $0.001s^{-1}$, $0.1s^{-1}$, $1s^{-1}$, 100^{-1} and $1000s^{-1}$. Recently, Van Sligtenhorst (2003) performed similar tests on fresh bovine semimembranosis muscle using a polymeric Split Hopkinson Pressure Bar. In these tests, specimens were loaded at the following strain rates: quasi-static, $1120s^{-1}$, $1430s^{-1}$ and $2250\ s^{-1}$. Figure 3.2 plots the compressive response as measured using true stress and true strain of both experiments for comparison to the original tissue model. This graph shows that although the original material model (heart tissue) has a hyperelastic response, it does not capture the significant rate effects shown to be important in auto crash simulation.

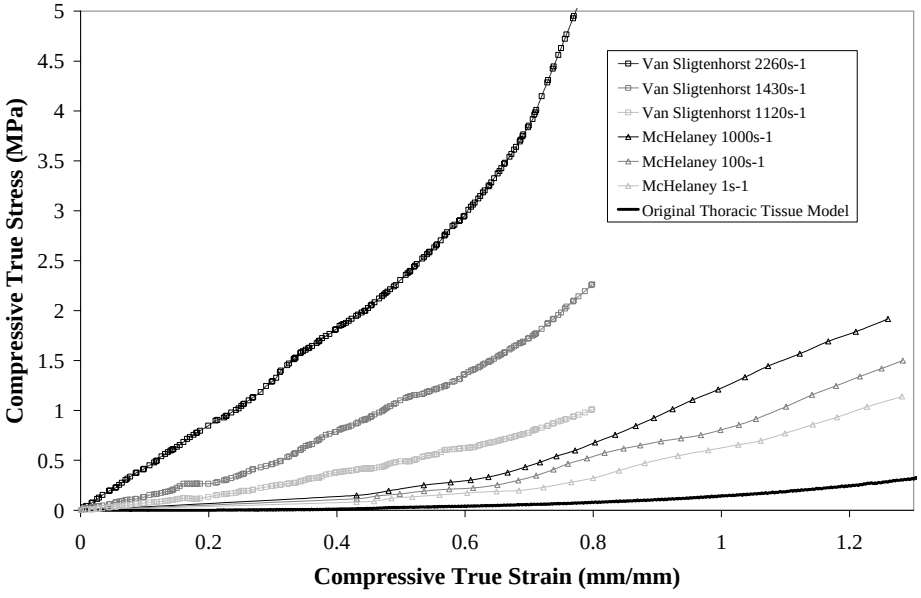

Figure 3.2 Experimental and simulation tissue stress-strain curves

Constitutive Material Model

The material response shown in Figure 3.2 could be modeled using linear or quasi-linear viscoelasticity approaches. However, given that the loading is essentially monotonic, a simplified approach can be considered. A rate dependent hyperelastic material model as developed by Du Bois (2003) was used to model the hyperelastic and viscoelastic dependent properties exhibited by the muscle tissue. This material uses unique stress-strain curves at specific strain rates to define material response and capture these complex properties. The stress-strain curves used for this model are those developed by McElhaney (1965) and Van Sligtenhorst (2003) and the pertinent parameters required for this model are listed in Table 3.1.

Table 3.1 Muscle material parameters

Parameter	Value	Description
RO	1040 kg/m^3	Density
K	2.48E3 MPa	Bulk Modulus (calculated below)
MU	0.1	Damping coefficient value (recommended by Du Bois (2003))
G	0	Shear modulus damping (no damping used)
SIGF	0	Limit stress for damping (no damping used)
SGL	1 mm	Specimen gauge length (engineering stress/strain input data used)
SW	1 mm	Specimen width
ST	1 mm	Specimen thickness (engineering stress/strain input data used)
TBID	N/A	Table ID number. Table contains strain rate values that link to an engineering stress/strain curve for that strain rate.
TENSION	0	Rate effect parameter (rate effects considered for compressive loading)
RTYPE	1	Strain rate type (engineering stress/strain input data used)
AVGOPT	1	Strain rate calculation (12-point running average to reduce numerical noise)

The bulk modulus was calculated using muscle material properties and the following formula, assuming the bulk modulus greatly exceeds the shear modulus:

$$K = \rho \cdot C_o^{\,2} \tag{3.1}$$

Where ρ is the density of the tissue and C_o is the tissue sound speed. The density of human muscle tissue, 1040 kg/m^3, was used (Geddes and Baker, 1967) and the sound speed as measured in human pectoralis muscle, 1545 m/s, was used (Goss, 1978).

As noted earlier, the density of the thoracic tissue was maintained at 2400 kg/m^3 following the developments by Chang (2001) to generate appropriate mass distribution throughout the torso. However, the use of such a high density when coupled with the selection of a realistic bulk modulus effectively decreases the material wave speed. On the other hand, if an accurate wave speed was desired, this would require the use of an elevated bulk modulus. The three following factors must be taken into account when appointing these properties: the contact stiffness calculation of the tissue, the pressure-volume response of the tissue and the stress equilibrium state of the tissue. The contact stiffness and pressure-volume response of the tissue depend on the appointed bulk modulus, and the stress equilibrium state of the tissue depends on the wave speed. With a realistic bulk modulus and low wave speed, the contact stiffness calculation and pressure-volume response are accurate, while the time required for the tissue to achieve stress equilibrium increases. This could artificially stiffen the material and elevate the force response during impact. On the other hand, with an elevated bulk modulus and realistic wave speed, the contact stiffness and pressure-volume response of the model increase, and the time required for the tissue to achieve stress equilibrium is accurate. This could also artificially stiffen the material and elevate the force response during impact. The pressure-volume response however was believed to play an insignificant role on tissue stiffness as the strain rates observed during the impacts investigated in this study primarily provide a deviatoric deformation as opposed to a hydrostatic deformation.

To evaluate which set of properties would provide a more accurate impact response, a preliminary frontal pendulum impact simulation was conducted where the thoracic tissue was impacted with a large blunt object. Under the two cases, the impact force was measured between the torso and impactor. The results indicated a 10% increase in peak force when the model was run using an elevated bulk modulus and realistic wave speed.

This suggests that the contact stiffness calculation is the primary influence of the impact force response, and that the use of a realistic bulk modulus and elevated wave speed would provide a more accurate impact. Table 3.2 lists the material properties as used for the arm and thoracic tissue.

Table 3.2 Revised material model parameters

Material	Density	Bulk Modulus
Thoracic	2400 kg/m^3	2.48x10^3 MPa
Arm	1000 kg/m^3	2.48x10^3 MPa

Thoracic Muscles Tissue Mesh Refinement

The mesh density of the thoracic tissue was improved by dividing the vertical dimension of the elements by two. This provided a mesh density increase of 100% and better matching of mesh densities when compared to the underlying thoracic components. Figure 3.3 shows the results of this change as compared to the original model, indicating that the element aspect ratio was also improved in this refinement.

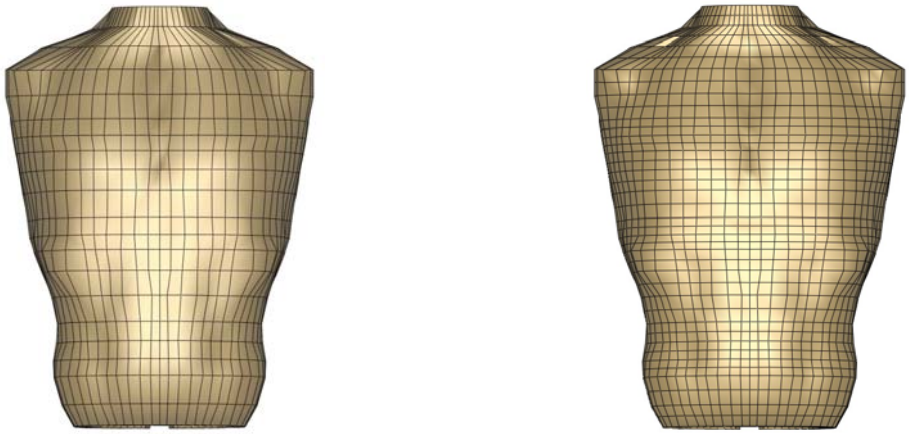

(a) (b)

Figure 3.3 Thoracic mesh refinement (a) old mesh (b) new mesh

3.3 Shoulder Model Improvements

The shoulder response of the human body is known to be important in side impact crash as it transmits load from the impacting surface to the thoracic cage. When directly engaged, the shoulder acts as a point of energy absorption, reducing the resultant energy

absorbed by the thorax. Producing an accurate shoulder response is therefore pertinent for developing an accurate thoracic response during side impact crash. The detailed shoulder model as developed by Chang (2001) provided a realistic kinematic response of the upper extremities for the front and side thoracic pendulum impact tests. However, preliminary analysis by the author showed that the model lacked several key components resulting in unrealistic impact responses when subjected to shoulder pendulum impact tests. Severe rotation of the scapula during these tests was observed highlighting two areas requiring improvement. First, the muscle material model and geometry within this region was improved and remodeled, and second, ligaments absent in the model were added.

Another important aspect of the original model that has been addressed in this study was that it could not predict injury during impacts with the shoulder. While it is understood that injury to this region is a common occurrence in side impact scenarios (Frampton, 1997, Bolte, 2003), the development of an injurious shoulder model was not attempted. Instead, the existing model was evaluated during injurious shoulder impacts in order to evaluate the effects of using a non-injurious shoulder model during injurious impacts. A following chapter presents impact and injury analysis performed with emphasis on the response of the thorax due to the use of the non-injurious shoulder model.

3.3.1 Anatomy of the Shoulder

The shoulder structure is a complex system of bones, ligaments and muscles, which interact with one another to produce a series of joints providing the high level of free motion the upper limbs posses. The bony components consist of the humerus, clavicle and scapula, which act as the support structure. The bones connect to form the following three effective joints: sternoclavicular joint (connects the clavicle to the sternum), acromioclavicular joint (connects the scapula to the clavicle) and the glenohumeral joint (connects the humerus to the scapula). At each joint, a complex series of ligaments facilitate the connection between the bony components, as outlined in Figure 3.4. Seventeen muscles connect the skeletal structure to either the thoracic cage or itself in

order to facilitate controlled motion. The muscles are thick fibrous bands, each with an origin and insertion at either end that attach at a point, along a line or across a plane.

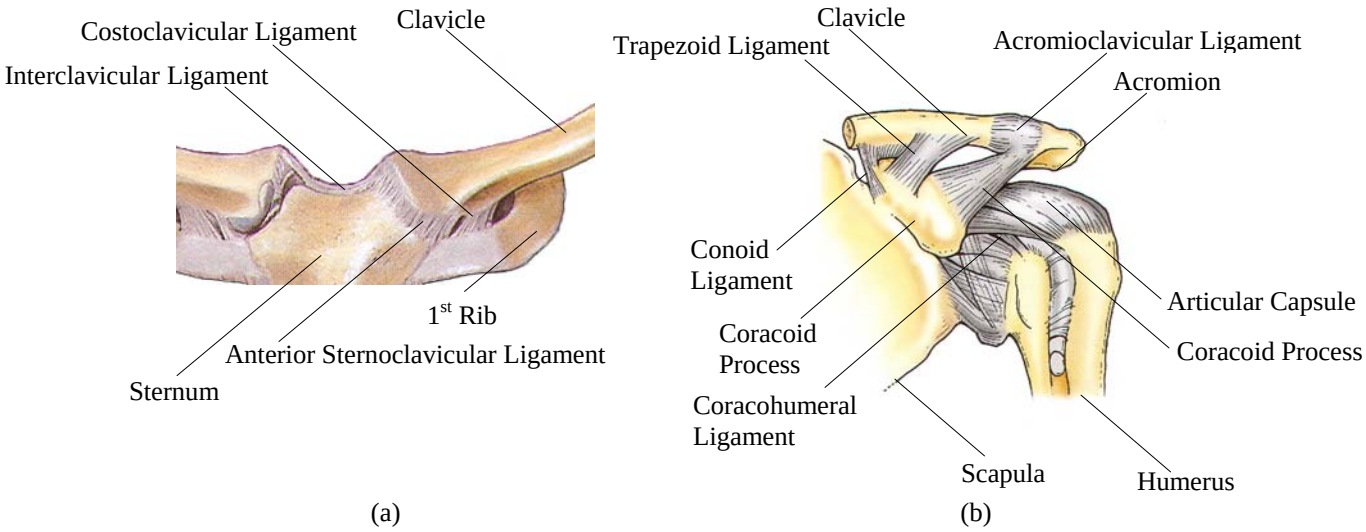

Figure 3.4 Shoulder anatomy and joints (a) sternoclavicular joint – anterior view (b) acromioclavicular and glenohumeral joint – anterior view

3.3.2 Original Numerical Shoulder Model

Chang (2001) developed the detailed representation of the shoulder and upper limbs with bony and limited muscle structures. The humerus, clavicle and scapula were modeled as isotropic linear elastic materials with properties obtained from Yamada (1970). The sternoclavicular joint, acromioclavicular joint and glenohumeral joint were modeled using spherical joints with three rotational degrees of freedom. For the glenohumeral joint moment and damping curves were obtained from experimental testing, while for the sternoclavicular joint and acromioclavicular joint the moment and damping responses were adopted from the costosternal joints. This approach was used as little to no data could be found on the stiffness response of the sternoclavicular or acromioclavicular joint. Although not important to the shoulder development presented in this research, it is also noted that the elbow joint and wrist joint were modeled using the same spherical joint approach; thereby joining the humerus to the radius and ulna, and the radius and ulna to the carpal bone. A linear elastic material with properties obtained from Yamada (1970) was used for each bone.

Eight shoulder muscles were modeled to simulate the passive muscle response between the shoulder bones and the thoracic cage. The subscapularis and infraspinatus were modeled using both solid and beam elements while the latissimus dorsi, rhomboideus major and minor, teres major and minor and the lower trapezius were modeled with beam elements. Each muscle was split into a discrete number of beams intended to represent the combined effect of a single muscle. These elements were modeled using a specific cross-sectional area and Young's modulus acting only in tension, to govern the muscle response, however the origin of this information was uncertain. The solid elements of the subscapularis and infraspinatus were connected to the scapula, while contact with these parts was defined with the thoracic cage and outer tissue in order to allow the scapula to move over the scapulothoracic gliding plane (i.e. outside of thoracic cage posteriorly). The solid elements were modeled using the same heart tissue material model as used for the thoracic and arm tissue.

3.3.3 Improved Numerical Shoulder Model

Shoulder Muscles

Three changes were made to improve the shoulder muscle representation as developed by Chang (2001). First, all the original beam muscles within the thorax were given new attachment and insertion points as defined in anatomy books (Moore and Dalley, 2002, Rohen and Yokochi, 1983) and muscle measurements made on PMHS (Chancey et al., 2003).

Second, new beam elements were added to model pertinent muscles absent within the original model, which was particularly important for muscles connected to the scapula. The following five new muscles were added to improve the shoulder model: upper trapezius, levator scapulae, pectoralis major, pectoralis minor and sternocleidomastoid. The origin and insertion points were obtained from the same information sources as used to define the corrected muscle attachments. The improved and added muscles can be seen in Figure 3.5 along with the old muscle model implementation. It is easy to see that

while the original model consisted of numerous muscles, it lacked a far greater number also just as important.

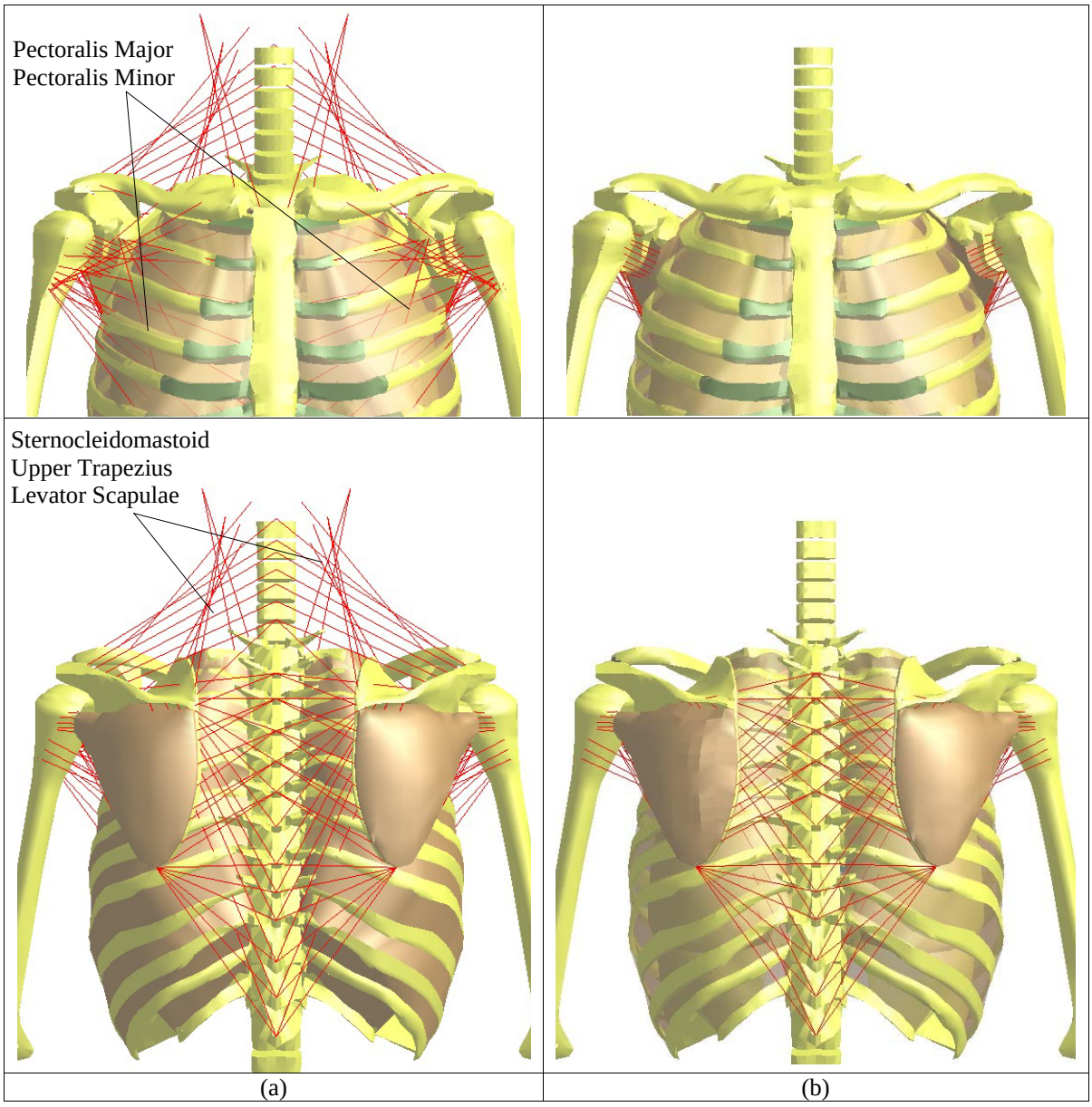

Figure 3.5 Muscle model view posteriorly (top) and anteriorly (bottom) (a) new model (b) Chang model

Third, the material models used for both the solid and beam muscle elements were replaced with more appropriate models. The soft tissue material model used for the solid elements, was replaced with the same hyperelastic rate dependent soft tissue developed

for the thoracic and arm tissues. The density was assumed to be the same as the arm tissue with a similar bulk modulus.

The original linear elastic material used to model the beam elements was replaced with a Hill-type muscle material model as developed by Hill (1928) and Winters (1990). This material consists of a contractile element (CE), which describes the active muscle force F_{CE} generated by muscle contraction and a parallel elastic element (PE), which describes the passive force F_{PE} generated by energy storage from muscle elasticity. For the purposes of this model only the passive force has been included since the numerical model is validated against passive PMHS testing.

The passive force is described as a normalized force using the following exponential function:

$$f_{PE} = \frac{F_{PE}}{F_{\max}} = \frac{1}{e^{K_{sh}} - 1} \cdot \left[e^{\left(\frac{K_{sh}}{L_{\max}} \cdot (L-1) \right)} - 1 \right] \tag{3.2}$$

Where F_{max} is the peak isometric force generated by the passive muscle, L_{max} is the length at which the maximum force is generated and K_{sh} is a dimensionless shape parameter controlling the rate of rise of the exponential function. The model requires the input of the initial length (L_0) of the muscle as observed in the body, along with L_{max} and F_{max}. L_0 was calculated as the linear distance between the origin and insertion of each muscle beam. An L_{max} of 0.7 was used as recommended by Winters (1995). The F_{max} was calculated using the following formula:

$$F_{\max} = \frac{\sigma_{\max} \cdot PCSA}{n} \tag{3.3}$$

Where σ_{max} is the peak isometric stress generated in the muscle, *PCSA* is the physiological cross-section of the muscle and n is the number of beams used to represent the muscle. A σ_{max} of 0.6 MPa was used which was taken from recommendations made

by Winters and Stark (1988). The PSCA used were obtained from PMHS muscle measurements made by Veeger et al. (1991) and Van Ee et al. (2000). Table 3.3 lists the muscles modeled with the number of elements used, the PCSA and the F_{max} values.

Table 3.3 Muscle material parameters (Veeger et al., 1999, Van Ee et al., 2000)

Muscle	PCSA	n	F_{max}
Infraspinatus	951	5	114.120
Latissimus Dorsi – Lower	865	6	86.450
Latissimus Dorsi – Upper	865	2	259.350
Levator Scapulae	282	5	33.840
Pectoralis Major	1365	13	63.000
Pectoralis Minor	374	5	44.820
Rhomboideus Major	627	10	37.590
Rhomboideus Minor			
Sternocleidomastoid	492	2	147.600
Subscapularis	1386	8	103.950
Teres Major	1002	3	200.300
Teres Minor	273	3	54.600
Trapezius	1599	20	47.960

It should be noted that the use of beam elements here is an approximation of actual muscles. Muscles tend to follow more complex paths better represented by curves. For example, the trapezius connects from various points along the spine, wrapping over the outside of the scapula, to attach to various points on the scapula. When the scapula is rotated, the trapezius is pulled across its surface inhibiting its motion. With the simplified modeling approach in this study this effect was less pronounced as the beams are able to pass through various parts. An attempt was made to model this wrapping effect using shell elements stretched over top of the scapula as seen in Figure 3.6. However, due to numerical instabilities the more simplified approach was taken. This could however be considered for further developments in the future.

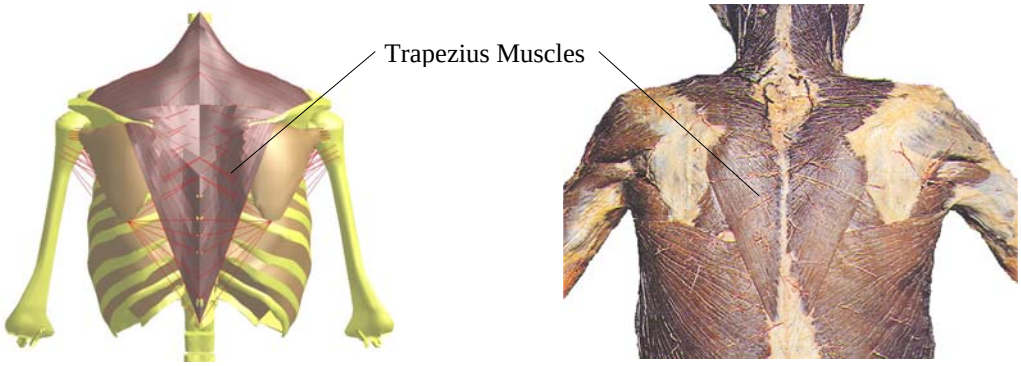

Figure 3.6 Trapezius muscle (a) model (b) post mortem human subject

Shoulder Ligaments

For the ligament modeling performed on the existing model, identifying the pertinent ligaments that effect the scapular rotation was the first established. Experimental testing by Fukuda et al. (1986) revealed that the conoid and trapezoid ligament were the primary source of scapular restraint when the acromioclavicular joint undergoes large rotational displacements about the vertical axis, i.e. the direction of elevated rotation observed in the model. This can be seen in Figure 3.7 and as a result, the conoid and trapezoid ligaments have been modeled.

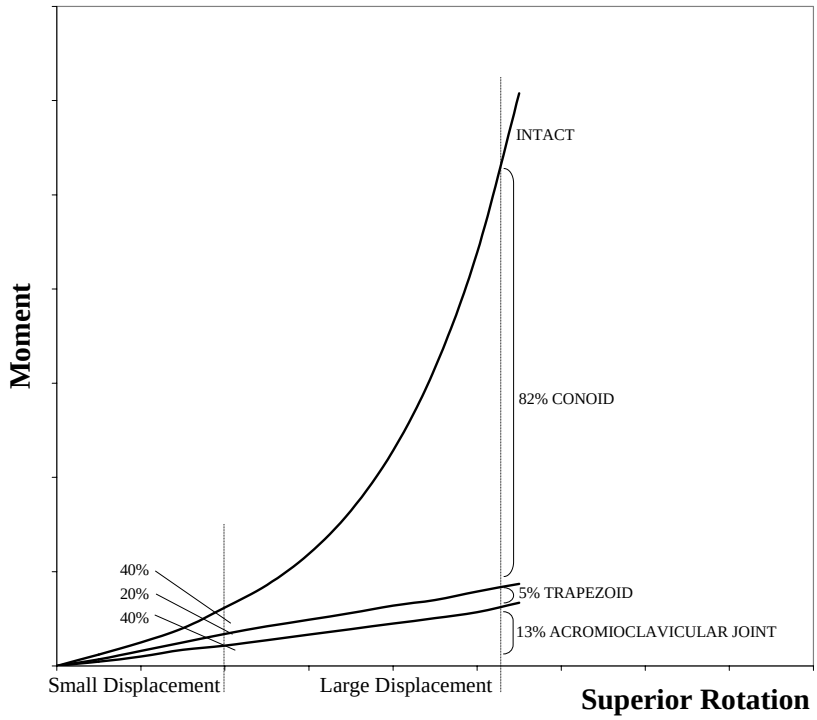

Figure 3.7 Acromioclavicular joint displacement and rotational load distribution

The conoid and trapezoid ligaments are thin bands of tissue that attach to the scapula and clavicle. To model each ligament, two beams were used to represent the edges of the ligaments with attachment points as obtained from PMHS measurements (Boehm et al., 2003). The combined cross-sectional area of each beam represents a typical ligament obtained from PMHS measurements (Costic et al., 2003, Makhsous et al., 1999, Harris et al., 2001). The material used to model the ligaments is a linear elastic isotropic material with a Young's modulus of 10 MPa based on high rate tensile testing by Koh et al. (2004). It is noted that human ligaments are inherently nonlinear viscoelastic and such an approach is a simplification. However, the Young's modulus used here was obtained from the high rate experiments by Koh et al. (2004) which was believed to be a reasonable representation of the loading experienced during both the pendulum and side sled impacts. Figure 3.8 shows the ligaments as implemented in the model with a shell structure overlaying the beams to highlight the ligaments. The darker ligament is the trapezoid, while the lighter ligament is the conoid.

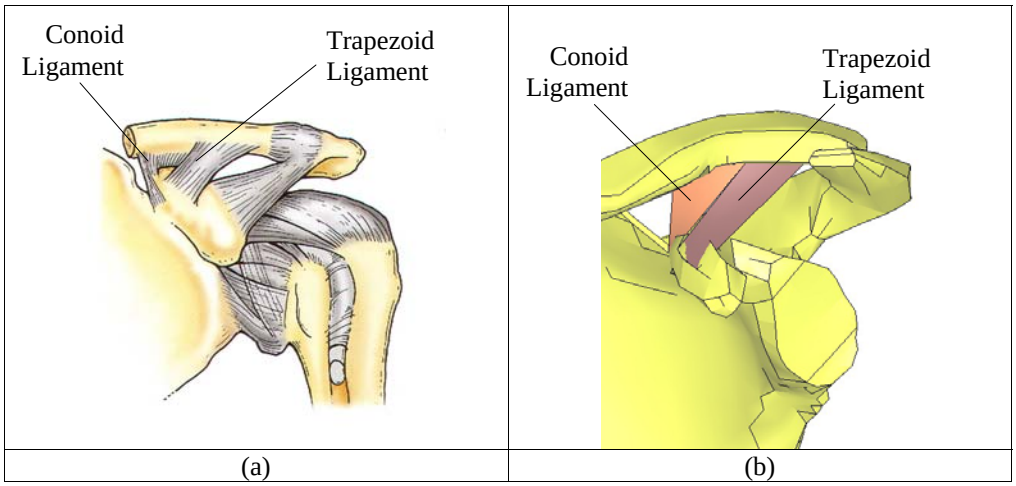

Figure 3.8 Trapezoid and conoid ligament (a) numerical model (b) anatomical reference

The effect of these implementations became evident when in simulated shoulder pendulum impacts showed a reduction in scapular rotation, producing values with better correlation to the experimental results. This is outlined in more detail in a following chapter.

3.3.4 Model Arm Positioning

A key aspect of the human body models is the ability to position the body for various types of tests, where arm and shoulder position are very important. For the impact scenarios presented in this research, various arm positions were used throughout. While the details of each impact scenario can be found in following sections and chapters, the modeling techniques used to achieve these positions and the positions themselves are described here. The following three unique arm positions were identified from the various impact scenarios: arms raised over the head in a vertical position ("arms-vertical"), arms held in front of the body in a horizontal position ("arms-horizontal") and arms resting at the side of the body with the forearms placed in the lap ("arms-rest"). During the "arms-rest" position, the upper arm was laterally positioned as close to the torso as possible, without causing interpenetration of the upper arm and thoracic muscle tissues.

Since the model was given to the author in the "arms-horizontal" position, this became the reference position to describe the rotation required to achieve the "arms-up" position and the "arms-rest" position. The point defining the center of the glenohumeral joint acted as the center of rotation, and rotation was performed with respect to two axis systems as seen in Figure 3.9.

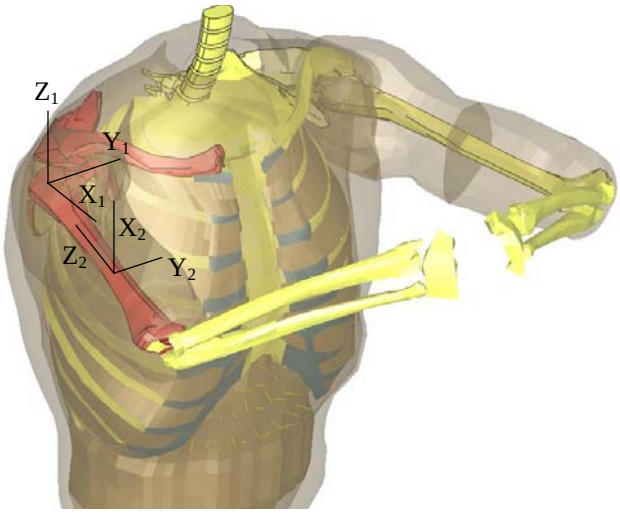

Figure 3.9 Glenohumeral joint rotation coordinate system

The first axis system was defined with the origin at the glenohumeral joint center, the x-axis in the anterior-posterior direction, the y-axis in the medial-lateral direction and the z-axis in the superior-inferior direction. The second axis system was defined with the origin at the center of the humerus (both radially and longitudinally), the z-axis aligned with the humerus length, the x-axis in the superior-inferior direction and the y-axis orthogonal from both following the right hand rule. Table 3.4 outlines the rotations required to place the arms in the correct positions.

Table 3.4 Glenohumeral joint rotations

Arms – Up		Arms – Rested	
Rotation Axis	Rotation	Rotation Axis	Rotation
X_1	0º	Y_1	80º
Y_1	-82.4º	X_1	-4º
Z_1	0º	Z_2	5º

These rotations also required the adjustment of the moment-rotation curves governing glenohumeral joint response. Recall, the rotational stiffness curves were based on the passive stiffness of the joint using experimental in vivo testing. This simulated a joint rotation stiffness that accounted for the interaction of the muscles and ligaments that attach to the bones surrounding the joint. The nominal position of the arm, wherein no stiffness is present in any rotational direction, occurs when the arms are aligned with the body in the down position. When the arms are rotated out of that position, the stiffness within the joint increases as the ligaments and muscles are stretched. This was especially true at the limits of rotation, which with respect to the model was observed only during the “arms-up” position.

Within the original model, where no ligaments were modeled and the muscles provided no force effects when stretched, the use of these curves was quite valid. However, within the new model, where the force effects of the muscles when stretched are present, a slight adjustment of the load curves was required. It was observed that with both the new muscles and old joint load curves, unrealistic rotation of the scapula was occurring during impacts where the model was positioned with the “arms-up”. While it is understood that

both the ligament and muscle tissues govern the rotational stiffness of the joint, especially at the rotational limits, the contribution of each component could not be established from the literature. To compensate, the load curves governing the stiffness of the joint were adjusted, such that in the "arms-up" position only the muscles provided rotational force on the joint. The stop angles of the joints, originally implemented by Chang (2001), remained the same as a precautionary measure to ensure that over rotation of the joint did not occur.

3.4 Costal Cartilage Improvements

During the later stages of this research, it became apparent that the material properties of the costal cartilage played a significant role on the response of the thorax. As a result, an investigation was implemented to identify these effects. While, this has been completed, several improvements should be considered for future models as outlined below.

The costal cartilage as developed through the first two iterations of the model, was modeled using a linear elastic isotropic material with a Young's modulus of 12 GPa. Deng et al. (1999) quoted this as being augmented from the literature to account for the bone-cartilage-bone complex with the reasoning that the sharp contrast of material properties between the ribs and the cartilage within the model was not representative of an actual human. Instead Deng et al. (1999) suggested that a greater stiffness would be encountered due to the smooth transition from one material to the other. It should be noted that the augmentation placed the costal cartilage stiffness approximately 300 times greater than values as listed in the literature (Wang and Yang, 1998, Yamada, 1970). Figure 3.10 outlines the modeled costal cartilage.

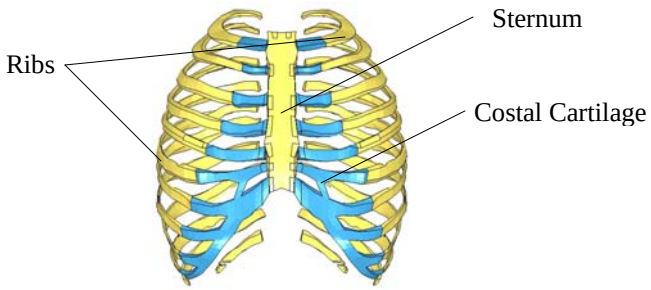

Figure 3.10 Costal cartilage and ribcage

While not explicitly stated, it is believed that this augmentation was also implemented to account for two deficiencies within the model. First, the voids between the internal thoracic organs and the thoracic cage, as noted in a previous section, caused the model to produce an overly compliant response. Second, the lack of a physical abdomen within the model, which normally provides thoracic compression resistance, also resulted in an overly compliant response. To compensate for these issues, the costal cartilage stiffness was increased, which in turn produced a model response that matched the experimental results. Throughout this research, the abdomen has been implemented within this development, however the voids between organs and thoracic cage have not been corrected.

It is understood that the use of a realistic costal cartilage Young's modulus would produce a sounder theoretical basis for addressing the issues at hand. However, preliminary analysis showed that such an approach produced a highly compliant thoracic response with unrealistic force and compression results during side impact scenarios. Since the voids within the thorax were not corrected, this author took up a similar approach as taken by Deng et al. (1999) in an effort to account for the void spaces within the thorax. This was not a desired approach, but the remodeling of the thoracic organs was outside the scope of this project. A Young's modulus of 400 MPa was used, an increase of one magnitude as compared to actual costal cartilage. This became the baseline costal cartilage stiffness for all impacts, which is addressed in one form or another throughout the following chapter. For future developments of this model, the voids within the thorax should be filled, providing a more realistic mass distribution and allowing for the implementation of a realistic costal cartilage stiffness.

3.5 Simplified Pelvis Development

Injuries sustained by the pelvis during side impact collisions have been found to account for 8% of all injuries with an AIS≥4 (Lewis, 1996). While substantial, it was believed that the need to represent these injuries would not noticeably affect the goal of predicting thoracic injury. However, preliminary analysis of the high speed film from side sled PMHS testing showed that while pelvic injury may not be important, accurate

deformation response of the pelvic region was imperative in order to predict global body response. During such impacts, the body was observed to absorb the impact along its entire length. As a result, the simplified pelvic model was developed such that characterization of the pelvic deformation could be achieved. Verification of the simplified model was performed in order to ensure the appropriate response during a more controlled impact, which could then be used in the more complex side sled impacts.

3.5.1 Pelvic Anatomy

Pelvic Anatomy

The pelvis is comprised of bony, ligamentous and muscular tissue, and is situated in the both the abdominal and pelvic cavities. Its funneled shape encloses the urinary bladder, genital organs, rectum, blood vessels and portions of the intestines and colon. The pelvis is comprised of two irregularly shaped hipbones, the sacrum and the coccyx. The hipbones connect anteriorly to one another through the pubic symphysis (cartilaginous joint) and posteriorly to the sacrum through the sacroiliac joints (synovial). The sacroiliac joints are strong with little to no articulation between the hipbones and the sacrum due to the strong ligaments and interlocking bones. The sacrum connects to the fifth lumbar vertebrae through the lumbosacral joint and various ligaments, similar to common vertebral connections. The pelvis is a strong structure with load bearing capacity required to transfer weight from the upper body through the spine to the lower extremities. Figure 3.11 shows the pelvic anatomy connected to the spine as compared to the simplified pelvis developed here.

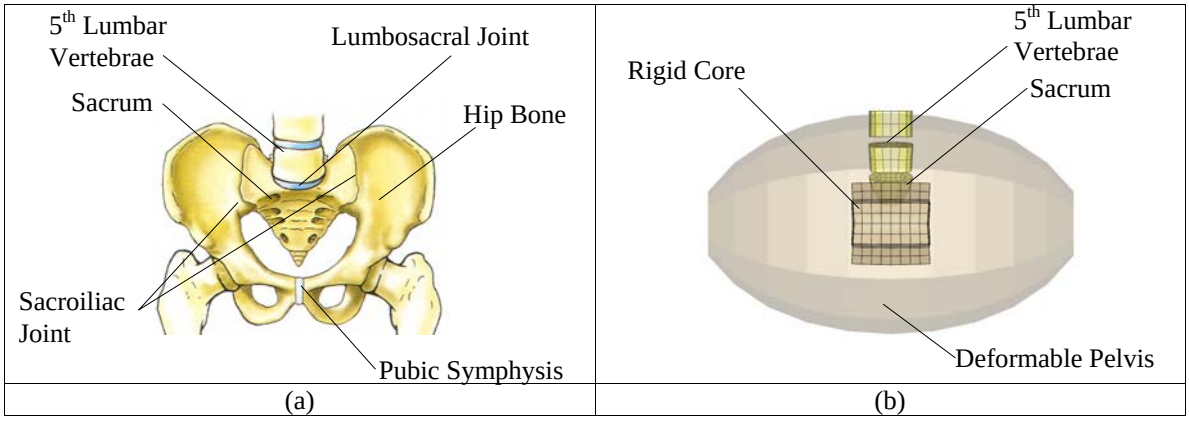

Figure 3.11 Pelvis anatomy - anterior view (a) human (b) simplified model

Pelvic Injury

While no pelvic injuries are modeled throughout this study, explanations of each type have been outlined here for reference purposes later in the thesis. In side impact, pelvic injury stems from door impacts to the greater trochantor of the femur; which pushes on the acetabulum and induces pelvic fracture. Two common types of fracture exist; pubic rami fractures and acetabular fractures. Rami fractures are more common (Guillemot, 1997) and result from bending loads applied to the acetabulum. Acetabular fractures result from compressive loads applied through the femoral head.

3.5.2 Simplified Pelvic Model

During the first two iterations of this model, the pelvis was represented using a single point mass attached to the sacral vertebrae within the model. Here, a simplified pelvis has been developed as a single uniform component, as seen in Figure 3.11, with dimensions defined by the GEBOD rigid body model. Solid elements were used to generate the ellipsoid shape, which is comprised of a rigid core with surrounding deformable elements. The core facilitates the rigid attachment of the pelvis to the sacrum to represent the limited motion of the sacroiliac joints. The location of the pelvis was set relative to existing body components based on anthropometric measurements as made by Robbins (1983b). The deformable elements represent the pelvis as a whole, providing the soft tissue and bony component representation within a single part. Figure 3.12 shows the pelvis and rigid core as implemented in the model.

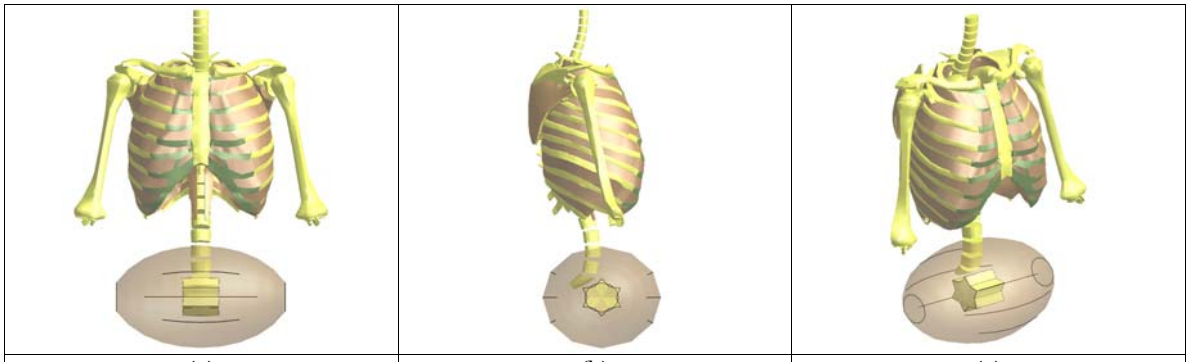

(a)	(b)	(c)

Figure 3.12 Pelvic model (a) anterior view (b) lateral view (c) isometric view

To define the deformation response of the pelvis, the same rate-dependent hyperelastic material model as used for the muscle tissue was implemented here. Again, this material model uses unique stress-strain curves at specific strain rates to define material response and capture the hyperelastic and rate dependent properties. The inputs to the model however, are significantly different.

The density of the pelvis was established through the use of anthropometric volume fractions. The original implementation included a point mass to represent the pelvis and legs. To separate this mass into its individual components, (pelvis, upper legs, lower legs and feet), volume fractions (McConville et al, 1980), of each component with respect to their total were multiplied by the original total mass. While this assumes a constant density within these regions, a phenomenon not found in the human body, comparison to the segment mass distributions as developed by Robbins (1983b) suggested these approximations were acceptable. It is noted that while the total masses are almost identical significant differences exist between the mass of the pelvis and upper legs. This was due to the difference in segment definitions in which Robbins includes the soft tissue and bony regions of the upper thigh within the upper leg measurement while McConville on the other hand includes the soft tissue and bony regions within the pelvic measurement. The reasoning for the choice of this mass distribution shall become clear when the development of the legs are described.

Table 3.5 Pelvis and leg mass development

Component	Volume (cm^3)	Volume Fraction	Mass (kg)	Mass (kg) (Robbins, 1983b)
Pelvis	18186	0.447	16.640	11.4
Upper Legs	12888	0.317	11.790	17.2
Lower Legs	7690	0.189	7.040	7.17
Feet	1928	0.047	1.750	1.96
Total	40537	1	37.240	37.73

Since the pelvic region is comprised of highly compliant abdominal tissues, relatively stiff muscle tissue and extremely stiff bony components, establishing an appropriate bulk modulus representative of the entire part must be approached with care. However, since

it has been established that the contact stiffness of these impacts plays the most important role when selecting a bulk modulus, and the region of the pelvis experiencing the first impact is the soft muscle tissue surrounding the pelvis, the value as established for muscle tissue in Section 3.2 was used.

To define the stress strain curves, experimental testing by Viano et al. (1989b), which subjected seven PMHS to blunt lateral impact loadings with a 23.4 kg pendulum at velocities of 4.5, 6.7 and 9.4 m/s centered on the greater trochanter was used. The intention was to replicated the force-deflection response of the pelvis using the data gathered from the experimental results. For the purposes of this development, only male subjects were used providing a sample size of five for the 4.5 m/s impact, one for the 6.7 m/s impact and five for the 9.4 m/s impact. Table 3.6 lists the pertinent anthropometric data from the experimental testing. It is noted that while the subject size was limited to only seven, the number of impacts was increased to eleven through the use of multiple impacts. While some researchers have questioned the validity of multiple impact scenarios, Viano et al. (1989b) stated that in the event where a subject was used for multiple impacts, x-ray analysis performed after each impact ensured that no injury had been sustained in the previous tests.

Table 3.6 Side pelvic PMHS anthropometric data (Viano et al., 1989b)

Test No.	PMHS No.	Age	Mass (kg)	Hip Breadth (mm)	Impact Speed (m/s)
44/45	U0M2	64	76	395	4.5/6.7
21/22	986	29	70	335	4.5/9.4
25/26/27	047	62	84	345	4.5/4.5/9.4
38/39	U0M1	37	68	325	4.5/9.4
16	993	49	71	325	9.4
35	063	64	49	320	9.4

Impact force was calculated by multiplying the pendulum acceleration, as measured using an accelerometer, by the mass of the impactor and deflection results were obtained by analyzing the high-speed film results, which were taken at 2000 frames per second.

Figure 3.13 shows the average force deflection data of the PMHS at the three impact speeds.

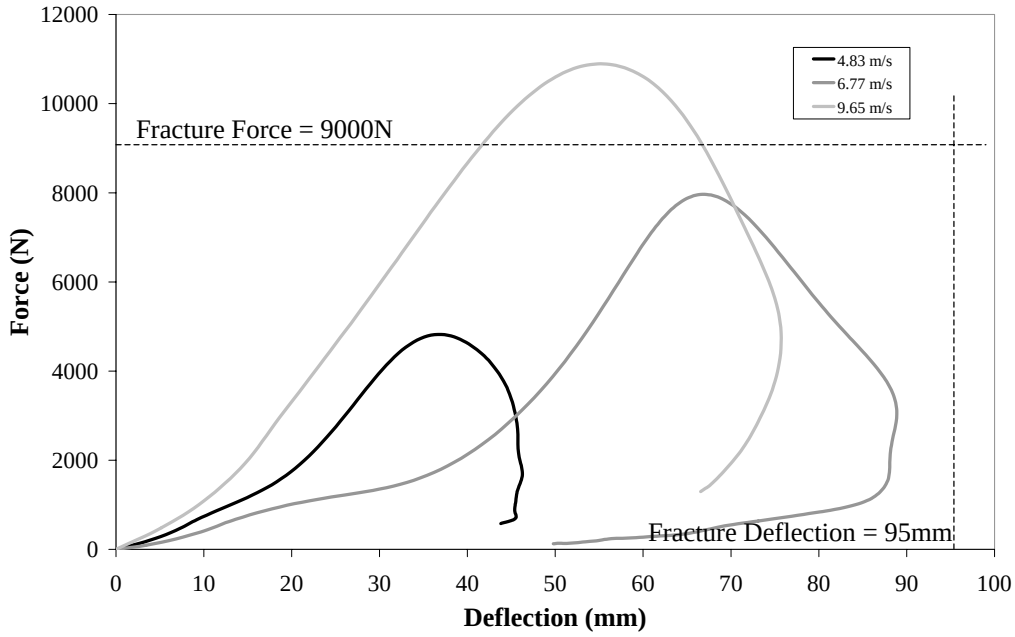

Figure 3.13 Average PMHS pelvic impact force-deflection response (Viano et al., 1989b)

To generate the stress response for the model, the average force was divided by the cross-sectional area of the modeled pelvis. Since the cross-sectional areas of the modeled pelvis varies along its width, the average was used. To generate the strain response, the deflection was divided by the original PMHS hip breadth. It is noted here that as a result of the narrowed cross-sectional area at the ends of the ellipsoid shaped pelvis, a lower force shall be registered upon impact providing a response closer to that of an actual human.

Injury during these tests was found to occur in only two of the 9.4 m/s impacts. Even so, Viano et al. (1989b) used Logist analysis to correlate both the force and compression response of the pelvis to pubic-ramus fracture. While compression was found to be the only good correlate to fracture, at 27%, Viano et al. (1989b) still calculated the average fracture force from the two cases of fracture as 9.78 ± 0.52 kN. When compared to the other PMHS pelvic impact data, similar force values were obtained. Cesari et al. (1982) proposed a fracture force of 10kN when PMHS endured pelvic pendulum impacts at a

similar speed. Cavanaugh et al. (1992) proposed a fracture force of 8kN when PMHS endured side sled pelvis impacts at 6.67 m/s and 8.8 m/s. As such, a fracture force of 9 kN and a fracture compression of 27% were considered here to establish the boundaries of fracture. The limits of fracture are plotted on the force-deflection curve (Figure 3.13). The fact that the 9.4 m/s curve does not achieve the fracture deflection was a reflection of the use of average responses to define this curve. Remember only two of the five impacts sustained fracture, while the remainder did not

These limits were then applied to the stress-strain curves in order to simulate the effect of compression if the limits are reached. If during impact the fracture stress is surpassed, the stress no longer increases in order to simulate the lack of resistance commonly observed during fracture impacts (Viano et al., 1989b). In the case where neither the curve was extrapolated up tot eh fracture limits at which point the stress was leveled off. Figure 3.14 shows the results of these calculations. It is noted that this model did not account for hysteresis, as observed during the unloading of the experimental tests (Figure 3.13), and forces the unloading response to match the loading response. This was deemed acceptable, as the goal here was to produce a realistic impact response during loading, with the focus on accurately modeling the injury response of the thorax.

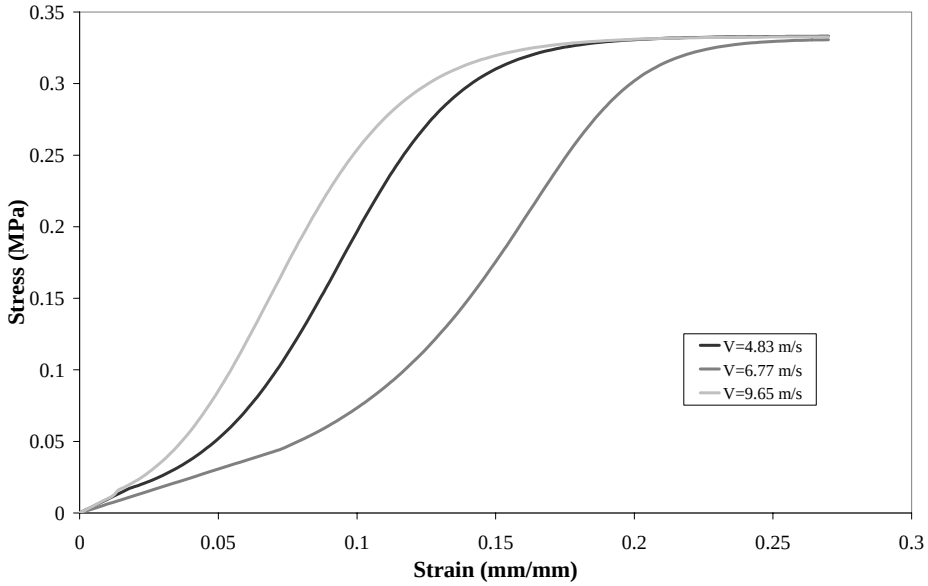

Figure 3.14 Calculated average pelvic stress-strain response

During the first half of deformation, the stiffness of the 6.77 m/s curve was observed to be lower than that of the 4.83 m/s curve, a trait inconsistent with expected viscoelastic characteristics common with bone and soft tissue. This was believed to be due to the small sample size used for the 6.7 m/s curve (1 subject) versus the larger sample size used for the 4.5 and 9.4 m/s curves (5 subjects each). On top of that, the PMHS used for the 6.7 m/s tests was reported as having the largest hip breadth of all PMHS used throughout the testing. This larger breadth may have been a result of an increased level of soft tissue at the point of impact, thereby delaying the onset of maximum compression and producing the results observed. This theory was supported by a single test case at the 4.5 m/s impact as observed in Figure 3.15. The peak force generated by the PMHS from Test #44 is late in the compression compared to the remaining tests. The PMHS used in this test was the same PMHS used for one of the 6.7 m/s tests. As a result, the use of this curve for defining the stress-strain relationship of the pelvis has been eliminated.

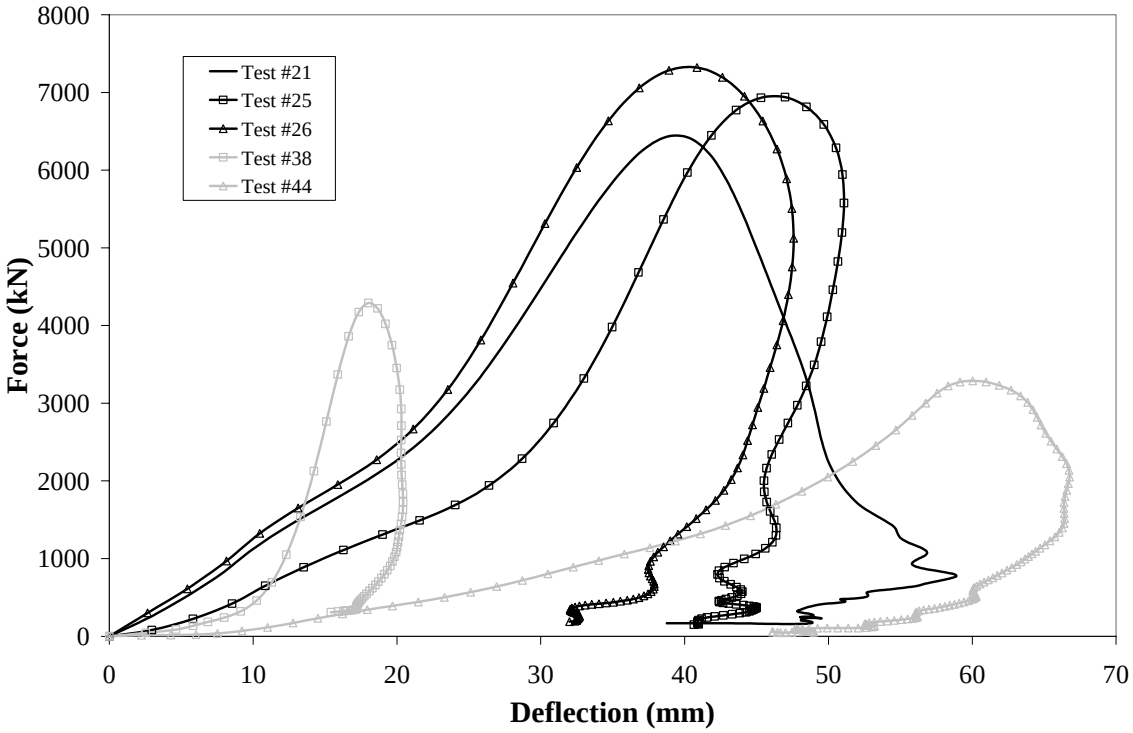

Figure 3.15 PMHS 4.5 m/s force-deflection responses

To define the strain rate of each impact type, the impact velocity was divided by the average hip breadth of the PMHS. It is understood that this is average strain-rate only

representative at the time of impact; however, the pelvic model developed here was only an estimated representation of an actual pelvis that has been implemented to increase the accuracy of the whole body response during side impact.

3.5.3 Pelvic Model Verification

Verification of this model was conducted by subjecting the model to the same impacts as used to define the material behaviour, i.e. the PMHS testing performed by Viano et al. (1989b). The objective was to ensure the model responded appropriately given the assumptions made to develop the material.

Simulation Development

The pendulum impactor was modeled as a rigid cylinder, 152.4 mm in diameter using 3 mm thick shell elements. The pendulum was given a mass of 23.4 kg and was assigned an initial velocity based on the appropriate impact speed with a free flight trajectory to produce uninhibited motion following the impact. For contact purposes, a Young's modulus similar to aluminum (70 GPa) was given to the pendulum for all tests. The use of a rigid impactor was deemed acceptable, as the relatively high stiffness of the aluminum produces little to no deformation when compared to the soft tissues. By doing so, the calculation time can be reduced.

Measurable Responses

Since the intention of this body component was to provide a simplified response representing an actual pelvis such that appropriate interaction with the thoracic region is achieved, only the following two measurements were made:

force: impact force between impactor and body.
compression: deflection divided by initial pelvic width.

These have been plotted against the experimental average and corridors as defined by one standard deviation.

Results and Discussion

Figure 3.16 shows the pelvis and body as impacted at various times throughout the simulation. The pelvis is seen to deflect, followed by global acceleration and motion of the body.

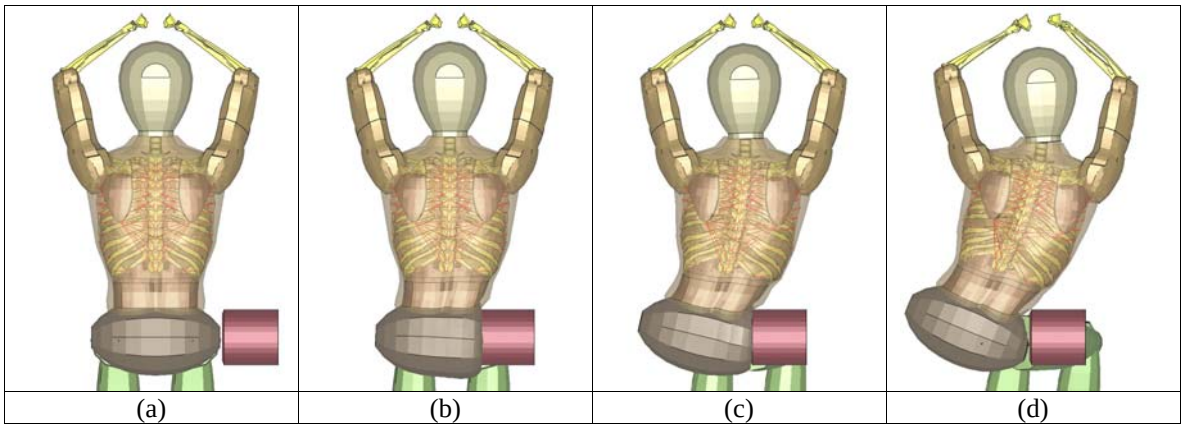

(a) (b) (c) (d)

Figure 3.16 Pelvic impact simulation (a) t=0 sec (b) t=0.015 sec (c) t=0.030 sec (d) t=0.045 sec

Experimentally, the force response of the pelvic pendulum impact produces first a slow onset of force, followed by a swift onset to a maximum, as seen in Figure 3.17(a) and (c). These two regions characterize first the initial compression of soft tissue surrounding the pelvis, and second the high resistance to impact of the stiff bony pelvis structure. The experimental compression response presents a steady onset of compression, and reaches a maximum after the peak force has dropped. It can also be observed that the pelvic compression achieves a plateau, most likely indicative of injuries sustained during the impact.

The simulation force response at both impact speeds can be seen in Figure 3.17(a) and (c) as compared to the experimental results. The shape of the force curve appears to follow well with the experimental results capturing both the peak force and unloading characteristics. The loading response however possesses an elevated response suggesting a high initial stiffness. This was due to the method used to model the pelvic material encompassing the effects of both the soft tissue and bony components. As a result, the ramped force observed during the PMHS testing, which captures the compression response of the soft tissue was lost.

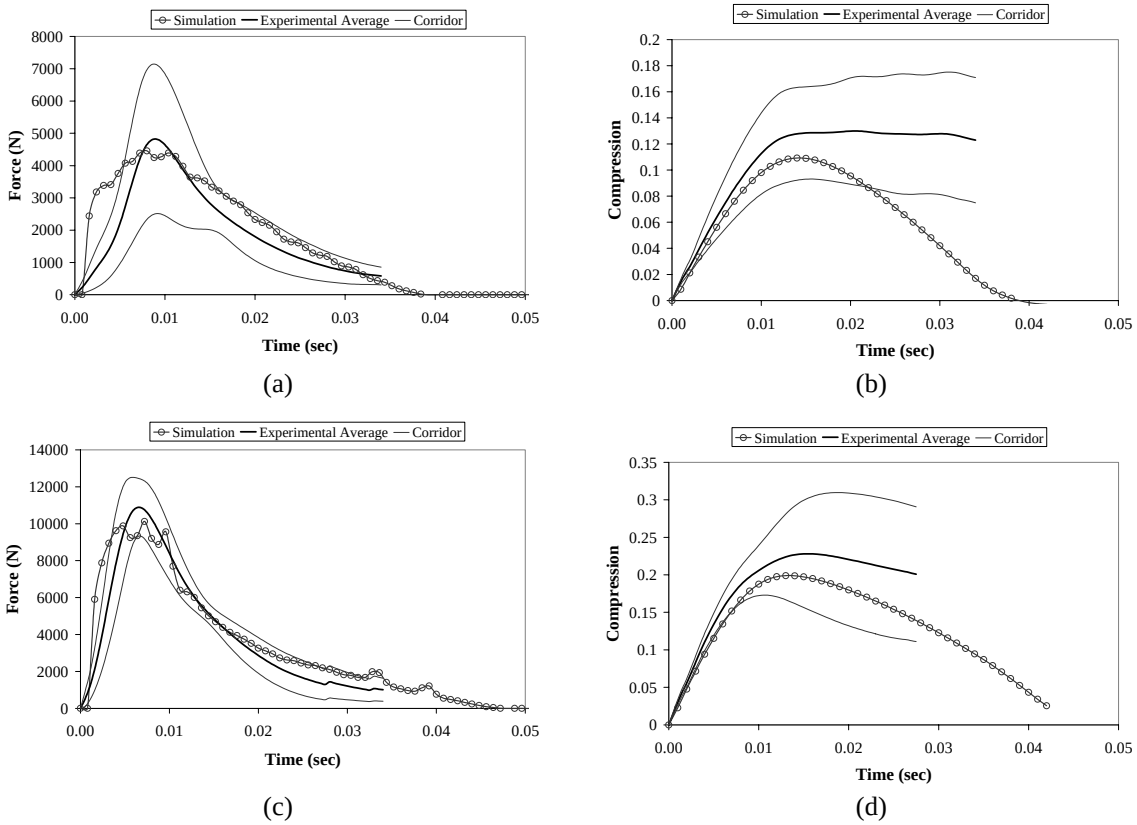

Figure 3.17 Pelvic impact simulation results (a) 4.83 m/s force (b) 4.83 m/s compression (c) 9.65 m/s force (d) 9.65 m/s compression

The compression response of the model, appears to capture the PMHS response at both loading and peak compression, as seen in Figure 3.17(b) and (d). The swift reduction of compression during the unloading phase of the impact was again due to the modeling method. As noted earlier, the material used to represent the pelvis was unable to accept unloading curves, forcing the pelvis to unload along the loading curves, and miss the hysteretic effects often observed in the experimental results. As well, this model was unable to physically capture the injury due to these impacts. Although, the stress-strain response of the model was designed to generate a leveled stress response at the fracture limits, it was unable to capture the permanent displacements cause by the fracture. Meanwhile the PMHS remained in a permanently deformed state. These results were deemed acceptable, since the unloading of the pelvis should have a negligible affect on the injury response of the thorax.

3.6 Simplified Leg Development

Injuries sustained by the legs during both frontal and side impacts have been found to account for approximately 2% of all automotive injuries (Otte, 1996). Of this 2%, only 28.1% are as a result of side impact scenarios. Further, injuries to the legs only develop injury of AIS 3 or less. Such findings, suggested that the development of a detailed leg model was unwarranted for the project goal of producing accurate thoracic injury response. However, through the developments presented here, it became clear that approximating the kinematic and impact response of the legs was important to reflect the overall response of the thorax.

3.6.1 Leg Anatomy

The legs are comprised of bony, ligamentous and muscle tissue that provide locomotion, combine to support the upper body weight, and maintain equilibrium. Each leg is divided into three the following three major regions: upper leg, lower leg and foot. The upper leg is comprised of the femur bone with surrounding tissues and connects to the pelvis at the acetabulum through the head of the femur. This joint acts much like a spherical joint with three degrees of rotational freedom. The lower leg is comprised of the tibia and fibula bone with surrounding tissues and connect to the upper leg at the distal end of the femur through the proximal end of the tibia. This forms the knee joint and in a simplified fashion acts much like a rotational joint with one degree of rotational freedom. The foot is comprised of a number of bones with surrounding tissues and connects to the lower leg at the distal end of the tibia and fibula to form the ankle joint. This joint acts much like a spherical joint with three degrees of rotational freedom.

3.6.2 Simplified Leg Model

The original thoracic model considered the legs as a single point mass. Its intention was to represent the inertial properties attaching to the sacral vertebrae within the model. In this study, ellipsoid shapes based on the geometry of the GEBOD were used to model the upper legs, lower legs and feet. Spherical joints attached the upper legs to the pelvis, the lower legs to the upper legs and the feet to the lower legs. Moment and damping

properties and stop angles as implemented in the GEBOD model (Cheng et al., 1994) were used for each joint. The first development stage of the legs modeled each component as rigid parts. However, preliminary analysis showed that during full body side sled impact scenarios, the legs rebounded from the impact surface at a much faster rate than the remainder of the body. This motion pulled the pelvis away from the impact wall, which in turn caused significant shearing in the lumbar spine. To prevent this, each component of the legs was developed using a rigid core representing the bone, surrounded by deformable elements representing muscle tissue. This was found to provide adequate impact results without causing detrimental effects on the impact of the thorax. This modeling technique can be observed in Figure 3.18. Where the upper legs intersect the pelvis, the surrounding tissue was removed to produce a more accurate distribution of mass.

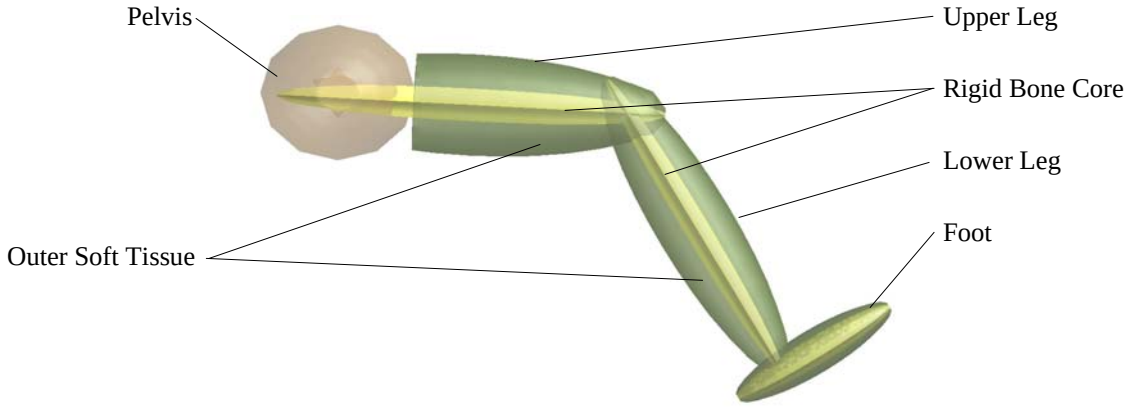

Figure 3.18 Leg model

The bony core of each leg component was modeled using a rigid material to reduce the run time of the model. Densities were assigned to each component, accounting for both the bone and soft tissue, based on the volumetric distributions as observed in anthropometric data. This was the same technique as detailed in the pelvic development. The surrounding deformable soft tissue was modeled using the same material as used the thoracic soft tissue. Verification of this model was not completed throughout development, however these components are evaluated in the side sled tests as they are engaged throughout the impact.

3.7 Simplified Abdomen Development

Development of the abdomen was found to be necessary in order to create continuity between the simplified pelvis and the detailed thorax. Analysis of common human anatomy showed that the lower region of the thoracic cage encloses a substantial portion of the abdomen (see Figure 3.19) and as a result, can play a substantial role in defining the thoracic deformation response. While it was understood that injuries sustained to the abdomen during side impact collisions account for a substantial number of serious injuries (20%, Augenstein et al., 2000), it was believed that the need to represent these injuries would not noticeably affect the goal of predicting thoracic injury.

Since the development of a detailed abdominal model presents a substantial task on its own, requiring the development of ten major organs with unique geometric and material properties, a simplified approach similar to that for the pelvis was taken in order to fulfill the main goals of this project. A single component was developed with the intent of capturing the deformation response of the entire abdomen, while providing the added advantage of computational efficiency.

3.7.1 Abdominal Anatomy

The abdomen is comprised of various soft tissue organs and lies between the thoracic diaphragm and the pelvic inlet. The diaphragm forms the top of the cavity and extends as high as the 6^{th} rib. Consequently, the thoracic cage protects some of the higher abdominal organs. The pelvic inlet is a boundary outlined by the superior pelvic aperture, which has been designated for describing the abdominal and pelvic cavities separately. Figure 3.19 illustrates the region of the abdominal cavity.

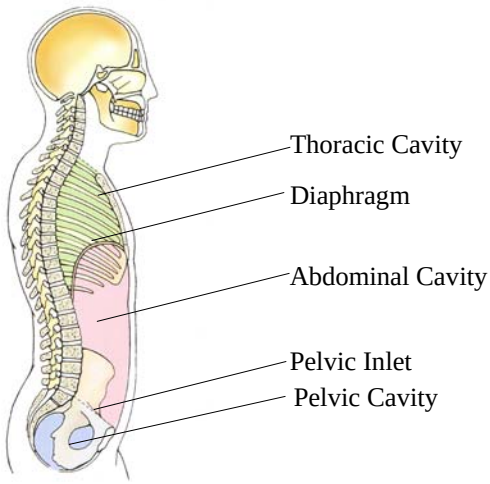

Figure 3.19 Abdominal Cavity (modified from Moore and Dalley, 2002)

The organs within the abdomen are the liver, spleen, stomach, gallbladder, colon, pancreas, right and left kidneys, small intestines and large intestines. Figure 3.20 shows the location of each organ in the abdomen.

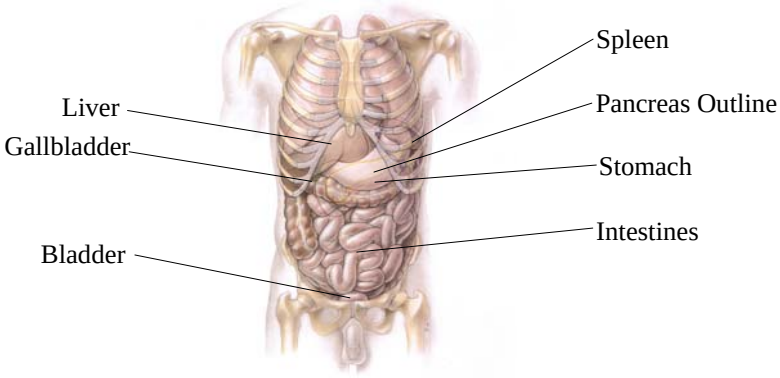

Figure 3.20 Abdominal Organs (modified from Moore and Dalley, 2002)

Each organ presents individual mechanical properties making this region very complex to model. For example, in side impact automotive trauma, injury to the abdominal area primarily occurs in the solid abdominal organs (i.e. the liver, spleen and kidney) while the hollow organs (i.e. stomach, gallbladder, colon, pancreas, small intestines and large intestines) remain relatively unharmed (Bondy, 1980).

3.7.2 Original Numerical Abdomen Model

The abdomen was originally modeled using four point masses equaling 1.2088 kg each, attached to the L1, L2, L3 and L4 vertebrae. In total, they generated a representative mass of 4.835 kg (Deng, 2000), which were meant to represent the inertial effects during the pendulum impact simulations. Deng et al. (1999) arrived at this mass by multiplying the volume of the space between the diaphragm and bottom of the thoracic tissue by the density of water ($1g/cm^3$). This was done since water is the major component of soft tissue. The resultant mass was compared to body region masses as developed by McConville et al. (1980) and was found to be appropriate. This approach was deemed to be acceptable for the simplified pendulum loading conditions as produced by Deng et al. (1999) and Chang (2001) following validation of the model with experimental results.

3.7.3 Simplified Abdomen Model

The geometry of the abdomen for this study was obtained by filling the gap between the diaphragm and the spheroidal pelvis within the thoracic muscle. A single continuum part was used to represent all abdominal organs as the development of a detailed abdominal model remained outside the scope of this project. The abdomen was meshed in a layered fashion, with two different layer thicknesses. In the region between the pelvis and the bottom of the ribcage, each layer was aligned with a layer on the thoracic muscle tissue. In the region between the bottom of the ribcage and the diaphragm, the layer thickness was halved to accurately model the increased geometric complexity within this region. Figure 3.22 shows the abdomen, identifying the regions of complexity.

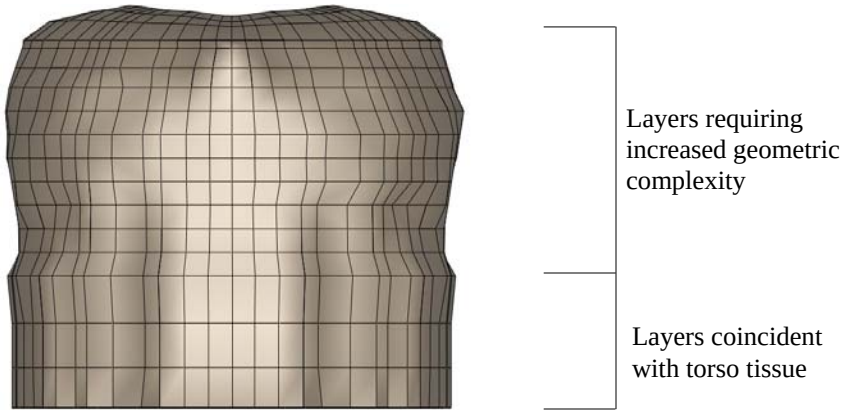

Figure 3.21 Abdomen model details

Connectivity with the body was achieved through attachment to the surrounding muscle tissue and the pelvis. Coincident nodes and beam elements were used for connection to the thoracic tissue as outlined in Figure 3.22(a). The beam elements act only in tension and have a linear-elastic response with a modulus obtained from muscle tensile data as listed by Yamada (1970). Rivet like joints connect individual nodes on the bottom of the abdomen to individual nodes on the top of the pelvis, which maintain the same distance between the respective nodes throughout the simulation. Figure 3.22(b) outlines this attachment method. This was believed to provide adequate representation of the actual situation, where the abdomen is enclosed by the pelvis.

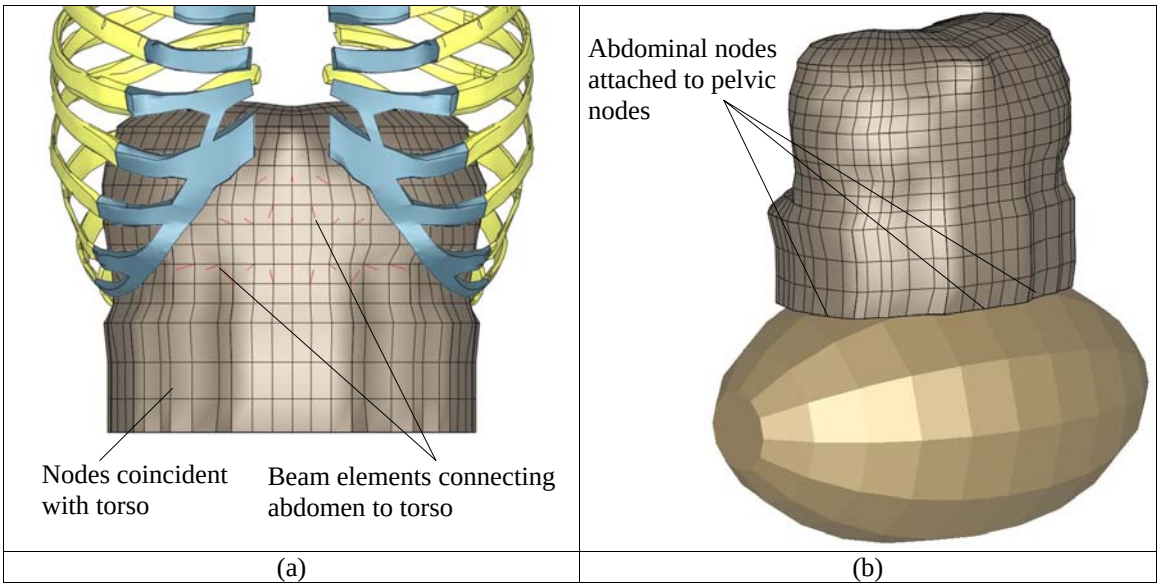

Figure 3.22 Abdominal connectivity (a) with thoracic muscle tissue (b) with pelvis

In the human body, abdominal organs do not reside in behind the lumbar vertebrae. Instead, deep back muscles and the transverse processes of the lumbar vertebrae fill this area. Since these parts do not exist in the current human body model, the abdomen was modeled to surround the lumbar region of the spine to fill this gap and produce the appropriate mass distribution.

3.7.4 Abdominal Material Model

To accurately model the material properties of the abdominal region, in vivo experimental testing on Rhesus monkey kidneys and livers loaded in direct impacts was

used. The loading was performed at the following three rates: $2.5s^{-1}$, $125s^{-1}$ and $250s^{-1}$. The intention of the abdominal model was to use a single material to represent the entire abdomen. To achieve this Melvin's (1973) data was compared to the high rate bovine tissue data developed by Van Sligtenhorst (2003) and McHelaney (1965). Figure 3.23, Figure 3.24 and Figure 3.25 shows this comparison for rates similar in both tests. These graphs show the stiffness of the liver lower than the stiffness of the bovine tissue and the stiffness of the kidney higher than the stiffness of the bovine tissue. As a result, the stress-strain data of the bovine muscle was used to model the abdominal material as a desirable medium between the liver and kidney. The same rate-dependent hyperelastic model as developed for the previous muscle tissue was used along with the same stress strain curves.

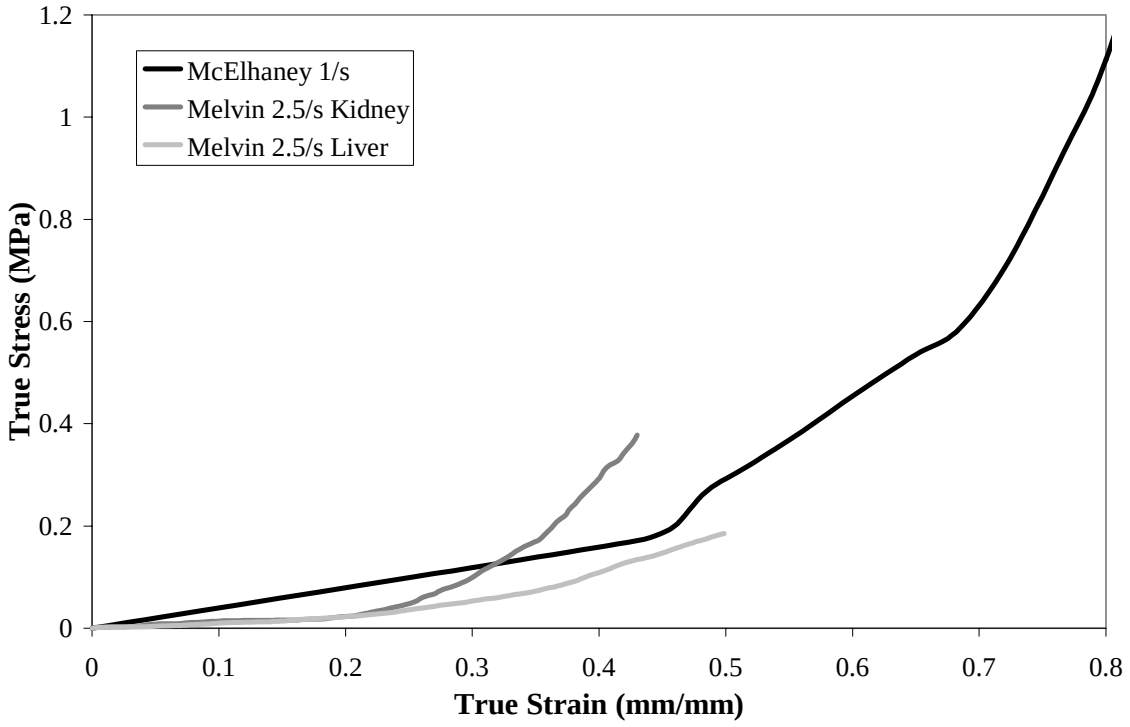

Figure 3.23 Low rate stress-strain curve for bovine muscle tissue and primate kidney and liver tissue

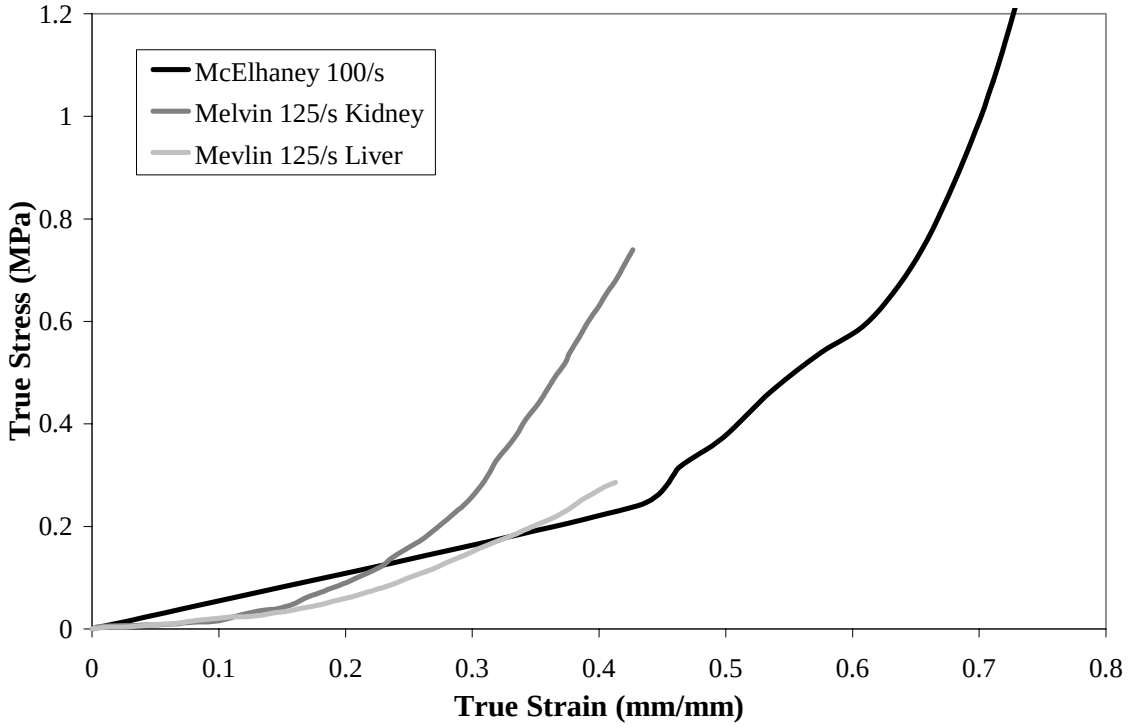

Figure 3.24 Mid rate stress-strain curve for bovine muscle tissue and primate kidney and liver tissue

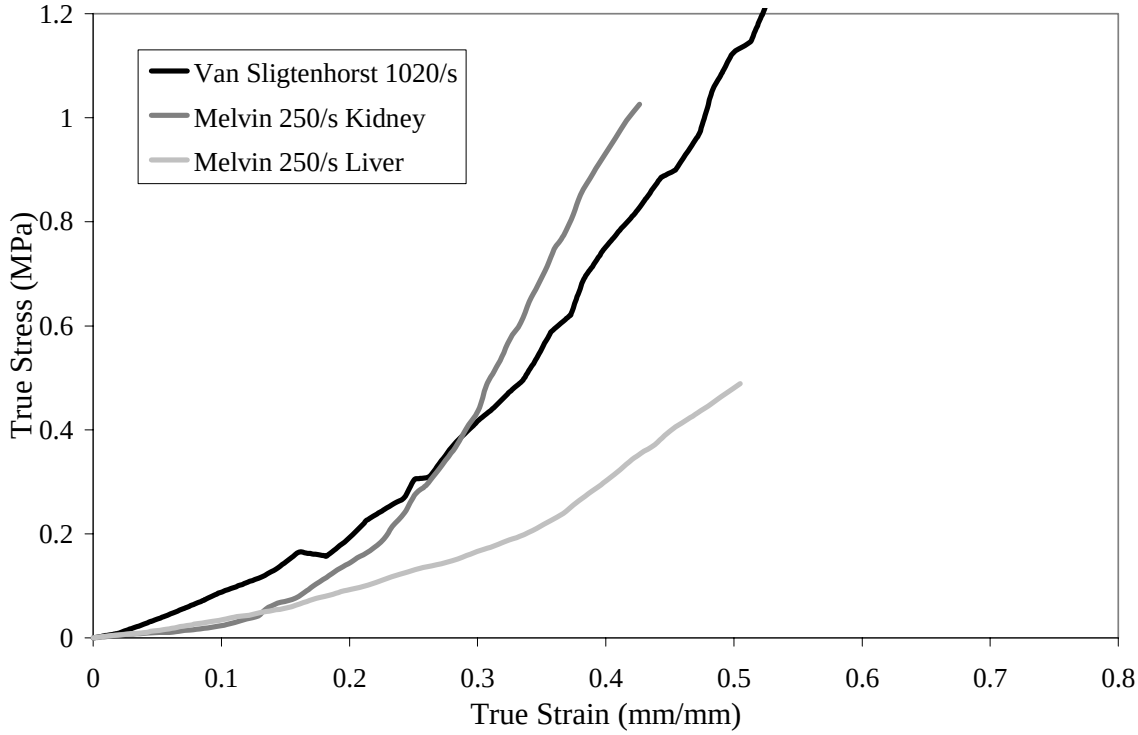

Figure 3.25 High rate stress-strain curve for bovine muscle tissue and primate kidney and liver tissue

The density of this material was based upon the volume of the modeled abdomen and the mass as designated by the point masses from the original model. The bulk modulus used for this material is calculated using the same method as used for the thoracic and arm tissue, using the density and sound speed of liver tissue (Goss et al., 1978). Table 3.7 lists the density and bulk modulus used for this material.

Table 3.7 Abdomen material properties (Goss et al., 1978)

Density	Bulk Modulus
1032 kg/m^3	2.37x10^3 MPa

3.7.5 Abdominal Model Verification and Optimization

Verification and optimization of the abdomen was conducted to ensure it provided a desirable response during impact with the assumptions made to develop the model. This was done by subjecting the model to a side pendulum impacts directly over the abdomen, with comparison to PMHS test data.

Experimental Data

Experimental testing conducted by Viano et al. (1989b) subjected ten unembalmed PMHS to abdominal impacts using a 23.4 kg impactor, with impact velocities of 4.5, 6.7 and 9.4 m/s. Each test was conducted with a 152.4 mm diameter impactor aligned 75 mm below the xiphoid process with the subject rotated 30º from the coronal plane. This assured that the axis of impact was directed through the center of gravity of the thorax, i.e. two centimeters anterior of the intrathoracic surface of the vertebrae (Viano, 1989b). The subject was suspended in an upright-seated position using a shoulder and arm harness that was released upon impact to produce an uninhibited impact scenario. Figure 3.26 shows the numerical model as compared to a sample PMHS impact test prior to impact.

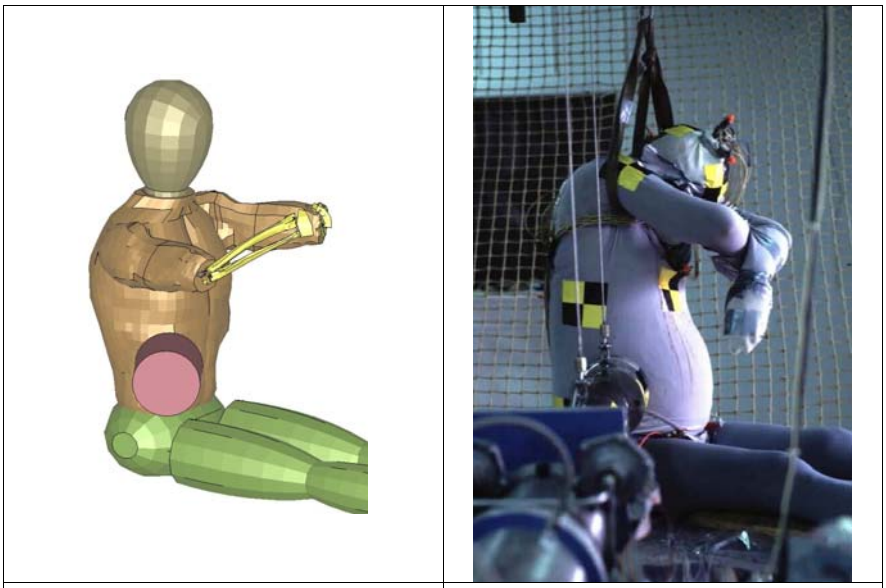

(a) (b)

Figure 3.26 Side abdominal pendulum impact test (a) simulation (b) experiment

Impact force was calculated by multiplying the pendulum acceleration, as measured using an accelerometer, by the mass of the impactor. Deflection results were obtained by analyzing high-speed film results, which were taken at 2000 frames per second. Impact force and chest deflections have been used here for comparison to the model, which were normalized to the 50^{th} percentile human male.

For the purposes of this analysis, only male subjects were used, providing a sample size of five impacts at 4.5 m/s, three impacts at 6.7 m/s and four impacts at 9.4 m/s. Table 3.8 lists basic anthropometric data of the PMHS used throughout the analysis. It is noted that the sample size is larger than the number of PMHS used during the testing, which was due to the repeated use of PMHS for different impact velocities. As mentioned during the pelvic impact simulations, this was believed to be of no significance to the response of the PMHS (Viano et al., 1989b). Simulation of this impact followed the same technique as used for the pelvic impacts and the details can be found in that section.

Table 3.8 Side abdominal PMHS anthropometric data (Viano et al., 1989b)

Test No.	PMHS No.	Age	Mass (kg)	Waist Breadth (mm)	Impact Speed (m/s)
19/20	986	29	70	280	4.5/9.4
23/24/28	047	62	84	345	4.5/4.5/9.4
42/43	U0M2	64	76	345	4.5/4.5
6	947	38	56	255	6.7
8	954	66	56	255	6.7
10	RNY2	64	62	330	6.7
15	993	49	71	315	9.4
34	063	64	49	340	9.4

Measurable Responses

To validate the side abdominal impact results, the following responses were used for comparison:

force: impact force between impactor and body.

compression: deflection divided by initial abdominal width as measured diagonally from impact sight to opposite side of thorax.

VC: viscous criteria; rate of deflection multiplied by compression.

injury: number of rib fractures.

Optimization

When the model was first subjected to the simulated impact, the two following response discrepancies were observed: low levels of compression and a high initial impact force. First, the low levels of compression were believed to be due to the stiffness of the material. Although the abdomen material was developed based on abdominal and muscle tissues, the lack of hollow organ representation generated an observed elevated stiffness. As such, the stiffness of the abdomen material was reduced to a quarter of the original stiffness. Second, the high initial impact force observed was believed to be due to the bulk modulus of the abdominal material, which was calculated using the sound speed and density of liver tissue. While this may hold true for the liver, the hollow organs would produce a greatly reduced bulk modulus. Comparison to previously developed detailed

abdominal models suggests that a value of around 3 MPa would be appropriate (Ruan et al., 2003). However, when the bulk modulus was reduced to this value, the model became unstable following contact between the abdomen and the rigid spinal structures. The elements on the outside of the part underwent uncontrolled volumetric deformations when the pressure was increased due to contact with the rigid spine. To solve this problem, a shelled structure surrounding the abdominal component could have been implemented to maintain stability. As this was not performed throughout this study, the bulk modulus of the part was reduced to a value where the model remained stable, thereby minimizing the high initial force observed at impact. The final bulk modulus used was 237 MPa, a reduction by one order of magnitude from the calculated value.

Results and Discussion

Figure 3.27 shows the abdomen and body as impacted at various times throughout the simulation. The abdomen and lower thorax are seen to deflect and absorb the impact.

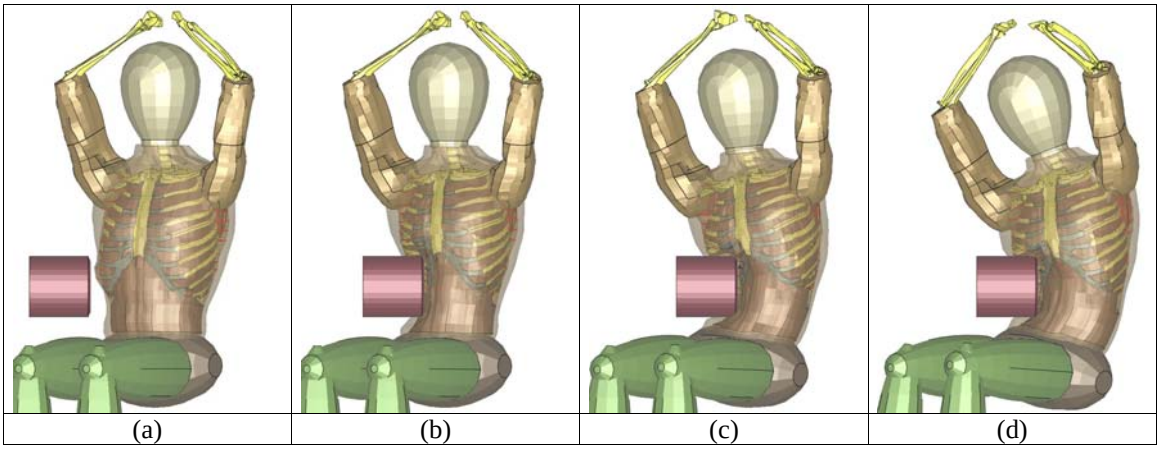

Figure 3.27 Abdominal impact simulation (a) t=0 sec (b) t=0.015 sec (c) t=0.030 sec (d) t=0.045 sec

The response of the abdomen and thorax during all three impact speeds produced similar force and compression responses increasing with impact velocity. As a result, only the high-speed impact scenario (9.40 m/s) results are presented here and the remaining figures can be found in Appendix A. Experimentally, the response of the abdominal impact produces a slow onset of force due to the lack of skeletal structures within this region and the high compliance of the hollow organs (Viano et al., 1989). Figure 3.28(a) shows the force response of the experimental abdominal impacts. The compression

response produces a maximum early in the impact almost simultaneous with the maximum force response. The resultant force-compression curve highlights this timing, producing a sharp unloading curve.

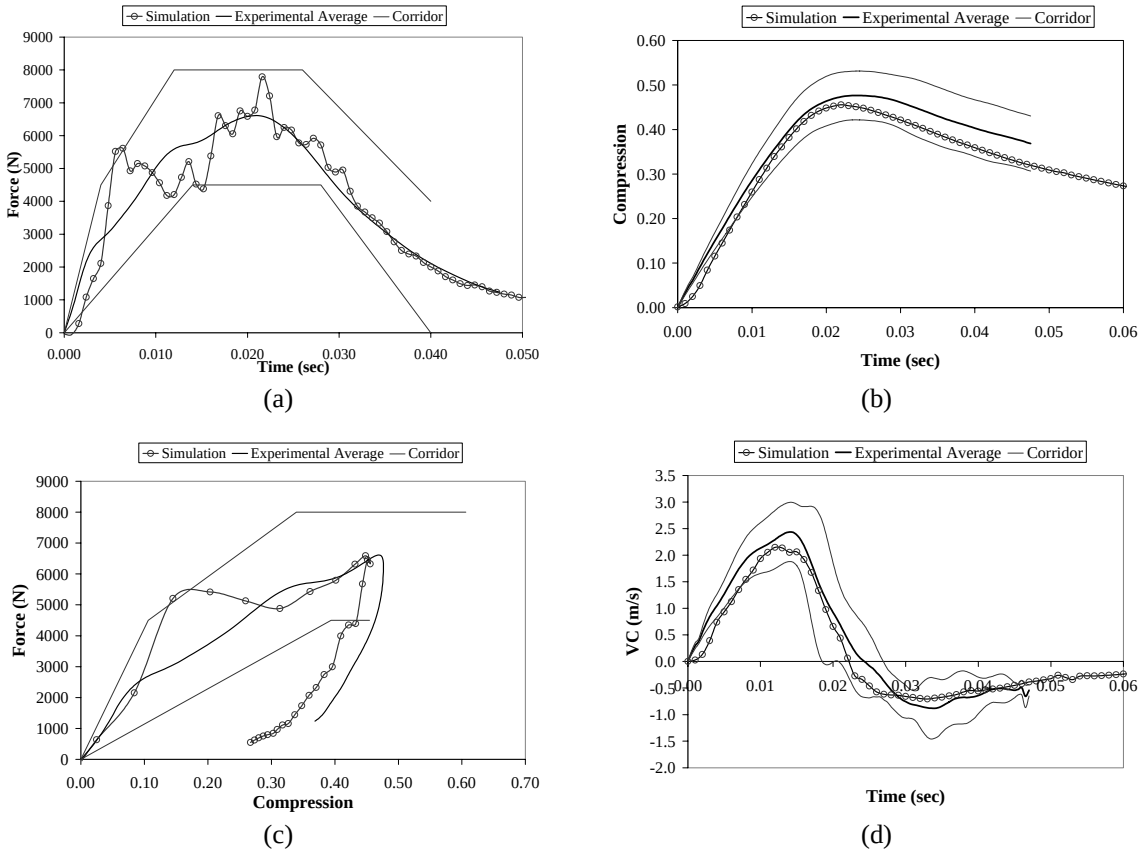

Figure 3.28 Abdominal impact simulation results at 9.40 m/s (a) force (b) compression (c) force-compression (d) VC

With the aforementioned optimizations, the simulation was analyzed against the experimental testing. The model captures the experimental force response throughout the impact as outlined in Figure 3.28(a). An elevated initial peak force has been generated as a result of the high bulk modulus, however, the response remains within the corridor. Throughout the remainder of the impact secondary peaks are observed, possibly representing fracture of ribs. Similar secondary peaks were observed during individual PMHS test responses.

The compression of the model captures the PMHS response falling within the established corridor as seen in Figure 3.27(b). Similarly, the stiffness of the abdomen as characterized by the force-compression response as seen in Figure 3.28 (c) captures the PMHS response throughout the impact. A slightly elevated initial stiffness was observed, indicative of the elevated bulk modulus. The VC response of the model as seen in Figure 3.28(d) captures the experimental response throughout the impact.

Table 3.9 summarizes the number of predicted rib fractures sustained during the simulation as compared to the experimental results. At all three impact velocities, the number of rib fractures of the simulation outnumbers the number of rib fractures during experiments. As well, sternal fractures were observed at the high-speed impact (9.40 m/s) while no sternal fractures were observed during any of the experiments. Both discrepancies are believed to be due to the elevated stiffness of the costal cartilage, which during impact forces the ribs to withstand more of the deflection, resulting in an elevated number of rib fractures and the presence of sternal fractures.

Table 3.9 Abdominal impact injury summary

Impact Velocity (m/s)	Experimental Average	Simulation
4.78	~1	6
6.83	~3	10
9.40	~4	13

3.8 Simplified Head Development

Understanding and predicting injury to the head is an important factor when considering occupant safety for both frontal and side impacts. For this project a detailed head model was not required and a simplified approach has been taken. It is noted however, that future work will involve the integration of this model and a detailed head and neck model currently under development (Deng and Fu, 1999).

3.8.1 Simplified Head Model

The original head as implemented by Deng et al. (1999) and Chang (2001) was represented using a point mass attached to the top cervical vertebra (C2). The mass was obtained using volume segment data from McConville et al. (1980).

The head modeled during this development was based upon geometry as obtained from the GEBOD model. The height and width of the head as measured from the shoulders matches the GEBOD, however since the GEBOD head is an ellipsoid, its shape was modified to visually produce a more representative average human head. The center of mass and moments of inertia as developed by Robbins (1983b) for the mid-sized male dummy were used for the modeled head. The mass of the head was kept the same obtained from the point mass implemented by Deng et al. (1999), which matches closely to the mass developed by Robbins (1983b). The mass and principle moments of inertia can be found in Table 3.10.

Table 3.10 Head geometric properties

Mass (kg)	Principal Moments of Inertia (kg m^2)		
	I_{xx}	I_{yy}	I_{zz}
4.063	0.020	0.022	0.015

The head was joined to the top cervical vertebrae using a spherical joint with the same moment and damping curves as used for the GEBOD head-neck joint. The joint location was in the center of the top cervical vertebral body and the head was positioned based on anthropometric data obtained from Robbins (1983b) as measured from the position of existing body components. The head can be seen as attached to the skeletal system in Figure 3.29. Similar to the simplified leg model, verification of this model was not performed as it is intended that a more detailed head and neck model will be implemented with the full body model.

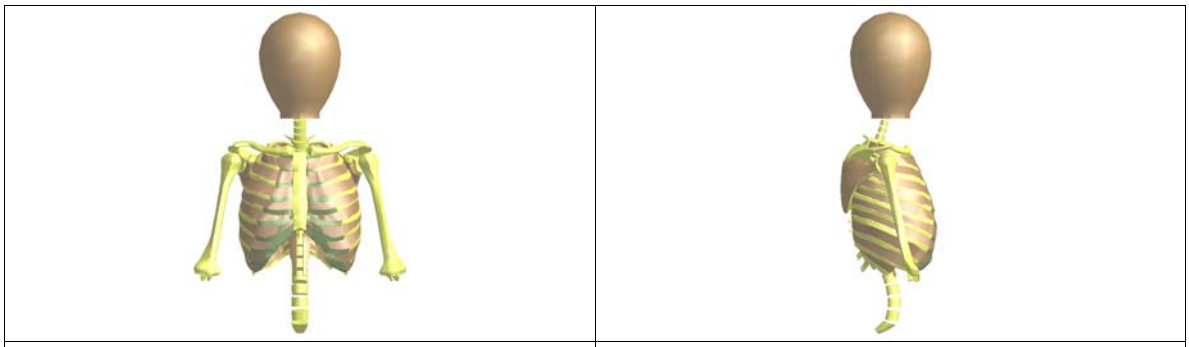

(a) (b)

Figure 3.29 Head model (a) anterior view (b) lateral view

3.9 Model Development Summary

The implementation of the aforementioned components has been based on material property data obtained from the literature. Improvements to the existing body components including the thoracic and arm muscle tissue and the shoulder were made, highlighting deficiencies with the first and second development iterations of the model. New components including the pelvis, legs, abdomen and head were implemented with the intention of producing a full body model for the prediction of side impact scenarios. Where necessary, these new parts were subjected to validation and calibration studies to ensure an appropriate response of the model, checking the applicability of the simplifications made on a regional basis. Figure 3.30 shows the final full body model following the developments presented in this study. At this stage it was believed that the model would produce an accurate response during validation tests in both pendulum impact scenarios and side sled impact scenarios. The following chapters detail the implementation and results from these tests.

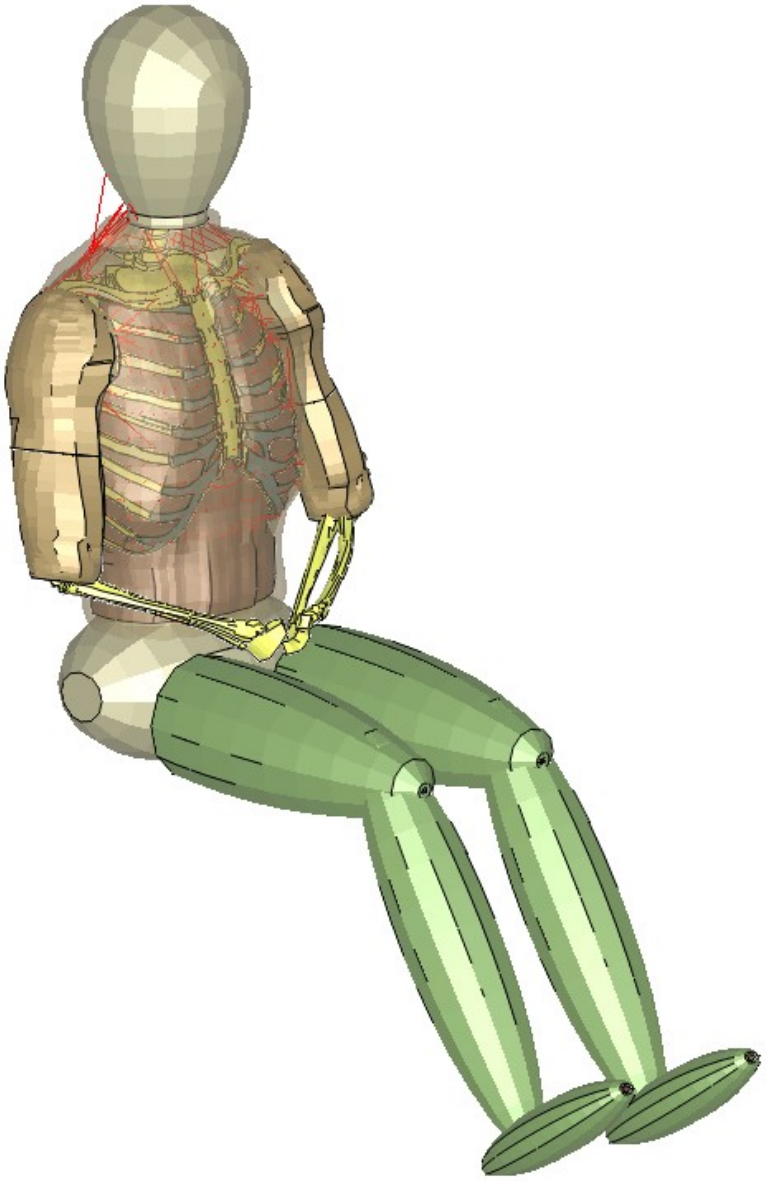

Figure 3.30 Full body model

-- CHAPTER 4 --

Pendulum Impacts – Model Response and Validation

4.1 Introduction

As previously discussed, post mortem human subject experimental testing provides significant insight into human impact biomechanics and the onset of injury. In the context of this research, PMHS testing provides measurable biomechanical information of the human body undergoing impacts that can be used to validate the numerical model.

PMHS tests involving pendulum impacts facilitate the reproduction of injuries common in automotive impact in a simplified fashion. Pendulum impact tests involve impacting an isolated region of the human body with a blunt object to reduce the influence of neighboring body regions and produce a specific load history. Many of the existing injury criteria have been developed from this type of testing.

The objective of this chapter is to investigate the biofidelity of the model during pendulum impact simulations by comparing the results to PMHS testing. A description of the experimental testing is provided along with the numerical modeling techniques required to simulate the impacts and following that, the assessment criteria used to

provide a qualitative analysis of the model validation is established. The validation analysis of the model will then be presented with a description of the experimental PMHS response intended to provide a complete understanding of the impact scenario, which further allows for the accurate analysis and correlation of the model response. The results provide insight into the simplifying assumptions made throughout the past and present developments of the model, and in the case where these assumptions generate discrepancies between the model and the experimental results, explanations were developed such that recommendations for future work can address and correct them. It should be noted that validation, in this context, means evaluation of model performance under specific impact conditions, for which the simplified components have not been calibrated or tuned.

4.2 Materials and Methods

The following three pendulum tests were used for regional validation of the detailed thoracic model: frontal thoracic pendulum tests, side thoracic pendulum tests and side shoulder pendulum tests. These regions were particularly important for this study, which intended to accurately model thoracic injury when undergoing side impact in automotive crashes. It is noted that although the primary objective of this research was to investigate side impact, the model was also subjected to frontal pendulum impacts for further validation. This falls under a long-term goal to develop a thoracic model that is predictive of alternative forms of automotive impacts such as frontal collisions. It was believed that investigating the model response in frontal pendulum impacts is the first step in identifying improvements required within the model to accurately predict frontal impact response.

4.2.1 Experimental Data

Front Thoracic Pendulum Tests

Front thoracic pendulum impact tests conducted by Kroell et al. (1971, 1974) have been used to validate the model's frontal thoracic deformation. Thirty-seven unembalmed PMHS were subjected to sternal impacts using impactors of mass ranging between 1.64

kg and 23.4 kg, with impact velocities ranging between 4.9 m/s and 14.3 m/s (Kroell et al., 1971, 1974). A 152.4 mm diameter wood impactor centered over the sternum at the fourth costal interspace was used for each impact. The subject's arms were restrained in a horizontal position to maintain posture, however they were released immediately prior to impact to produce an uninhibited impact scenario. Figure 4.1 shows the numerical model as compared to a sample PMHS impact test prior to impact.

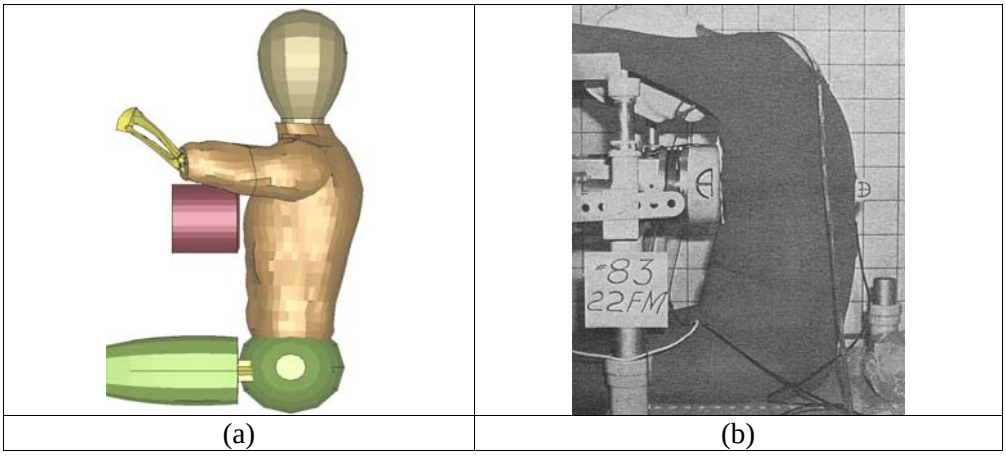

(a) (b)

Figure 4.1 Front thoracic pendulum impact test prior to impact (a) simulation (b) experiment (Kroell et al., 1971)

Impact force and the resultant deflection were recorded over time and correlated to produce force-deflection curves of the thorax. Forces were measured using a load cell attached to the impactor and chest deflection was measured by monitoring markers placed on the body and impactor using high-speed film. Both force and deflection results were used for comparison to the numerical model, where deflection was further used to calculate compression and VC. For the purposes of this analysis, only male subjects that underwent an impact speed of 6.7 m/s with a 23.4 kg impactor were used providing a sample size of five PMHS. This was the most aggressive impact condition and provides more representative loading for injury analysis. Table 4.1 lists the basic anthropometric data for the PMHS used throughout the analysis, along with the same dimensions as measured in the model.

Table 4.1 Frontal pendulum PMHS anthropometric data (Kroell et al., 1971)

Test No.	Age	Mass (kg)	Chest Depth (mm)
15FM	80	53	200
18FM	78	66	219
19FM	19	66	203
20FM	29	57	203
22FM	72	75	225
Model	N/A	76	237

All experimental force data has been normalized, as described by Eppinger et al. (1984), to represent the 50th percentile male using the following equation:

$$Force_{norm} = Force \cdot \left(\frac{75}{MASS} \right)^{2/3} \tag{4.1}$$

$$Deflection_{norm} = Deflection \cdot \left(\frac{75}{MASS} \right)^{1/3} \tag{4.2}$$

Where $Force_{norm}$ and $Deflection_{norm}$ are the normalized force and deflection respectively, *Force* and *Deflection* the measured force and measured deflection respectively, and *MASS* is the subject mass.

Side Thoracic Pendulum Tests

PMHS side thoracic pendulum impact tests have been studied by a number of researchers. As noted in the literature review, Eppinger et al. (1984) and Viano et al. (1989b) subjected numerous PMHS to free-flight side impact pendulum tests. However, research by Deng (1989) suggested that free-flight load-controlled impacts do not accurately represent the typical loading an occupant would undergo during a car-to-car side impact. Instead, it was suggested that deflection-controlled impacts using a high-energy, limited-stroke, velocity pulse pendulum, would better represent typical occupant loading during car-to-car side impact. As a result, experimental PMHS testing using a deflection-controlled impact has been chosen for validation of the model undergoing side thoracic pendulum impacts.

Chung et al. (1999) subjected four PMHS to side pendulum impact tests with a 50 kg wood impactor of 152.4 mm diameter. The impactor was centered over the 6th rib laterally and constrained to traverse 51 mm into the space occupied by the PMHS with a specified velocity-time profile as outlined in Figure 4.2. The average initial impact velocity was 5.6 ± 0.3 m/s.

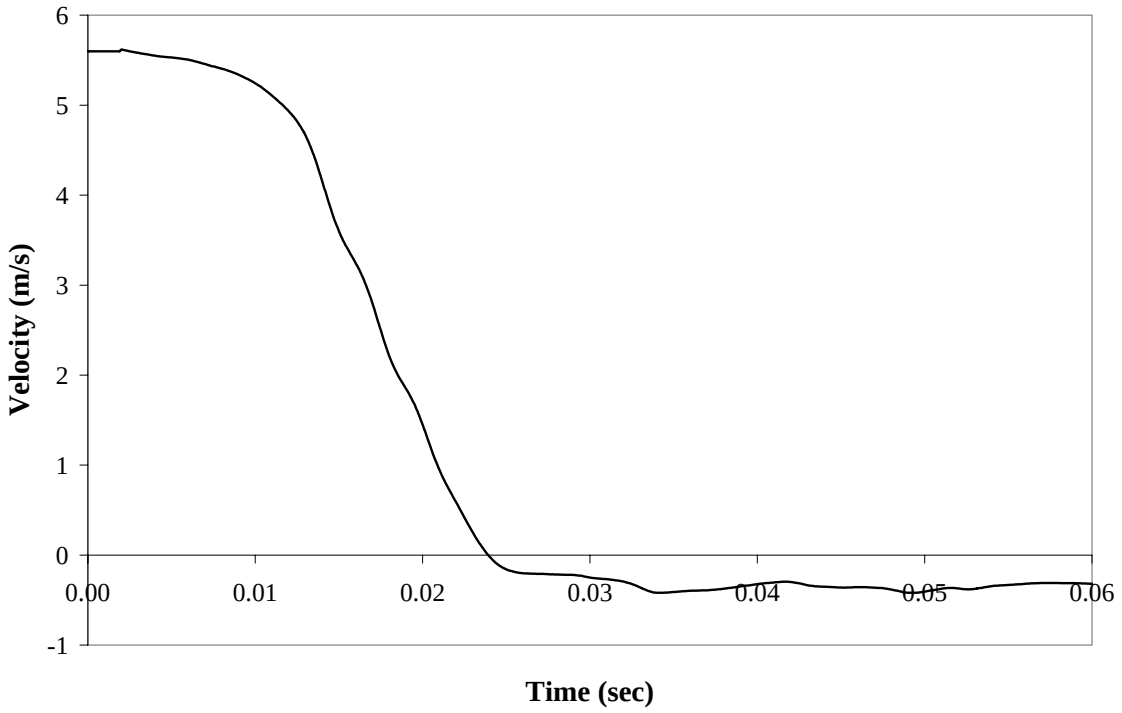

Figure 4.2 Typical side impactor velocity profile

Each subject was suspended in a seated upright position using a harness placed around the upper chest and shoulders. The arms were held above the head and immediately prior to impact the subject was released to produce an uninhibited impact scenario. Figure 4.3 shows the numerical model as compared to a sample PMHS impact test prior to impact.

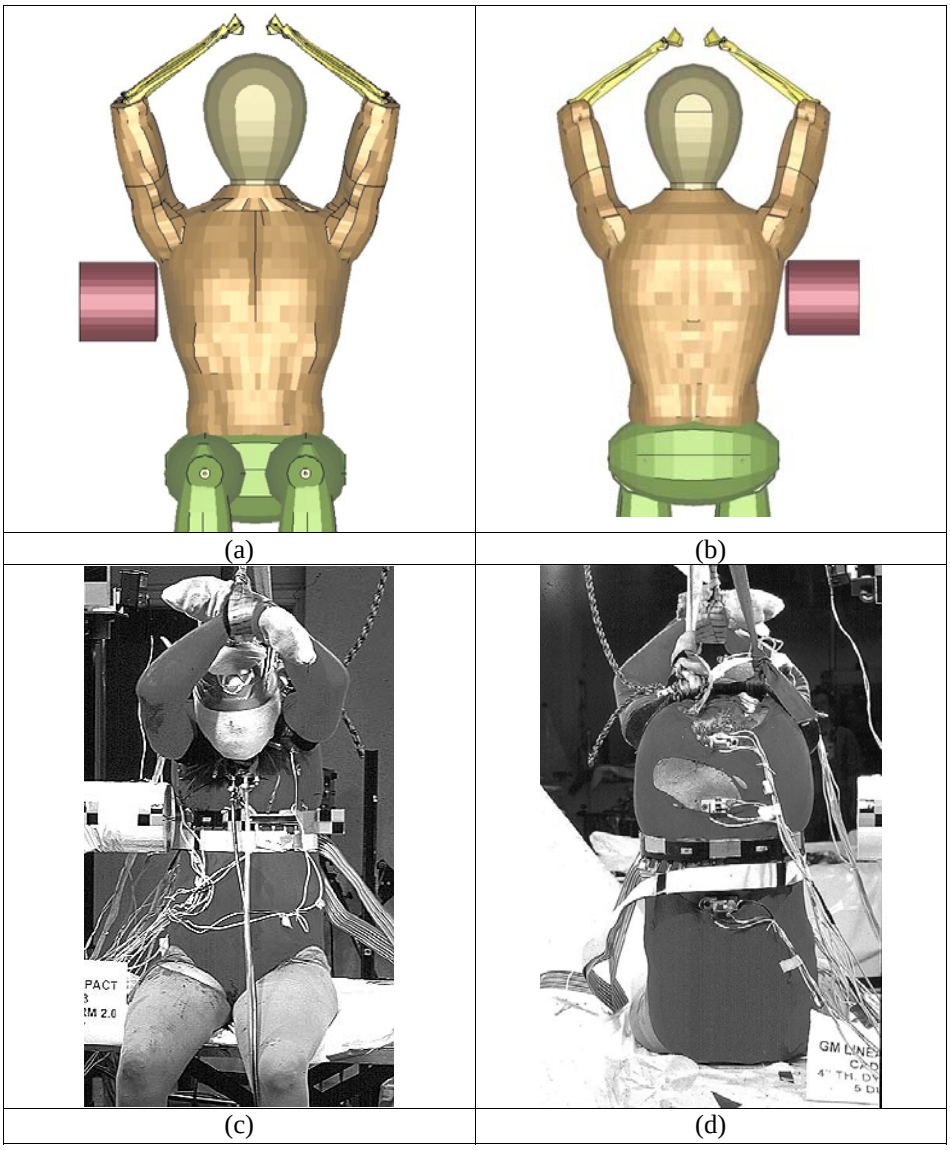

Figure 4.3 Side thoracic pendulum test (a)simulation, anterior view (b)simulation, posterior view (c)experiment, anterior view (d)experiment, posterior view (Chung et al., 1999)

The impact force was measured using a load cell in the impactor. Chest deflection was measured using a chest band, which provided the thoracic shape contours during the impact. The chest band was placed at the height of the impactor, i.e. the 6th rib. Both impact force and chest deflection have been used here for comparison to the model. Only male subjects were used throughout this analysis providing a sample size of three. Table 4.2 lists basic anthropometric data of the PMHS used throughout the analysis, along with the same dimensions as measured in the model.

Table 4.2 Side pendulum PMHS anthropometric data (Chung et al., 1999)

Test No.	Age	Mass (kg)	Chest Width (mm)
CAD1	54	103	336
CAD4	71	76	335
CAD6	45	82	326
Model	N/A	76	327

As with the frontal pendulum impact tests, the force and deflection results have been normalized for comparison to the 50^{th} percentile male according to Eppinger et al. (1984).

Side Shoulder Pendulum Tests

Side shoulder pendulum impact tests conducted by Compigne et al. (2004) have been used to validate the model side shoulder impact response. This test also facilitates the evaluation of the use of a non-injurious shoulder model, which was outlined as a project goal in the previous chapter. Seven unembalmed PMHS were subjected to right and left shoulder impacts using a 24.2 kg impactor, with impact velocities of 1.5, 3, 4 and 6 m/s. The low velocity impacts (1.5 m/s) were conducted on the right shoulder at three different angles in the horizontal plane (-15º, 0º, 15º), and the high velocity impacts were conducted on the left shoulder in a purely lateral direction. Each test was conducted with a 150 x 80 mm aluminum rectangular impact plate (thickness = 25 mm) with the 23.4 kg impact mass attached to the back and centered on the glenohumeral joint. The subjects were suspended in an upright-seated position using a cranial screw, which was released upon impact to produce an uninhibited impact scenario. Analysis by Compigne et al. (2004) suggested that the injuries observed during these impacts were consistent with injuries reported during actual side impact scenarios. Figure 4.4 shows the numerical model as compared to a sample PMHS impact test prior to impact.

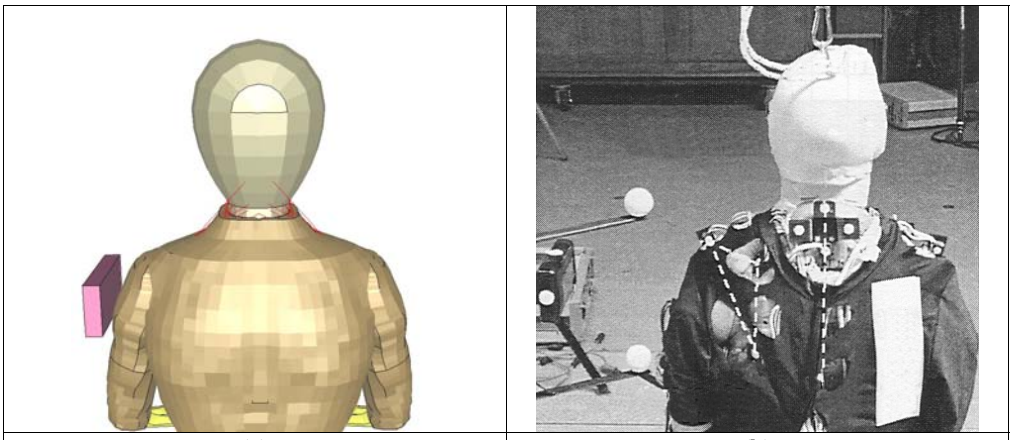

(a) (b)

Figure 4.4 Side shoulder pendulum impact test (a) simulation, posterior view (b) experiment, posterior view

Impact force was calculated by multiplying the pendulum acceleration, as measured using an accelerometer, by the mass of the impactor. Deflection results were obtained by tracking photographic markers recorded using high-speed filming, which was taken at 1000 frames per second. Photographic markers were placed on the 1st thoracic vertebrae, the upper sternum, the left and right acromion of the scapulae, the medial and lower angles of the scapula on the impacted side, and the upper and lower humerus. Impact force and deflection have been used here for comparison to the model, which were normalized to the 50th percentile male according to Eppinger et al. (1984).

The subject pool used for these experiments consisted primarily of female PMHS. As a result, to create a reasonably comparable sample size, both male and female subjects were used. It was believed the scaling should reasonably account for the anthropometric differences between the male and female subjects. Only the high velocity impacts (3, 4 and 6 m/s) were used for analysis as they are more indicative of scenarios observed during automotive impacts and are classed as ranging between non-injurious and injurious impact velocities (Compigne et al., 2004). This provides as sample size of two impacts at 3 m/s, three impacts at 4 m/s and 2 impacts at 6 m/s. Table 4.3 lists the basic anthropometric data of the PMHS used throughout the analysis along with the same dimensions as measured in the model.

Table 4.3 Side shoulder PMHS anthropometric data (Compigne et al., 2004)

Test No.	Sex	Age (years)	Mass (kg)	Shoulder Width (mm)	Shoulder Flesh Thickness (mm)		Impact Speed (m/s)
					Left	Right	
01	F	77	67	335	20	24	9
02	M	88	33	355	10	12	9
03	F	79	52	355	12	10	4
04	F	82	50	345	15	15	4
05	M	91	50	370	13	12	3
06	F	94	50	355	11	13	3
07	F	93	66.5	400	20	30	4
Model	M	N/A	76	410	21	21	3,4,6

4.2.2 Measurable Responses

As detailed above, only force and deflection have been chosen to provide analysis of the model response. It is noted however, that all of the aforementioned tests involved the use of accelerometers placed on the PMHS at various locations. While a significant amount of data can be gathered from these results, the measurement of acceleration also provides several problems when attempting to conduct response comparisons to the model. First, acceleration measurements produce a lot of noise during experimentation, an inherent problem in dynamic measurements. Second, as the accelerometers are attached to the bony components of the human body, injury at that location can cause poor response. This is especially true where accelerometers are attached to ribs, a common area of fracture. Thirdly, the method used to measure acceleration during simulation does not accurately mimic the experimental method. Within the model, accelerations were measured by tracking individual nodes at the appropriate locations. Preliminary analysis of the nodal accelerations showed highly variable responses even when comparing adjacent nodes. A method more representative of the experiments would be to attach a rigid part to the requisite locations, simulating the accelerometer and thereby producing more consistent results. However as this was no implemented in the models presented here, acceleration has not been considered for these analyses.

The remaining measurements, force and deflection, have been used along with the calculated injury criteria derived from these measures including, compression and VC, for comparison to the model. As the model was also able to predict rib and sternal fractures, specific injury of this kind has also been compared. During the results section, each impact scenario begins with a short description of the measured and calculated responses unique to the specific impact scenario.

4.2.3 Simulation Setup

For each impact scenario, the human body model was positioned to reflect the position observed during the PMHS testing as seen in Figure 4.1, Figure 4.3 and Figure 4.4. The legs were rotated about the joint centers and the arms were rotated following the method presented in Chapter 3. Table 4.4 lists the arm positions for each test condition.

Table 4.4 Impact condition arm position

Test Condition	Arm Position
Front Thoracic	arms-horizontal
Side Thoracic	arms-up
Side Shoulder	arms-rest

The pendulums used for the frontal and side thoracic impact tests were modeled as rigid cylinders, 152.4 mm in diameter using 3 mm thick shell elements. The density of the pendulums was based on wood generating a mass of 0.285 kg. During the front thoracic impact test, a point mass of 23.115kg was attached to the back of the pendulum, generating a total impact mass of 23.4kg. The pendulum was given an initial velocity of 6.67m/s simulating a free-flight impact. During the side thoracic impact tests a point mass of 49.715kg was attached to the back of the impactor, generating a total impact mass of 50kg. The pendulum was given a constrained velocity profile as noted in a previous section. For contact purposes, both pendulums were given a Young's modulus similar to wood (10 GPa).

The pendulum for the shoulder impacts was modeled as a 150x80x25 mm rigid block using solid elements. Solid elements were used in this case to avoid contact issues between the sharp edges of the impactor and the soft tissue. This was not an issue for the thoracic pendulum as its edges were chamfered at the point of impact. The density of the pendulum was based on aluminum generating a mass of 0.81kg. A point mass was attached to the back of the pendulum, generating in a total impact mass of 24.2kg. For contact purposes the pendulum was given a Young's modulus similar to aluminum (70 GPa).

The use of a rigid pendulum for all impact scenarios was believed to be acceptable, as the relatively high stiffness of the pendulum materials produced little to no deformation when compared to the impacted soft tissues. By doing so, the calculation time can be reduced. The mesh of each impact surface was chosen to reflect the mesh density on the impacted thoracic surfaces. Figure 4.5 shows the pendulum models.

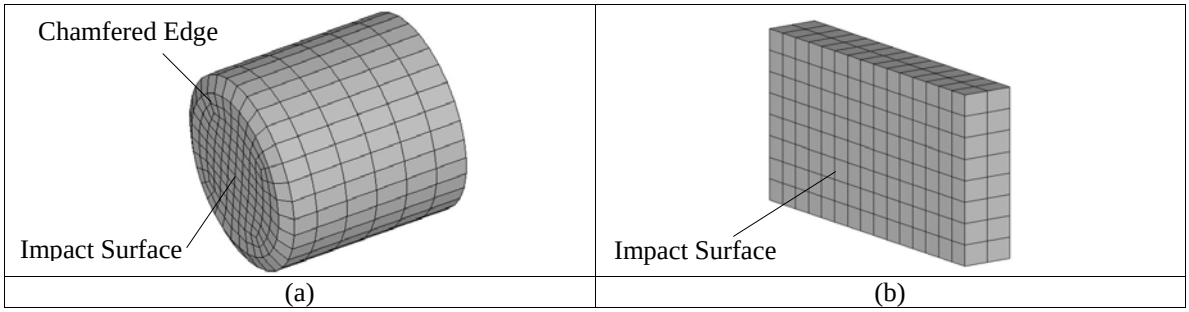

Figure 4.5 Pendulum impactors (a) thoracic (b) shoulder

4.2.4 Model Assessment Criteria

Validation of the model response required the development of a criterion such that a qualitative assessment could be made compared to the PMHS responses. A method similar to one used by the International Standards Organization (ISO) to assess the response of side impact dummies, as presented in Chapter 2, has been adopted for the purposes of this research (ISO, 1999).

Ideally, evaluating the model using the ISO method would be desirable not only for validation, but also for comparison to existing surrogate test dummies. However, such an undertaking would require the simulation of over 34 impact scenarios, each presenting extensive response assessment. Instead a similar method has been adopted based on the ISO standards, which has been applied to the validation studies performed on this model. The following terms describe the qualitative measures used to assess the model response:

- *good*: falling within the corridor of the experimental data.
- *reasonable*: falling outside the corridor of the experimental data but within one corridor width.
- *poor*: falling outside the corridor by more than one corridor width.

An increased level of assessment has been achieved by splitting the response curves into the loading, peak and unloading regions. The response corridors used have either come from development during the original experimental study, or by calculating the standard deviation of the available responses. The corridors developed during the experimental testing make for a more accurate response comparison as their development came about from extensive regression analysis. However, as this was not performed during this study, only standard deviations were used in the event where previously established corridors did not exist.

In the event where the experimental results provided fewer than four subjects, the simulation results were plotted against all experimental PMHS responses. Assessment was then made taking into account individual anthropometric measures along with the following qualitative measures:

- *good*: falling close to the experimental average or individual PMHS responses at the discretion of the author.
- *reasonable*: falling reasonably close to the experimental average or individual PMHS responses at the discretion of the author.
- *poor*: falling significantly far from the experimental average and individual PMHS responses at the discretion of the author.

4.3 Simulation Results

It is noted here that the data recorded during all simulated pendulum impact tests has been plotted using discrete points with a large time step. This was done to provide increased clarity for the reader and was observed by the author not to affect the shape of the curve.

4.3.1 Front Thoracic Tests

Measurable Responses

To validate the front thoracic impact simulations, the following responses were used for comparison:

- *force*: impact force between impactor and body.
- *compression*: deflection divided by initial thoracic depth as measured at the 6th rib anteriorly.
- *VC*: viscous injury criterion; rate of deflection multiplied by compression.
- *injury*: number of rib fractures.

Results and Discussion

Figure 4.6 shows the thorax and body at various times when impacted by a frontal pendulum. The thorax can be seen to deflect significantly, followed by global acceleration and motion of the body.

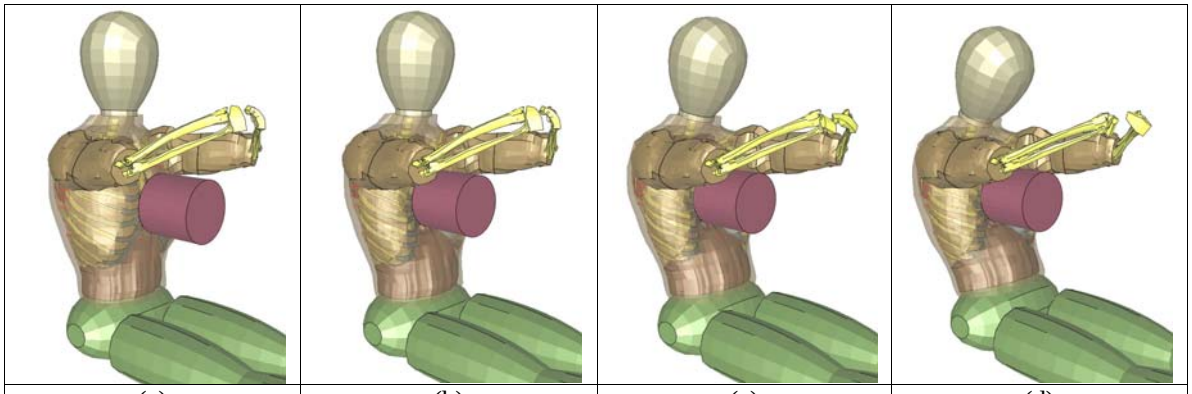

(a) (b) (c) (d)

Figure 4.6 Front thoracic impact simulation (a) t=0 sec (b) t=0.015 sec (c) t=0.030 sec (d) t=0.045 sec

Experimentally, the response of the thorax, as characterized by the force and compression results in Figure 4.7(a) and (b), presents many unique features throughout the impact. The force curve begins with a primary inertial impact peak where the tissue at the impact site is quickly accelerated to the speed of the impactor. Following that a plateau force can be observed, eventually dropping to zero once the thorax has completely absorbed the kinetic energy of the pendulum. Although not obvious in the average results and corridors presented here, all PMHS developed a secondary peak during the plateau. No specific reason was provided with the experimental results, however Kroell et al. (1971) found that younger specimens produced the secondary peak earlier in the plateau region. The compression response as seen in Figure 4.7(b) characterizes the posterior motion of the sternum and subsequent deformation of the ribcage. It increases to a maximum, after which time the thorax attempts to return to its initial state, which primarily depends on the extent of the permanent thoracic injury. The timing of the force and compression responses is best described by the force-compression curve (Figure 4.7(c)) wherein maximum compression was achieved after the force plateau has begun to decline. This curve also describes the stiffness of the thorax, which is large at initial impact due to the inertial effects and low throughout the remainder of the compression loading. The maintained compression is indicative of the type of impact being a free-flight pendulum type. After initial impact, the pendulum can no longer supply any additional force as its energy continues to decline. This curve also characterizes the hysteretic nature of the thorax, wherein the unloading path differs from the loading path. However, it is noted that the permanent injury sustained during the impact also effects contributes to these differences. The VC response of the thorax as observed in Figure 4.7(d), predicts a maximum injury much earlier in the impact as compared to the compression.

The force response of the simulation was found to produce *good* correlation to the experimentation. The initial impact peak was captured along with the secondary plateau peak, which Kroell et al. (1971) noted as being a characteristic of young specimens. Observations of the simulation revealed that this occurred when the sternum and costal cartilage engage in contact with the abdomen. The plateau observed in the simulation appears to decrease prematurely as compared to the experimental average but remains

within the corridor throughout unloading. Again, Kroell et al. (1971) noted that such a characteristic was indicative of the younger specimens. Table 4.4 summarizes the force correlation of the model.

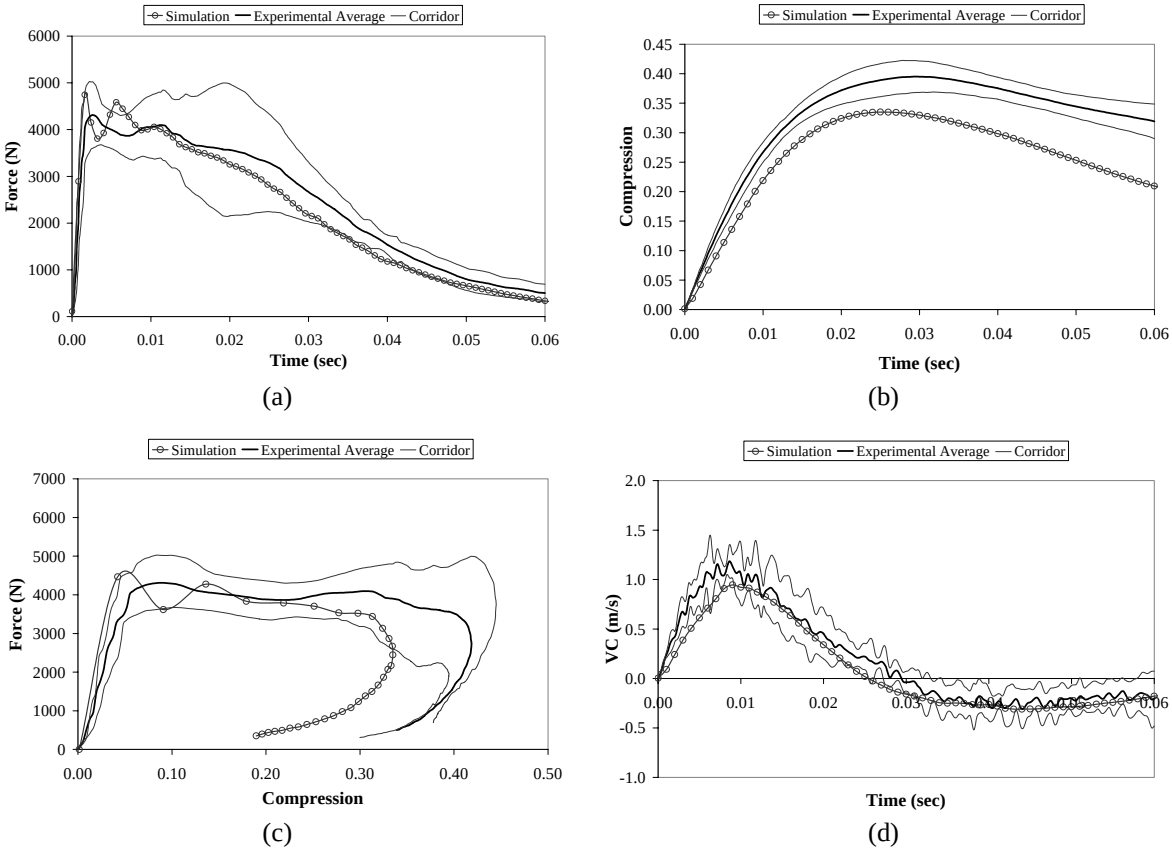

Figure 4.7 Front thoracic simulation results (a) force (b) compression (c) force-compression (d) VC

Observations of the simulation suggested that the compliance of the thorax during this impact was primarily afforded by bending deformation of the costal cartilage. Comparison to high speed film still shots as published by Kroell et al. (1971) at maximum compression showed a similar effect where the torso deforms around the impact surface of the pendulum. This was expected as the costal cartilage presents a significantly reduced stiffness compared to the ribs, and was the primary structure impacted beneath the soft tissue (Figure 4.8). However, it is noted that the costal cartilage within the model was assigned an elevated stiffness to account for the void spaces within the thorax.

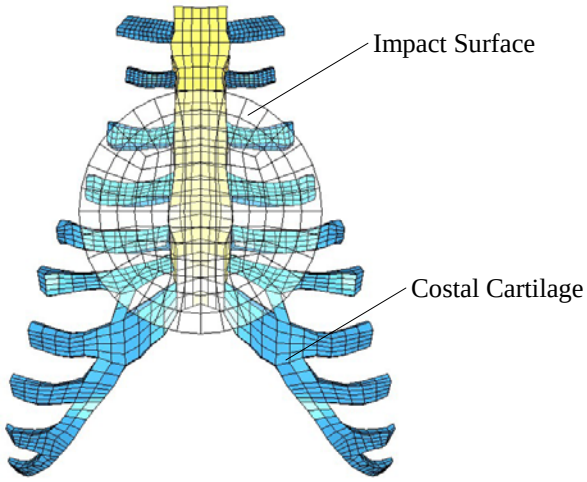

Figure 4.8 Costal cartilage impact area (tissue, ribs and organs not shown)

The compression response of the simulation as compared to the experimentation appears to present a slightly reduced maximum falling more than one standard deviation outside the corridor and occurring sooner in the impact as seen in Figure 4.7(b). It was believed that the interaction of the sternum and costal cartilage with the abdomen prevented the thorax from compressing fully. Recall, the abdomen part was optimized such that the abdominal force-compression response closely matched the experimentation during side pendulum impacts. Such results, suggest that while the abdomen provides accurate response characteristics of the model for side abdominal pendulum impacts, its response under frontal pendulum thoracic impacts may require a more detailed numerical representation to provide a more accurate result. The interaction of individual organ size, stiffness or relative motion during impact may affect the posterior motion of the sternum and costal cartilage during compression. However, this discrepancy may also have been due to the elevated costal cartilage material properties. Such properties may have affected the deformation within this region as the costal cartilage provides the majority of thoracic compliance, for frontal pendulum impacts. Table 4.5 summarizes the compression correlation of the model.

Table 4.5 Front thoracic impact correlation summary

Measurement	Impact Phase	Correlation
Force	Loading	*good*
	1st Peak	*good*
	Plateau/2nd Peak	*reasonable*
	Unloading	*good*
Compression	Loading	*reasonable*
	Peak	*reasonable*
	Unloading	*poor*
VC	Loading	*good*
	Peak	*good*
	Unloading	*good*

The stiffness of the thorax as described in the force-compression response in Figure 4.7(c) shows good correlation up to the point of full compression. The hysteretic nature of the impact was captured as the model unloads along a shallower slope, similar to the experimentation. However, as the compression response of the model was not fully captured, the model exhibits a shorter duration of the plateau force compared to the experiments.

The VC response of the model provided *good* correlation to the experimentation throughout the impact as outlined in Figure 4.7(d). This is considered very important since VC is a well accepted measure of trauma in the automotive community and has been used as an injury criteria for the model.

Table 4.6 summarizes the injury in the form of rib fractures for each PMHS and the simulation. The model predicted comparable rib fractures for three of the five PMHS. However, two PMHS presented no rib fractures throughout the impact, possibly due to their young age and associated higher material strengths. This suggests that while the stiffness of the ribcage and components was able to provide accurate simulation of the force response for the younger subjects, the failure strength may in fact require a higher value to accurately represent this age group.

Table 4.6 Frontal pendulum impact injury summary (rib fractures)

PMHS	Experimental	Simulation
15FM	13	14
18FM	14	
19FM	0	
20FM	0	
22FM	17	
Average	~9	

The location of rib fracture can provide a significant amount of information regarding the resultant injury. In the case of the experimental frontal pendulum experiments where rib fracture was reported, the fractures were for the most part evenly divided between the left and right side of the thorax at locations between the 1st and 7th ribs as seen in Table 4.7. This was expected as the impactor was aimed over the center of the sternum. It is noted that slight differences exist between each PMHS, however no significant pattern could be observed. During the simulated impacts the rib fractures were also evenly divided between the left and right side of the thorax at locations between the 1st and 5th ribs. The simulation also produced significant fracture of the first rib, not commonly found during the PMHS testing. This was believed to be due to the elevated costal cartilage stiffness, which forced the ribs to withstand more of the deformation.

Table 4.7 Frontal thoracic pendulum impact rib fracture locations

Rib	15FM		18FM		22FM		Model	
	Left	Right	Left	Right	Left	Right	Left	Right
1st				1			1	1
2nd	1	1	1	1	1	1	1	
3rd	2	2	1	1	2	3	1	2
4th	2	1	1	1	3	2	2	3
5th	2	1	1		2	1	2	1
6th		1	2	2	1	1		
7th			2					
Total	7	8	8	6	9	8	7	7

4.3.2 Side Thoracic Tests

Measurable Response

To validate the side thoracic impact simulation, the following responses were used for comparison:

- *force*: impact force between impactor and body.
- *compression*: deflection as measured at the 6th rib anteriorly, divided by initial thoracic depth.
- *VC*: viscous injury criterion; rate of deflection multiplied by compression.
- *injury*: number of rib fractures.

Results and Discussion

Figure 4.9 shows the thorax and body as impacted at various times throughout the simulation. The thorax is seen to deflect significantly, followed by global acceleration and motion of the body. The results in this test have been plotted against the individual PMHS responses (CAD1, CAD4 and CAD6), as only three subjects were available for comparison.

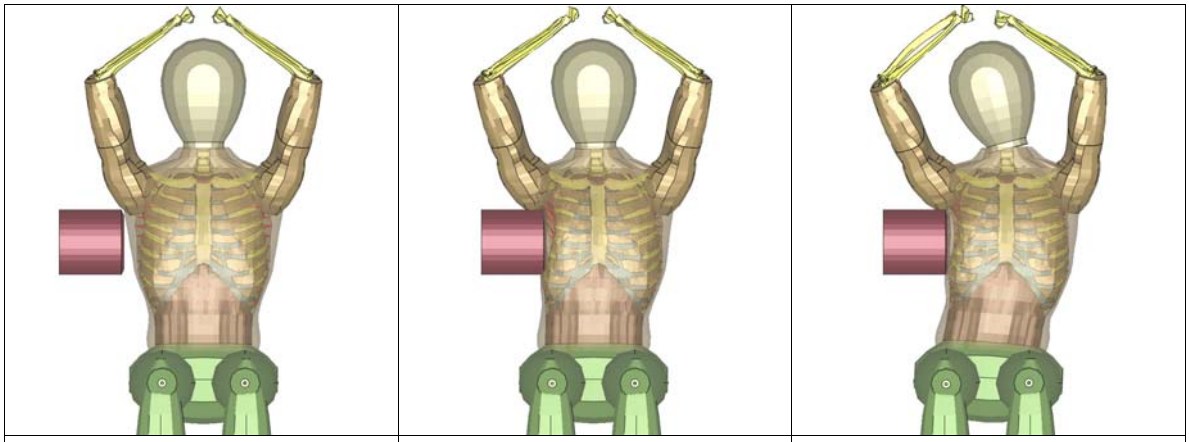

(a) (b) (c)

Figure 4.9 Side thoracic impact simulation (a) t=0 sec (b) t=0.015 sec (c) t=0.030 sec

Description of the experimental force and compression response of the side thoracic impact tests can best be described by comparing the similarities and differences between this impact and the front thoracic impacts. The experimental force-time curve as seen in Figure 4.10(a) provides a reduced onset of maximum force as compared to the frontal

impacts. This has often been attributed to the rib cage geometry, which provides a lower initial stiffness since the ribs are flatter and less supported in side impacts (Viano et al., 1989). No plateau force was observed during this impact since the impactor was displacement controlled and stopped externally as opposed to being stopped by the thorax. Recall this was a velocity pulse impact, which prescribed the impactor to traverse a limited distance into the thorax. This was the key difference between this impact and the free flight pendulum frontal impacts. This difference was also reflected in the compression-time response, which reached a maximum sooner during the impact and decreased at a faster rate. Similarities with the front thoracic impacts were observed in the force-compression response, which produces a hysteretic loading and unloading response. It was also noted that that maximum compression was achieved after the force has begun to decline, as at that time the impactor had yet to reach zero velocity, providing a continued compression response.

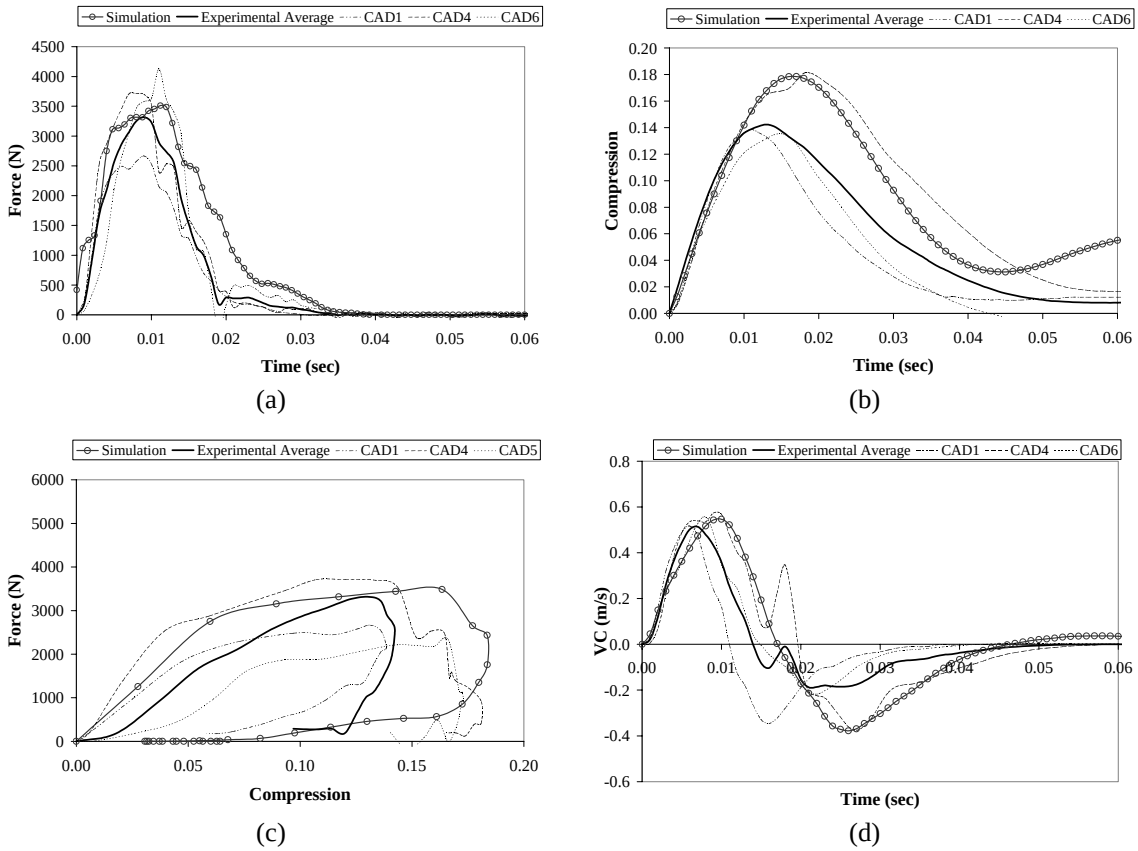

Figure 4.10 Side thoracic pendulum impact simulation results (a) force (b) compression (c) force-compression (d) VC

Figure 4.10(a) shows the model force response providing *good* correlation during loading and unloading and a *good* peak force correlation. Although the response was slightly elevated as compared to the average, comparison to a single PMHS (CAD04) with matching mass (76 kg) and chest width (~335mm) provided better correlation. During unloading however, the force response appears slightly elevated. The force curve also produced small valleys and peaks throughout the impact, a similar phenomenon found in the experimentation, possibly indicative of rib fractures resulting in redistribution of the load.

Observations of the simulation revealed that the compliance of the thorax was primarily afforded by the bending of the ribs. During this impact the costal cartilage acts to distribute the load, which occurs in an axially compressive manner as opposed to bending. However, as the costal cartilage extends further from the center of the thorax at the lower ribs (6-10) as opposed to the upper ribs (1-5), some bending was observed at the level of the lower ribs.

The compression response of the model presented *good* correlation throughout the impact as seen in Figure 4.10(b). At maximum compression the model appears slightly elevated, but again comparison to a single anthropometrically matching subject (CAD04) showed excellent correlation. Unlike the frontal tests, the inclusion of the abdomen appears to have no adverse effects on the lateral response of the model. Again, the abdomen was validated in side pendulum impacts, which was expected to produce accurate results during side thoracic pendulum impacts. However, the void spaces within the thoracic numerical model may produce an increase in compression later in time. Since continuity of the model within this region was not maintained, it lacked the full damping effects of the visceral components.

Similar to force and compression, the stiffness response of the model compares better to a single PMHS (CAD04) as opposed to the experimental average as seen in Figure 4.10 (c). The previously mentioned elevated force at peak compression becomes apparent when

the plotted here. The source of this was not clear, however may be due to the elevated stiffness of the costal cartilage. Table 4.8 summarizes the force and compression correlation of the model.

Table 4.8 Side thoracic pendulum impact correlation summary

Measurement	Impact Phase	Correlation
Force	Loading	*good*
	Peak	*good*
	Unloading	*good/reasonable*
Compression	Loading	*good*
	Peak	*good*
	Unloading	*good*

The VC response of the experimental results, as expected, reaches a maximum prior to full compression as seen in Figure 4.10(d), while the VC response of the model a similar response and shows *good* correlation throughout the impact. Again, these results better correlate to the single test case with matching anthropometric measures (CAD04).

Table 4.9 summarizes the number of rib fractures for the PMHS and the simulation. The model predicted comparable rib fractures to the experimental average. Unfortunately the rib fracture locations could not be obtained from the experimental testing for comparison to the model. However, 8 of the 11 rib fractures predicted in the model were observed to occur the impacted (right) side of the thorax. More than likely a similar phenomenon was observed during the experimental testing.

Table 4.9 Side thoracic impact injury response (rib fractures)

PMHS	Experimental	Simulation
CAD01	4	11
CAD04	15	
CAD05	10	
Average	~10	

4.3.3 Shoulder Pendulum

Measurable Responses

To validate the side shoulder impact results, the following responses were used for comparison:

- *force*: impact force between the impactor and body.
- *deflection*: impacted acromion to middle upper point of sternum
  impacted acromion to opposite acromion
  impacted acromion to T1 vertebrae
  impactor to T1 vertebrae
  sternum to T1 vertebrae

Note: deflection measurements are considered here as opposed to compression as the initial distances required to calculate compression could not be obtained from the experimentation. Figure 4.11 outlines the deflection measurements.

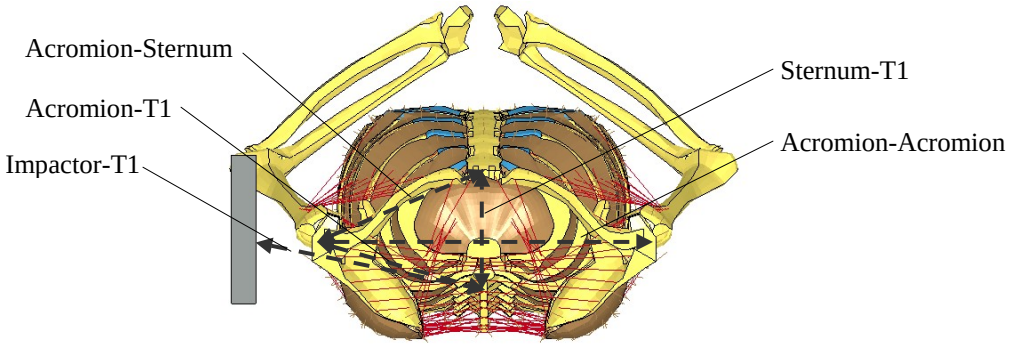

Figure 4.11 Shoulder impact deflection measurements

Results and Discussion

Figure 4.12 shows the shoulder and body as impacted at various times throughout the simulation. The shoulder is seen to deflect significantly, followed by global acceleration and motion of the body.

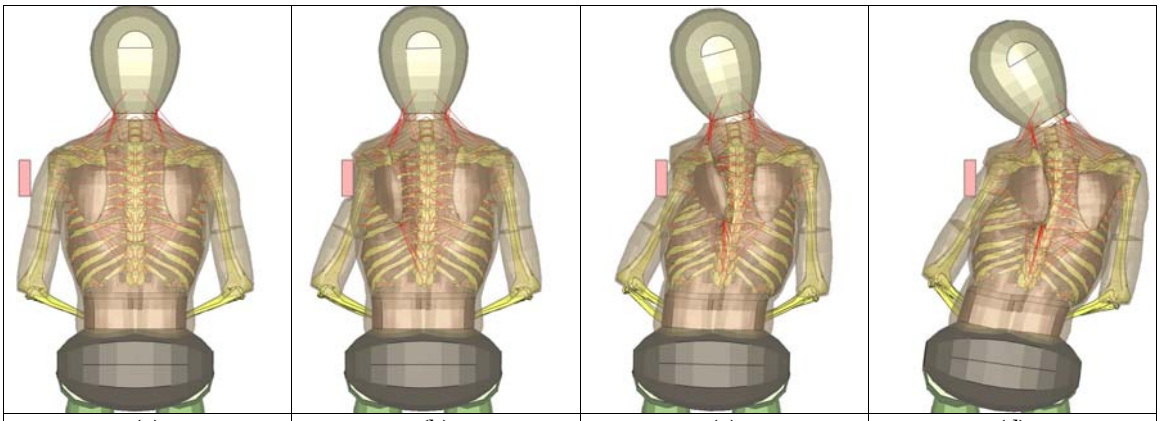

(a) (b) (c) (d)

Figure 4.12 Shoulder impact simulation (a) t=0 sec (b) t=0.015 sec (c) t=0.030 sec (d) t=0.045 sec

Before analyzing the results, it should be reiterated that the current state of the shoulder model presented here does not address common shoulder injuries experienced during automotive impacts, such as clavicle fracture, acromion fracture or joint separation (Compigne et al., 2004). Instead the shoulder has been modeled to produce non-injurious shoulder motion during impact. Therefore the non-injurious and injurious impacts have been analyzed separately; where the 3 and 4 m/s tests were considered the non-injurious impacts and the 6 m/s impacts were considered the injurious impacts. This follows conclusions arrived at by Compigne et al. (2004) who stated that the injury threshold was approximately 4 m/s for the scenario simulated here.

The simulation results from the non-injurious impacts have been plotted using experimentally established response corridors, as five subjects were available for comparison, while the simulation results from the injurious impacts have been plotted against individual PMHS responses (Test #01 and Test #02), as only two subjects were available for comparison.

Non-Injurious Shoulder Pendulum Impact

Compigne et al. (2004) combined the 3 and 4 m/s impacts in an effort to generate more comprehensive corridors for both force and deflection during the non-injurious impacts. Such findings contradict the inherent viscoelasticity of the human body, however the

analysis performed throughout their study showed that for all measurements during tests where no injury was reported, similar responses were observed. Only a slight increase in force and deflection was noted during the 4 m/s impacts.

The experimental force response of the non-injurious shoulder impacts, as seen in Figure 4.13, provides a gradual onset of force capturing the deformation of the soft tissue, along with a distinct peak, indicative of the maximum impact resistance. The experimental deflection responses as seen in Figure 4.14 produced a swift onset to its maximum, indicative of a high stiffness, for all measures except the impactor to T1 deflection. In the latter case, interaction with the shoulder soft tissues generated a delayed onset to its maximum, while the other bone-to-bone measurements provided a stiffer response (Compigne et al., 2004).

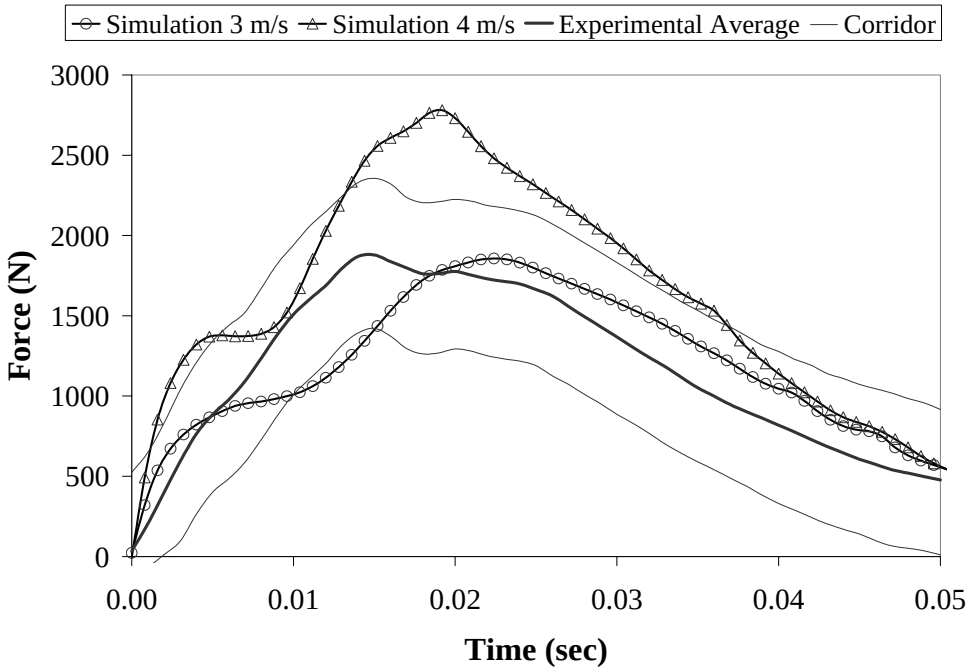

Figure 4.13 Shoulder impact simulation force at 3 and 4 m/s scenarios

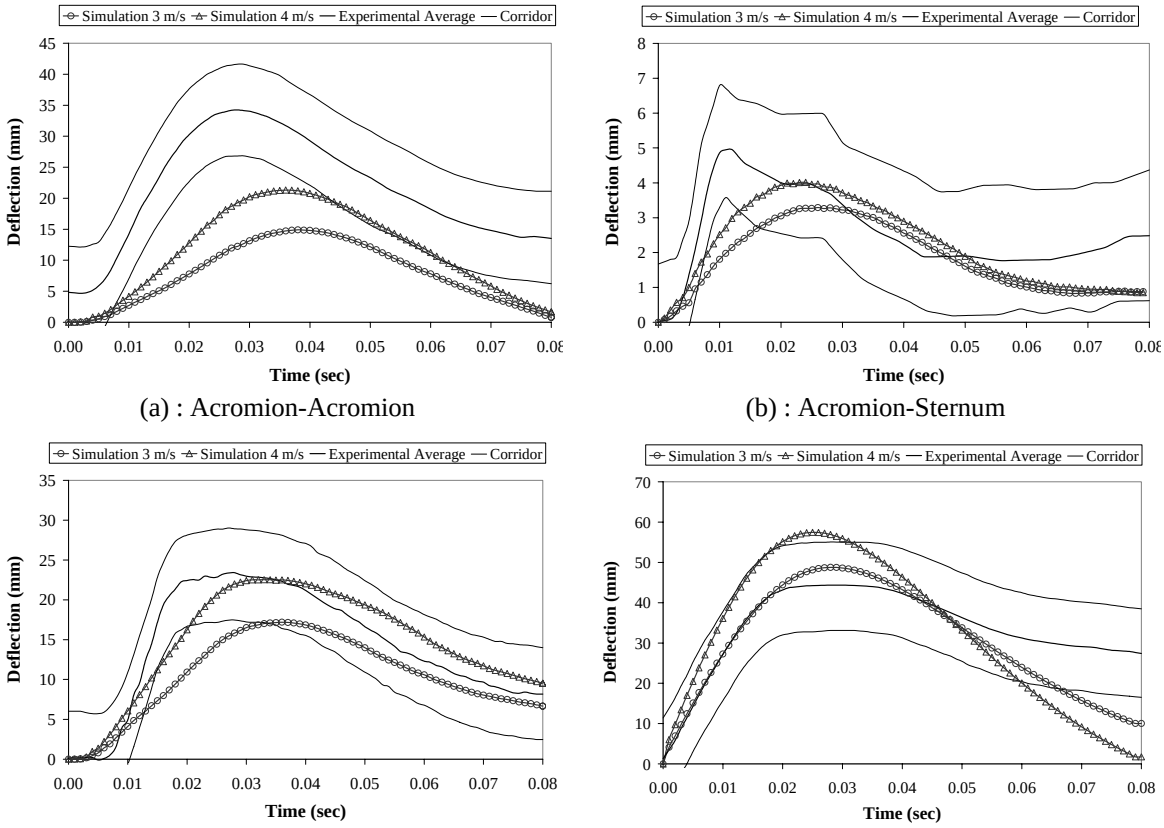

(a) : Acromion-Acromion

(b) : Acromion-Sternum

(c) : Acromion-T1

(d) : Impactor-T1

Figure 4.14 Shoulder impact deflection at 3 and 4 m/s (a) acromion-acromion (b) acromion-sternum (c) acromion-T1 (d) impactor-T1

The force response of the simulation was found to produce *good* correlation during the 3 m/s impact and *reasonable* correlation during the 4 m/s impact as seen in Figure 4.13. Most notably the peak responses for both impacts appeared to be slightly elevated. This may have been due to the lack of ligaments at the joints, which were instead modeled as spherical joints resulting in zero compliance. Table 4.10 summarizes the force correlation response of the model throughout the impact

The deflection responses of the simulation as compared to the experimental results produced *good* to *reasonable* correlation throughout the impact as observed in Figure 4.14, however some discrepancies were apparent. During the loading phase, the bone-to-bone deflections produced *reasonable* correlation but were unable to capture the high stiffness as measured during the experiments. This was believed to be due to the slightly

lateral position of the arms prior to impact. As noted in Chapter 3 the arms were positioned slightly lateral from perfectly vertical to avoid interpenetration of the arm tissue with the torso tissue. However, in doing so, this forced an initial impact to occur below the humeral head. A delayed reaction was observed for all measurements, as the impactor was required to compress additional soft tissue. The good correlation of the maximum values suggests that in fact the model does capture the deformation response experienced during these impacts. Unfortunately however, the *poor* correlation of the acromion-acromion deflection could not be attributed to any particular effect.

Table 4.10 Non-injurious impact correlation summary

Impact Velocity (m/s)	Impact Phase	Force Correlation	Deflection Correlation			
			Acrom-Acrom	Acrom-Stern	Acrom-T1	Impactor-T1
3	Loading	*good*	*poor*	*reasonable*	*reasonable*	*good*
	Peak	*good*	*poor*	*good*	*good*	*good*
	Unloading	*good*	*poor*	*good*	*good*	*good*
4	Loading	*good*	*poor*	*reasonable*	*reasonable*	*good*
	Peak	*reasonable*	*poor*	*good*	*good*	*good*
	Unloading	*good*	*poor*	*good*	*good*	*good*

Injurious Shoulder Pendulum Impacts

The most common injury observed throughout the experimental pendulum impacts was distal clavicle fracture. This injury allows the shoulder to move medially with little resistance, which was observed in both the force and deflection responses. The experimental force produced a plateau capturing the lack of resistance to deformation as seen in Figure 4.15, while the deflection produced increased maximums with a slower onset capturing the nearly uninhibited medial motion of the shoulder as seen in Figure 4.16.

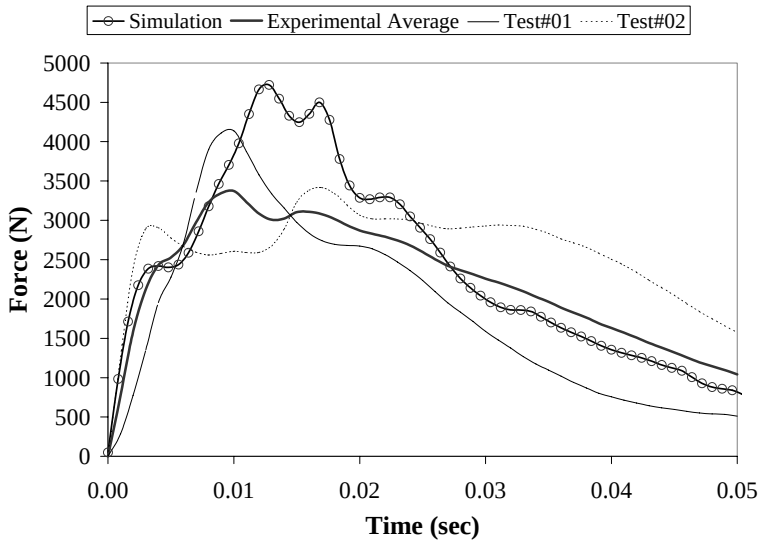

Figure 4.15 Shoulder impact force at 6 m/s

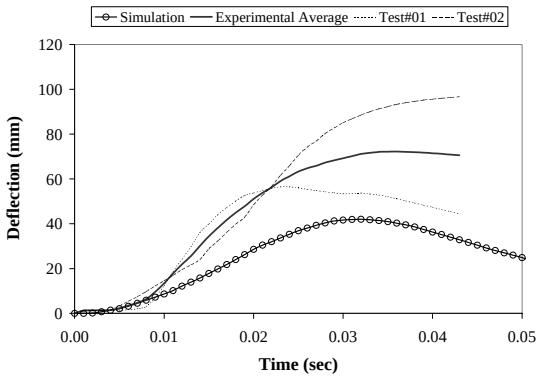

(a) : Acromion-Acromion

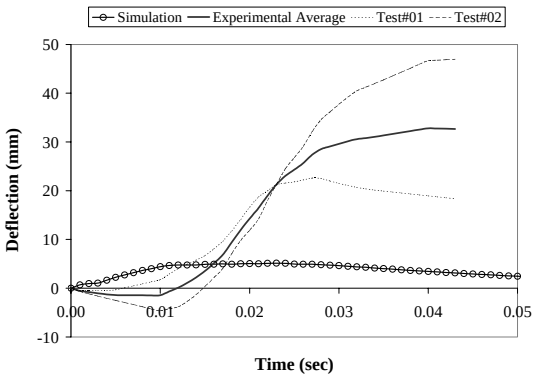

(b) : Acromion-Sternum

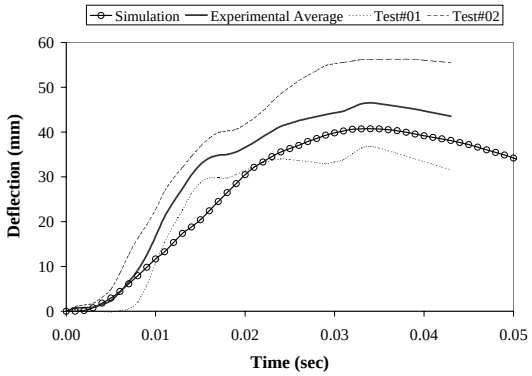

(c) : Acromion-T1

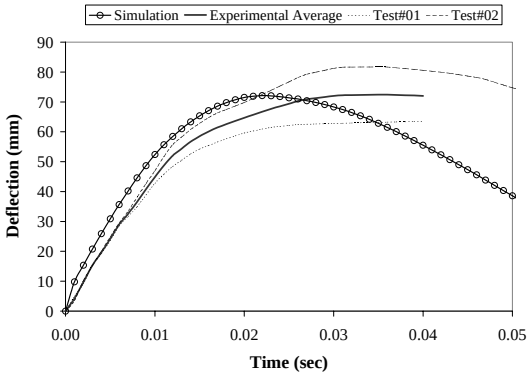

(d) : Impactor-T1

Figure 4.16 Shoulder impact deflection at 6 m/s (a) acromion-acromion (b) acromion-sternum (c) acromion-T1 (d) impactor-T1

During the simulation, the force results present *good* loading and unloading characteristics and a *reasonable* peak force correlation as seen in Figure 4.15. As no injury was modeled, the shoulder continues to resist the impactor generating a high peak force.

The deflection results present *poor* correlation of the acromion-acromion and acromion-sternum deflections and *good* correlation of the acromion-T1 and impactor-T1 deflections as seen in Figure 4.16. This can be explained by understanding the motion experienced by the clavicle. As impact occurs, the clavicle was rotated about its sternoclavicular joint, moving the acromion in a medial and posterior direction. Figure 4.17 highlights this rotation. This movement pushed the acromion away from the sternum, resulting in *poor* correlation, and towards the T1, resulting in *good* correlation. The poor correlation of the acromion-acromion deflection meanwhile remains low, as the impacted acromion did not move in the medial direction to the extent as expected when clavicle fracture occurs.

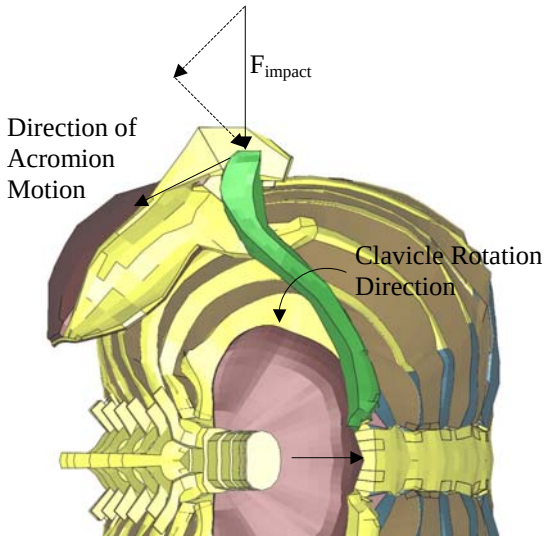

Figure 4.17 Clavicle motion and applied force during impact

The sternum-T1 deflection was also compared, to further investigate the effect of the non-injurious model. Compigne et al. (2004) reported the deflection between the sternum and T1 vertebrae produced a maximum of approximately 5 mm regardless of impact speed. This deflection occurs as the clavicle was rotated about the sternoclavicular joint,

generating a force on the sternum in an anterior direction as outlined in Figure 4.17. During the simulations, the non-injurious impacts produced *good* correlation to the experimentation, however the injurious impacts did not. As no clavicle fracture is modeled, the continued rotation of the clavicle continues to push anteriorly on the sternum generating elevated deflection. Table 4.11 lists the maximum deflection values.

Table 4.11 T1-to-Sternum deflection

Impact Speed (m/s)	Maximum T1-to-Sternum Deflection (mm)	
	Experimental Average	Simulation
3	5.3 ± 1.7	3.7
4		6.0
6		17.9

This was also believed to be the cause of fracture of the first rib, which was observed during the simulated injurious impact. The force acting on the sternum in the anterior direction as transferred through the clavicle, forces the rib to deflect excessively and fracture. As no injuries regarding the rib structure were reported to a significant degree throughout the experimentation, confirmation of this effect could not be made. However, this effect has been taken into account for analysis of the side sled impacts.

4.3.4 Pendulum Impact Summary Discussion

The aforementioned results demonstrate the biofidelity of the numerical model to predict a variety of pendulum impact simulations using globally measured parameters, injury criteria and specific injury when compared against PMHS tests. With the addition of the components as developed in this study the model produced results for the most part with *good* or *reasonable* correlation for all impact scenarios.

The frontal thoracic pendulum impacts showed *good* correlation of force and *poor* correlation of compression, while the side thoracic pendulum impacts showed *good* correlation of both force and compression. Both however, predicted a similar number of rib fractures as compared to experimentation. These results also highlighted the possible effects of using an elevated costal cartilage stiffness in order to compensate for the voids

within the thoracic cage. The results from the frontal thoracic pendulum impacts showed the model was able to capture the response of younger PMHS as opposed to older subjects with expected lower material properties. However, the frontal thoracic compression response was found to be slightly low as compared to the experimental results, highlighting the possible need for a more complex abdominal model, or the need to calibrate the abdomen separately for frontal and side abdominal impact scenarios.

The shoulder impact simulation test results showed *good* to *reasonable* correlation during the non-injurious impacts, and *good* to *poor* correlation during the injurious impacts. This was expected for the injurious impacts where clavicle fracture (not modeled) significantly changed the response. Most notably, the motion of clavicle when not fractured applied a substantial amount of force on the sternum in an anterior direction inducing fracture of the first rib. This is extremely important to keep in mind, as the impacts experienced during the side sled tests are conducted at speeds beyond the injury threshold as defined by Compigne et al. (2004).

-- CHAPTER 5 --

Side Sled Impacts – Model Response and Validation

5.1 Introduction

PMHS tests involving the entire human body provide the impact and injury response during impact scenarios intended to replicate full body automotive crash. The results provide information regarding the complex interaction of all body regions and their influence on the injury response. For the purposes of this research, side sled PMHS testing as been considered for comparison of the full body numerical model with the objective of investigating the model biofidelity.

This chapter will start with a description of the experimental testing used throughout the analysis along with the numerical modeling techniques required to simulate the impacts. The same assessment criteria as used during the pendulum impact simulations (refer to section 4.2.4) have been used here, and a brief summary description is provided. The validation analysis of the model will then be presented with a description of the experimental PMHS response intended to provide a complete understanding of the impact scenario, which further allows for the accurate analysis and correlation of the model response. The results provide insight into the simplifying assumptions made

throughout the past and present developments of the model and in the case where these assumptions generate discrepancies between the model and experimentation, explanations were developed such that recommendations for future work can address and correct them.

5.2 Materials and Methods

Two different side sled impact configurations were utilized to validate the model in side sled impact scenarios. Both consider unembalmed PMHS in a left side impact against a rigid wall; however each test uses a different impact wall orientation and records slightly different experimental results. Tests conducted by Pintar et al. (1997) impacted PMHS against a National Highway Traffic Safety Administration (NHTSA) load wall, while tests conducted by Cavanaugh et al. (1990) impacted PMHS against a Wayne State University (WSU) load wall.

5.2.1 Experimental Data

NHTSA Side Sled Tests

A series of 26 PMHS side sled impact tests were conducted by Pintar et al. (1997) at the Medical College of Wisconsin and the NHTSA Vehicle Research and Test Center through the Ohio State University College of Medicine to evaluate human side impact injury tolerance. PMHS were loaded in a side sled test apparatus based on the original Heidelberg type sled (Kallieris et al., 1981) with modifications made to the plate orientation. The apparatus was made up of a 1.3 meter long bench coated in Teflon™ to minimize friction between the PMHS. Two horizontal tubes provided support for the PMHS back and head when placed on the seat. The sled was accelerated to approximately 6.67 m/s (24 kph) or 8.89 m/s (32 kph) and suddenly decelerated causing the PMHS to slide down the Teflon bench and impact the rigid wall. At the point of impact, the sled had a velocity of 0 m/s and the PMHS had a velocity of approximately 6.67 m/s or 8.89 m/s. From top to bottom, the rigid wall consisted of four plates with a configuration such that the first plate impacted the mid thorax, the second plate impacted the abdomen, the third plate impacted the pelvis and left upper leg, and the fourth plate

impacted the left upper leg, lower leg and foot. This configuration was chosen to represent the average windowsill height as observed in automobiles and therefore does not directly involve the shoulder (Pintar, 1997). Figure 5.1 shows the dimensions and orientation of the sled test apparatus and Figure 5.2 shows the numerical model compared to the PMHS impact prior to impact.

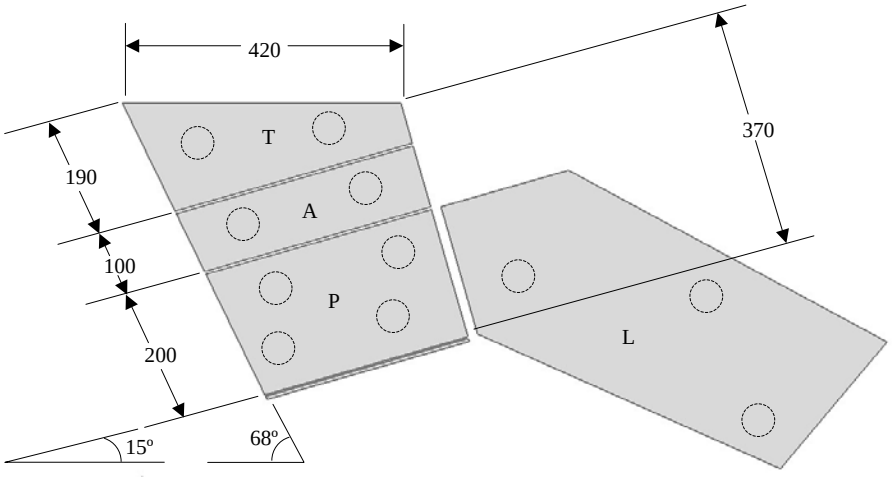

Figure 5.1 NHTSA side sled device dimensions (Pintar et al., 1997)

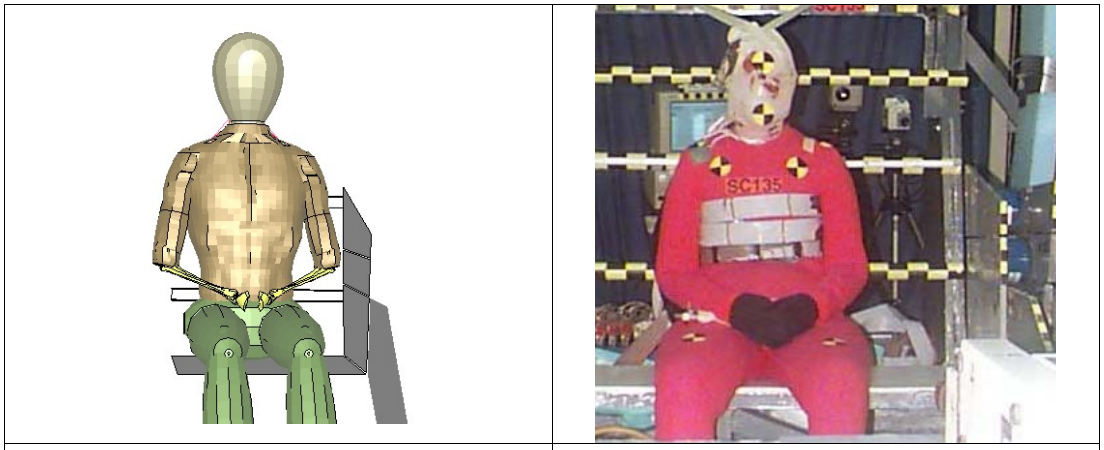

(a) (b)

Figure 5.2 NHTSA side sled test (a) simulation (b) experiment (Pintar and Yoganandan, 2001a)

The impact plates were instrumented with 11 load cells to measure the impact force. Chest deflection was measured using chest band at the following locations: the lateral level of the 4th rib, the level of the xiphoid process and the lateral level of the 10th rib. These are termed the upper band, middle band and lower band throughout this chapter. Both force and deflection results are used for comparison to the model.

The PMHS were tested in the seat using the following wall surface conditions: a rigid (steel) wall, a padded (10cm Ethafoam) wall and a rigid wall with 120mm pelvic plate offset. The latter two were intended to simulate an automobile interior. The model detailed here was impacted against a rigid wall representation, therefore only the flat rigid wall tests have been used for comparison. Only male subjects were used providing a sample size of three impacts at 6.67 m/s and five impacts at 8.89 m/s. Table 5.1 lists basic anthropometric data of the PMHS used throughout the analysis.

Table 5.1 NHTSA side sled PMHS anthropometric data (Viano et al., 1989b)

Test No.	PMHS No.	Age	Mass (kg)	Test Velocity (m/s)
3120	SC101	73	89	6.67
3122	SC102	27	73	6.67
3155	SC103	55	76	6.67
3322	W9305	73	72	8.89
3324	W9302	77	75	8.89
3422	SC108	44	83	8.89
3423	SC109	49	62	8.89
3579	W9310	68	98	8.89

The raw data from these tests were acquired from the NHTSA Biomechanics Test Database (NHTSA, 2004). All data was recorded at 12,500 Hz and for the purposes of comparison to the simulation results, has been filtered using an SAE filter channel class 180 following recommendations made by Kuppa et al. (2003). The force and deflection data has been normalized according to Eppinger et al. (1984) as noted in a previous chapter.

WSU Side Sled Tests

A series of 31 human PMHS side sled impact tests were conducted by Cavanaugh et al. (1990) at Wayne State University to evaluate human side impact injury tolerance. The side sled test apparatus used during these tests was also based on the original Heidelberg type sled with modifications made to the plate orientation. PMHS were impacted into a rigid wall at 6.67 m/s and 8.88 m/s using the same techniques as used by Pintar.

However, the impact wall was slightly different. From top to bottom, the impact wall was configured such that the first plate impacted the shoulder, the second plate impacted the thorax, the third plate impacted the abdomen, the fourth plate impacted the pelvis and upper leg, and the fifth plate impacted the knee. Figure 5.3 shows the dimensions and orientation of the sled test apparatus as observed from the side and Figure 5.4 shows the simulation prior to impact.

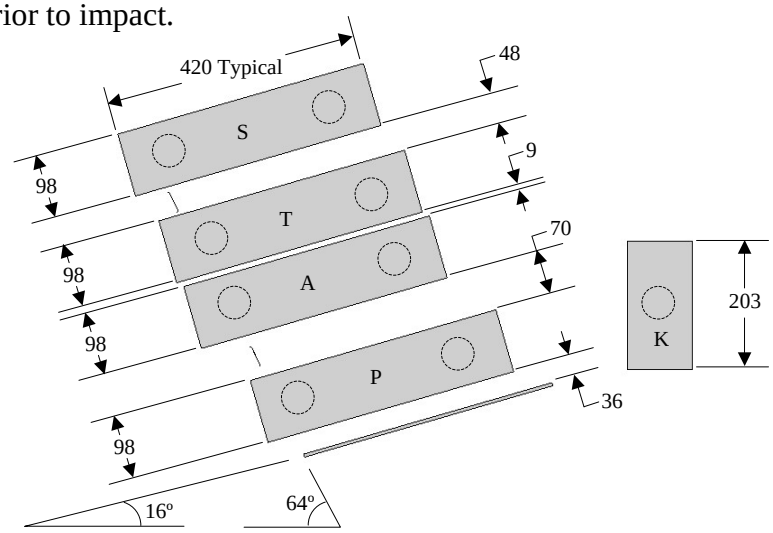

Figure 5.3 WSU side sled device dimensions (Cavanaugh et al., 1990)

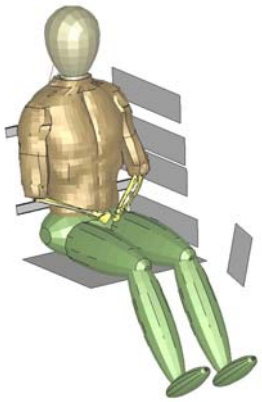

Figure 5.4 WSU side sled test simulation

The impact plates were instrumented with 9 load cells to measure the impact force. Chest deflection was measured by tracking targets mounted on the sternum of the PMHS at the T5 level. Both force and deflection results are used for comparison to the model.

The PMHS were tested in the seat using the following wall surface conditions: a rigid (steel) wall, a "soft" honeycomb padded wall, a "stiff" honeycomb padded wall and a rigid wall with a 152.4mm pelvic plate offset. The latter three were intended to simulate an automobile interior. The model detailed here was impacted against a rigid wall representation, therefore only the flat rigid wall tests have been used for comparison. Only male subjects were used providing a sample size of three for the low velocity impact and two for the high velocity impact. Table 5.2 lists basic anthropometric data of the PMHS used throughout the analysis.

Table 5.2 WSU side sled PMHS anthropometric data (Cavanaugh, 1990)

Test No.	PMHS No.	Age	Mass (kg)	Test Velocity (m/s)
5	SIC 05	67	44	6.67
7	SIC 07	66	74.8	6.67
4933	SC 131	48	75	6.67
4	SIC 04	69	57.6	8.89
6	SIC 06	60	61.2	8.89

It should be noted that while Test #4933 was conducted using the WSU sled test device, it was performed a decade after the other tests (Yoganandan and Pintar, 2001).

The raw data from these tests were acquired from the NHTSA Biomechanics Test Database (NHTSA, 2004). Only force data was available through the database while chest compression was acquired from the papers. Unfortunately, this meant only the average and standard deviations of chest compression could be obtained, which prevented comparison of the model to individual PMHS responses. The force data was filtered with SAE filter channel class 180 and normalized according to Eppinger et al. (1984).

5.2.2 Measurable Responses

Similar to the experimental pendulum impacts presented in Chapter 4, the acceleration data of the experimental side sled impact tests has not been used for the analysis presented here. Again, the accelerations were not used due to the noise generated during

testing, the attachment to bony structures with fracture potential and the lack of proper accelerometer representation during the simulation.

5.2.3 Sled Simulation

For both side sled impact scenarios, the impact plates, back support bars and seat bottom were modeled as 5 mm thick shell elements with the dimensions as previously labeled. All parts were rigid and were restricted from moving in any translational or rotational direction. For contact purposes, the plates have been given a Young's modulus equal to steel (210 GPa). The use of a rigid part for the impact plates was believed to be appropriate as the relatively high stiffness of the plate materials (steel) produced little to no deformation when compared to the impacted soft tissues.

The entire body was given an initial velocity of either 6.67 m/s or 8.89 m/s depending on the simulated test. Gravity was applied, however it was found to only have an effect after impact had occurred. The body was positioned to reflect the seated orientation of the PMHS during the experimental testing. The upper body and pelvis were rotated such that thorax was aligned with the back bars; the upper legs were rotated such that they were aligned with the seat plate; and the lower legs were rotated such that they were aligned with the leg plate. The arms were rotate to reflect the "arms-rest" position as described in Chapter 3.

5.2.4 Model Assessment Criteria

The model assessment criteria used throughout this analysis match the assessment criteria described in Section 4.2.4 for the analysis of the pendulum impact simulations, where the terms *good, reasonable* and *poor* were used to describe the correlation of the model. Again an increased level of assessment has been achieved by splitting the response curve into the loading, peak and unloading regions.

5.3 Simulation Results

This simulated side sled impacts are discussed in this section for both the NHTSA and WSU side sled devices. The differences between the two test scenarios allow for the

analysis of the model in differing fashions. The NHTSA sled test provided greater information for the analysis of chest compression through the use of chest bands. As well, these experiments included a larger subject pool, allowing for a more comprehensive correlation of the simulation. On the other hand, the WSU tests allowed for the analysis of the shoulder model as this sled provided direct impact within this region. As well, this test provided pelvic compression data, which was used for the analysis here. In both sets of tests the analysis of force, impulse and injury response was considered, which provided insight into the effects of assumptions made throughout past and present model developments, highlighting possible areas for improvement.

It is noted here that the data recorded during all simulated side sled impact tests has been plotted using discrete points with a large time step. This was done to provide increased clarity for the reader and was observed by the author not to affect the shape of the curve.

Measurable Responses

To validate both the NHTSA and WSU side sled impact results, the following responses were used for comparison:

- *timing*: timing of impact evaluated by the onset of force at each plate.
- *force*: impact force between the rigid wall and body.
- *impulse*: impulse measured throughout impact to account for the total body impact.
- *compression*: full width thoracic compression measurements made for NHTSA sled test and half width compression measurements made for WSU sled test.
- *VC*: impulse measured throughout impact to account for the total.
- *injury*: predicted number of rib fractures.

5.3.1 NHTSA Side Sled Impacts

Figure 5.5 shows the human body model as impacted during a 6.67 m/s side sled impact, compared to a similar PMHS test. The simulated body is observed to deform in a similar fashion compared to the PMHS.

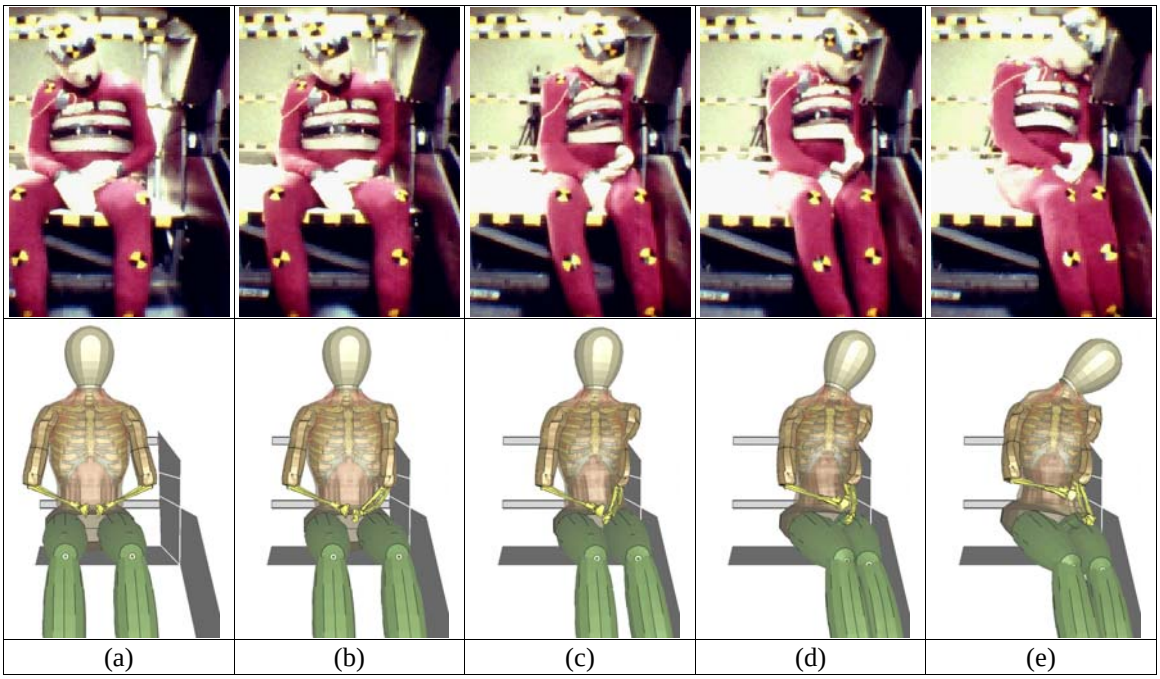

Figure 5.5 NHTSA sled impact experimental vs. simulation (a) t=0 sec (b) t=0.015 sec (c) t=0.030 sec (d) t=0.045 sec (e) t=0.060 sec

Since the model was subjected to a low-speed (6.67 m/s) and high-speed (8.89 m/s) impact, both require individual analysis. However, as both impact speeds produced similar trends in all measured responses, only the high-speed results are presented here. The low-speed graphs can be found in Appendix A, and a summary of the results from both impact speeds is presented here.

Timing of NHTSA Side Impacts

Since the human body presents varying levels of compliance within each body region, the timing of the impact at the various impact plates plays an important role in the measured force response. For the majority of the experimental NHTSA side sled PMHS impacts, the timing was consistent with the model predictions. Impact was initiated simultaneously at the thoracic and abdominal plates, followed by a similar simultaneous impact at the pelvic and leg plates approximately 0.005 seconds later. Observation of high-speed film showed that the slightly lateral positioning for the arm from the vertical constitutes the initial contact between the elbow and the abdominal and thoracic plates. Slight variations from test to test were observed depending on the extent to which the arm

was rotated. Figure 5.5(a) provides an example of a PMHS test where the arm was rotated causing initial impact between the elbow and the abdominal plate.

The simulation produced simultaneous initial impact at the thoracic and abdominal plate while the simultaneous impact at the pelvic and leg plates lagged by 0.01 seconds. The increased time between these impacts observed during the simulation as compared to the experimentation was due to the comparatively more lateral position of the arm. As described in the model development chapter, the arm was positioned in this way to avoid interpenetration of the arm tissue with the thoracic tissue.

It was also noted that during the experimental impacts, the head of the PMHS often rotated about the superior-inferior axis of the neck, which was due to the forward slouched positioning of the PMHS. This was observed to a lesser degree during the simulation, as the model was placed in an upright-seated position. Since the head model was a simplified representation, investigation of these effects could not be made, however it was believed to provide no influence on the response of the thorax. Integration of a detailed head and neck model with the thorax in future work may facilitate such an investigation.

Force Measurement of NHTSA Side Impacts

Experimentally, the force measured at each impact plate provided an indication of the relative stiffness of each body region and the distribution of mass within the body. The pelvic and thoracic plates produced the highest impact force due to the bony structures impacting these plates, while the abdominal and leg plates produced lower impact forces due to the compliant nature of the soft tissues impacting these plates. The experimental force response corridors highlight the variability of the human body as seen in Figure 5.6. In some cases the magnitude of the corridors was as high as 80% of the average value. However, the force as measured in total produced corridors widths less than 30% of the average value. This suggests that while the human body presents a high variability from subject to subject with respect to the body mass distributions, they still manage to produce comparable results when dealing with the total force response. As such, analysis

of the model has been completed at the individual plates (Figure 5.6) and using the total impact force (Figure 5.7).

The force results of the simulation at all impact plates can be seen in Figure 5.6 and the correlation summary can be found in Table 5.3. The thoracic and abdominal plate force responses show *good* correlation to the experimentation throughout the impact. This is an important result since the focus of this study was to predict thoracic responses. The thoracic plate appears to follow the average while the abdominal plate hovers just above the lower corridor. The abdominal plate also developed a fast initial impact peak followed by a sustained force response. The placement of the arm caused the first peak, which represented the initial impact of the elbow, while the sustained force represented the impact of the abdomen once the arm had been rotated into the torso.

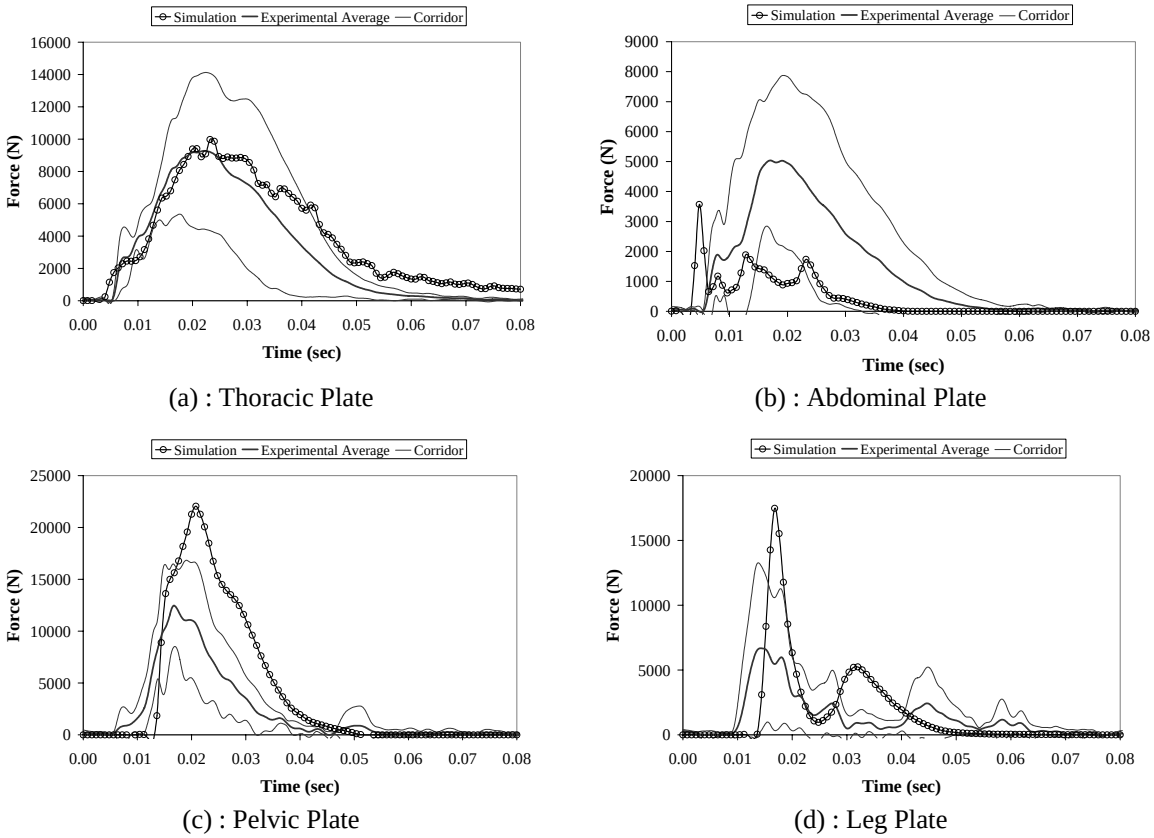

Figure 5.6 NHTSA side sled test high velocity impact force (a) thoracic plate (b) abdominal plate (c) pelvic plate (d) leg plate

The pelvic force response presented a similar shape as the experimentation, wherein the force increases and decreases sharply, capturing the reduced compliance inherent in this region. However, it was quite obvious that the maximum force generated *poor* correlation, falling outside the corridor by more than one corridor width. This was attributed to the simplifications made during pelvic model development. Recall, the pelvis was shaped as an ellipsoid based on the GEBOD model. When integrated with the abdomen, it was impossible to provide good transition between the regions without performing substantial remodeling of the abdominal area. As a result, the wider and stiffer pelvis absorbs the impact prior to the abdomen and a high resultant maximum force was produced. The relatively low force response of the abdominal plate confirms this.

The force response at the leg plate produced a *reasonable* to *poor* correlation throughout the impact, capturing the double peak that represented the initial impact of the left leg and the subsequent impact of the right leg into the left leg. The elevated response of the leg plate was believed to be due to the ellipsoid shape of the legs, which at initial impact concentrates the leg force at the ellipsoid apex. As impact continues, the leg soft tissue deforms spreading the impact along the length of the leg resulting in a sudden reduction of force. On top of that, the soft tissue of the leg was based solely on bovine muscle. While this provides a relatively good representation of the human leg, it was more than likely that many of the PMHS possessed varying levels of fat and skin along with the muscle. As these possess a lower stiffness, a lower force was measured.

The total force response of the impact as seen in Figure 5.7 showed *good* correlation during loading, *reasonable* correlation of the maximum force and *reasonable* correlation during unloading. The high response of the pelvic plate pushed the total response outside the experimental corridor.

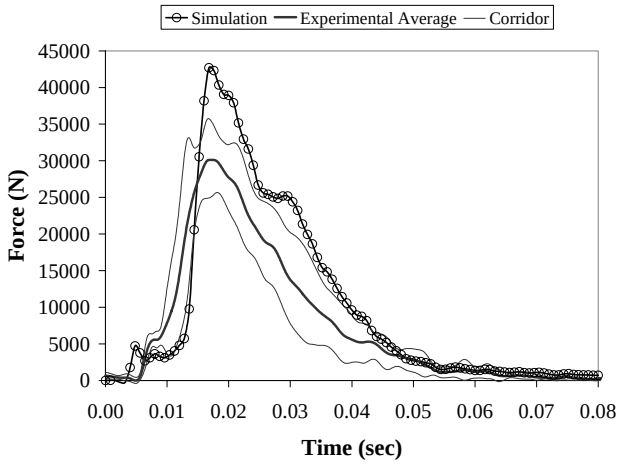

Figure 5.7 NHTSA side sled test high velocity total impact force

Table 5.3 NHTSA side sled simulated impact plate force correlation summary

Impact Plate	Impact Phase	Correlation	
		6.67 m/s	9.40 m/s
Thoracic	Loading	*good*	*good*
	Peak	*reasonable*	*good*
	Unloading	*good*	*good*
Abdominal	Loading	*good*	*good*
	Peak	*good*	*good*
	Unloading	*good*	*good*
Pelvic	Loading	*reasonable*	*reasonable*
	Peak	*poor*	*reasonable*
	Unloading	*poor*	*poor*
Leg	Loading	*poor*	*reasonable*
	Peak	*poor*	*poor*
	Unloading	*poor*	*reasonable*

Impulse Measurement in NHTSA Side Impacts

The impulse measured during the experimentation indicates how the force was distributed over the plates throughout the duration of the impact. Figure 5.8 indicates that

the greatest absorption of impact force occurred at the thoracic plate followed by the pelvic, abdominal and leg plates. Figure 5.9 shows the total experimental impulse.

The predicted impulse from the simulation is also shown in these figures. Similar to the force response, the impulse at the thoracic plate provides *good* correlation, the impulse at the abdominal plate provides *good* correlation, hovering just above the lower corridor, and the impulse at the pelvic plate provides *poor* correlation falling outside the corridor. Again, the lack of smooth transition between the abdomen and pelvis was believed to be the source of the elevated pelvic response and the low abdominal response. Unlike the force response at the leg plate, impulse measured here provided good correlation, supporting the belief that the geometric properties of the legs acts as the significant source of force discrepancy. In total, the model's impulse response provides *good* correlation during loading, but due to the elevated impulse measured at the pelvic plate was pushed outside the corridor producing only a *reasonable* correlation.

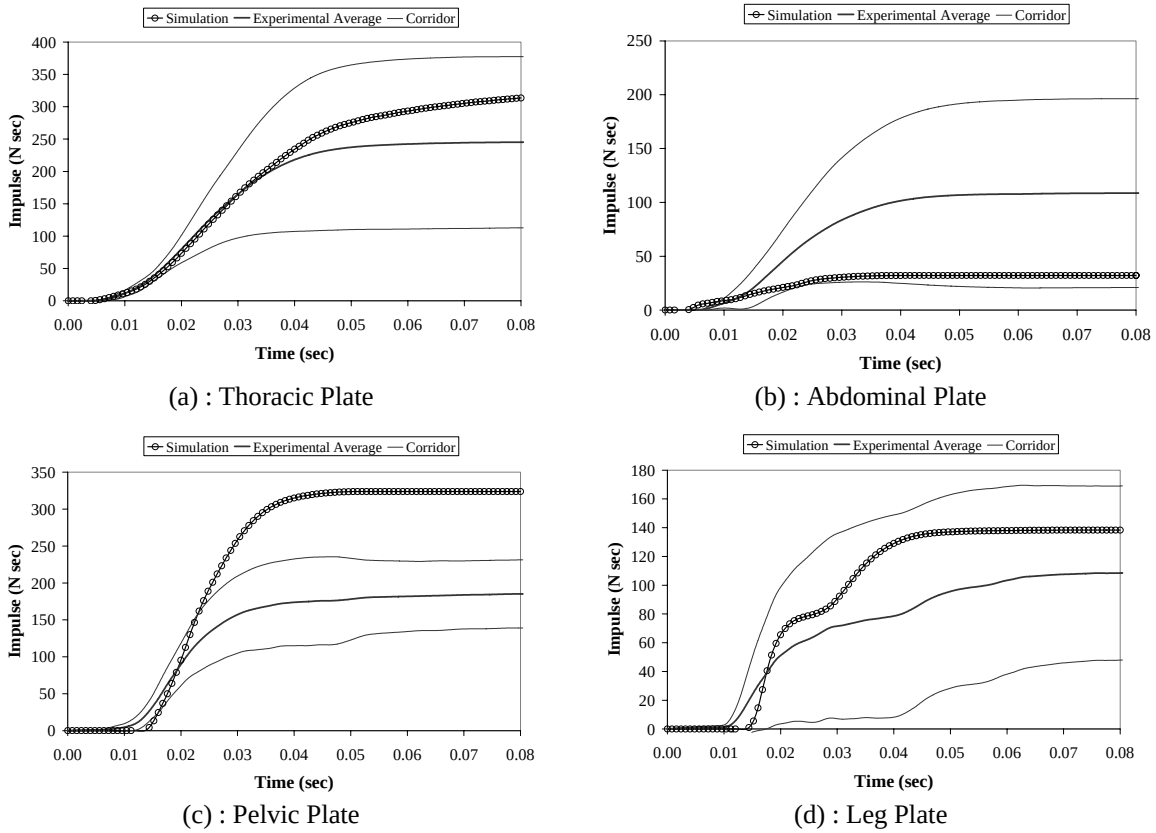

(a) : Thoracic Plate

(b) : Abdominal Plate

(c) : Pelvic Plate

(d) : Leg Plate

Figure 5.8 NHTSA high velocity sled test, impulse (a) thoracic plate (b) abdominal plate (c) pelvic plate (d) leg plate

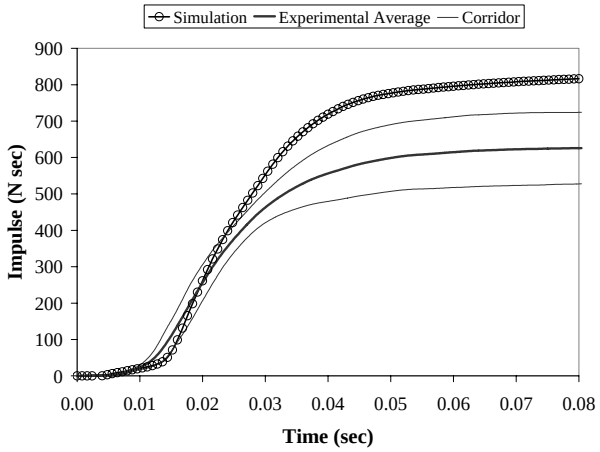

Figure 5.9 NHTSA high velocity sled test total impact impulse

Compression and VC Measurement in NHTSA Side Sled Impacts

The experimental compression response of the thorax depended on a number of factors. The most obvious one being thoracic cage stiffness, which can be affected by many factors such as age, weight, sex or quality of living for the individual test subjects. However analysis of the experimental chest band contours also showed that the position of the arm during impact had a significant effect on compression as it was directly involved in thoracic impact. It was found that when the arm was aligned with the coronal plane, the chest took on a cupped shape as the ribs deflected around the arm. Compression was aligned with this plane from the top of the thorax to the bottom of the thorax. As this directed the impact over a single plane, the level of compression was elevated. On the other hand, when the arm was angled slightly anterior, no longer being aligned with the coronal plane, the compression was distributed across a bigger lateral chest area producing a reduced level of compression. Add to that the fact that maximum compression then occurred forward from the coronal plane, the compression, which for this study was measured at the coronal plane, would produce a reduced maximum.

The effect of this was best highlighted by the comparison of chest band responses of the upper and middle band for two different experimental subjects, Test 3322 and Test 3325, as seen in Figure 5.10 and Figure 5.11 respectively (Pintar et al., 1997). These figures depict a cross-sectional view of the thoracic cage with the origin representing location of the spine. In the case of Test 3322 it was believed that the arm was aligned closer to the

coronal plane than as observed in Test 3325. As such the compression of Test 3322 was significantly greater than the compression of Test 3325 as measured at the coronal plane.

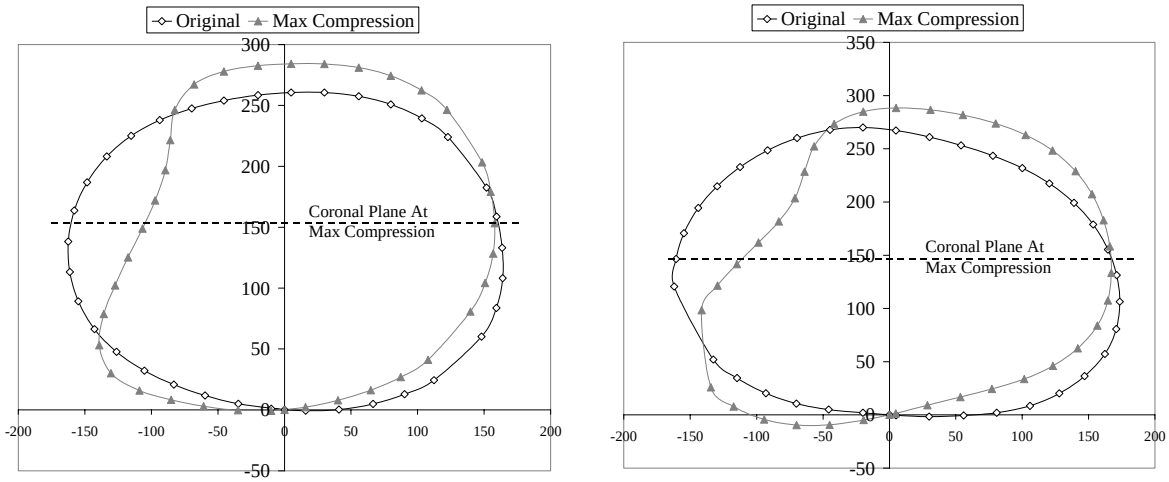

(a) : Test 3322 (b) : Test 3325

Figure 5.10 Experimental PMHS chest contours – top band (a) Test 3322 (b) Test 3325

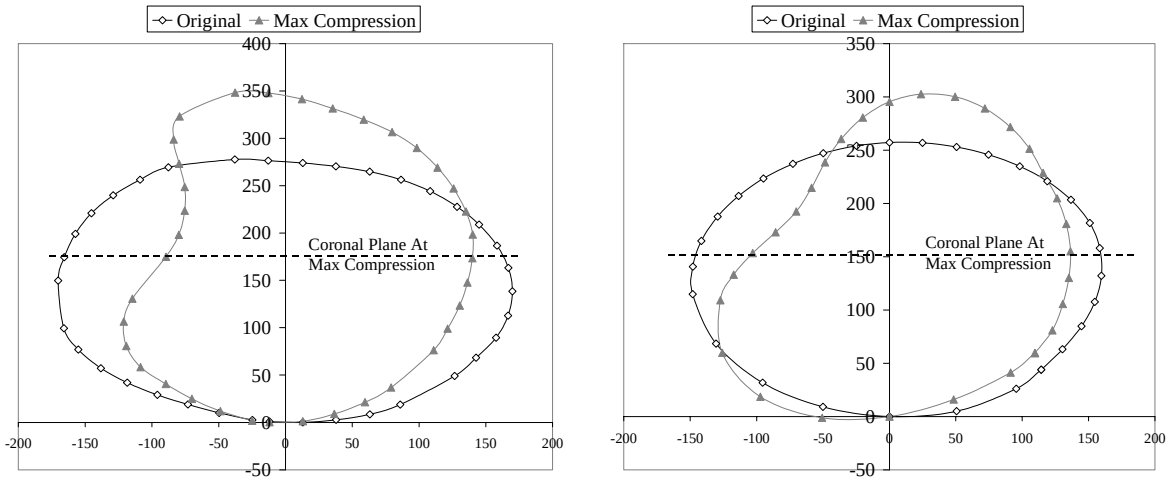

(a) : Test 3322 (b) : Test 3325

Figure 5.11 Experimental PMHS chest contours – middle band (a) Test 3322 (b) Test 3325

For the testing performed here, the arms have been aligned with the coronal plane to produce a more aggressive compression response and therefore a conservative estimate of injury. Figure 5.12(a) and (b) shows the compression response of the upper and middle band and Table 5.4 shows the correlation summary. Both show *good* to *reasonable* correlation throughout the impact, however produced an elevated peak response. This was believed to occur for two reasons. First, the conservative placement of the arm

concentrated the impact along the coronal plane and induced greater rib deformation. Second, the void spaces between the internal thoracic organs and the thoracic cage were believed to be a significant cause of the high compliance. It was observed that these spaces allowed the internal organs to move away from the point of compression, where normally they would provide a viscous resistance. As such, if these voids were filled, the compression response would be lowered, falling closer to the experimental average. While this went unobserved during the side pendulum impacts, it was believed that the more aggressive nature of this impact scenario initiated this mechanism of deformation leading to the increased compression compared to the experimental results.

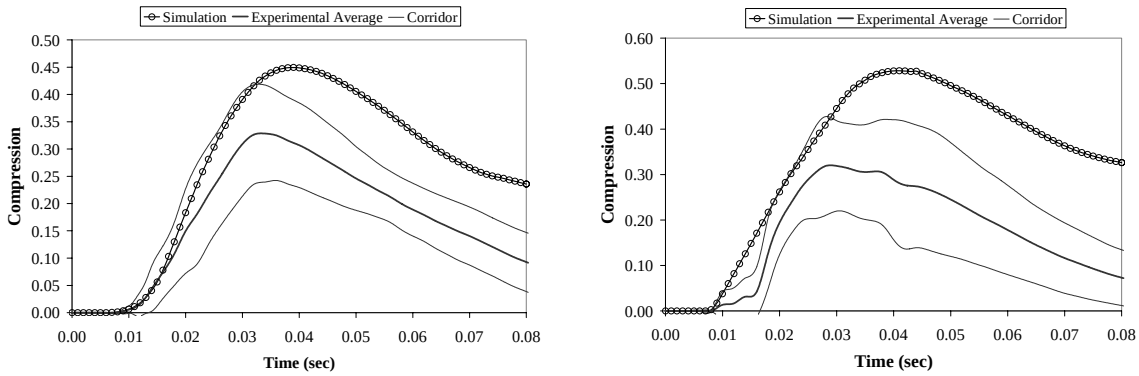

(a) (b)

Figure 5.12 NHTSA high velocity sled test compression response (a) upper band (b) middle band

Table 5.4 NHTSA side sled simulated impact chest compression correlation summary

Chest Band	Impact Phase	Correlation	
		6.67 m/s	9.40 m/s
Upper Band	Loading	*good*	*good*
	Peak	*good*	*reasonable*
	Unloading	*reasonable*	*reasonable*
Middle Band	Loading	*reasonable*	*good*
	Peak	*poor*	*reasonable*
	Unloading	*reasonable*	*reasonable*
Lower Band	Loading	*good*	*N/A*
	Peak	*reasonable*	*N/A*
	Unloading	*reasonable*	*N/A*

It should also be noted that while the high-speed experimental impacts recorded only the compression at two levels, upper and middle band, the low-speed impact recorded the compression at three levels, upper, middle and lower band. Measurement of compression at the lower band primarily involves deformation of the abdomen. The *good* to *reasonable* correlation of the compression at this level therefore confirms the applicability of the simplified abdominal model in side impact.

The experimental VC response at each of the chest bands can be seen in Figure 5.13(a) and (b). The response appears to be highly erratic presenting several peaks, which was more evident when individual subject responses were analyzed. The fact that the compression produced a smooth response while the VC remained variable, suggested a highly variable rate of deformation, characterizing the complex nature of this impact. Unfortunately this produces a very sensitive impact response, but is often overlooked as most researchers present only the max VC (Pintar et al., 1997, Kuppa et al., 2001, Kuppa et al., 2003). For completeness the entire response has been reported here.

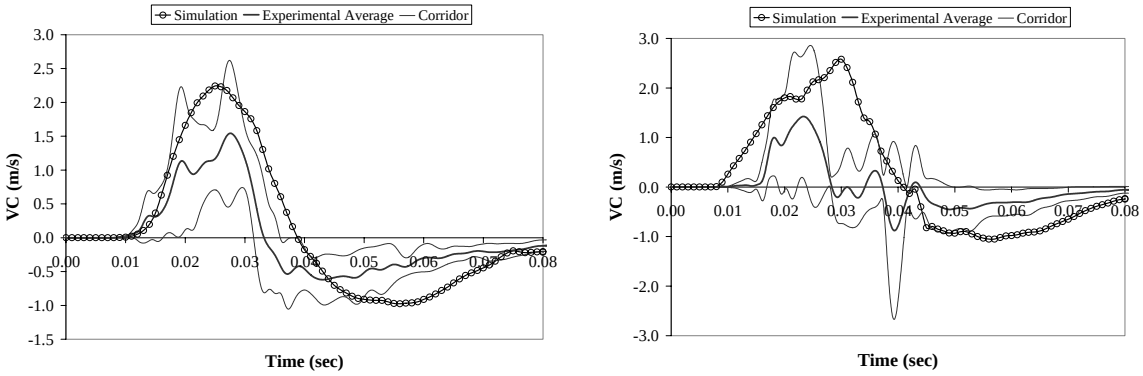

Figure 5.13 NHTSA high velocity sled test VC response (a) upper band (b) lower band

The response of the simulation can be seen to present *good* correlation throughout the impact at the top band and *reasonable* correlation at the middle band. Multiple VC peaks were observed at the middle band, similar to the experimental results. These results also show that even with an elevated level of compression, the model was able to accurately model the rate of deformation and subsequent $[VC]_{max}$. The high compression however, generated an extended VC response dropping to zero much later in the impact.

Injury in NHTSA Side Sled Impacts

Measurement of the injury response for the experimental testing primarily involved rib fractures throughout the thoracic cage. Internal organ damage was also reported however since this was not the focus of this study, comparison of the model response has not been performed here. Future research will consider injuries of this type.

The injury response of both the low and high velocity impacts in terms of rib fractures as compared to each PMHS test can be found in Table 5.5. Experimentally, the number of rib fractures was highly variable. In fact, one PMHS endured no injury of any kind when subjected to the low speed impact, while another endured 15 rib fractures. Pintar et al. (1991) primarily attributed this to age, where the younger subjects were able to sustain the impacts with less injury. The elevated number of rib fractures observed during the simulations at both impact speeds, confirmed the observations made during the frontal pendulum impacts that the fracture strength of the ribs were more representative of an older subject. However, it was also believed that the high levels of compression also caused the elevated number of fractures. Again, this occurred as a result of the aggressive placement of the arm within the model and the voids spaces within the thoracic cage.

Table 5.5 NHTSA side sled impact injury summary (rib fractures)

Low Velocity Impact (6.67 m/s)		
PMHS Test	Experimental	Simulation
3120	16	25
3122	0	
3155	11	
Average	~9	
High Velocity Impact (8.89 m/s)		
PMHS Test	Experimental	Simulation
3322	12	34
3324	34	
3325	16	
3422	4	
3579	21	
Average	~17	

The locations of the rib fractures could only be obtained for the low speed experimental NHTSA side sled impact tests. Fractures occurred primarily on the impacted side (left) of the thorax between the 2nd and 8th ribs with one to three fractures on each rib. A similar fracture pattern was observed during the simulation with one to three fractures occurring on each of the 2nd to 8th ribs; however two to three fractures were also observed on the 9th, 10th and 11th ribs as seen in Table 5.6. These constitute the extra rib fractures observed in the simulation, which was believed to be due to the aggressive placement of the arm. The elevated chest compression response observed in this area (middle and lower band) confirms this. The same fracture pattern was observed during the high-speed simulation with an increased number of rib fractures.

Table 5.6 NHTSA side sled low speed impact rib fracture locations

Rib	Test 3120		Test 3155		Model	
	Left	Right	Left	Right	Left	Right
1st					1	
2nd	2		2			
3rd	3		2		2	
4th	3	1	2		3	
5th	3		2		2	
6th	2		1		2	
7th	2		1		3	
8th			1		3	
9th					3	2
10th					2	
11th					2	
Total	16		11		25	

5.3.2 WSU Side Sled Impacts

Analysis of the simulated WSU side sled impacts followed a similar method as used during the analysis of the simulated NHTSA side sled impacts. However, as noted previously, less emphasis was placed on the chest compression response of the model and more emphasis was placed on the shoulder response and pelvic compression response of

the model. Figure 5.14 shows the human body model as impacted during the 6.67 m/s WSU side sled test. Unlike the simulated NHTSA sled test, the shoulder can be seen to engage the impact wall, contributing to the deflection experienced during this impact.

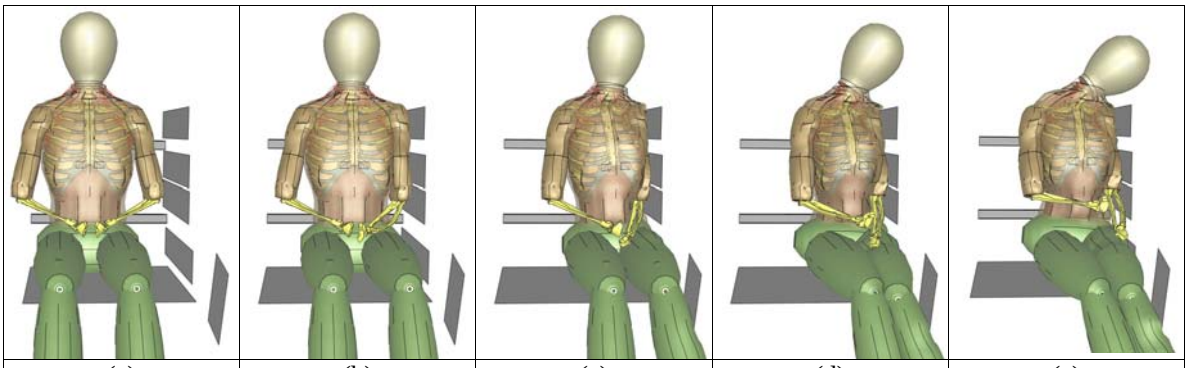

(a) (b) (c) (d) (e)

Figure 5.14 WSU side sled impact simulation (a) t=0 sec (b) t=0.015 sec (c) t=0.030 sec (d) t=0.045 sec (e) t=0.060 sec

Similar to the NHTSA sled tests, the WSU sled tests were performed at the same two impact velocities. Again, similar trends during both impact speeds were observed and only one impact speed has been detailed here. However, where the NHTSA sled impact analysis was performed on the high velocity tests, the analysis here was performed on the low velocity tests. This was chosen as the experimental results from the low velocity tests provided three PMHS, while the high velocity test provided only two PMHS. It should also be noted that the knee plate was eliminated from the analysis due to large experimental variation. Because the plate was relatively small, the point of impact on the body depended heavily on the anthropometric leg measurements of each PMHS. Since little to no data could be found to determine the point of impact for each PMHS, this can neither be confirmed nor denied. Nonetheless, the erratic responses of the knee plate experimental force results support this belief.

Timing of WSU Side Sled Impacts

The timing of impact of the experimental WSU side sled tests closely matches that of the NHTSA side sled tests. Contact was initiated simultaneously at the thoracic and shoulder plates, followed by contact at the abdominal plate approximately 0.005 seconds later and finished with contact at the pelvic plate approximately 0.01 seconds after initial impact.

Similar to the NHTSA tests, it was believed that the timing of impact was affected by the positioning of the arm. The results suggest that the arms were placed closer to the body, than as observed during the NHTSA sled tests and the simulated impacts, thereby producing initial contact at the shoulder and thoracic plates as opposed to the abdominal plate.

To analyze the simulation timing, the impact force as measured at the thoracic plate was synchronized with the experimentation. During the simulation contact was initiated at the thoracic and abdominal plates, followed by contact at the shoulder plate approximately 0.005 seconds later and finished with contact at the pelvic plate 0.01 seconds after initial impact. The slight difference between the simulation and experimental results was attributed to the more lateral position of the arm. This produced earlier onset of force at the abdominal plate, and a delayed onset of force at the shoulder plate. The delay at the pelvic plate as compared to the experimental average could not be explained as the experimentation presents inconsistent results from test to test.

Force Measurement of WSU Side Sled Impacts

Experimentally, the force response of the WSU sled tests highlights the relative stiffness of each body region and the distribution of mass within the body as seen in Figure 5.15. The force at the pelvis produced the highest impact force, followed by the shoulder, abdominal and thoracic plate. The shoulder and thoracic plate of the WSU impacts are often deemed equivalent to the thoracic plate of the NHTSA impacts, which was why the thoracic plate response was below both that of the shoulder and abdominal impact plates (Maltese et al., 2002).

The force response of the simulation at all impact plates can be seen in Figure 5.15 and the correlation summary can be found in Table 5.7. The shoulder, thoracic and abdominal plate responses show *good* correlation throughout the impact. The shoulder plate was observed to present a greater peak during the simulation, which was believed to be due to the lack of injury within the shoulder model. During the experimentation almost all subjects showed injury of the shoulder in the form of either acromion fracture

or acromioclavicular separation. When this occurred, the shoulder lacked the ability to provide additional resistance to impact and force plateaus.

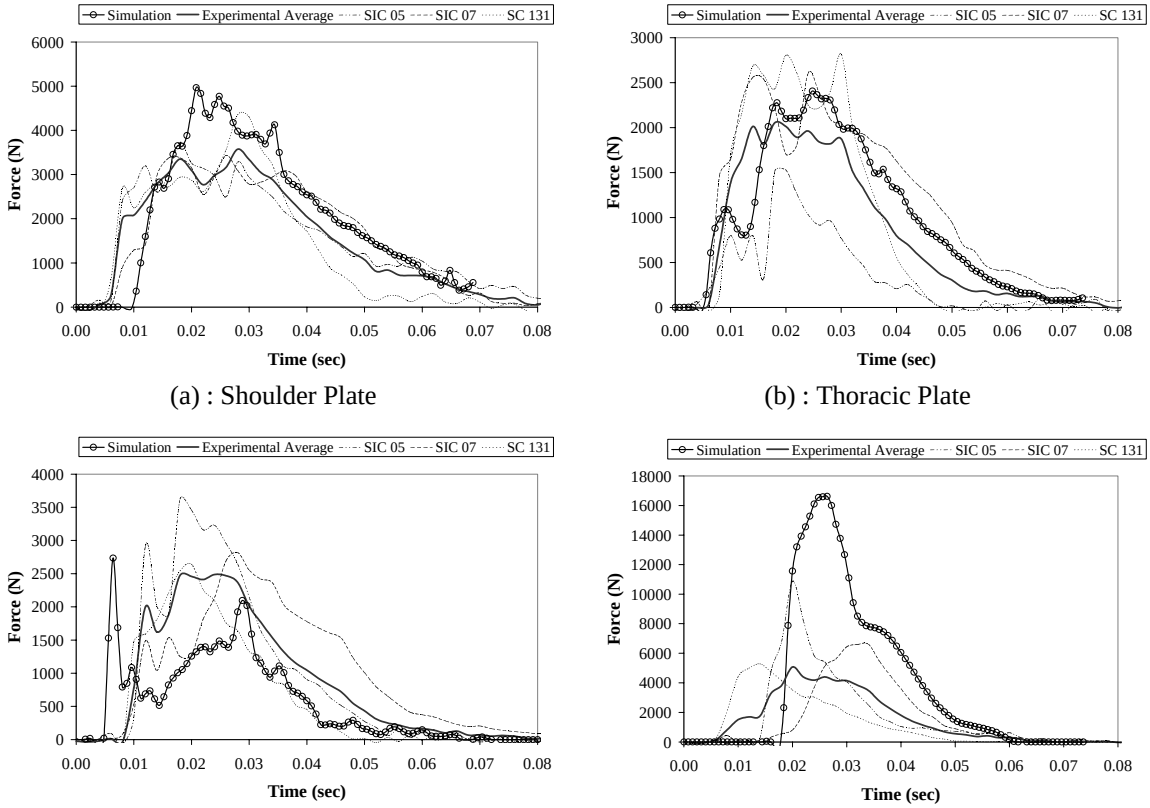

Figure 5.15 WSU side sled low velocity impact force (a) shoulder plate (b) thoracic plate (c) abdominal plate (d) pelvic plate

Both the simulated thoracic and abdominal plates showed an initial force peak, followed by a sustained force response. These represent the initial impact of the arm and subsequent impact of the torso as the arm was rotated against the body. Recall, the timing analysis suggested that the arm placement of the model was more lateral than the arm placement of the PMHS.

Once again the pelvic response provides *poor* correlation with a response similar to that observed during the NHTSA tests. However, comparison to a single PMHS (SIC05) showed a similar shape, wherein a sharp increase and subsequent decrease of force was observed.

Table 5.7 WSU sled test impact plate force correlation summary

Impact Plate	Impact Phase	Correlation	
		6.67 m/s	9.40 m/s
Thoracic	Loading	*good*	*good*
	Peak	*reasonable*	*good*
	Unloading	*good*	*good*
Abdominal	Loading	*good*	*good*
	Peak	*good*	*good*
	Unloading	*good*	*good*
Pelvic	Loading	*reasonable*	*reasonable*
	Peak	*poor*	*reasonable*
	Unloading	*poor*	*poor*
Leg	Loading	*poor*	*reasonable*
	Peak	*poor*	*poor*
	Unloading	*poor*	*reasonable*

Impulse Measurement in WSU Side Sled Impacts

The impulse indicated how the force was distributed across the plates throughout the impact and can be seen in Figure 5.16. Experimentally, the impulse showed the greatest absorption of impact was at the pelvic plate followed by the shoulder, abdominal and thoracic plates. The low impulse as measured at the thoracic plate, when compared to the NHTSA tests, was indicative of the influence of the shoulder plate during these impacts.

The predicted impulse from the simulation, as observed in the same figure, generally shows *good* correlation of the shoulder, thoracic and abdominal plates, while the pelvic plate falls well outside the corridor with more than double the impulse. Again this was attributed to the simplified pelvic model used here as noted during the NHTSA side sled tests.

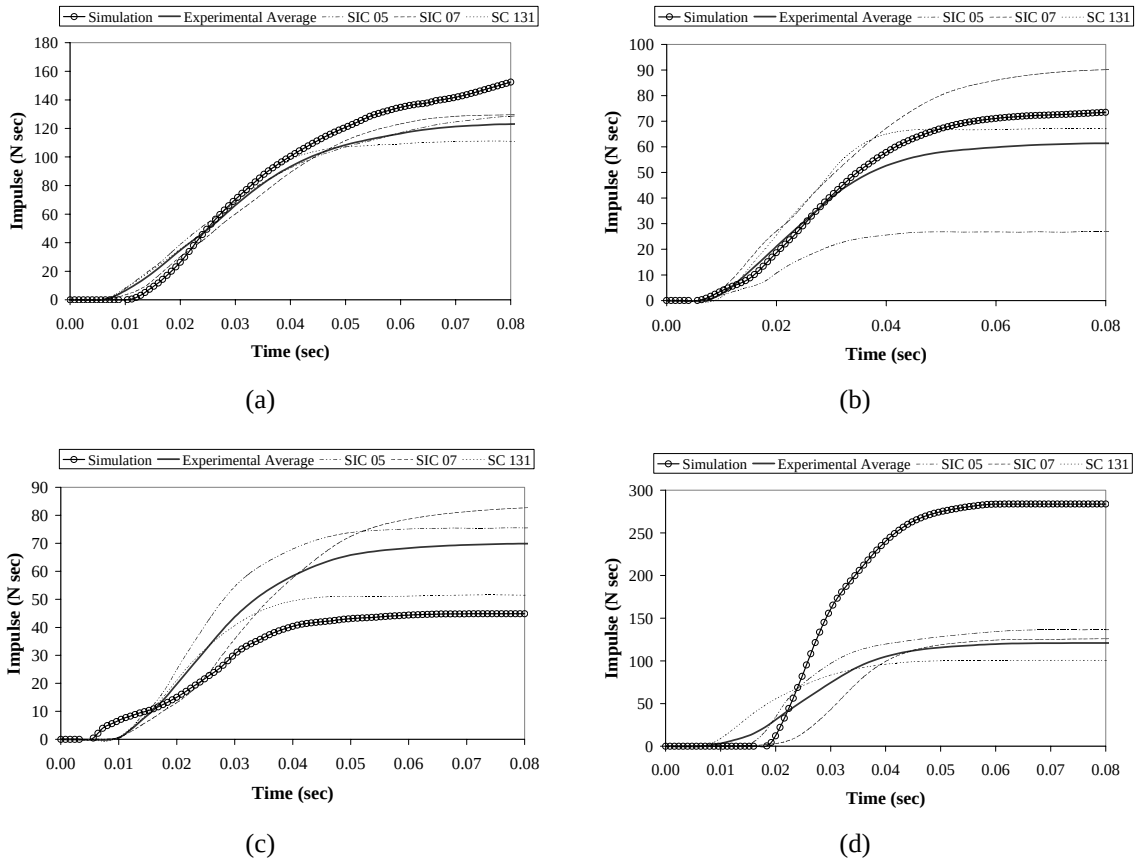

Figure 5.16 WSU low velocity impact impulse (a) shoulder plate (b) thoracic plate (c) abdominal plate (d) pelvic plate

Compression and VC Measurement in WSU Side Sled Impacts

As previously mentioned, compression was measured during experimentation by tracking targets located on the sternum at the level of the T5 vertebrae. Measuring the distance between the impact wall and the sternal target represented half thoracic compression. This measurement however lacked the local deformation response of the rib cage due to the intrusion of the upper arm. As a result, comparison of the model to these experimental measures and any analysis derived from it provides only limited information.

The compression response of this model was however able to elucidate the differences between the simulated WSU sled test and the simulated NHTSA sled test, wherein the

NHTSA sled tests produced higher levels of compression at the height of all three chest bands during all impact speeds. This was attributed to two effects. First, the interaction of the shoulder plate spreads the impact across a larger area for a more distributed compression load during the WSU side sled impacts. Second, the lack of a shoulder plate during the NHTSA sled tests produced a cantilevered effect on the humerus, wherein the momentum of the shoulder carried the humeral head past the impact plates, rotating the lower humerus into the thoracic cage resulting in a subsequent increase in compression. The same phenomenon was observed in the experimental high-speed film, which occasional resulted in fracture of the upper humerus.

Pelvic compression was experimentally measured by tracking the distance between a target fixed to the sacral vertebrae, and the impact wall. The experimental curve was characterized by a compression plateau, indicative of pelvic fractures often found throughout these impacts. The simulation response presented good correlation throughout the loading and at peak compression, however lacked the unloading plateau response of the pelvis as seen in Figure 5.17. As noted during the pendulum impact tests, the lack of injury representation prevents the pelvis from producing the plateau response, quickly returning to its initial form.

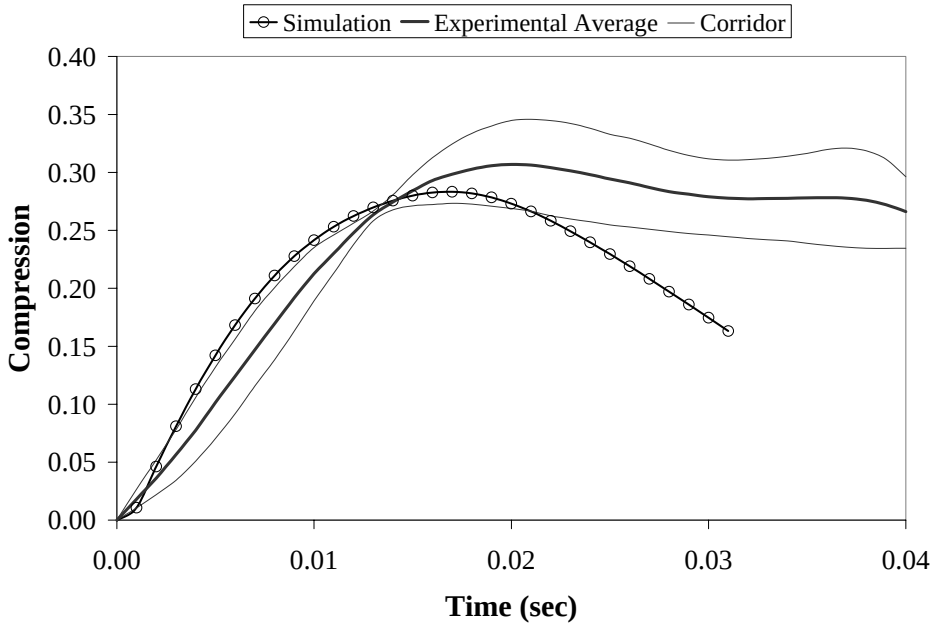

Figure 5.17 WSU low velocity pelvic compression response

Injury in WSU Side Sled Impacts

Experimentally, the average number of rib fractures during these tests was slightly elevated as compared to the NHTSA sled tests. However, due to the low number of subjects during the WSU tests, no statistical evidence could be found to support any trend suggesting a difference between the two tests as observed by rib fractures. Similar to the NHTSA experiments however, the subject age played an important role, where the younger subjects exhibited fewer rib fractures than the older subjects.

The injury response of both the low and high velocity simulated impacts as compared to each PMHS test can be found in Table 5.8. These simulations show an elevated number of rib fractures as compared to the experimental results. However this cannot be attributed to a high level of compression since the experimental results did not provide the detailed compression data required for such an analysis. Alternatively, since the high levels of compression were proven to cause the elevated rib fracture in the NHTSA sled tests, one can say that the elevated number of rib fractures observed here indicated the existence of high levels of compression. The slightly reduced number of rib fractures observed in these simulations, as compared to the NHTSA simulations, corresponds to the reduced level of compression also observed.

Table 5.8 WSU side sled impact injury summary

Low Velocity Impact (6.67 m/s)		
PMHS Test	Experimental	Simulation
5	20	25
7	16	
4933	8	
Average	~15	
High Velocity Impact (8.89 m/s)		
PMHS Test	Experimental	Simulation
4	22	33
6	15	
Average	~19	

The locations of the rib fracture were obtained for all WSU experimental side sled impact tests and Table 5.9 outlines the fractures sustained during the low speed impacts. During the experimental low speed impacts, rib fractures occurred on both sides of the thorax, but focused primarily on the impacted side (left) between the 1st and 11th ribs with one to two fractures on each rib. The simulation produced a similar distribution of fractures between the ribs, with an increased number of fractures between the 7th and 8th ribs. Again, this was most likely due to the aggressive placement of the arm. The same phenomenon was observed during the high-speed impacts and the details of rib fracture location can be found in Appendix A.

Table 5.9 WSU side sled low speed impact rib fracture locations

Ribs	Test 5		Test 7		Test 4933		Model	
	Left	Right	Left	Right	Left	Right	Left	Right
1st	2	2	1	1			2	1
2nd	2	1	2	1			3	1
3rd	2	1	2				1	
4th	2	1	2		2		4	
5th	2	1	2	1			3	
6th	2	1	2		1		2	
7th		1	2		1		2	
8th					1		2	
9th					1		2	
10th							2	
11th					1			
Total	20		16		8		25	

Shoulder Response in WSU Side Sled Impacts

The injury response of the shoulder recorded during the experiments provided insight into the shoulder response and the use of a non-injurious shoulder model. Almost every experimental test case reported the fracture of either the acromion or clavicle, while the model was unable to report fracture of this kind. As a result, the model was observed to generate excessive element deletion (predicted fracture) of the first rib. This was the

same phenomenon observed during the pendulum shoulder impact tests where the clavicle was rotate posteriorly and medially, inducing an anterior force on the sternum. This in turn caused excessive bending of the first rib and culminated in fracture. The impact speeds experienced during these tests were much greater and the amount of fracture was far worse, occurring at two locations; at the to the vertebral attachment site and in the middle of the rib. While this injury was reported during almost all the PMHS impacts, it was believed that the influence of the non-injurious shoulder model induced the excessive fracture.

In an attempt to understand the shoulder interaction with the thoracic cage during the experimental WSU impacts, Irwin et al. (1993) studied the PMHS scapular rotation. It was hypothesized that the motion of the shoulder was attributable to differences found in the structural integrity of the thorax. During impact, the ribs either bulge posteriorly and anteriorly, or fracture resulting in flail chest, causing a section of the ribs to move into the thoracic cage. Figure 5.18 outlines these differing responses, where Irwin et al. (1993) found that the bulge experienced with no flail chest caused the scapula to wing outwards.

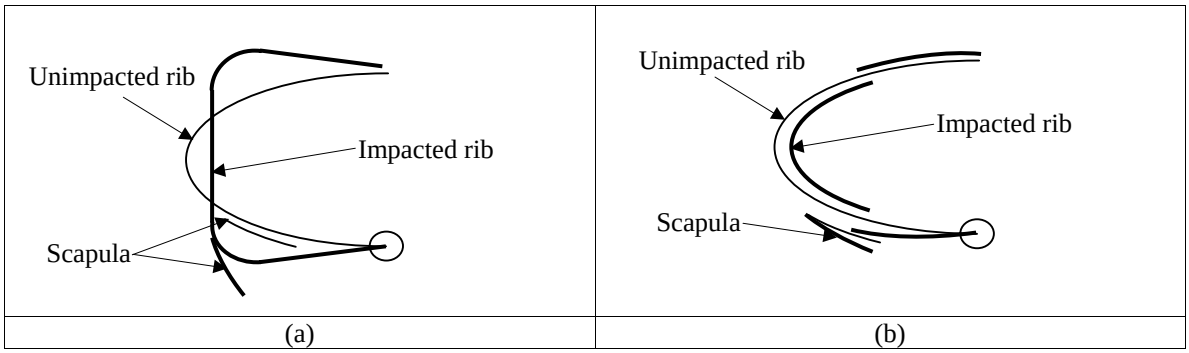

Figure 5.18 Cross-section of chest outlining the different responses of the thoracic cage and scapula during WSU side sled impacts (a) bulging (b) flail chest

During the simulated WSU side sled impacts a similar phenomenon was observed. This was believed to be due to the single point integration scheme used to model the ribs. Recall, the rib material was developed to provide fractures by deleting elements once the yield stress was surpassed. However, since the ribs have only single point integration, full through fracture was not possible and the rib remained intact throughout the impact. This was observed during the high speed impacts where some ribs were held together by

only one or two elements. While this has been shown to provide good prediction of rib fracture, it lacks the ability to model flail chest injuries and causes caused the shoulder to produce excessive outward rotation.

5.4 Side Sled Test Summary Discussion

The NHTSA and WSU side sled test simulation results as discussed above, were intended to evaluate biofidelity of the numerical model to simulate complex impact scenarios such as side sled tests using globally measured parameters, injury criteria and specific injury when compared to PMHS tests. With the addition of the components as developed in this study the model produced results for the most part with *good* or *reasonable* correlation for all impacts. In particular, the response of the thorax to side impact was characterized as *good* in all cases.

The NHTSA side sled tests provided significant information regarding the impact and subsequent deformation response of the model. Force as measured at the thoracic and abdominal impact plates provided *good* correlation, while the force at the pelvic plate provided *poor* correlation. The lack of transitional smoothness between the abdomen and pelvis forced the pelvis experience higher impact forces. While elevated, it was believed that the force response of the pelvis did not adversely affect the response of the thorax. The impulse response reflected similar results also highlighting that the geometric simplifications made to model the legs did not adversely affect the long-term force response of the model.

The high levels of compression and elevated number of rib fractures in the model highlighted the effect of the voids throughout the thoracic cage as being a major problem. Attempts were made to compensate for these voids by using an elevated costal cartilage stiffness. While this provided *good* correlation during side pendulum impacts, it took the rigorous and more concentrated impacts as observed during sled tests to show that such an approximation does not accurately represent the realistic viscous response of the thoracic organs. However, the high levels of compression within the thorax were

primarily attributed to the aggressive placement of the arm, which was aligned with the coronal plane, causing maximum deflection to occur at the measurement location.

The WSU side sled tests also provided significant information regarding the impact and subsequent deformation response of the model, furthermore highlighting responses unobserved during the NHTSA sled tests. Force and impulse measured at all plates, except the pelvic provided *good* correlation to the experimentation. While the compression response of the thorax provided *good* correlation, it could not be evaluated extensively due to the type of measurements made throughout the experimentation. However, the models showed that the NHTSA sled tests generally produced a higher level of compression when compared to the WSU sled tests. This could be used to infer that the NHTSA sled tests provide a more aggressive impact scenario, which may be better for evaluation of side impact dummies. The compression response of the pelvis provided *good* correlation however lacked the injury response and subsequent unloading response of the PMHS testing. The shoulder response of the model showed the effect of using a non-injurious shoulder model and the effect of using a single point integration scheme to produce rib fractures.

-- CHAPTER 6 --

Conclusions and Recommendations

6.1 Conclusions

The purpose of this study was to develop a model to predict thoracic response and injury in side impact auto crash scenarios, with the ultimate goal of using this model in vehicle crash simulations to predict injury. A previously developed detailed thoracic model was used, which showed good correlation to simple experimental pendulum impact results but included a number of simplifications that did not make it applicable to general side impact scenarios. As such, a full human body numerical model was constructed utilizing the existing detailed thoracic model that was improved and integrated with a simplified head, abdomen, pelvis and legs.

The project began with the goal of simply adding to the detailed thorax the following four major body components: a head, an abdomen, a pelvis and legs. However, as the research progressed deficiencies within the original thoracic model were observed resulting in the substantial enhancement of the following thoracic components: surface muscle tissue, shoulder muscles, shoulder ligaments and costal cartilage.

The development of the abdomen and pelvis involved the use of PMHS pendulum impact testing to define and calibrate the force-deflection response for the simplified representations in these regions. The legs were implemented with basic deformation characteristics as preliminary analysis showed the use of rigid components resulted in severe shearing of the lumbar spine during impact. The head was implemented as a rigid body simply to provide the inertial and dynamic effects during impact. The present model was not capable of predicting head injury, however plans to integrate the body and thorax from this study with a detailed head and neck model are underway. The improvement of existing surface muscle tissue, both in material and mesh properties, allowed for the representation of strain-rate and hyperelastic effects, which were considered important during dynamic impacts, reducing the extreme straining observed in the original model. The improvements to the shoulder muscles and ligaments produced an improved dynamic response during impacts.

The model was validated using pendulum impact tests to isolate and assess the biofidelity of the detailed thoracic model with the added and improved components. Simulated frontal and side thoracic pendulum impact tests, and side shoulder pendulum impact tests were performed on the model and validation was made against PMHS testing. The validation assessment was achieved by adopting a technique used by ISO where the terms *good*, *reasonable* and *poor* provided a qualitative definition of the model response. The *reasonable* compression response of the frontal thoracic pendulum tests, combined with the *good* compression response of the side thoracic pendulum tests, led to the understanding that while the abdomen had been calibrated for side impact scenarios, its lack of frontal impact calibration produced slightly adverse effects. However, the intention of this study was to develop the model with accurate side impact thoracic response and the development of the frontal impact thoracic response constitutes a long-term goal to be addressed in future studies. The side shoulder pendulum impact tests highlighted the need for a more detailed shoulder model to represent damage and failure for injurious shoulder impacts. With the current model high forces and low deflections were measured along with an adverse expansion of the thoracic cage resulting in non-realistic fracture of the first rib.

Simulation of the numerical model during NHTSA and WSU side sled impact tests facilitated the validation and biofidelity assessment of the full body model during tests that involved the complex interaction of full body impacts. The thoracic response during both impacts scenarios produced excellent response characteristics at both impact speeds as compared to the PMHS tests, with *good* correlation of the force response and *reasonable* correlation of the compression response. Arm placement during these tests was found to play an important role on the thoracic compression response, and in the cases presented here, the arms were placed in the most aggressive location possible. This in turn produced an elevated level of compression and an elevated number of rib fractures as compared to the experimental average. However, the elevated compression was also affected by the voids found between the internal thoracic organs and the thoracic cage. Upon impact, the organs were able to move away from the point of compression with little to no resistance. While an attempt was made to compensate for this effect by providing an elevated stiffness of the costal cartilage, it lacked the realistic response of the thoracic cage.

Most importantly these simulations highlighted potential areas of improvement for both the simplified components and the detailed thoracic model, which have been detailed in the following section.

6.2 Recommendations

The current development of the detailed human body model presented here could be used to numerically analyze safety features during automotive side impact scenarios as it provides very good prediction of thoracic response and injury. Interaction with a fully modeled automobile, or a passenger compartment could be implemented. However, in doing so, four aspects should be considered. First, arm positioning will play an important role on the thoracic compression response. For a conservative estimate, it is recommended that the arms be placed in the same position as described throughout this study.

Second, high levels of compression may also be caused by the voids within the thoracic cavity. It its recommended that these voids be filled such that the compensatory costal cartilage stiffness and elevated thoracic tissue density can be eliminated. This should also produce a more realistic response during future simulated impact scenarios.

Third, the geometric differences observed between the abdomen and pelvis may produce an elevated force response at the height of the pelvis and a reduced force response at the height of the abdomen. However, it was shown that such a response does not adversely affect the response of the thorax during this type of impact. For completeness though, it may be beneficial to remodel the abdomen and pelvic region in more detail to provide a smoother transition between the abdomen and pelvis.

Fourth, the use of a non-injurious shoulder model during injurious shoulder impacts may cause the first rib to fracture unrealistically. It is therefore recommended that a more accurate shoulder model be developed as it has been shown that the shoulder injury response can affect the thoracic response. This may simply require the implementation of a new material model for the bony shoulder components, or the replacement of the spherical joints with a more accurate representation of the complex ligaments within this region.

The use of this model in frontal impact scenarios requires further development. The frontal pendulum impact scenario showed that while the model produces a good force response, interaction with the abdomen inhibits appropriate compression correlation. It may be beneficial to model the individual organs within this region, providing a more realistic interaction during impact. However, it is possible that by filling the void spaces within the thorax and appointing more appropriate material properties for the costal cartilage and thoracic tissue, the response of the thorax during frontal pendulum impacts may in fact provide an accurate response with the current abdomen.

References

Abbreviated Injury Scale (AIS), 1990 Revision, American Association for Automotive Medicine, Morton Grove, Illinois

Abe, H., Hayashi, K., Sato, M., 1996, Data Book on Mechanical Properties of Living Cells, Tissues, and Organs, Springer-Verlag, Tokyo

Andriacchi, T., Schultz, A., Belytschko, T., Galante, J., 1974, A Model for Studies of Mechanical Interaction Between the Human Spine and Ribcage, Journal of Biomechanics, Vol. 7, pp. 497-507

Augenstein, J. Bowen, J., Perdeck, E., Singer, M., Stratton, J., Horton, T., Rao, Al, Digges, K., Maliaris, A., Steps, J., 200, Injury Patterns in Near-Side Collisions, SAE Paper No. 2000-01-0634, SAE 200 World Congress, Society of Automotive Engineers

Baker, S.P., O'Neill, B., Naddon, W., Long, W.B., 1974, The Injury Severity Score: A Method for Describing Patients with Multiple Injuries an Evaluating Emergency Care, Journal of Trauma, Vol. 14, pp. 187-196

Bir, C.A., Viano, D.C., 1999, Biomechanical Prdictor of Commotion Cordis in High-Speed Chest Impact, Journal of Trauma: Injury, Infection and Critical Care, Vol. 47, No. 3, pp.468-473

Blincoe, L., Seay, A., Zaloshnja, E., Miller, T., Romano, E., Luchter, S., Spicer, R., 2000, The Economic Impact of Motor Vehicle Crashes, 2000, U.S. Department of Transportation National Highway Traffic Safety Administration, DOT HS 809 446

Cavanaugh, J.M., Walilko, T.J., Malhotra, A., Zhu, Y., King, A.I., 1990, Biomechanical Response and Injury Tolerance of the Pelvis in Twelve Sled Side Impacts, Proceedings of the 34th Stapp Car Crash Conference, 902305

Cavanaugh, J.M., Walilko, T.J., Malhotra, A., Zhu, Y., King, A.I., 1990, Biomechanical Response and Injury Tolerance of the Thorax in Twelve Sled Side Impacts, Proceedings of the 34th Stapp Car Crash Conference, 902307

Cavanaugh, J.M., Zhu, Y., Huang, Y., King, A.I., 1993, Injury and Response of the Thorax in Side Impact Cadaveric Tests, Proceedings of the 37th Stapp Car Crash Conference, 933127

Cavanaugh, J.M., Walilko, T., Walbridge, A., Huang, Y., King, A.I., 1994, An Evaluation of TTI and ASA in SID Side Impact Sled Tests, Proceedings of the 38th Stapp Car Crash Conference, 942225

Chapon, A., 1984, Thorax and Upper Abdomen: Anatomy, Injuries and Possible Mechanisms of Injury, The Biomechanics of Impact Trauma, Elsevier Science Publishers, Amsterdam

Cheng, H., Obergefell, L., Rizer, A., 1994, "Generator of Body (GEBOD) Manual." Wright-Patterson Air Force Base, Ohio, AL/CF-TR-1994-0051

Compigne, S., Caire, Y, Quesnel, T., Verries, J.P., 2004, Non-Injurious and Injurious Impact Response of the Human Shoulder Three-Dimensional Analysis of Kinematics and Determination of Injury Threshold, Proceedings of the 48th Stapp Car Crash Conference

Creasy, J.D., Chiles, C., Routh W.D., et al., 1997, Overview of Traumatic Injury of the Thoracic Aorta, Radiographic, v. 17(1), pp. 27-45

Deng, Y.C., 1989, The Importance of the Test Method in Determining the Effects of Door Padding in Side Impact, Proceedings of the 33rd Stapp Car Crash Conference, 892429

Deng, Y.C., Kong, W., Ho, H., 1999, Development of A Finite Element Human Thorax Model for Impact Injury Studies, SAE International Congress and Exposition, Detroit, Michigan, SAE Paper 1999-01-0715

Deng, Y.C., Chang, F., 2000, F8B: Development of a Finite Element Human Thorax Model, Final Report, General Motors Internal Report

Deng, Y.C., Fu, J., 2002, F2A: Development of a Finite element Head/Neck Model, Final Report, General Motors Internal Report

Du Bois, P.A., 2003, A Simplified Approach to the Simulation of Rubber-Like Materials Under Dynamic Loading, 4th European LS_DYNA Users Conference, Material I

Eiband, A.M., 1959, Human Tolerance to Rapidly Applied Acceleration. A Survey of the Literature, NASA Memo No. 5-19-59E., National Aeronautics and Space Administration, Washington, D.C.

Eppinger, R.H., Marcus, J.H., Morgan, R.M., 1984, Development of Dummy and Injury Index for NHTSA's Thoracic Side Impact Protection Research Program, SAE Publication No. 840885, Government/Industry Meeting and Exposition, Washington, D.C.

Federal Motor Vehicle Safety Standards and Regulations, Motor Vehicle Safety Standard No. 208, "Occupant Crash Protection." U.S. Department of Transportation, National Highway Safety Bureau, Effective October 1, 2002

Fung, Y.-C., Tong, P., Patitucci, P., 1978, Stress and Strain in the Lung, ASCE Journal of the Engineering Mechanics Division, Vol. 104, No. 1, pp. 201-223

Fung, Y.C., 1984, Biomechanics: Mechanical Properties of Living Tissues, Second Edition, Springer-Verlag, New York

Fung, Y.C., Yen, R.T., Tao, Z.L., Liu, S.Q., 1988, A Hypothesis on the Mechanism of Trauma of Lung tissue Subjected to Impact Load, Journal of Biomechanical Engineering, Vol. 110, pp 50-56

Furusu, K., Watanabe, I., Kato, C., Miki, K., Hasegawa, J., 2001, Fundamental Study of Side Impact Analysis Using the Finite Element Model of the Human Thorax, Japanese Society of Automotive Engineers Review, Vol. 22, No. 2, pp. 195-199

Gadd, C.W., Patrick, L.M., 1968, Systems Versus Laboratory Impact Tests for Estimating Injury Hazard, SAE paper 680053, Society of Automotive Engineers, New York

Geddes, L.A., Baker, L.E., 1967, The Specific Resistance of Biological Material – A Compendium of Data for the Biomedical Engineer and Physiologist, Medical

Granik, G., Stein, I., 1973, Human Ribs: Static Testing as a Promising Medical Application, Journal of Biomechanics, Vol. 6, pp 237-240

Greendyke, R.M., 1966, Traumatic Rupture of the Aorta: Special Reference to Automobile Accidents, Journal of the American Medical Association, v. 195, 527-530

Guccione, J.M., McCulloch, A.D., Waldman, L.K., 1991, Passive Material Properties of Intact Ventricular Myocardium Determined From a Cylindrical Model, Journal of Biomechanical Engineering, Vol. 113, pp. 42-55

Guccione, J.M., McCulloch, A.D., 1991, Finite Element Modeling of Ventricular Mechanics, in Theory of Heart, Glass, L., Hunter, P., McCulloch, A., Springer-Verlag, New York, pp. 121-137

Happee, R., Hoofman, M., van den Kroonenberg, A.J., Morsink, P., Wismans, J., 1998, A Mathematical Human Body Model for Frontal and Rearward Seated Automotive Impact Loading, Proceedings of the 42nd Annual Stapp Crash Conference, 983150

Hill, A.V., The Heat of Shortening and the Dynamic Constants of Muscles, Proceedings of the Royal Society, B126:136-195

Huang, Y., King, A.I., Cavanaugh, J.M., 1994a, Finite Element Modeling of Gross Motion of Human Cadavers in Side Impact, Proceedings of the 38th Stapp Car Crash Conference, 942207

Huang, Y., King, A.I., Cavanaugh, J.M., 1994b, A MADYMO Model of Near Side Human Occupants in Side Impact, Journal of Biomechanical Engineering, ASME, Vol. 116

HUMOS Human Model for Safety Consortium, Final Public Report / Version A1, 2001

Imatani, R.J., 1975, Fractures of the Scapula: A Review of 53 Fractures, Journal of Trauma, Vol. 15, No. 6, pp. 473

Irwin, A.L., Walilko, T.J., Cavanaugh, J.M., Zhu, Y., King, A.I., 1993, Displacement Responses of the Shoulder and Thorax in Lateral Sled Impacts, Proceedings of the 37th Stapp Car Crash Conference, 933124

ISO, ISO/TR9790, 1999, Road Vehicles – Anthropomorphic Side Impact Dummy – Lateral Impact Response Requirements to Assess the Biofidelity of the Dummy, Technical Report 9790, International Standards Organization, American National Standards Institute, New York, NY

Iwamoto, M., Miki, K., Mohammad, M., Nayef, A., Yang, K.H., Begeman, P.C., King, A.I., 2000, Development of a Finite Element Model of the Human Shoulder, Proceedings of the 44th Stapp Car Crash Conference

Iwamoto, M., Miki, K., Yang, K.H., 2001, Development of a Finite Element Model of the Human Shoulder to Investigate the Mechanical Responses and Injuries in Side Impact, Japanese Society of Mechanical Engineers International Journal, Series C., Vol. 44, No. 4

Jamulitrat, S., Sangkerd, P., Thongpiyapoom, S., Na Narong, M., A Comparison of the Mortality Predictive Abilities Between NISS and ISS in Trauma Patients, Journal of the Medical Association of Thailand, Vol. 84, No. 10, pp. 1416-1420

Janda, D.H., Bir, C.A., Viano, D.C., Cassatta, S.J., 1998, Blunt Chest Impacts: Assessing the Relative Risk of Fatal Cardiac Injury from Various Baseballs, Journal of Trauma-Injury Infection and Critical Care, Vol. 44, No. 2, pp. 298-303

Jonsson, A., Clemedson, C.J., Sundqvist, A.B., Arvebo, E., 1979, Dynamic Factors Influencing the Production of lung Injury in Rabbits Subjected to Blunt chest Wall Impact, Aviation Space and Environmental Medicine, Vol. 50, No. 4, pp. 325-337

Kallieris, D., Mattern, R., Schmidt, G., Eppinger, R.H., 1981, Quantification of Side Impact Response and Injuries, Proceeding of the 25th Annual Stapp Car Crash Conference, 811009

Kilgo, P.D., Meredith, J.W., Hensburry, R., Osler, T.M., 2004, A Note on the Disjointed Nature of the Injury Severity Score, Journal of Trauma, Vol. 57, No. 3, pp. 486-487

Klienberger, M., Sun, E., Eppinger, R., Kuppa, S, Saul, R., 1998, Development of Improved Injury Criteria for the Assessment of Advanced Automotive Restraint Systems, NHTSA Docket 98-4405-9

Koh, S.W., Cavanaugh, J.M., Zhu, J., 2001, Injury and Response of the Shoulder in Lateral Sled Tests, Proceedings of the 45th Stapp Car Crash Conference, 2001-22-0005

Kroell, C.K., Schneider, D.C., Nahum, A.M., 1971, Impact Tolerance and Response of the Human Thorax, Proceedings of the 15th Stapp Car Crash Conference, 710851

Kroell, C.K., Schneider, D.C., Nahum, A.M., 1974, Impact Tolerance and Response of the Human Thorax II, Proceedings of the 18th Stapp Car Crash Conference, 741187

Kroell, C.K., Pope, M.E., Viano, D.C., Warner, C.Y., Allen, S.D., 1981, Interrelationship of Velocity and Chest Compression in Blunt Thoracic Impact to Swine, Proceedings of the 25th Stapp Car Crash Conference, 811016

Kuppa, S., Eppinger, R.H., McKoy, F., 2003, Development of Side Impact Thoracic Injury Criteria and Their Application to the Modified ES-2 Dummy with Rib Extensions (ES-2re), Proceedings of the 47th Annual Stapp Car Crash Journal, 2003-22-0010

Lau, I.V., Viano, D.C., 1981, Influence of Impact Velocity on the Severity of Non-Penetrating Hepatic Injury, Journal of Trauma, Vol. 21, pp. 115-123

Lau, I.V., Viano, D.C., 1985, Thoracic Impact: A Viscous Tolerance Criterion, Proceedings of the Tenth Experimental Safety Vehicle Conference, Oxford, England

Lau, I.V., Viano, D.C., 1986, The Viscous Criterion - Bases and Applications of an Injury Severity Index for Soft Tissues, Proceedings of the 30th Stapp Car Crash Conference, 861882

Lewis, P.R. Jr., Molz, F.J. IV, Schmidtke, S.Z., Bidez, M.W., 1996, A NASS-Based Investigation of Pelvic Injury within the Motor Vehicle Crash Environment, Proceedings of the 40th Stapp Car Crash Conference, 962419

Lobdell, T.E., Kroell, C.K., Schneider, D.C., Hering, W.E., Nahum, A.M., 1973, Impact Response of the Human Thorax, Proceedings of the Symposium from Human Impact Response Measurement and Simulation, New York, London, Plenum Press, pp. 201-245

LSTC (Livermore Software Technology Corp.), "LS-DYNA 970 Keyword User's Manual, Version 970", April 2003

McConville, J.T., Churchill, T.D., Kaleps, I., Clauser, C.E., Cuzzi, J., 1980, Anthropometric Relationships of Body and Body Segment Moments of Inertia, Air Force Aerospace Medical Research Laboratory, Wright-Patterson AFB, Ohio, AFB AMRL-TR-80-119

McCulloch, A.D., Omens, J.H., 1991, Non-Homogeneous Analysis of Three-Dimensional Transmural Finite Deformation in Canine Ventricular Myocardium, Journal of Biomechanics, Vol. 24, No. 7, pp. 539-548

Mertz, H.J., Prasad, P., Irwin, A.L., 1997, Injury Risk Curves for Children and Adults in Frontal and Rear Collisions, Proceedings of the 41st Stapp Car Crash Conference, 973318

Moore, K.L., Dalley, A.F., 1999, Clinically Oriented Anatomy, Fourth Edition, Lippincott Williams and Wilkins, Baltimore

Mohan, D., Melvin, J., 1982, Failure Properties of Passive Human Aortic Tissue - Uniaxial Tension Tests, Journal of Biomechanics, Vol. 15, No. 11, pp. 887-902

Mohan, D., Melvin, J., 1983, Failure Properties of Passive Human Aortic Tissue II - Biaxial Tension Tests, Journal of Biomechanics, Vol. 16, No. 1, pp. 31-44

Morgan, R.M., Marcus, J.H., Eppinger, R.H., 1986, Side Impact - The Biofidelity of NHTSA's Proposed ATD and Efficacy of TTI, Proceedings of the 30th Stapp Car Crash Conference, 861877

Moss, S., Wang, Z., Salloum, M., Reed, M., van Ratingen, M., Cesari, D., Scherer, R., Uchimura, T., Beusenberg, M., 2000, Anthropometry for WorldSID A World-Harmonized Midsize Male Side Impact Crash Dummy, SAE Technical Paper Series, 2000-01-2202

Nahum, A.M., Melvin J.W., 2002, Accidental Injury Biomechanics and Prevention, Second Edition, Springer-Verlag Inc., New York

National Highway Traffic Safety Administration, 2001, A Compilation of Motor Vehicle Crash Data from the Fatality Analysis Reporting System and the General Estimates System, Traffic Safety Facts 2001, DOT HS 809 484

National Highway Traffic Safety Administration, Biomechanics Test Database, http://www-nrd.nhtsa.dot.gov/database/nrd-51/bio_db.html

National Highway Traffic Safety Administration, 2004, Federal Motor Vehicle Safety Standards; Side Impact Protection; Side Impact Phase-In Reporting Requirements; Proposed Rule, Federal Register, Part IV, Department of Transportation 49 CFR Parts 571 and 598, Docket No. NHTSA-2004-17694

Neathery, R.F., 1974, Analysis of Chest Impact Response Data and Scaled Performance Recommendations, Proceeding of the 18th Stapp Car Crash Conference, 741188

Neathery, R.F., Kroell, C.K., Mertz, H.J., 1975, Prediction of Thoracic Injury from Dummy Responses, Proceeding of the 19th Stapp Car Crash Conference, 751151

Newman, R.J., Rastogi, S., 1984, Rupture of the Thoracic Aorta and its Relationship to Road Traffic Accident Characteristics, Injury: The British Journal of Accident Surgery, Vol. 15, No. 5, pp. 296-299

Ochsner, M.G., Champion, H.R., Chambers, R.J., Harviel, J.D., 1989, Pelvic Fracture as an Indicator of Increased Risk of Thoracic Aortic Rupture, Journal of Trauma, Vol. 29, 1376-1379

Oshita, F., Omori, K., Nakahira, Y., Miki, K., 2002, Development of a Finite Element Model of the Human Body, 7th International LS-DYNA Users Conference

Osler, T., Baker, S.P., Long, W., 1997, A Modification of the Injury Severity Score that Both Improves Accuracy and Simplifies Scoring, Journal of Trauma – Injury, Infection and Critical Care, Vol. 43, No. 6, pp. 922-926

Otte, D., 1996, Biomechanics of Lower Limb Injuries of Belted Car Drivers and the Influence of Intrusion and Accident Severity, Proceedings of the 40th Annual Stapp Car Crash Conference, 962425

Panjabi, M.M., Brand, R.A., White A.A., 1976, Three Dimensional Flexibility and Stiffness Properties of the Human Thoracic Spine, Journal of Biomechanics, Vol. 9, No. 4, pp. 185-192

Patrick, L.M., Kroell, C.K., Mertz, H.J., 1965, Forces of the Human Body in Simulated Crashes, Proceedings of the 9th Stapp Car Crash Conference, 650961

Pintar, F.A., Yoganandan, N., Hines, M.H., Maltese, M.R., et al., 1997, Chestband Analysis of Human Tolerance to Side Impact, Proceedings of the 41st Annual Stapp Car Crash Conference, 973320

Plank, G.R., Eppinger, R.H., 1989, Computed Dynamic Response of the Human Thorax From a Finite Element Model, Proceedings of the 12th International Technical Conference of Experimental Safety Vehicle

Robbins, D.H., Schneider, L.W., Snyder, R.G., Pflug, M., Haffner, M., 1983a, Seated Posture of Vehicle Occupants, Proceedings of the 27th Annual Stapp Car Crash Conference, 831617

Robbins, D.H., 1983b, Anthropometric Specifications for the Mid-Sized Male Dummy, Volume 2, The University of Michigan Transportation Research Institute, U.S. Department of Transportation National Highway Traffic Safety Administration, UMTRI-83-53-2

Robbins, D.H., Melvin, J.W., Stalnaker, R.L., 1976, The Prediction of Thoracic Impact Injuries, Proceedings of the 20th Annual Stapp Car Crash Conference, 760822

Rohen, J.W., Yakochi, C., 1983, Color Atlas of Anatomy, A Photographic Study of the Human Body, Igaku-Shoin Medical Publishers Inc., New York

Schultz, A.B., Benson, D.R., Hirsch, C., 1974a, Force-Deformation Properties of Human Costo-Sternal and Costo-Vertebral Articulations, Journal of Biomechanics, Vol. 7, No. 3, pp. 311-312

Schultz, A.B., Benson, D.R., Hirsch, C., 1974b, Force-Deformation Properties of Human Ribs, Journal of Biomechanics, Vol. 7, pp 303-309

Shah, C.S., Yang, K.H., Hardy, W., Wang, H.K., King, A.I., 2001, Development of a Computer Model to Predict Aortic Rupture Due to Impact Loading, Proceedings of the 45th Stapp Car Crash Conference, 2001-01-0007

Somers, R.L., 1983, The Probability of Death Score: An Improvement of the Injury Severity Score, Accident Analysis Prevention, Vol. 15, pp. 247-257

Stapp, J.P., 1951, Human Exposure to Linear Decelerations, Part 2: The Forward Facing Position and the Development of a Crash Harness, AFTR 5915, Wright-Patterson AFB, Dayton, Ohio

Stapp, J.P., 1970, Voluntary Human Tolerance Levels, Impact Injury and Crash Protection, Ed: Gurdjian, E.S., Lang, W.A., Patrick, L.M., Thomas, L.M., pp. 308-349, Charles C. Thomas, Springfield, IL.

States, J.D., 1969, The Abbreviated and the Comprehensive Research Injury Scales, Proceedings of the 13th Stapp Car Crash Conference, 690810

Sundaram, S.H., Feng, C.C., 1977, Finite Element Analysis of the Human Thorax, Journal of Biomechanics, Vol. 10, pp. 505-516

Thollon, L., Arnoux, P.J., Kayvantash, K., Cavallero, C., Brunet, C., 2002, Human Injury Evaluation using HUMOS RADIOSS Finite Element Model, IRCOBI Conference 2002

TNO Automotive, 2003, MADYMO, Human Models Manual, Version 6.1, March 2003

Van Ee, C.A., Nightingale, R.W., Camacho, D.L.A., Chancey, V.C., Knaub, K.E., Sun, A.E., Myers, B.S., 2000, Tensile Properties of the Human Muscular and Ligamentous Cervical Spine, Proceedings of the 44th Stapp Car Crash Conference, 2000-01-SC07

Van Sligtenhorst, C.R., Cronin, D.S., Brodland, W.G., 2003, High Strain Rate Compressive Properties of Soft Tissue, American Society of Mechanical Engineers, Bioengineering Division BED, Vol. 55

Vawter, D. L., 1980, A Finite Element Model for Macroscopic Deformation of the Lung, Journal of Biomechanical Engineering, Vol. 102

Veeger, H.E.J., Van Der Helm, F.C.T., Van Der Woude, L.H.B., Pronk, G.M., 1991, Inertia and Muscle Contraction Parameters for Muscoskeletal Modeling of the Shoulder Mechanism, Journal of Biomechanics, Vol. 24, No. 7, pp. 615-629

Vlesis, A.A., Trunkey, D.D., 1997, Non-penetrating Injury of the Thorax, In: Scientific Foundations of Trauma, ed. Cooper, G.J., Dudle, H.A.F., Gann, D.S., Little, R.A., Maynard, R.L., Butterworth- Heinemann, Linacre House, Jordan Hill, Oxford

Viano, D.C., 1978, Evaluation of Biomechanical Response and Potential Injury from Thoracic Impact, Aviation, Space and Environmental Medicine, Vol. 49, pp. 125-135

Viano, D.C., 1983, Biomechanics of Non-penetrating Aortic Trauma: A Review, 1983, Proceedings of the 27th Stapp Car Crash Conference, 831608

Viano, D. C., 1986, Biomechanics of Bone and Tissue: A Review of Material Properties and Failure Characteristics, SAE 861923

Viano, D.C., 1987a, Evaluation of the SID Dummy and TTI Injury Criterion for Side Impact Testing, Proceedings of the 31st Stapp Car Crash Conference, 872208

Viano, D.C., 1987b, Evaluation of the Benefit of Energy-Absorbing Material in Side Impact Protection: Part I, Proceedings of the 31st Stapp Car Crash Conference, 872212

Viano, D.C., 1987c, Evaluation of the Benefit of Energy-Absorbing Material in Side Impact Protection: Part II, Proceedings of the 31st Stapp Car Crash Conference, 872213

Viano, D.C., Lau, I.V., 1988, A Viscous Tolerance Criterion for Soft Tissue Injury Assessment, Journal of Biomechanics, Vol. 21, pp. 387-399

Viano, D.C., King, A.I., Melvin, J.W., Weber, K., 1989a, Injury Biomechanics Research: An Essential Element in the Prevention of Trauma, Journal of Biomechanics, Vol. 22, No. 5, pp 403-417

Viano, D.C., Lau, I.V., Asbury, C., King, A.I., Begeman, P., 1989b, Biomechanics of the Human Chest, Abdomen, and Pelvis in Lateral Impact, Proceedings of the 33rd Association for the Advancement of Automotive Medicine

Viano, D.C., 1989c, Biomechanical Responses and Injuries in Blunt Lateral Impact, Proceedings of the 33rd Stapp Car Crash Conference, 892432

Winters, J.M., Stark, L., 1988, Estimated Mechanical Properties of Synergistic Muscles Involved in Movements of a Variety of Human Joints, Journal of Biomechanics, Vol. 21

Winters, J.M., 1990, Hill-based Muscle Models: A Systems Engineering Perspective, in Multiple Muscle Systems: Biomechanics and Movement Organization, Winters, J.M., Woo, S.L.-Y., ed., Springer-Verlag

Winters, J.M., 1995, How Detailed Should Muscle Models be to Understand Multi-Joint Movement Coordination, Human Movement Science, Vol. 14

Workgroup Data Processing Vehicle Safety, 2004, Crash Analysis Criteria Description, Version 1.6

Yamada, H., 1970, Strength of Biological Materials, Evans, F.G., ed., Lippincott Williams and Wilkins, Baltimore

Yen, M.R.T., 1999, Mechanical Properties of Human Heart, Lung and Aorta for Highway Safety Research, Final Report of Research Project

Yen, R.T., Fung, Y.C., Liu, S.Q., 1988, Trauma of Lung Due to Impact Load, Journal of Biomechanics, Vol. 21, No. 9, pp. 745-753

Yoganandan, N., Pintar, F.A., 1998, Biomechanics of Human Thoracic Ribs, Journal of Biomechanical Engineering, Transactions of the ASME, Vol. 120, N. 1, pp 100-104

Yoganandan, N., Skrade, P.A., 1991, Thoracic Deformation Contours in a Frontal Impact, Proceedings of the 35th Stapp Car Crash Conference, 912891

Yoganandan, N., Pintar, F.A., 2001a, SC135 Side Impact Test with Human Surrogate, DOT NHTSA, Cooperative Agreement No, DTNH22-93-Y-17028

Yoganandan, N., Pintar, F.A., 2001b, SC131 Side Impact Test with Human Surrogate, DOT NHTSA, Cooperative Agreement No, DTNH22-93-Y-17028

Zeng, Y.J., Yager, D., Fung, Y.C., 1987, Measurement of the Mechanical Properties of the Human Lung Tissue, Journal of Biomechanical Engineering, Vol. 109, pp. 169-174

Appendix A

Simulation Test Data

A.1 Abdominal Pendulum Impacts

Force

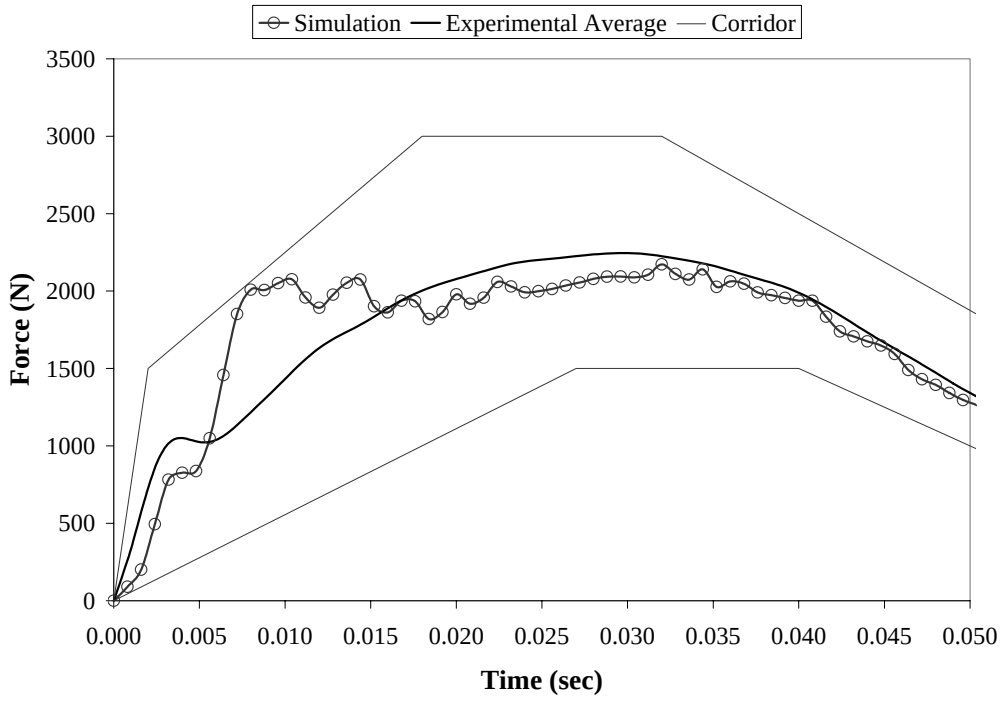

Figure A.1 Abdominal pendulum force at 4.83 m/s

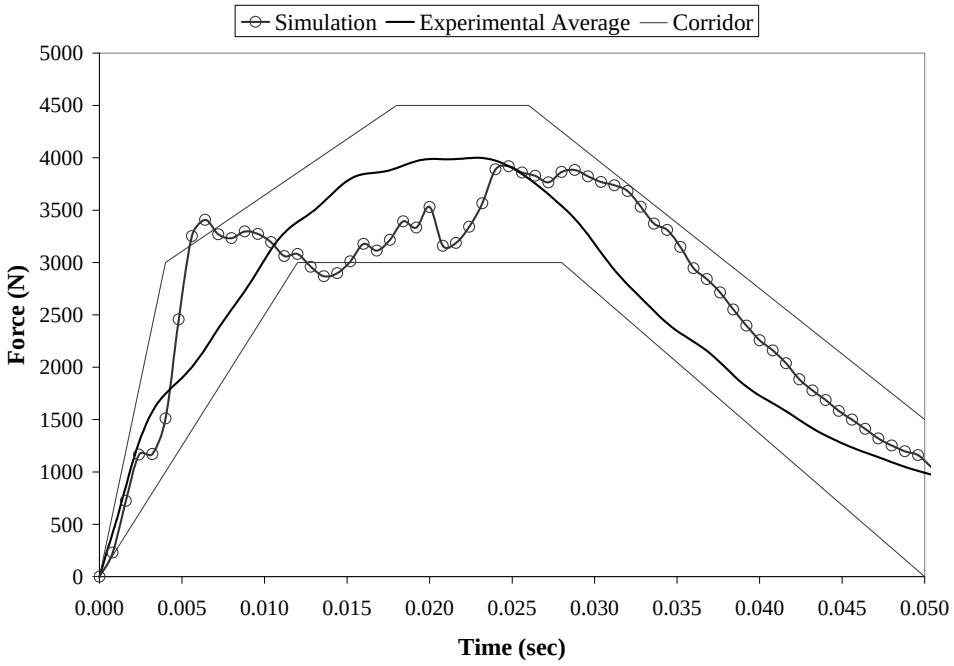

Figure A.2 Abdominal pendulum force at 4.83 m/s

Compression

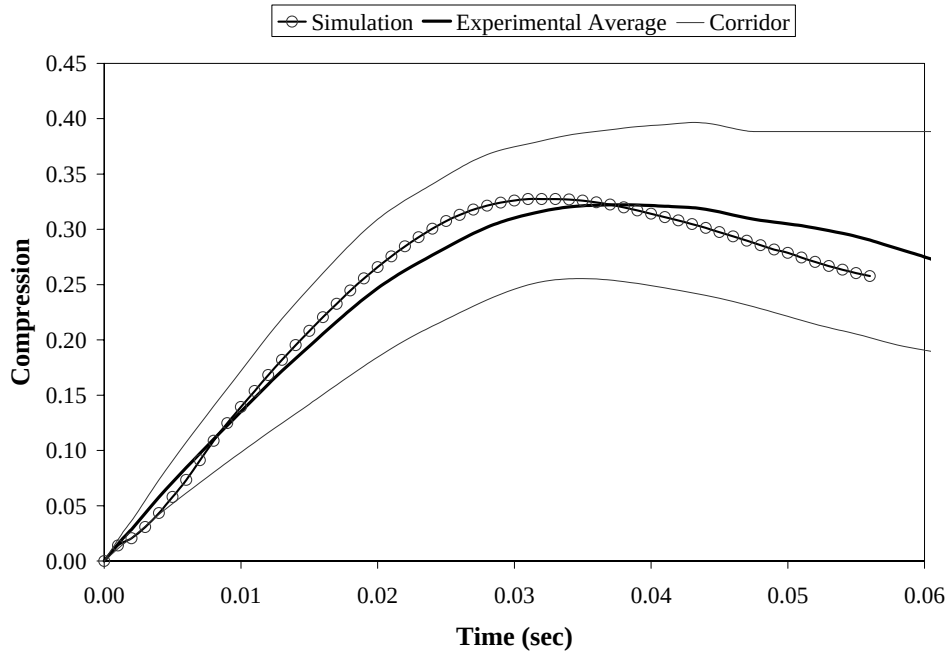

Figure A.3 Abdominal pendulum force at 4.83 m/s

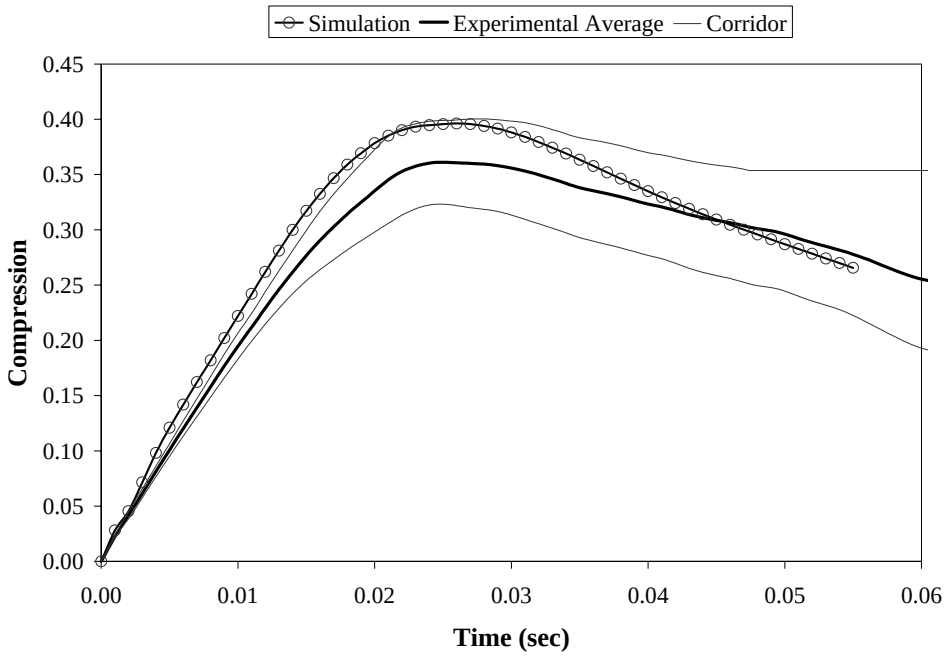

Figure A.4 Abdominal pendulum force at 4.83 m/s

VC

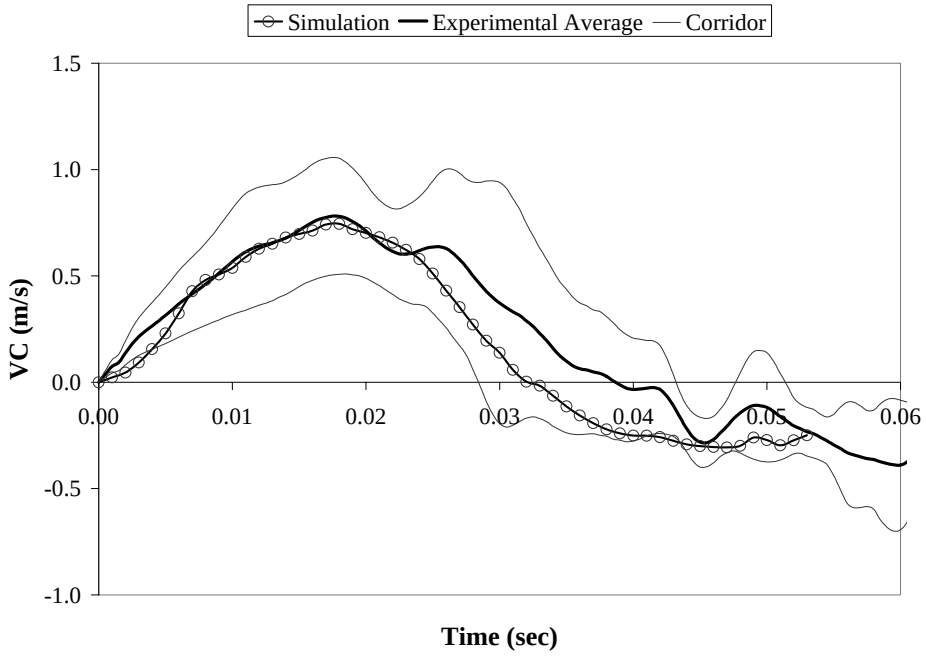

Figure A.5 Abdominal pendulum force at 4.83 m/s

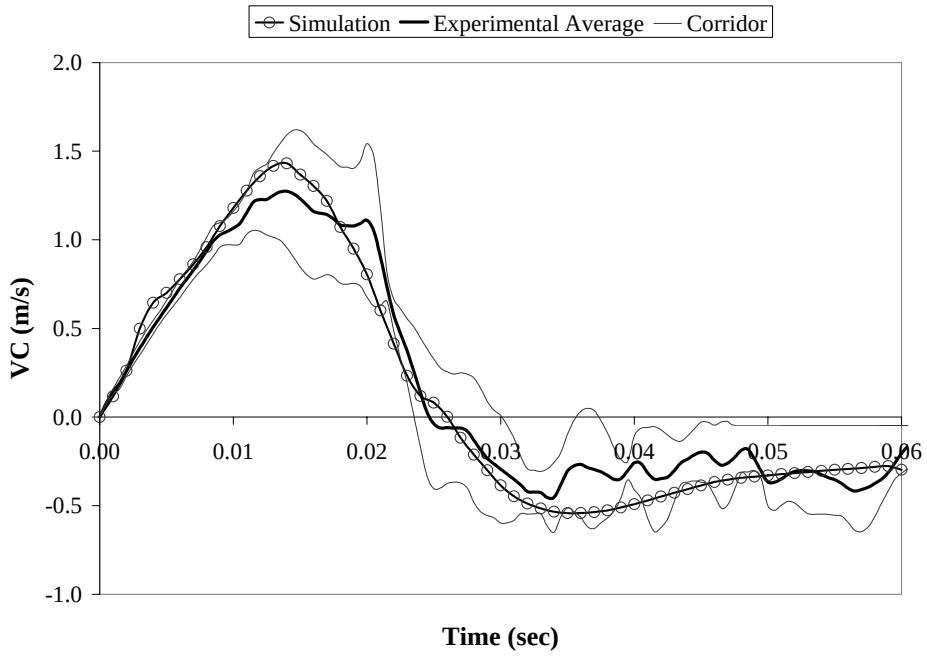

Figure A.6 Abdominal pendulum force at 4.83 m/s

Force – Compression

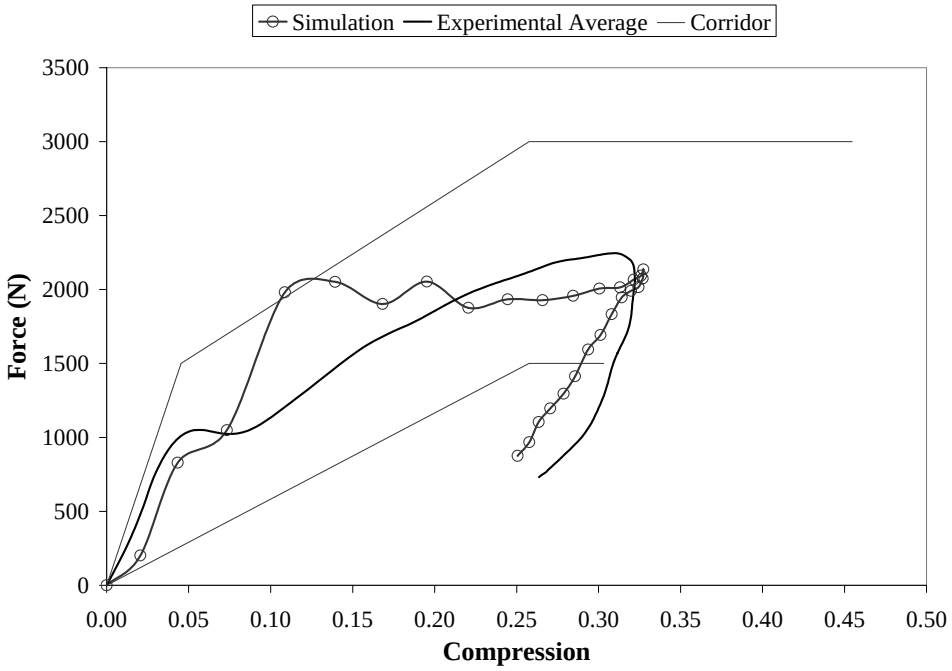

Figure A.7 Abdominal pendulum force at 4.83 m/s

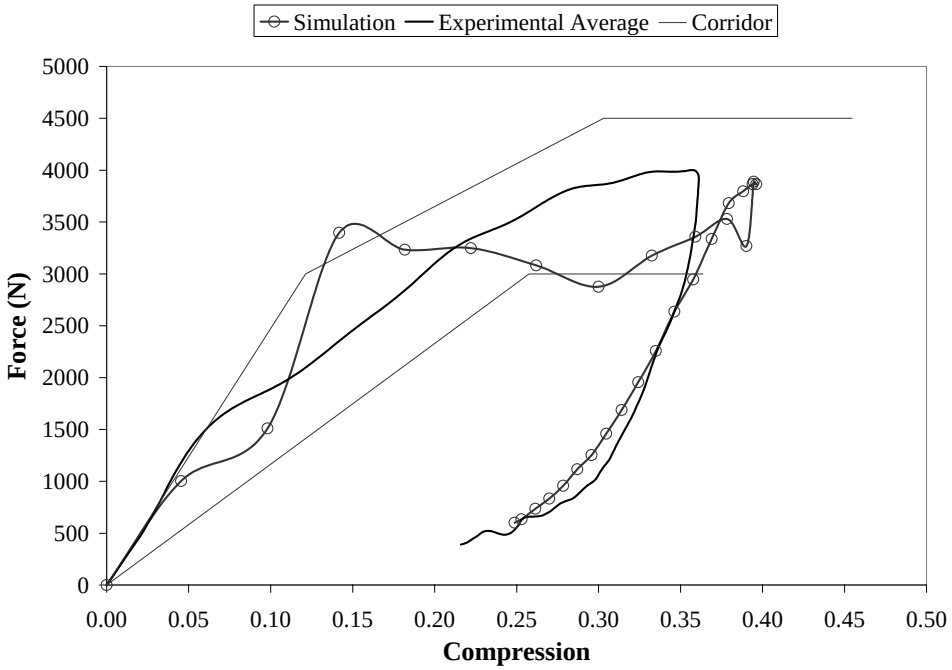

Figure A.8 Abdominal pendulum force at 4.83 m/s

A.2 NHTSA Side Sled Test – Low Speed

Force

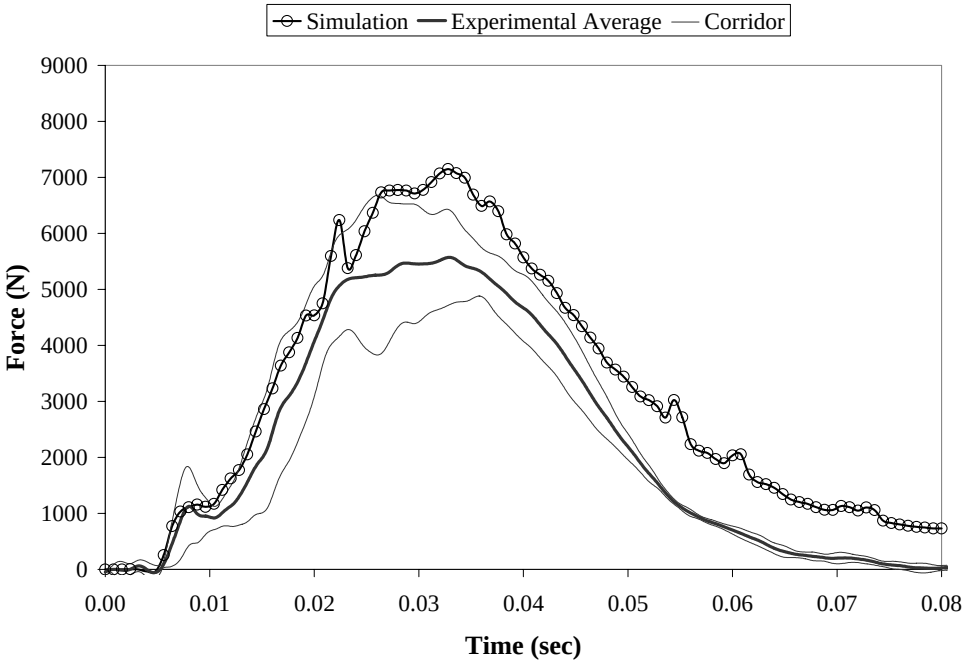

Figure A.9 Thoracic plate impact force

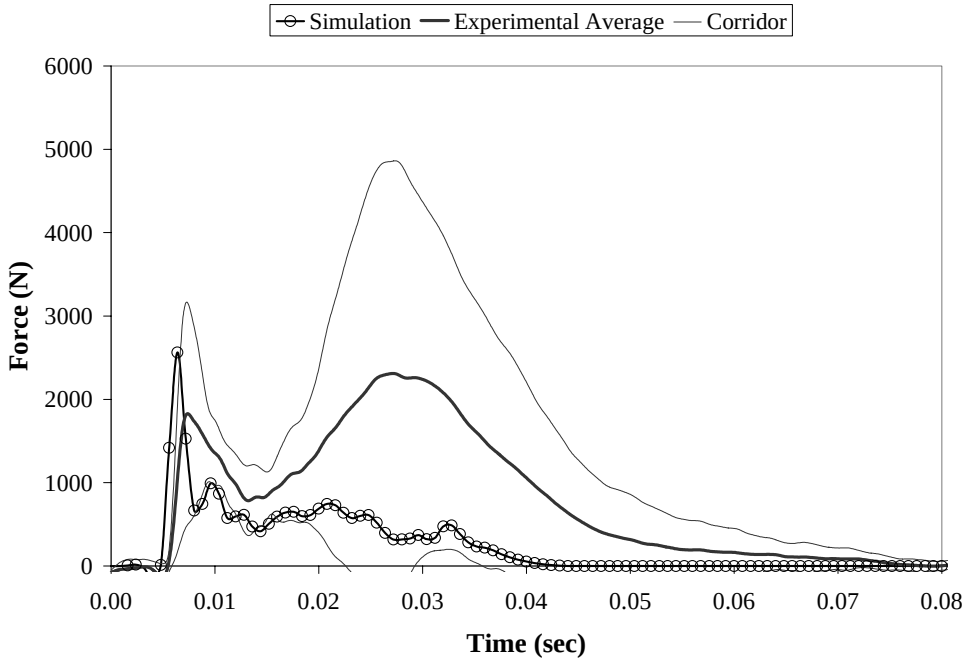

Figure A.10 Abdominal plate impact force

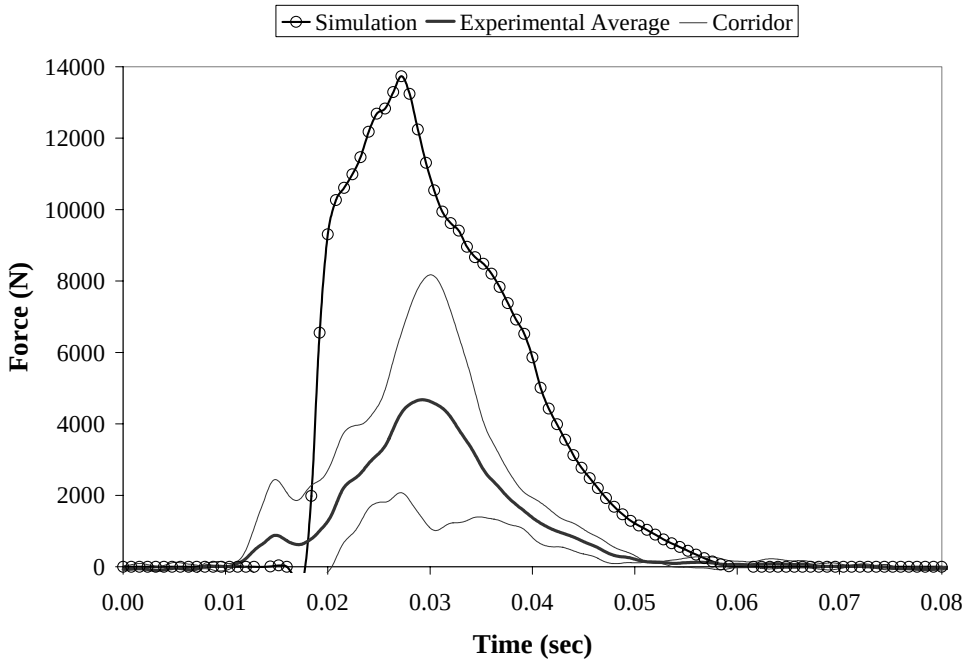

Figure A.11 Pelvic plate impact force

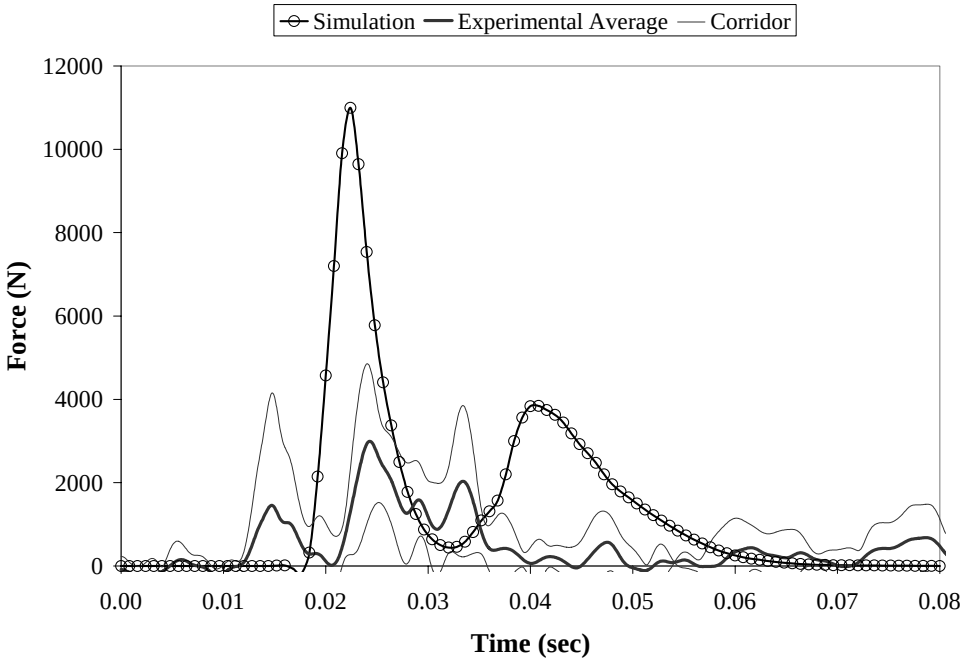

Figure A.12 Leg plate impact force

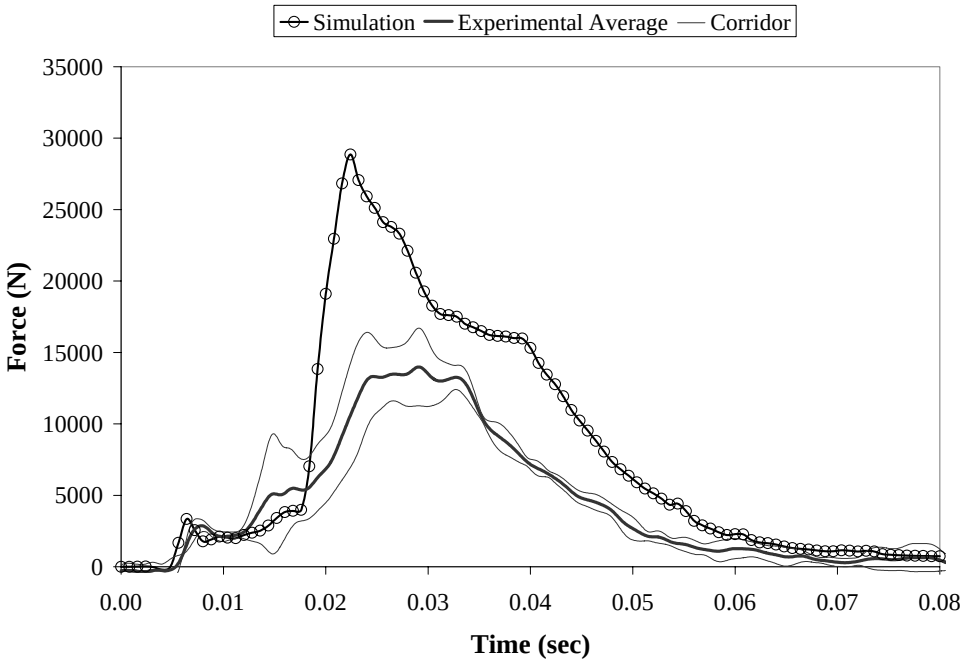

Figure A.13 Total plate impact force

Impulse

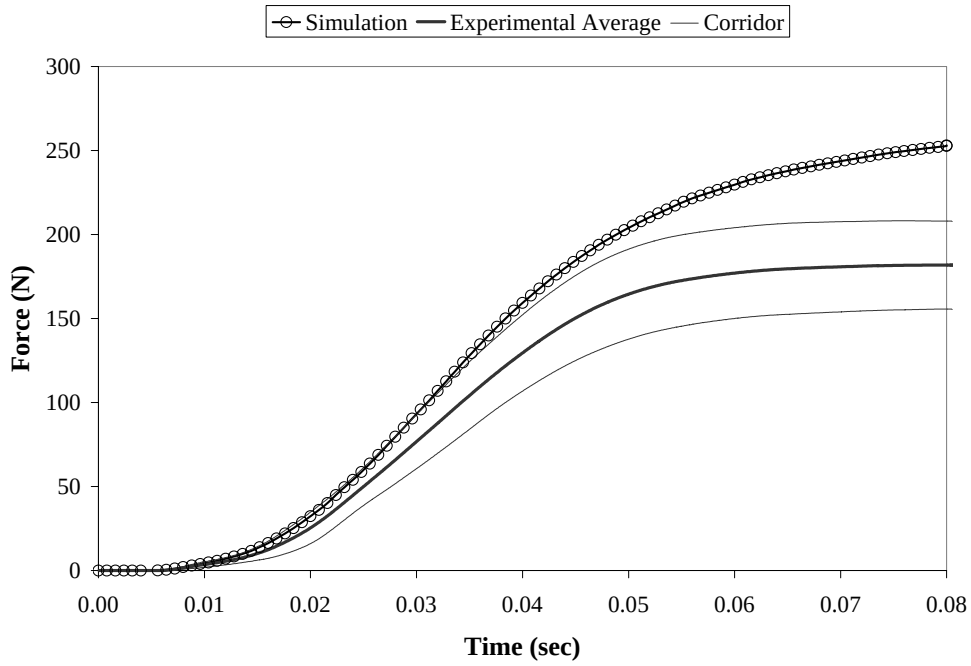

Figure A.14 Thoracic plate impact impulse

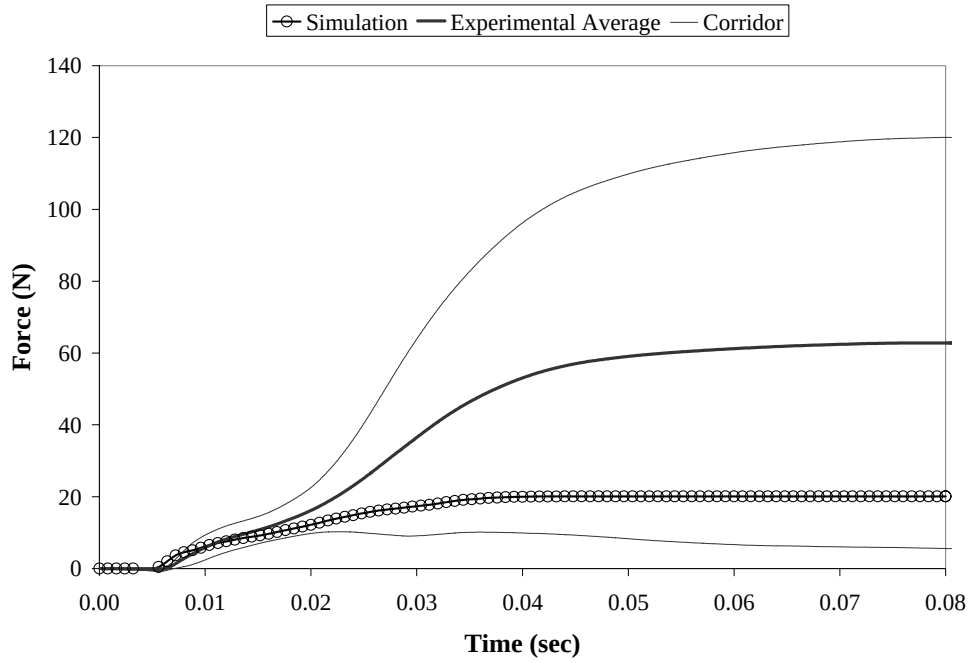

Figure A.15 Abdominal plate impact impulse

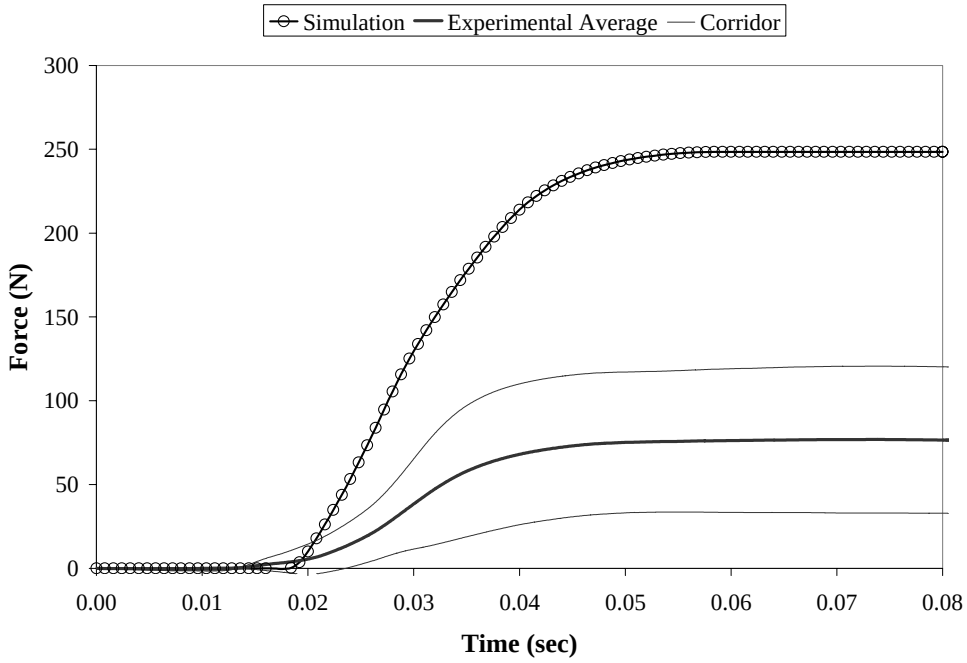

Figure A.16 Pelvic plate impact impulse

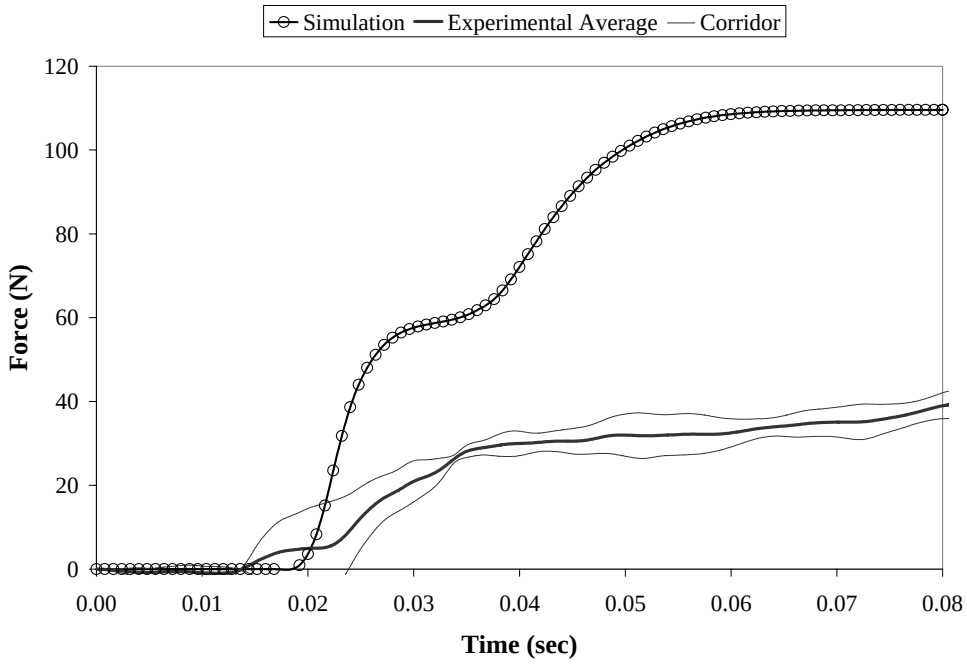

Figure A.17 Leg plate impact impulse

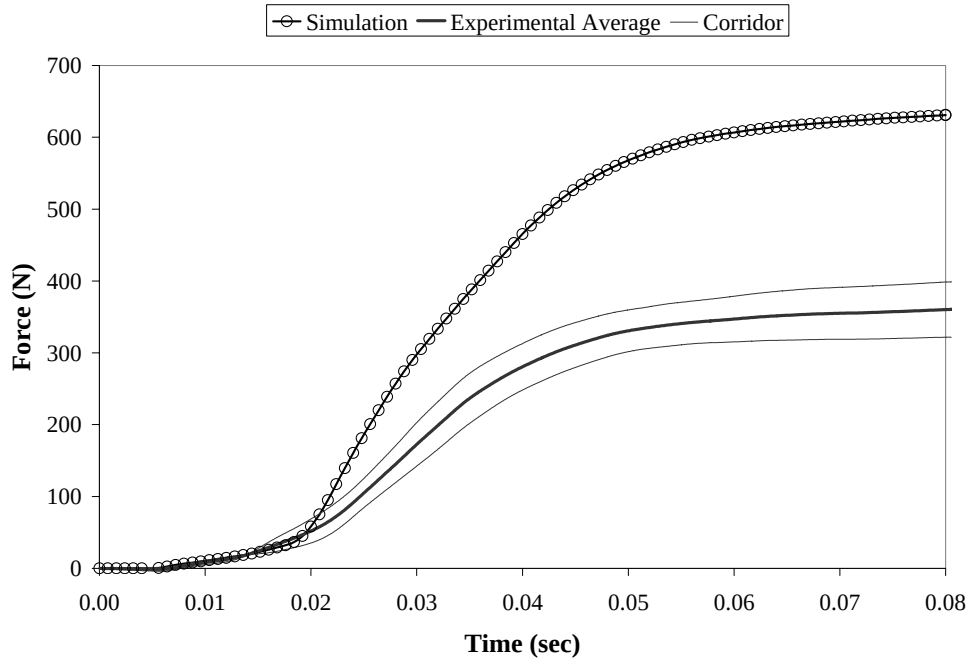

Figure A.18 Total plate impact impulse

Compression

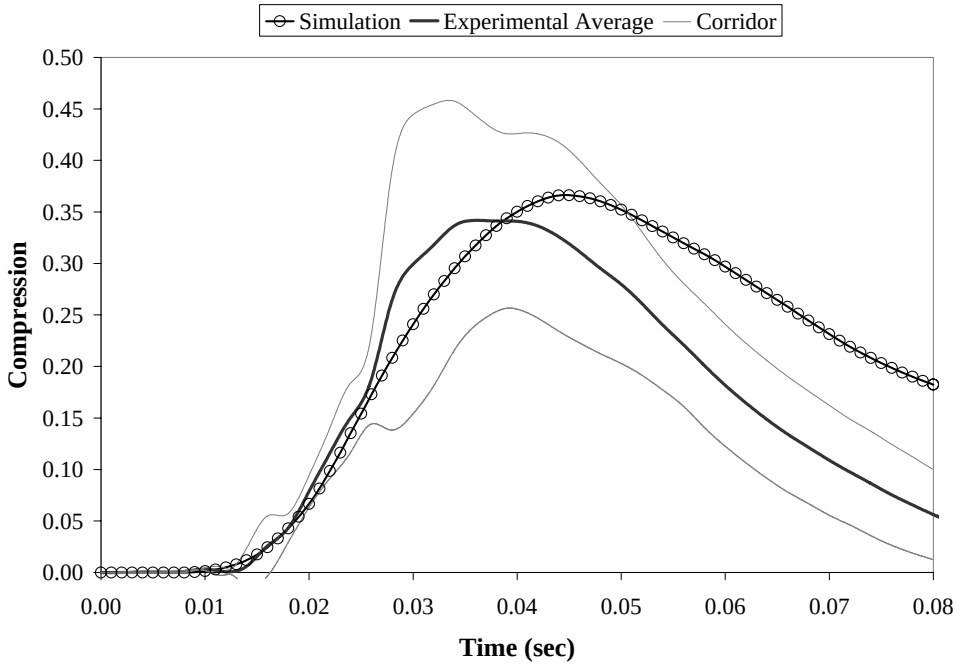

Figure A.19 Upper band compression

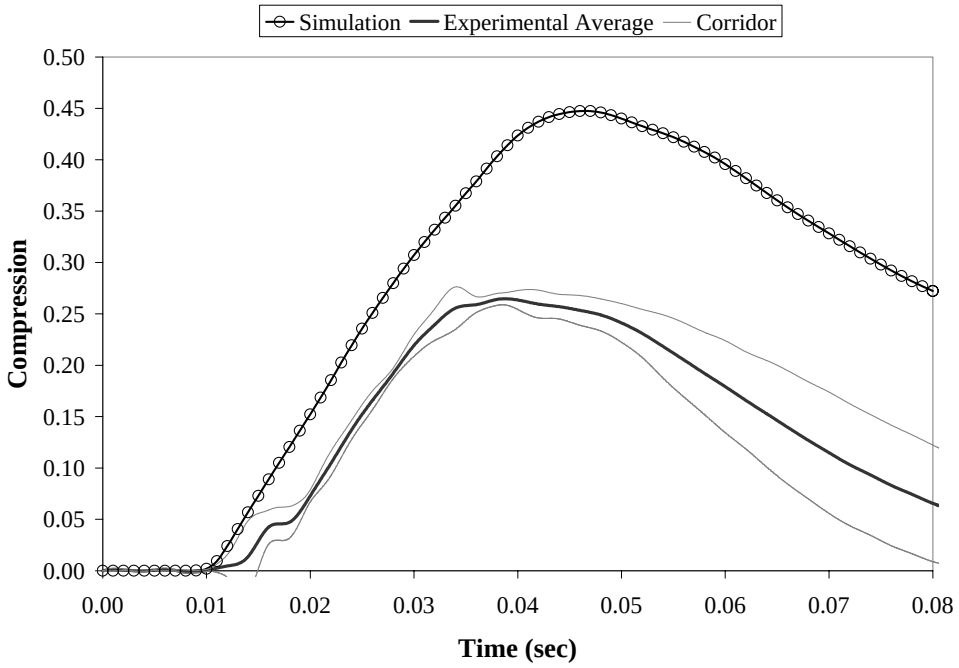

Figure A.20 Middle band compression

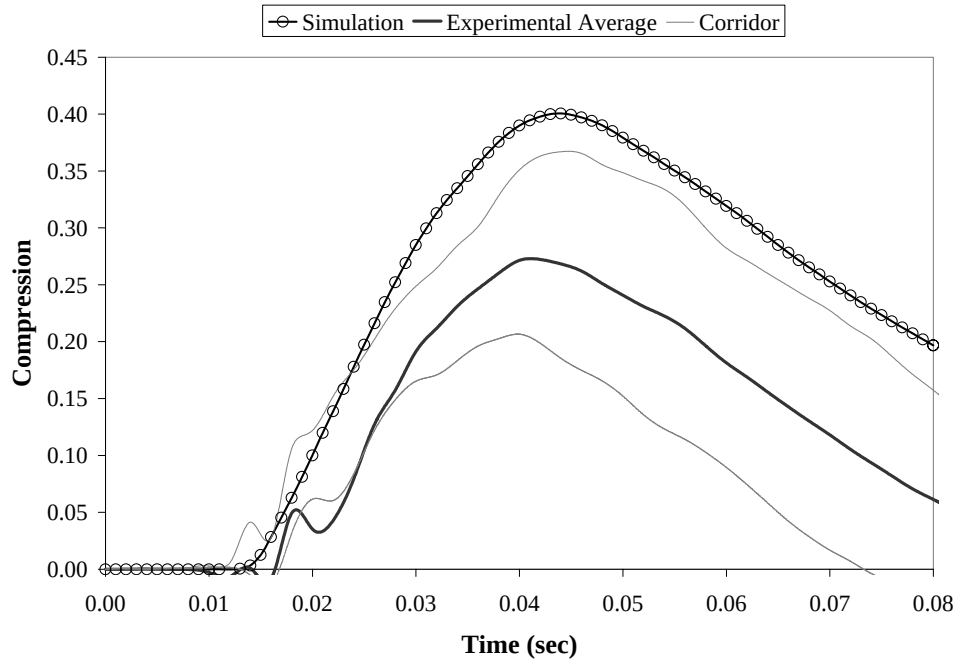

Figure A.21 Lower band compression

VC

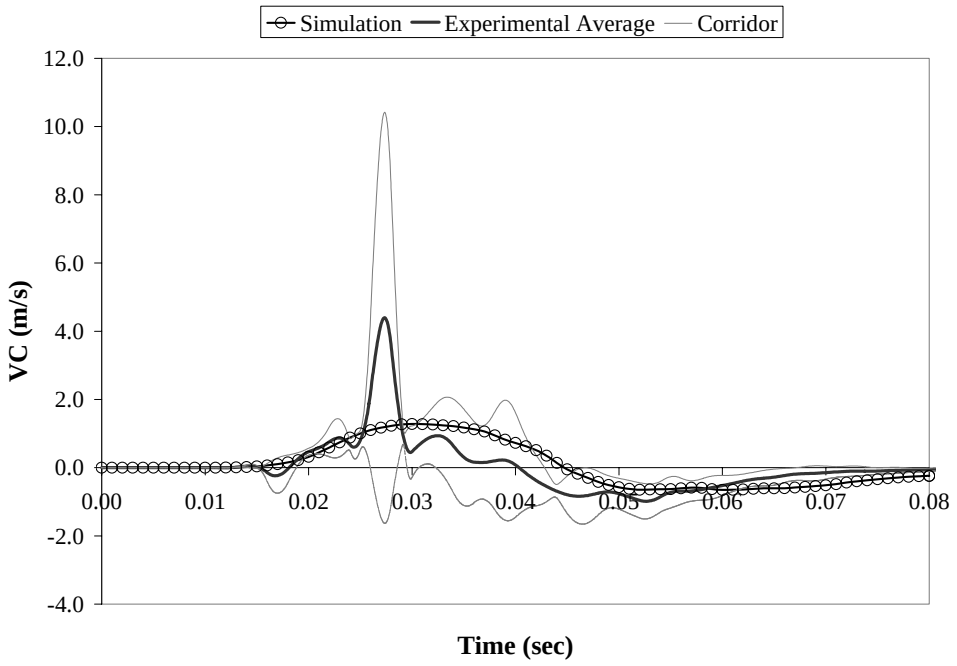

Figure A.22 Upper band VC

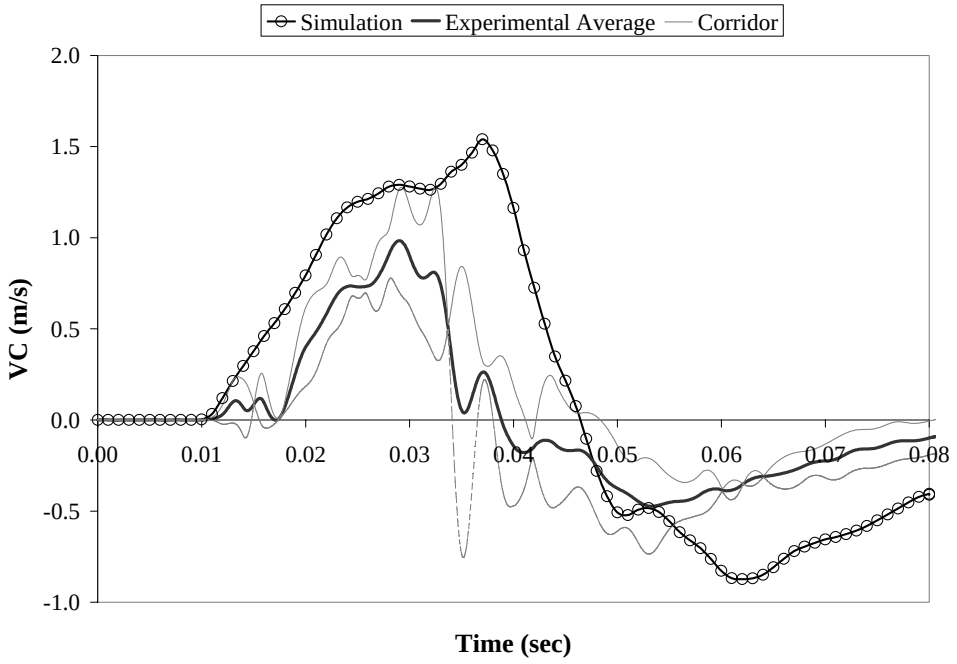

Figure A.23 Middle band VC

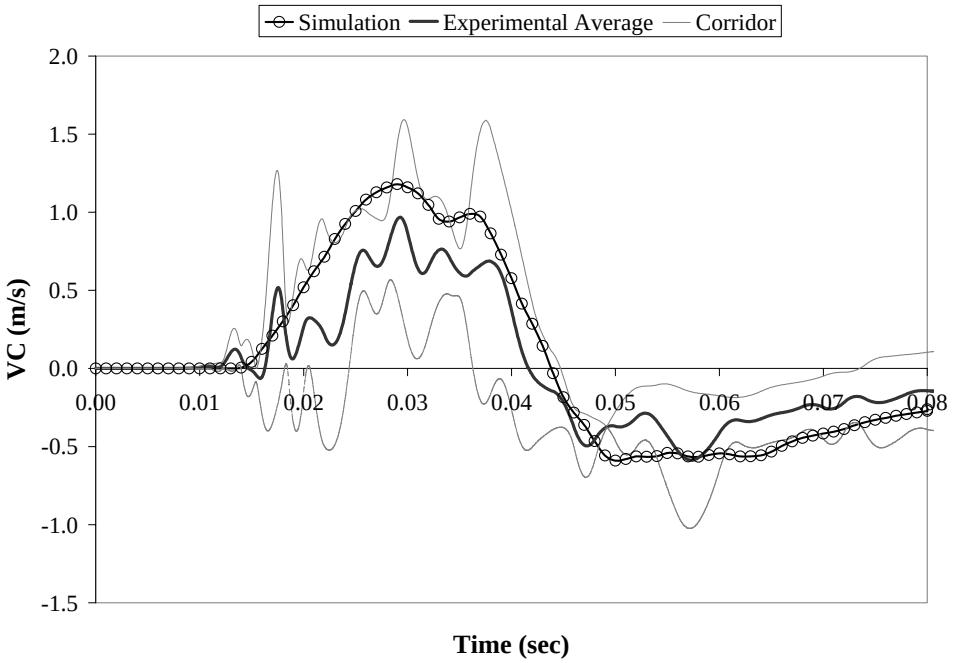

Figure A.24 Lower band VC

A.3 WSU Side Sled Test – Low Speed

Chest Compression

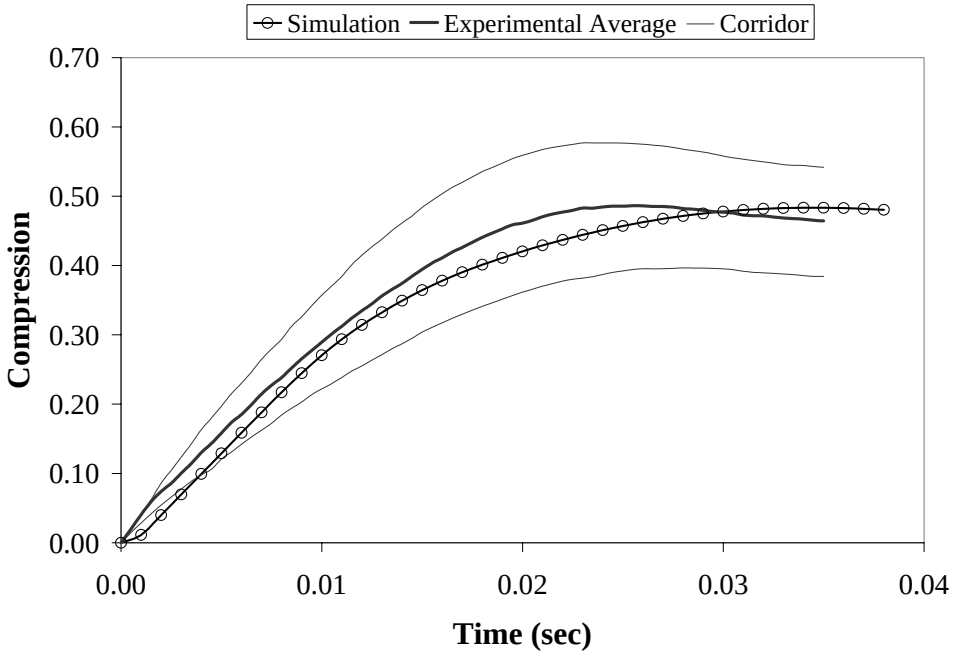

Figure A.25 Half width chest compression

Chest VC

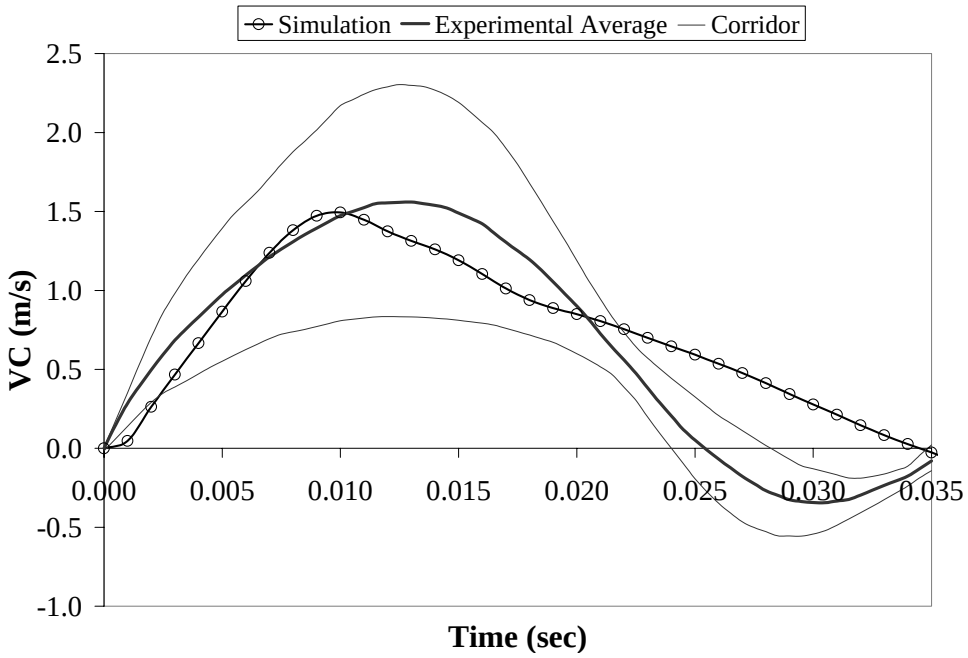

Figure A.26 Half width VC

A.4 WSU Side Sled Test –High Speed

Force

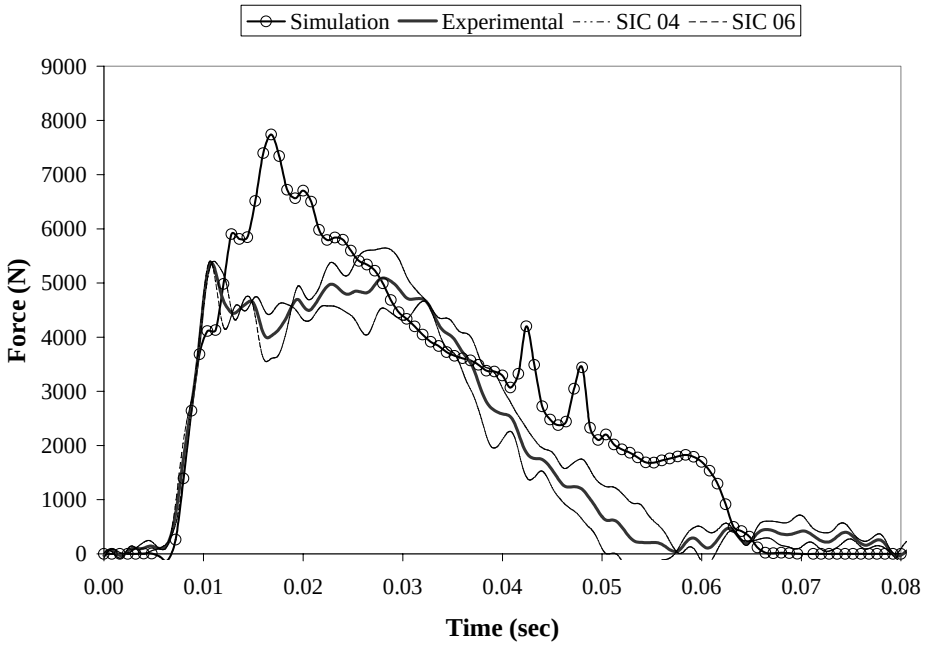

Figure A.27 Shoulder plate impact force

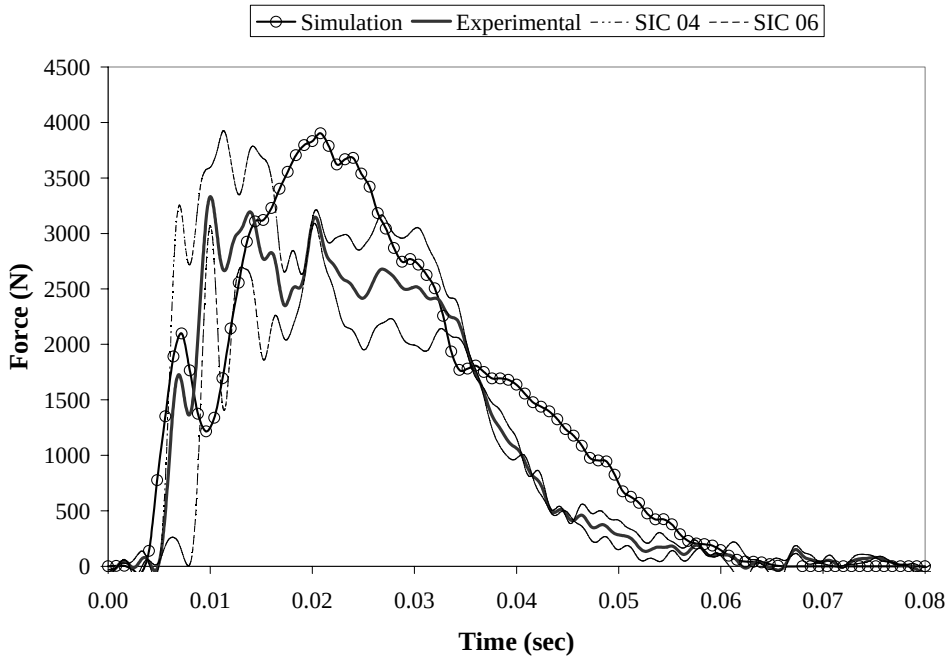

Figure A.28 Thoracic plate impact force

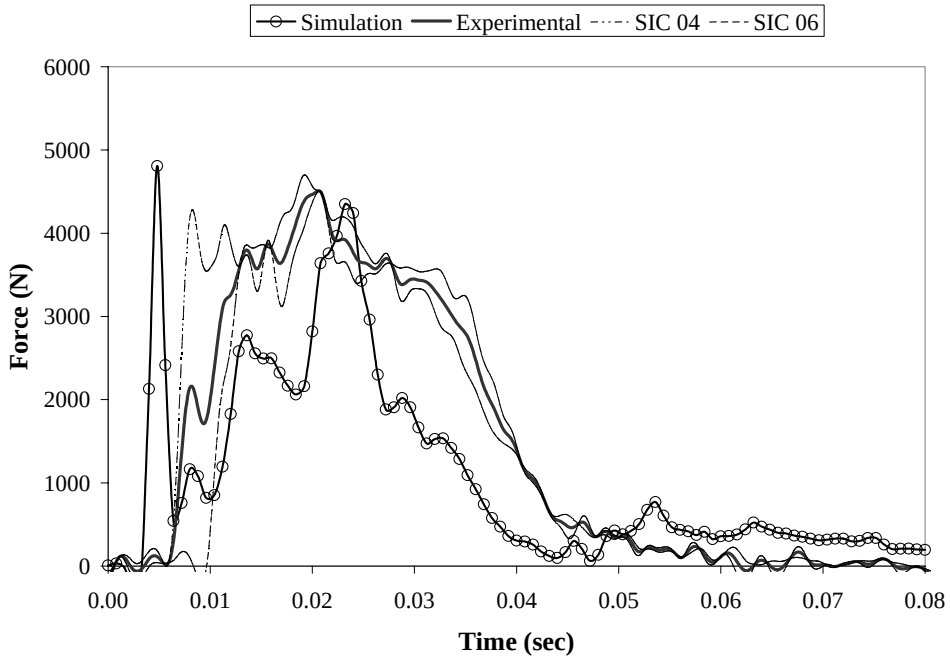

Figure A.29 Abdominal plate impact force

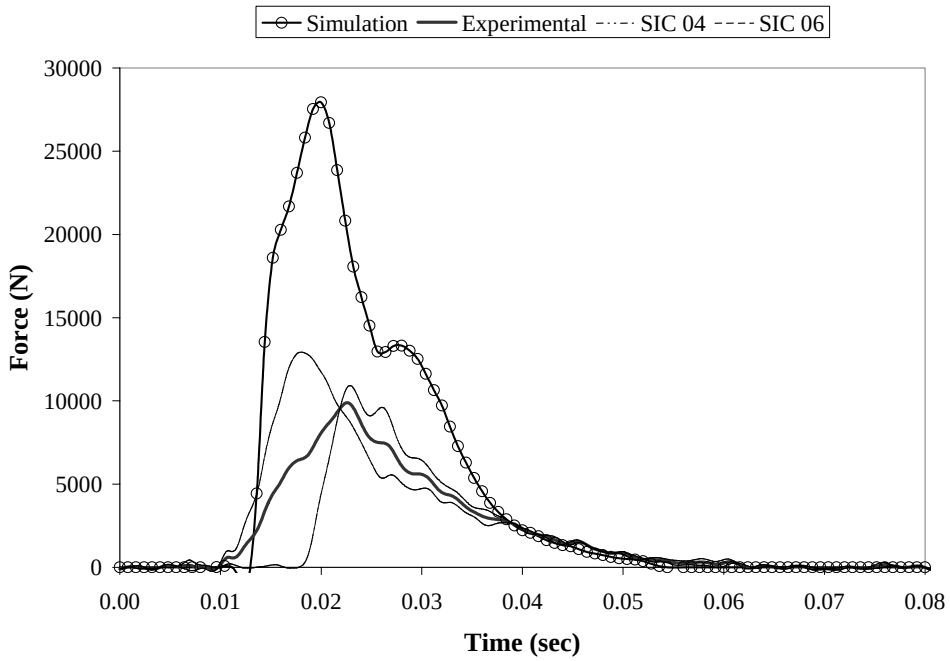

Figure A.30 Pelvic plate impact force

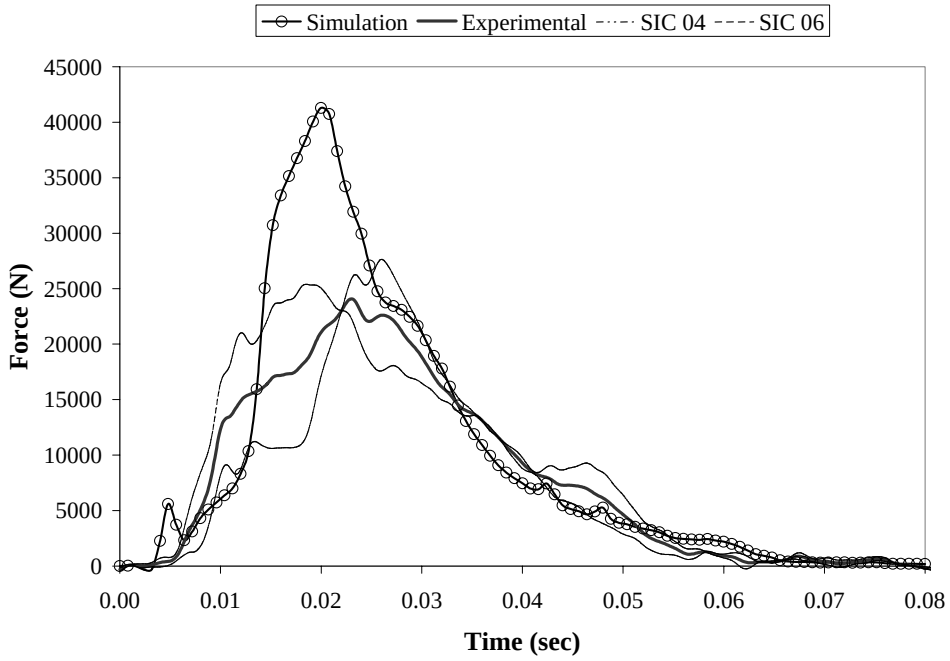

Figure A.31 Total plate impact force

Impulse

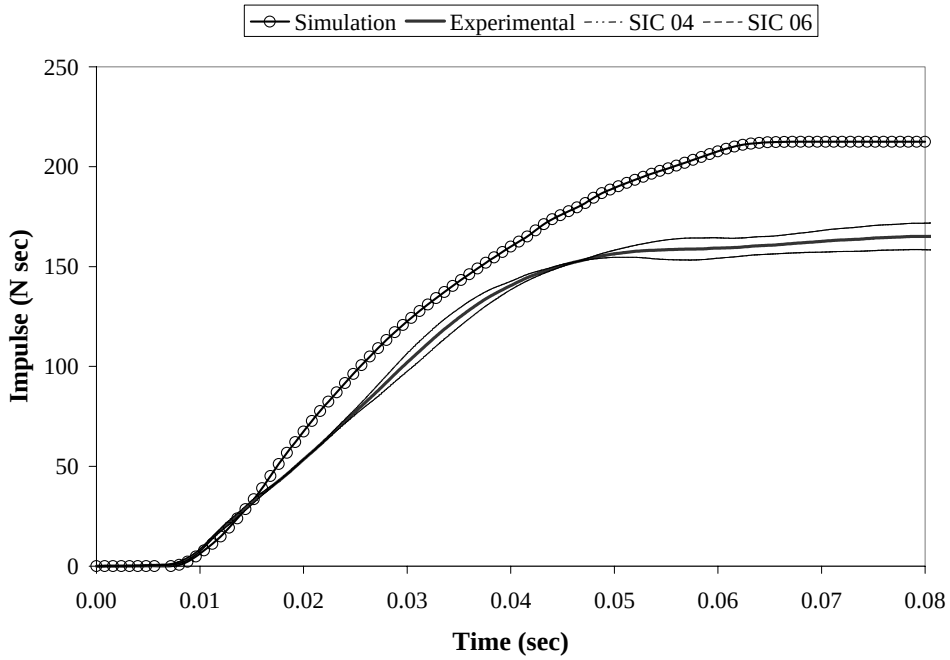

Figure A.32 Shoulder plate impact impulse

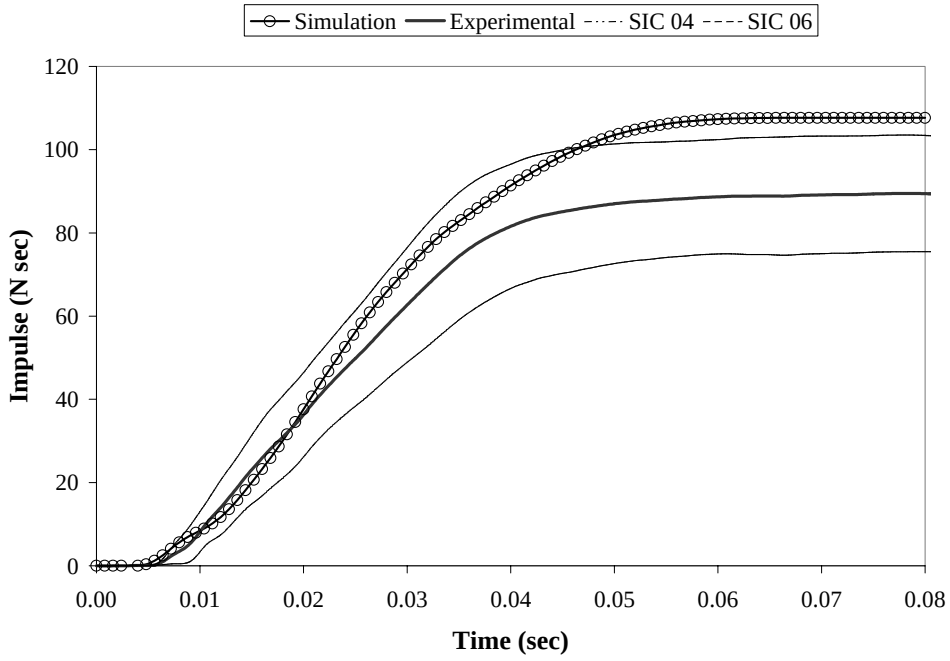

Figure A.33 Thoracic plate impact impulse

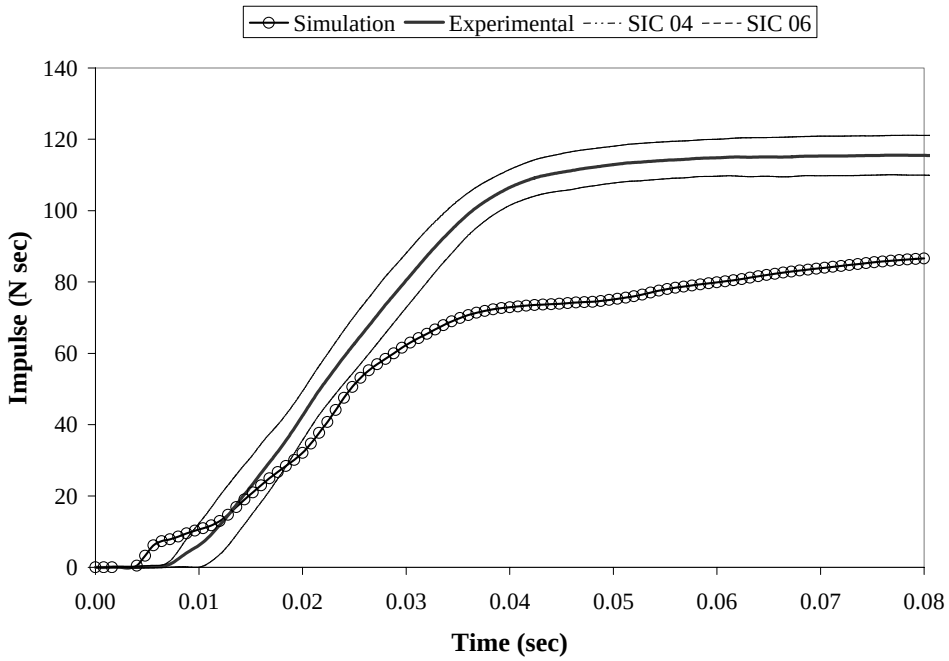

Figure A.34 Abdominal plate impact impulse

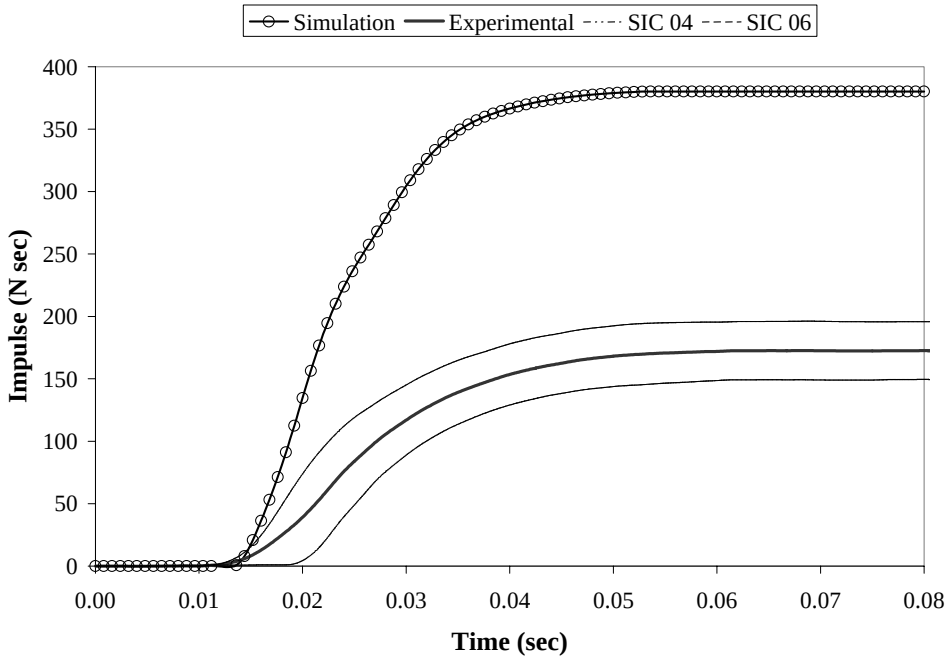

Figure A.35 Pelvic plate impact impulse

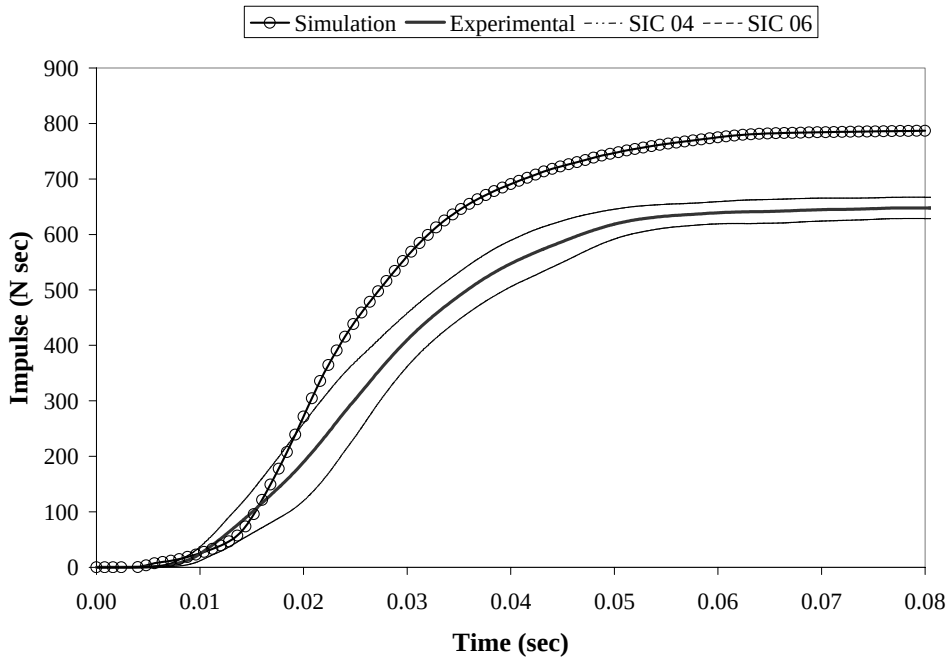

Figure A.36 Total plate impact impulse

Compression

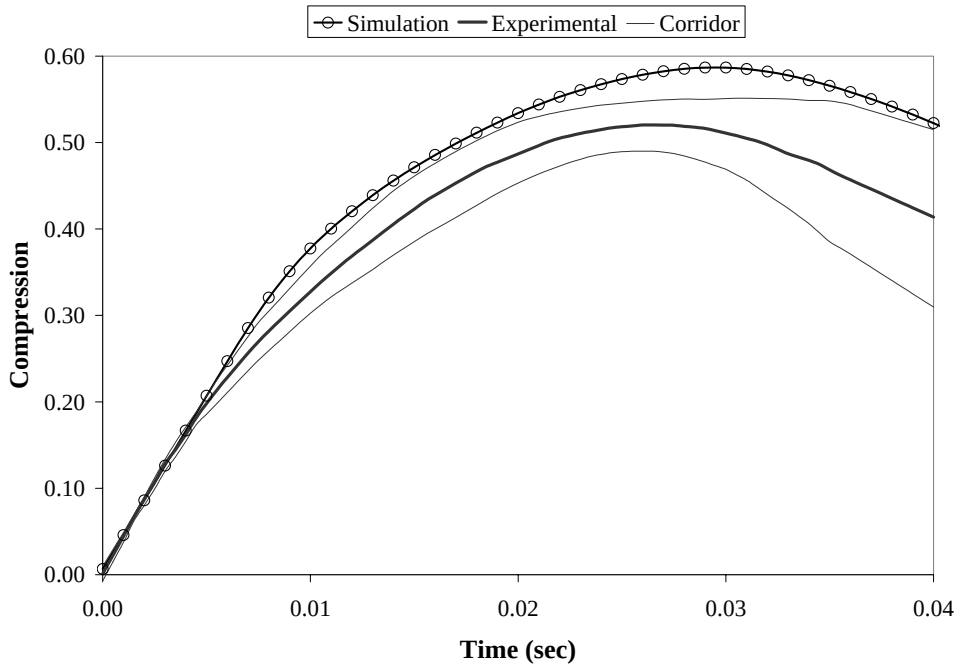

Figure A.37 Half width chest compression

VC

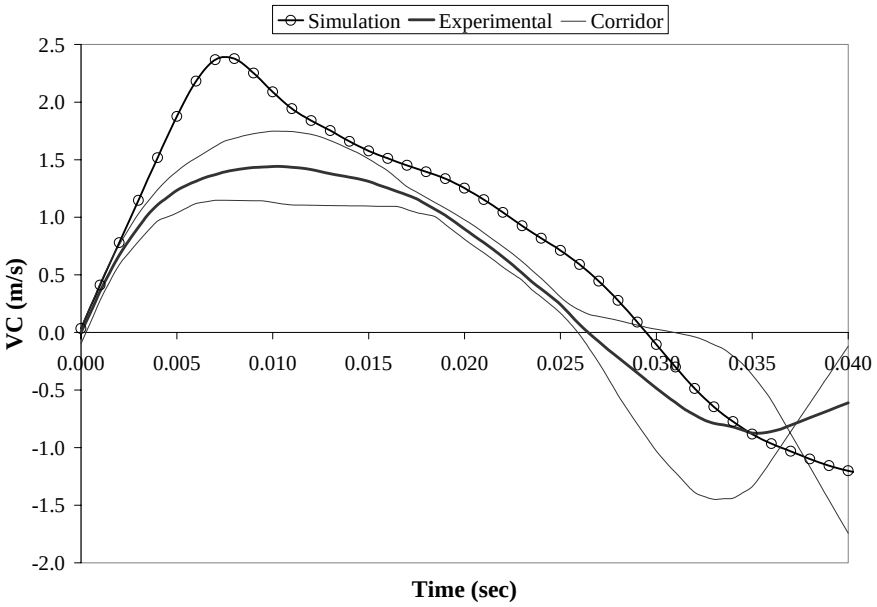

Figure A.38 Half width chest VC

Injury

Table A.1 WSU high-speed rib fracture locations

Rib	Test 4		Test 6		Model	
	Left	Right	Left	Right	Left	Right
1st	1	1	1	1	2	1
2nd	2		1		3	2
3rd	3		2		3	1
4th	2	1	2		3	
5th	2		2	1	3	
6th	2		2		2	
7th	2		1		3	
8th	2	1			4	
9th	2				2	
10th	1				2	
11th					2	
Total	22		15		33	

Appendix B

Modeling Blunt Ballistic Impacts – Canadian Biomaterials Society Abstract

Numerical Modeling of Blunt Ballistic Impacts to the Thorax

P.A. Forbes, D.S. Cronin

Department of Mechanical Engineering, University of Waterloo, Waterloo, Canada

INTRODUCTION

Blunt ballistic impacts to the thorax, defined as 20-200g projectiles impacting at 20-250 m/s [1], possess significant injury potential. These types of impacts may occur in common activities such as sports like baseball or lacrosse, and for less common impacts such as non-lethal projectiles for crowd control. Although a plethora of biomechanical data is available for automotive impacts, it has been shown that the human response differs in blunt ballistic impacts [1]. Understanding the biomechanics and injury response of the human body during an impact of this type is crucial to reducing injury.

A detailed numerical thoracic model [2,3,4] has been used to simulate blunt ballistic impacts to the torso. The model was originally developed for impacts observed in automotive crash scenarios and has been improved to model blunt ballistic impacts. The results have been compared against experimental testing performed on 13 post mortem human subjects with PVC impactors, representing typical non-lethal projectiles, under three impact conditions: 140g at 20 m/s, 140g at 40 m/s and 40g at 60 m/s [1].

METHODS

The model used for this study has undergone three iterations in development and incorporates representations of spine, ribs, heart, lungs, major blood vessels [2], rib cage, surface muscles and upper limbs, with improvements to several material models [3], and simplified representations of the abdomen, pelvis, legs and head [4].

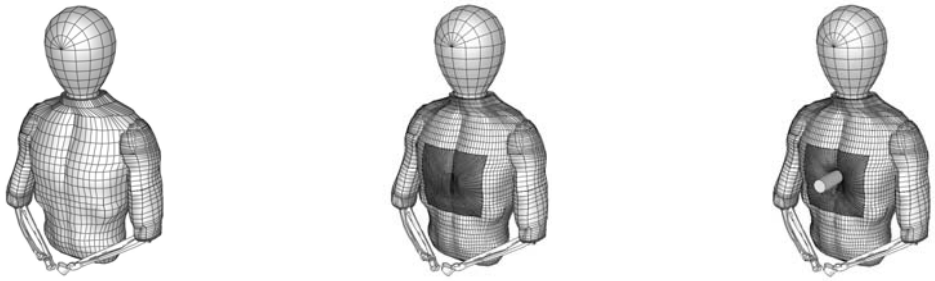

(a) (b) (c)

Figure 1 Detailed thoracic model (a) original mesh (b) refined mesh (c) mid-impact

Since this model was originally developed to simulate auto crash scenarios, which produce large global thoracic deformations, the original model was unable to accurately predict the more localized impact and deformation of blunt high velocity impacts. As a result development of the model for this study focused on refining the finite element mesh while making improvements to the soft tissue material properties and thoracic stiffness properties. The original model incorporated a relatively coarse mesh appropriate for auto crash. To address this, the mesh density of the impacted surface on the thorax was increased to better match the mesh density of the impacting object (Figure 1). The original model used an elevated density of the outer tissue and an elevated stiffness of the costal cartilage to account for mass distribution issues and thoracic stiffness issues

respectively [2][3]. While appropriate for auto crash, these properties increased the local stiffness and reduced resultant deflection when simulating NLW impacts. To eliminate these effects, the mass of the outer tissue at the impact surface was lowered to that of real soft tissue, and the stiffness of the costal cartilage was reduced to match data found in the literature [5].

Predicted force and deflection responses of the thorax under the three blunt ballistic impact conditions were compared against available post mortem human subject test data [1]. Force was measured by multiplying the acceleration of the impactor and its mass, and deflection was measured from sternum to spine following the techniques used to analyze the experimental test data.

RESULTS AND DISCUSSION

The predicted response of the torso falls within the experimental response corridors of both force and deflection and is in reasonable agreement with the average values. In all cases an early peak force was observed, indicative of initial contact between the impactor and outer tissue, followed by a secondary peak, indicative of contact between the outer tissue and internal components. The double peak occurs because of slight gaps between the outer tissue and surrounding components in the model, which causes a slight delay in the transferred force. Figure 2 shows both the predicted deflection and force response for the 140 g impactor at 20 m/s as compared to the average experimental results and experimental response corridors [1].

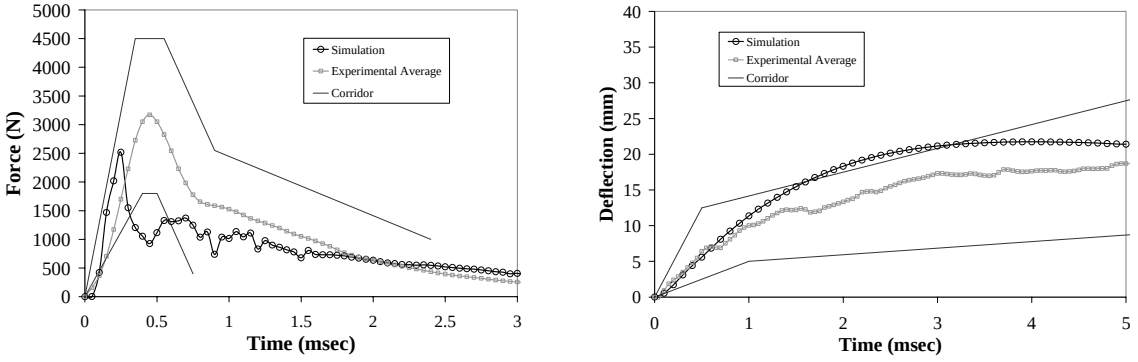

(a) (b)

Figure 2 Low mass high velocity impact results (a) force (b) deflection

The improvements made to the thoracic model highlight the importance of finite element mesh density and accurate material properties for simulating localized impacts such as those experienced during blunt ballistic impacts. The model improvements presented here produced accurate representations of the impact scenarios, providing insight into injury while proving the applicability of the model.

REFERENCES

[1] Bir, C.A et al., 2004, J. of Biomechanics, 37, 1, 73-79 [2] Deng, Y.C. et al., 1999, SAE Inter. Cong. and Exp., SAE Paper 1999-01-0715 [3] Chang, F., 2001, ASME Inter. Mech. Eng. Cong. and Exp., AMD-Vol. 251 [4] Forbes, P.A. et al., 2005, IUTAM Symp. on Impact Biomech. – Fund. Insights to App. [5] Viano, D.C., 1986, SAE Paper 861923